ACSNANO

www.acsnano.org

REVIEW

Single Atom Catalysts for Selective Methane Oxidation to Oxygenates

Pawan Kumar,* Tareq A. Al-Attas, Jinguang Hu, and Md. Golam Kibria*

Cite This: https://doi.org/10.1021/acsnano.2c02464

Read Online

ACCESS | Metrics & More | Article Recommendations

ABSTRACT: Direct conversion of methane (CH_4) to C_{1-2} liquid oxygenates is a captivating approach to lock carbons in transportable value-added chemicals, while reducing global warming. Existing approaches utilizing the transformation of CH_4 to liquid fuel via tandemized steam methane reforming and the Fischer−Tropsch synthesis are energy and capital intensive. Chemocatalytic partial oxidation of methane remains challenging due to the negligible electron affinity, poor C−H bond polarizability, and high activation energy barrier. Transition-metal and stoichiometric catalysts utilizing harsh oxidants and reaction conditions perform poorly with randomized product distribution. Paradoxically, the catalysts which are active enough to break C−H also promote overoxidation, resulting in CO_2 generation and reduced carbon balance. Developing catalysts which can break C−H bonds of methane to selectively make useful chemicals at mild conditions is vital to commercialization. Single atom catalysts (SACs) with specifically coordinated metal centers on active support have displayed intrigued reactivity and selectivity for methane oxidation. SACs can significantly reduce the activation energy due to induced electrostatic polarization of the C−H bond to facilitate the accelerated reaction rate at the low reaction temperature. The distinct metal−support interaction can stabilize the intermediate and prevent the overoxidation of the reaction products. The present review accounts for recent progress in the field of SACs for the selective oxidation of CH_4 to C_{1-2} oxygenates. The chemical nature of catalytic sites, effects of metal−support interaction, and stabilization of intermediate species on catalysts to minimize overoxidation are thoroughly discussed with a forward-looking perspective to improve the catalytic performance.

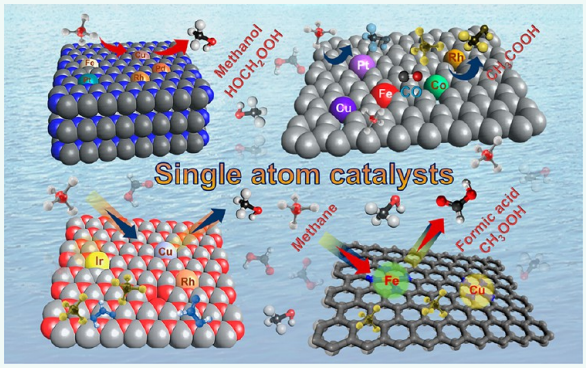

KEYWORDS: *single atom catalysts, greenhouse gas reduction, methane conversion, C−H activation, biomimetics, metal−support interaction, photocatalysis, two-dimensional materials, small molecules activation, density functional theory calculations*

1. INTRODUCTION

Methane, a greenhouse gas (GHG) 80 times more powerful than carbon dioxide (CO_2), is a prime component of natural gas and is used for 22% of the world's electricity production. Methane is the second most abundant anthropogenic GHG after CO_2, accounting for about 20% of global emissions.[1,2] Over 10 billion cubic meters/day of natural gas is produced per day to meet ever-increasing energy demands. Anthropogenic activities account for 60% of the total methane, while natural emissions (wetlands, swamps, wild ruminants, etc.) contribute the remaining 40%. Human sources include livestock, gas and petroleum exploitation, rice farming, mining (particularly coal mining), and landfills. Water reservoirs are another main source of methane which generate 1.3% of all greenhouse gases worldwide each year. The anthropogenic release of methane in the environment will accelerate global warming which will accelerate permafrost thawing.[3] Permafrost holds a significant organic matter in the frozen state, and when that material thaws in wet and anaerobic conditions, microorganisms can turn it into methane. The release of methane from permafrost will further intensify the thawing of more permafrost and methane emission.[4] Methane clathrate or methane hydrate ($CH_4{\cdot}5.75H_2O$) is the largest source of methane than all of the world's oil, natural gas, and coal resources combined which might be exploited in the near future for energy.[5] Horizontal drilling and hydraulic fracturing have already revolutionized shale gas production. The production of methane from shale gas avails the utilization of hydrocarbon trapped in sedimentary rock, however it poses

Received: March 11, 2022
Accepted: May 24, 2022

ecological challenges and climate change. In the recently held 26th session of the Conference of the Parties (CoP26) to the United Nations Framework Convention on Climate Change (UNFCCC) summit, considering the immediate contribution of methane to global temperature rise, 104 countries including the United States, Europe agreed to cut their CH_4 emissions up to 30% by 2030. As per the IPCC report, just 0.3% CH_4 reduction is equivalent to net-zero for CO_2, which can reduce further warming of the earth (Figure 1a,b).[6−9] To tackle the problem of rising CH_4 concentration, the leaking of CH_4 from oil and gas wells, pipelines, and other fossil fuel infrastructure will be reduced.

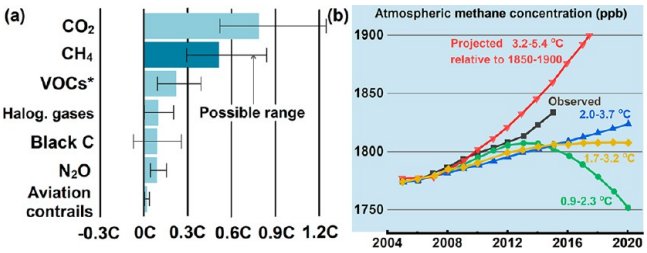

Figure 1. (a) The contribution methane in global warming Source IPCC six assessment report 2021.[6,7] (b) Atmospheric methane concentration (ppb) pathways from IPCC and observations from the NOAA measuring network. Adapted with permission under a Creative Commons CC BY 3.0 License from ref 8. Copyright 2016 IOP Science.

Methane is an essential chemical feedstock for many chemicals, such as methanol, olefins, aromatic hydrocarbons, acetic acid, dimethyl ether, and so on.[10] Therefore, the utilization of methane with high reaction efficiency has great potential for relieving energy crises and atmospheric pollution. The direct conversion of methane to value-added chemicals is incredibly challenging, as CH_4 is the most stable and inert hydrocarbon (ΔH_{C-H} = 104 kcal mol^{-1}: C−H bond dissociation enthalpy of 4.55 eV at 298 K). The dissociation of the first CH_3−H bond is even highly challenging due to small polarizability (2.84×10^{-40} C^2 m^2 J^{-1}) and requires almost 435 kJ mol^{-1} energy.[11] Methane is usually transformed into the syn-gas mixture by steam methane reforming (SMR) to produce chemicals, which is a highly endothermic process (consumes heat, ΔH_r= 206 kJ/mol) operating at 700−1000 °C and 3−25 bar pressure in the presence of catalysts. The produced hydrogen is mainly used for the production of ammonia. Additionally, the syn-gas mixture is used to produce synthetic fuels using Fischer−Tropsch synthesis (GTL technology). Recently, scientists have developed a technique of dry reforming for directly converting methane to carbon and hydrogen using molten tin, Ni:In alloy, and $MnCl_2$−KCl salts.[12−15] Though the overall process is carbon negative with intensive energy requirements, storage/transport of hydrogen, unutilized carbon, and loss of tin catalyst with produced carbon are baffling challenges. The complete oxidation of CH_4 to CO_2 in solid oxide fuel cells to generate electricity is also being investigated; however, high operating temperature (300−700 °C), rapid drop in efficiency due to coke deposition, and sulfur poisoning are other unsolved issues.[16,17] Another, approach to utilize methane as a feedstock is thermocatalytic nonoxidative partial dehydrogenation to alkenes and aromatics which requires high temperature. Partial dehydrogenation is advantageous over complete dehydrogenation, as it produces platform chemicals that can be directly used for the chemical synthesis along with hydrogen. Again, the lack of suitable catalysts that can work at low temperatures with a satisfactory conversion rate is an obstacle.

The transformation of CH_4 to liquid oxygenates products is considered a holy grail to use widely abundant natural gas as a feedstock to produce chemicals with added value.[18,19] Partial oxidation of CH_4 to oxygenates via oxidative dehydrogenation using O_2 as oxidant at high temperature has been implemented intensively on various metal oxides and metal-supported catalytic systems. However, after the first C−H bond cleavage, preventing further oxidation at elevated temperature becomes challenging, and CO and CO_2 are produced dominantly, sacrificing the input energy and CH_4 feedstock. Also, catalytic surface deactivation, due to coking, oxidation, and sulfur poisoning (from crude CH_4 feed), are inevitable. Low-temperature oxidation of CH_4 to liquid oxygenates is desirable to substitute energy-intensive protocols. Though the electrochemical approach presents significant promise such as low temperature and modular design, the lack of active and selective catalysts and overoxidation of CH_4 to CO_2 are some of the key challenges for practical application.[20−23] Additionally, the use of external oxidants such as H_2O_2 should be avoided by developing catalytic systems which can in situ produce reactive oxidation species (ROS) from water. Engineering catalysts with a high affinity toward C−H bond activation to selectively produce value-added products is an active area of research that can solve major energy and global warming-related issues. Several catalytic systems composed of the metal complexes such as Hg, Pt, Pd, Au, Ru, Rh, and V have been explored, but low catalytic activity, the requirement of corrosive acids, unselective oxidation, and difficult/non-feasible separation remain an obstacle.[24−28] Other components such as molecular sieves, ZSM-5, metal−organic frameworks (MOFs), etc., have also been investigated for the direct methane conversion.[29−32] The large energy gap between the highest occupied molecular orbitals (HOMO) and lowest unoccupied molecular orbitals (LUMO), weak polarizability ($2.84 \times 10-40$ C^2m^2 J^{-1}) with identical electronics environment, high ionization energy (≈12.6 eV),[33] low proton affinity (543.9 kJ mol^{-1})[34] and weak acidity ($pK_a \approx 48$)[35] make CH_4 activation via the first C−H bond cleavage a highly unfavorable reaction.[36] Despite the inactivity of the CH_4 molecule, it can be activated due to the fractional contribution of the ionic resonance structure. As per calculations by Hiberty and Cooper, the resonance structures of CH_3−H are composed of 74% ground state and 26% ionic ($CH_3^+H^-$ and $CH_3^-H^+$) resonance structures.[37] Transition metal with d-orbital (d_{z^2}, d_{xz} and d_{yz} orbitals) can supply electrons to empty C−H σ^* antibonding MO while facilitating the back-donation of electrons from C−H σ bonding MOs. Transition-metal catalysts either in a nanomorphological state such as colloids, nanoparticles, or immobilized on a support have shown great promise to activate the C−H bond of methane.[38,39] Unfortunately, they are nonselective and produce a number of oxygenates such as CH_3OH, methyl hydroperoxide (CH_3OOH), and formic acid (HCOOH) and rely on H_2O_2 as an oxygen source.[40] Further controlling the oxidation degree is another challenge for selective methane oxidation. The size reduction of transition metal catalysts in nanoregime is found to increase the catalytic performance due to increased surface energy of the activated catalytic centers. However, stabilization of small subnanoparticles is challenging due to agglomeration,

https://doi.org/10.1021/acsnano.2c02464
ACS Nano XXXX, XXX, XXX−XXX

leading to the deactivation of catalytic sites. The stabilization of nanoscopic particles in the support matrix has been found useful to maintain the catalytic activity. Further, improvement in the catalytic performance can be achieved by careful selection of support materials that stabilize the intermediate and synergistically improve the performance. Even though the catalytic performance is increased by reducing the size of the nanoparticles, selectivity remains an issue. The presence of unidentical catalytic sites on different exposed facets and corners leads to a wide range of product distribution. Further, size reduction of metal from nano to atomic regime displayed entirely new properties absent in bulk material. Reducing the size of metal increases the gap between the energy levels due to the quantum size effects and discretization of energy levels.[41] Under atomic dispersion, nonreactive metals such as Au become extremely active.[42,43] This concept led to the development of single atom (SA) catalysis by atomically distributed metal on stabilizing supports. Though the effect of size on activity and selectivity was known for years, the seminal work of Flytzani-Stephanopoulos and Pérez-Ramírez and finally affirming Pt SA on FeO_x surface revolutionized the research in this direction.[44−46] Recently, single atom catalysts (SACs) have gained significant attention for the selective conversion of CH_4 due to their potential to drive catalytic reactions under mild reaction conditions. SACs with homogeneous distribution of metal and specific coordination with support can afford a higher activity and selectivity for methane oxidation. Despite the wide potential of SACs in CH_4 oxidation and possible further development, only few experimental studies are available. Most reports are limited to density functional theory (DFT) modeling and very few catalysts have been evaluated in the laboratory. However, these studies have fueled the research to develop robust, selective, and economical catalysts for scissoring the C−H bond of CH_4 to produce high-value products and minimize the impact on climate. This review focuses on the recent advances in chemical fixation of CH_4 using SACs under mild reaction conditions (Figure 2). The structural coordination, chemical reactivity, and mechanism of CH_4 oxidation are investigated in detail while covering the computational studies predicting the structural and catalytic properties of catalysts. The metal−support interaction, defect/dopant engineering, and photoactive SACs are primely discussed considering future modification that will lead to more exotic materials with high activity and selectivity.

2. SINGLE ATOM CATALYSTS: BIOMIMETIC CATALYST FOR CH_4OR

The C−H bond activation is an essential part of biological survival, and several enzymatic systems have evolved for the selective cleavage of C−H bonds. In nature, methanotrophic bacteria containing methane monooxygenase (MMO) and anaerobic archaea with methyl coenzyme M reductase (MCR) metalloenzymes can selectively transform methane to oxygenates (methanol) and hydrocarbons via C−H bond activation.[3,47] Usually, two MMOs named particulate methane monooxygenase (pMMO) with a copper active site and soluble methane monooxygenase (sMMO) with diiron sites are the main catalytic centers to promote CH_4 activation.[48] Figure 3a,b displays the structure of the di-iron-based sMMO enzyme coordinated with two histidine and four glutamate ligands.[49,50] The CH_4OR occurs at a carboxylate-bridged diiron center of a hydroxylase protein (MMOH) where the active site resides in

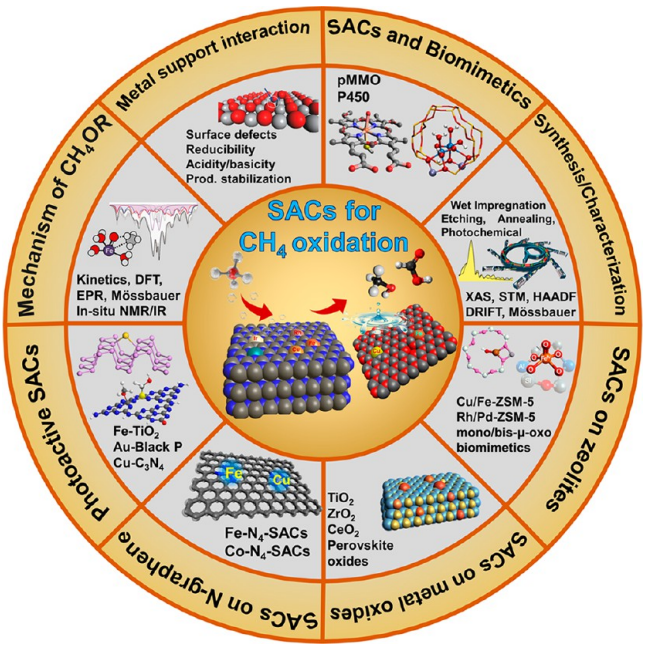

Figure 2. Outline of the review showing various dimensions of SACs for methane oxidation.

a four-helix bundle of the α-subunit. The ground state diiron(III) sites ($MMOH_{ox}$) are bridged with two hydroxide ligands which form diiron(II) after the reduction ($MMOH_{red}$) in which one Fe remains bonded to the H_2O ligand, while the second Fe site is available for C−H bond activation.[49,51] Similar to Fischer−Tropsch which converts gas to liquid, bio-GTL using methanotrophs is proposed; however, low turnover numbers of 0.16−13 s^{-1} posed upstream challenges.[52] Genetic engineering is a parallelly explored option that is yet to overcome the issue of stability under contaminants present in natural gas and gene expression in heterologous hosts.[53] Cytochrome P450s (P450s), another class of enzymes that utilizes a similar C−H bond activation mechanism as MMOs, are a better alternative for methane oxidation due to their ubiquitous nature (Figure 3c).[54,55] Usually, these enzymes are composed of a large protein molecule containing a metal center in a macrocyclic assembly. The most pertinent examples of such enzymes are cytochrome P450s constituted of a heme center with a single Fe-thiolate linkage which plays a significant role in a variety of reactions from the oxidation of fatty acid/toxins to the biosynthesis of various molecules such as hormones etc.[56] The iron metal center in the heme unit can form a high-valent iron(IV)-oxo porphyrin π-cation radical intermediate which promotes C−H bond activation via proton abstraction.[57] Figure 3d displays the proposed catalytic cycle of dioxygen activation and oxygen atom transfer by cytochrome P450 enzymes (CYP 450) involving high-valent iron(IV)-oxo porphyrin π-cation radicals for C−H bond activation.[58]

Indeed, metallozymes are nature's meticulous engineering which sustains several biological and environmental processes (i.e., carbon cycle). They suffer several drawbacks (poor efficiency, deactivation/denaturation in oxidative/harsh environment) to deploy at the industrial scale. On the other hand, bioinspired catalysts may have an added advantage over metalloenzymes due to its scalability, robust catalytic sites, and wide substrate scope either via the same catalysts or manipulation of chemical structure.[59] Like natural mono-

https://doi.org/10.1021/acsnano.2c02464
ACS Nano XXXX, XXX, XXX−XXX

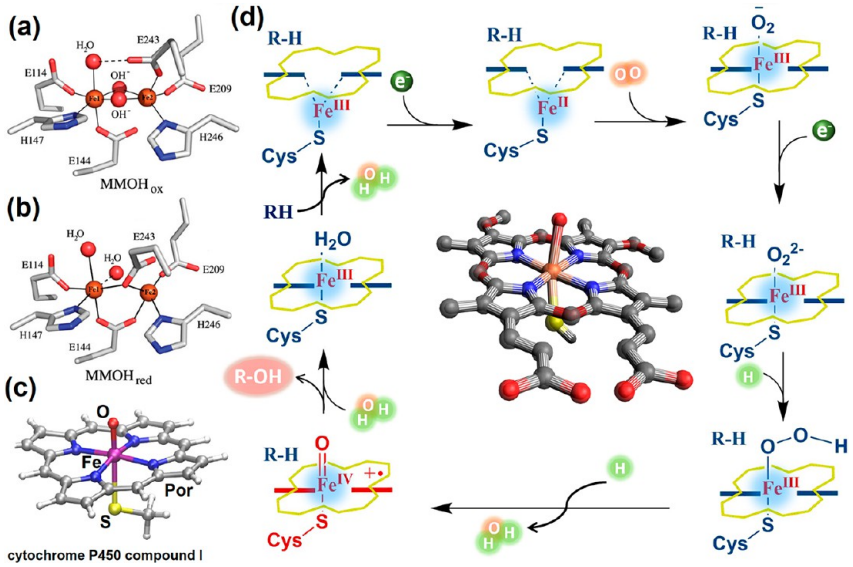

Figure 3. Diiron active site structures of (a) Mc MMOHox (PDB ID 1MTY) and (b) Mc MMOHred (PDB ID 1FYZ). Reprinted with permission from ref 49. Copyright 2011 American Chemical Society. (c) Chemical structure of cytochrome P450 compound I. Reprinted with permission from ref 54. Copyright 2021 Elsevier (d) Proposed catalytic cycles of CYP 450 Adapted with permission from ref 58. Copyright 2007 American Chemical Society.

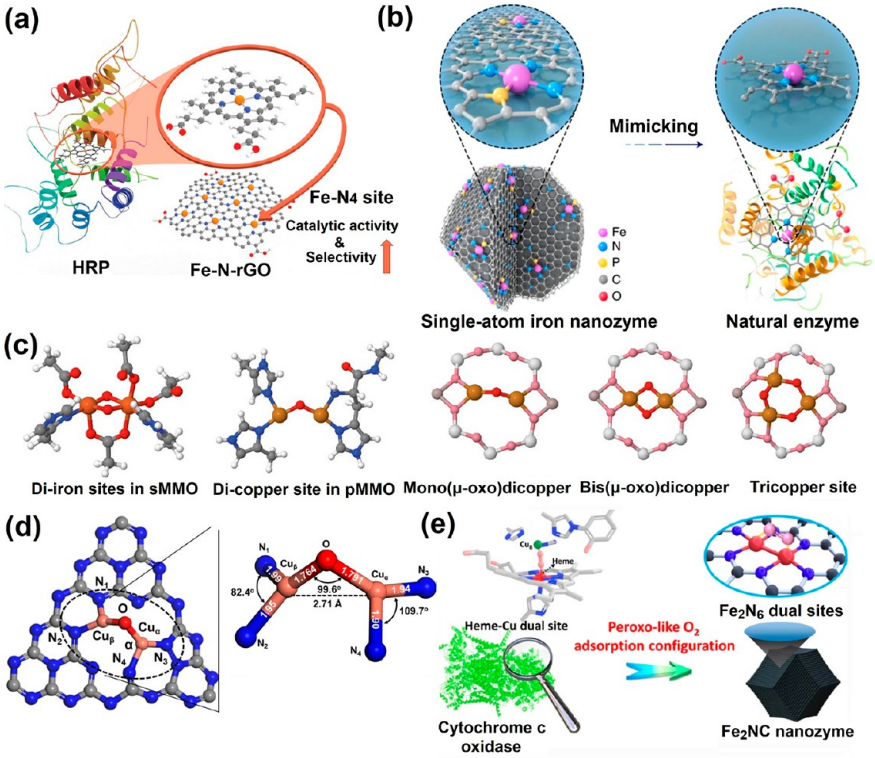

Figure 4. (a) Fe-N-rGO mimicking the cofactor structure of HRP. Reprinted with permission from ref 80. Copyright 2019 Wiley-VCH. (b) The chemical structure similarity of MOF-derived FeN_3P-SAzyme with HRP enzyme promotes better peroxidase-like activity. Reprinted with permission from ref 81. Copyright 2021 Springer Nature. (c) Structural similarity between natural di-iron and dicopper sites s/pMMO enzymes versus zeolite-based copper catalysts active sites for methane oxidation.[98−100] Reprinted with permission from ref 82. Copyright 2019 Springer Nature. (d) Oxo dicopper anchored carbon nitride ($Cu_2@C_3N_4$) mimicking the structure of pMMO and used for photocatalytic methane oxidation. Reprinted with permission under a Creative Commons CC-BY License from ref 96. Copyright 2022 Springer Nature. (e) Peroxo-like O_2 adsorption configuration of cytochrome *c* oxidase and Fe_2NC nanozyme. Reprinted with permission from ref 97. Copyrights 2022 Tsinghua University Press and Springer.

metallic pMMO and P450 enzymatic systems which utilize hypervalent single metal sites for the catalytic activation of CH_4, many catalysts with isolated metal sites have been developed in recent years. For example, MOFs with exposed metallic centers have displayed improved CH_4 catalytic activity.[60,61] In a recent report, Simon et al. demonstrated

https://doi.org/10.1021/acsnano.2c02464
ACS Nano XXXX, XXX, XXX−XXX

that a MOF with Fe(II) sites within Fe_3-μ_3-oxo nodes can promote selective oxidation of CH_4 to CH_3OH.[62] In another example, Baek et al. utilize imidazole units of MOF-808 MOF as a protein backbone for the metalation to form pMMO type bis(μ-oxo)dicopper active sites for CH_4 oxidation to methanol.[63] The maximum methanol yield using MOF-808-Bzz-Cu as a catalyst at 150 °C was 71.8 ± 23.4 μmol $g_{MOF\text{-}808\text{-}L\text{-}Cu}^{-1}$. Unfortunately, poor yield, along with the requirement of high temperature, tedious synthesis, and vulnerability of degradation of organic ligands, remains an issue. Single atom catalysts constituted of isolated SA decorated on active supports are an attractive alternative to conventional catalytic systems due to their specific geometric configuration, high reactivity, and selectivity.[64,65] SACs can achieve a high atomic economy like homogeneous catalysts due to the populated concentration of isolated SAs on catalysts surface, while at the same time they are recyclable like heterogeneous catalysts.[66] Additionally, due to the presence of under-coordinated atomic sites and strong metal−support interactions, SACs can promote reactions at an accelerated rate while maintaining selectivity.[67] The specific coordination of metal centers with support makes them thermally and chemically stable due to the ensemble effect. SACs have been widely studied for a plethora of selective reactions such as CO oxidation, selective hydrogenation of alkenes, aromatics, nitroaromatics, biomass conversion (including oxidative dehydrogenation), oxygen reduction reactions, CO_2 photo/electro/photoelectrocatalytic reduction, NO reduction, water splitting, etc.[68−74] Since metal centers in SACs occupy a well-defined coordination environment on support, entirely new catalytic properties are manisfested. Like metallozymes in biological systems where metal centers coordinated with ligand and proteins scaffold can achieve almost 100% selectivity, SACs with precise coordination environment displayed high selectivity for a variety of organic reactions.[64,66] Considering the structural similarity and specificity, SACs can work as bioinspired single atom nanozymes (SAzymes) to mimick several bioenzymatic reactions.[75,76] Numerous SAzymes have been developed in the recent past, demonstrating compelling performance for several biological and chemical reactions.[77] SAzymes can work in harsh reaction conditions without deactivation, and in contrast to metallozymes, SACs can promote a wide variety of reactions. The most promising category of SAzymes is M-N_4-C catalyst supported on graphenic or carbon backbones.[78,79] The M-N_4 mimics the metal porphyrin counterpart of biological enzymatic systems, while the carbonaceous backbones immitate the protein part and serve as a scaffold for the SAs. However, compared to the protein counterpart which controls the three-dimensional (3D) shape and geometry and ligand-exchange chemistry, the C scaffold in M-N_4-C catalysts controls the charge distribution and concomitantly the activity of the metal center. The porphyrinic structure is an essential component of many enzymes and electrons/gas transport relays such as cytochrome, peroxidase, hemoglobin, myoglobin, etc. Among all available possible metal variants, Fe-N_4-C components are most appealing due to their high activity originating from specific affinity to oxygen and facile $Fe^{(IV)}$═O formation. Kim et al. reported that Fe-N_4 single site embedded graphene (Fe-N-rGO) catalysts displayed excellent peroxidase-like activity reaching 5 million times higher activity per iron ion compared to Fe_3O_4 NPs (Figure 4a).[80] The reactivity/selectivity of these SAzymes can be controlled/increased by manipulating the coordination patterns of metal in the ring (M-N_{3-5}, M_2-N_{5-6}), N atom exchange with other heteroatoms, and doping of carbonaceous scaffold. For example, Ji et al. demonstrated MOF and hexachlorophosphazene-mediated synthesis of the N substituted FeN_3P-SAzyme, which has applications in the therapeutic strategy for inhibiting tumor cell growth due to superior peroxidase-like activity (Figure 4b).[81] Considering the CH_4OR, these SAzymes share similar features to P450 and can promote room temperature oxidation of CH_4 to oxygenates. In nature, mono/di oxo iron/copper sites containing s/p-MMO achieve the anaerobic oxidation of CH_4 to oxygenates (Figure 4c).[82] However, their industrial-scale implementation including bioreactor digestion or enzyme extraction is tedious due to the denaturation of enzyme. On the other hand, many artificially synthesized μ-oxo mono/di/tri copper centers supported in mesoporous silica which might be tagged as dual single atom catalysts (DSACs) have demonstrated selective aerobic oxidation of methane to oxygenates (Figure 4c).[82−85] However, SAzymes and μ-oxo dual metal catalysts require pressurized CH_4 and H_2O_2 as oxidants, which should be excluded to afford sustainable biomimetic conversion and reduce the overall cost of the process. Interestingly, photoactive SACs have shown great promise since they can produce H_2O_2 from water oxidation and promote CH_4OR in situ using abundant light as an energy source. Besides conventional support materials, several new materials with tuned cavity, optoelectronic properties, and coordination have increased research on the synthesis of user-tailored SACs. Black phosphorus (BP) and carbon nitride (CN) with specific bonding and visible absorbing nature are materials of choice.[86−90] Like photosystem-II of natural photosynthesis, where chlorophyll (Mg-chlorin; the slightly reduced form of porphyrin) absorbs the visible photon and generated holes to oxidize water (electrons flow to reduction sites), certain materials mimicking natural light harvesters can afford artificial water splitting under visible light. For example, modified CN (K and −C≡N) nanozyme displayed efficient in situ generations of H_2O_2 from water/light followed by glucose oxidation mimicking the peroxidase enzyme.[91] Similarly, Cu SA stabilized in heptazine's N cavity can achieve selective CH_4OR to CH_3OH and even C_2H_5OH.[92] A new population of catalysts with two or more isolated metal centers working cooperatively is emerging which can overcome the issue of isolated centers and mimics more complex biological systems. Many homo and heteronuclear DSACs have been designed recently demonstrating superior performance for various applications.[93,94] The cooperative interaction in two SA sites can impart an activity and selectivity that is not possible even after doubling-tripling the concentration of SACs. For example, iridium SA pinned on TiO_2 (Ir_1/TiO_2) displayed 38% selectivity and 87% conversion toward nitro-styrene reduction, while Mo SA on TiO_2 (Mo_1/TiO_2) was almost inactive for the reaction. Fascinatingly, when a heteronuclear DSAC composed of Ir and Mo (Ir_1Mo_1/TiO_2) exhibited a >96% at 100% conversion.[95] These concepts are exploited in CH_4OR too, where homonuclear DSACs composed of either Cu and Fe sites displayed better performance. For example, pMMO-like oxo-dicopper moiety containing CN catalysts can sustain the methane oxidation rate higher than the benchmark Cu/ZSM-5 catalyst (Figure 4d).[96] In another work, Fe_2N_6 dimer with two iron supported on graphene network could activate the O_2 atom due to per-oxo-like O_2 adsorption configuration (Figure 4e).[97−100] Despite the advancement, the use of heteronuclear

https://doi.org/10.1021/acsnano.2c02464
ACS Nano XXXX, XXX, XXX−XXX

Table 1. Various Strategies for the Synthesis of Sacs and Representative Examples[a]

Methods	Representative Examples	Ref.	Methods	Representative Examples	Ref.
Wet impregnation	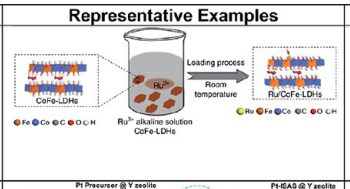	112	Co-precipitation	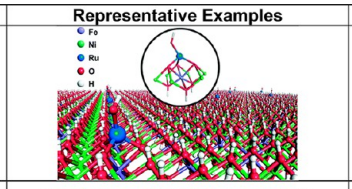	114
In-situ confinement	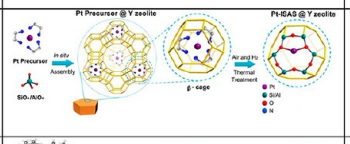	116	Anchoring on defects	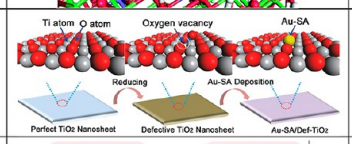	117
Ionic liquids assisted synthesis	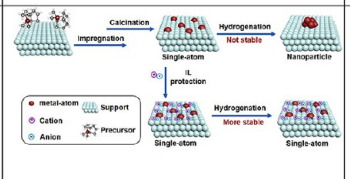	118	Bulk Nanoparticles to SACs	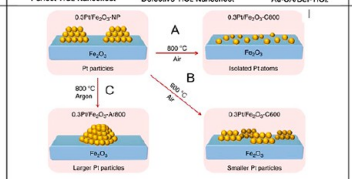	119
Carbonization	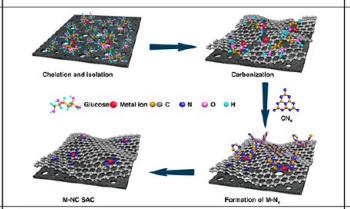	120	Template assisted shape control	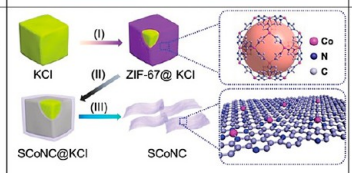	122
Carbon quantum dots assisted synthesis	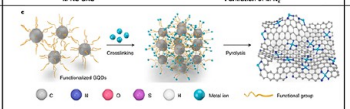	123	Chemical etching		124
MOF assisted synthesis	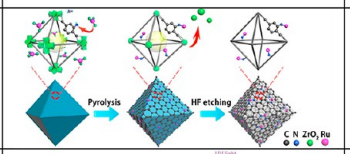	125	Laser-assisted solid-phase synthesis	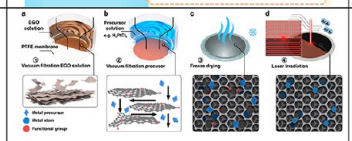	127
Photochemical	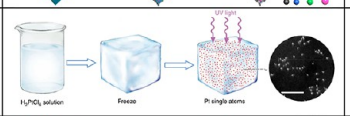	128	Gas transport approach	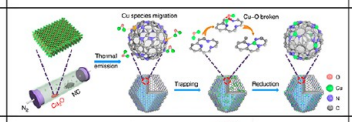	129
Solid diffusion synthesis	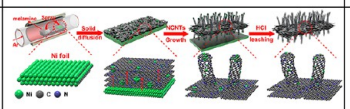	130	Chemical structure modification of carbon support	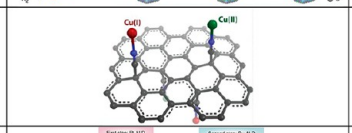	134
Ball milling	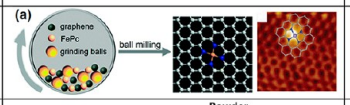	139, 140	Atomic layer deposition	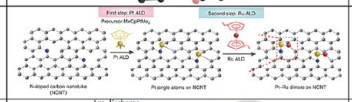	136
Flame spray pyrolysis	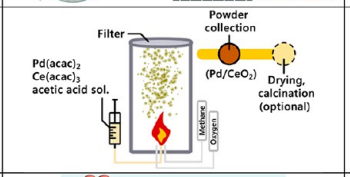	137	Arc discharge	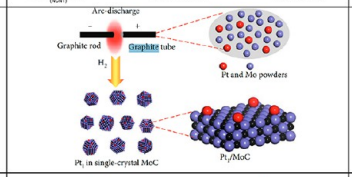	141
Galvanic replacement	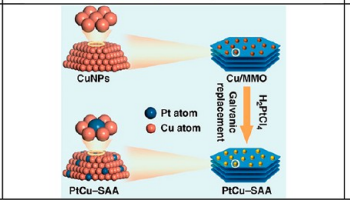	145	Electrochemical deposition	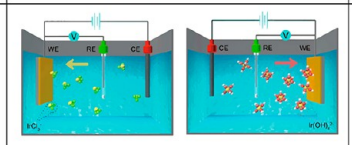	147

[a]Figures in the table are reprinted with permission from the respective references. Reprinted with permission under a Creative Commons CC-BY License from ref 112. Copyright 2019 Springer Nature. Reprinted with permission from ref 114. Copyright 2019 Royal Society of Chemistry. Reprinted with permission from ref 116. Copyright 2019 American Chemical Society. Reprinted with permission from ref 117. Copyright 2018 Wiley-VCH. Reprinted with permission from ref 118. Copyright 2019 Elsevier. Reprinted with permission under a Creative Commons CC-BY License from ref 119. Copyright 2019 Springer Nature. Reprinted with permission under a Creative Commons CC-BY License from ref 120.

https://doi.org/10.1021/acsnano.2c02464
ACS Nano XXXX, XXX, XXX−XXX

Table 1. continued

Copyright 2019 Springer Nature. Reprinted with permission from ref 122. Copyright 2019 Wiley-VCH. Reprinted with permission from ref 123. Copyright 2021 Springer Nature. Reprinted with permission from ref 124. Copyright 2021 Wiley-VCH. Reprinted with permission from ref 125. Copyright 2017 American Chemical Society. Reprinted with permission under a Creative Commons CC-BY License from ref 127. Copyright 2021 Springer Nature. Reprinted with permission under a Creative Commons CC-BY License from ref 128. Copyright 2017 Springer Nature. Reprinted with permission under a Creative Commons CC-BY License from ref 129. Copyright 2019 Springer Nature. Reprinted with permission from ref 130. Copyright 2019 Elsevier. Reprinted with permission from ref 134. Copyright 2019 Wiley-VCH. Reprinted with permission under a Creative Commons CC-BY License from ref 136. Copyright 2019 Springer Nature. Reprinted with permission from ref 137. Copyright 2021 Springer Nature. Reprinted with permission from ref 139. Copyright 2019 Royal Society of Chemistry. Reprinted with permission under a Creative Commons CC BY-NC 4.0 License from ref 140. Copyright 2015 AAAS. Reprinted with permission under a Creative Commons CC BY-NC 4.0 License from ref 141. Copyright 2020 SPJ and AAAS. Reprinted with permission under a Creative Commons CC-BY License from ref 145. Copyright 2019 Springer Nature. Reprinted with permission under a Creative Commons CC-BY License from ref 147. Copyright 2020 Springer Nature.

DSACs that can produce interesting chemistry are not explored for CH_4OR leaving plenty of room for future investigation. Furthermore, bioinspired complex oligomeric homoheteronuclear isolated site catalysts capable of promoting two or more reactions selectively will bolster the catalysis field.

3. SYNTHESIS OF SACS

Since the advent of heterogeneous catalysis, synthetic chemists have been trying to manipulate the morphological and chemical structures of catalysts to improve their catalytic performance. For example, size reduction, exposing specific planes to control the nature of catalytic centers, and alloying to get synergistic effect are widely investigated in the past century.[101] Among these, size reduction demonstrated the most profound effect on the catalytic activity. Subnanometer size reduction in metal nanoclusters brings up entirely new catalytic properties due to increased quantum confinement, unsaturated coordination sites (catalytic sites), and better utilization of metal content.[102,103] Further, size reduction to atomic-scale avails the maximum utilization of metal and the ability to control product selectivity due to uniform catalytic centers like in homogeneous catalysts. Unfortunately, the atomic size reduction also increases the surface energy which makes them vulnerable to agglomeration.[66,104] Thus, controlling the atomic distribution of SAs on the supporting material is challenging and requires an appropriate selection of the latter that can favorably coordinate with SAs to exclude agglomeration. As a general rule, the coordination strength between SAs and the neighboring support atoms (M−S) should be higher than metal−metal (M−M) bonds to prevent agglomeration.[105] The past decade has witnessed a significant advancement in the design of stable and inexhaustible SACs. Many dedicated review articles discussing various strategies of the synthesis of SACs and their pros and cons are already available.[72,106−109] For readers' understanding, only a brief discussion summarizing key synthetic protocols, advantages/disadvantages, and limitations are discussed and summarized in Table 1. The wet impregnation (WI) method is the most common and widely utilized approach for the SACs synthesis, which entails the soaking of support materials in a very dilute solution of the metal salt that prevents immediate contact of two metallic entities during deposition on the support. These porous supporting materials including high surface area silicates and oxides are frequently used for the deposition of SAs. Despite the simplicity, the agglomeration due to Ostwald ripening and removal of ligand leads to agglomeration and induces unsymmetrical size distribution.[110] To improve the dispersibility and exclude aggregation, porous and defect-rich surfaces, and high surface area materials such as MOF and zeolites, are also used.[106,111] Other approaches include the intercalation of SAs in layered materials. For example, Li et al. demonstrated the synthesis of ruthenium anchored CoFe-LDHs (Ru/CoFe-LDHs) SACs via a simple mixing of ruthenium precursor and LDH which displayed superior OER performance.[112] Hydrolyzing the $RuCl_3$ followed by binding with the surface hydroxyl groups on LDHs. Postsynthesis decoration of CN with SAs is mainly achieved by the WI approach in which metal ions become entrapped in the heptazine (C_6N_7) cavity via coordination with terminated pyridinic nitrogen.[113] The coprecipitation further widens the scope of WI by adjusting the pH of the solution, adding a small concentration of reducing agents such as $NaBH_4$, NH_2NH_2, $NaCO_3$, etc. The reduction of a metal precursor followed by deposition on support led to a robust bonding stabilizing the SACs. For example, Qiao et al. synthesized Pt_1/FeO_x catalysts using $H_2PtCl_6{\cdot}6H_2O$ and $Fe(NO_3)_3{\cdot}9H_2O$ precursors by adjusting pH using Na_2CO_3 as a weak base followed by calcination.[46] In another example, Wang et al. demonstrated the synthesis of Ru SA deposited on a monolayer NiFe-LDH via coprecipitation of $Ni(NO_3)_2{\cdot}6H_2O$, $Fe(NO_3)_3{\cdot}9H_2O$, and $RuCl_3{\cdot}3H_2O$ in a pH-adjusted solution using formamide as a weak reducing agent. Interestingly, Ru atom was not randomly distributed but confined to the top of the Fe-metal atom and coordinated to three Fe atoms.[114] In the above-mentioned approach controlling the coordination environment of SAs, stabilization of SA on specific sites/ligands remains a challenge. The confinement of SA on a specific position in the substrate during in situ synthesis is possible by using certain ligands, which also leads to better dispersion and high metal loading. For example, metal precursors mixed with precursors of MOFs can coordinate with organic ligands of MOF, which upon calcination can produce spatially separated SACs. Cao et al. displayed that when $H_2IrCl_6{\cdot}6H_2O$ was hydrothermally reacted with UiO MOF's precursors ($ZrCl_4$, H_2BDC), and Ir@UiO-66 was obtained which upon annealing produces Ir@ZrO_2@C SACs with a relatively high loading ca. 0.6 wt %.[115] Similar ligand assisted in situ confinement was also demonstrated for Y-zeolite where Pt coordinated with ethylenediamine was introduced to Y-zeolite precursors that lead to the formation of Y-zeolite with Pt-EDA trapped in β-site.[116] The thermal treatment of Pt-EDA@Y-zeolite in air and H_2 leads to the formation of isolated platinum atoms that are firmly stabilized by skeletal oxygens. Defects on the supporting materials create coordination sites for SAs stabilization. Easily reducible materials such as TiO_2 and CeO_2 with defect-rich surfaces are frequently used as supporting materials for the stabilization of SACs.[117] Regardless of the opportunity of getting a dense

https://doi.org/10.1021/acsnano.2c02464
ACS Nano XXXX, XXX, XXX−XXX

population of SAs, populated defect creation also comes with the drawback of altered physicochemical properties that are sometimes undesirable. The agglomeration of SAs on inorganic support at a high temperature can also be avoided by using ionic liquids which improve the stability of SAs and also facilitate better interaction of the metal with support. Ding et al. demonstrated $PtCODMe_2$ with Pt as the precursor stabilized on a HAP support by means of butyl-3-methylimidazolium [$Bmim^+$]-based ionic liquids which maintain atomic dispersion after annealing. On the contrary, under identical conditions, nonionic liquid stabilized precursors tend to agglomerate.[118] Nondefect stabilization of SAs on support requires strong coordination between the former and latter, preventing the movement of the SAs during high-temperature annealing. In contrast to most of the reports with diluted metal salt precursor for the deposition of SAs on support, Lang et al. were able to demonstrate Pt nanoparticles can be used as a metal source for defect-free stabilization on FeO_x surface.[119] They observed that at elevated temperatures, Pt NPs release mobile PtO_2 species which can be ultimately trapped by a reducible support. Interestingly, the lower temperature and inert atmosphere favor the formation of Pt NP, and the maximum SAs distribution was achieved in the air at 800 °C, demonstrating PtO_2 species formation at high temperature.

Carbonization is one of the most popular methods of the synthesis of SACs with high-temperature annealing of a metal salt, in the presence of a carbonaceous (glucose/citrate/dopamine/GO) and nitrogenous precursor (urea, melamine, EDA, etc.) in an inert atmosphere that leads to carbonization and graphitization. Mostly M-N_x-C materials are synthesized by this approach, and a relatively high density of SAs can be obtained. However, due to high thermal treatment, the clustering is dominant, and it requires postsynthesis acid treatment to obtain isolated SA sites. The complexation of a metal salt with ligands or precursors itself has been found to reduce agglomeration. Zhao et al. achieved an astonishing 12.1 wt % loading of metal via a cascade anchoring strategy.[120] First, the metal chelated with glucose was anchored onto an oxygen-species-rich porous carbon support followed by a second step of mixing with melamine and further annealing to gain M-N_4-C catalysts. Using metal complexes such as phthalocyanine, metal bipyridyl complexes as the source reduces agglomeration via stabilization of the metal during heating and also integration of the N-coordination sites with carbon backbone for spatial separation. Phthalocyanine and porphyrins-based metal complexes are the most used precursors due to their planar structure, stable tetra-N coordination, and thermal stability. In some cases, porphyrinic materials without metal coordination are used as carbon scaffolds and in conjugation with metallic counterparts provides the opportunity to maintain spatial separation. For example, He et al. by Friedel−Crafts alkylation fabricated a macromolecular two-dimensional (2D) structure of tetraphenylporphyrin platinum (PtTPP) as a metal precursor and Pt-free TPP (PtTPP:TPP = 1:40, mol:mol) as diluent to maintain spatial separation upon which pyrolysis yielded agglomeration free M-N_x-C SACs.[121] The carbonization of MOFs, either directly or after modification with metal salt/metal complexes, is identified as another route for the preparation of high-density M-N_x-C type SACs. Using templates such as KCl for the growth of MOF precursor followed by annealing was found to be impressive to stabilize the high density of SA sites. Wu et al. demonstrated that KCl particles wrapped with a Co-based organic framework (ZIF-67) can impart a population density for the SA Co as high as ≈15.3%.[122] Recently, amino-functionalized carbon quantum dots coordinated with Ir atoms were found to achieve a metal density up to 40 wt %, which is the highest recorded metal density for SACs.[123] In contrast to water-soluble templates that can only work for the solid phase synthesis, other hard templates such as SiO_2, Al_2O_3 and LDHs provide an opportunity to react with a precursor in solution and high temperature followed by etching of template.[124] Even MOFs assisted synthesis also suffers from the problem of agglomeration and requires postacid treatment. Therefore, choosing an appropriate ligand that can stabilize the SA species during the annealing step is vital to getting atomically distributed catalysts. Wang et al. synthesized UiO-66, [$Zr_6O_4(OH)_4(BDC)_6$ (BDC = 1,4-benzenedicarboxylate)], modified with NH_2 (UiO-66-NH_2), which can stabilize the Ru sites and after annealing maintain the atomic dispersion.[125] Apart from the density of SACs, another important feature of N-carbon/graphene-based SACs that governs the catalytic performance is the coordination environment. As per the DFT calculation, pyridinic Ns coordinated SA is more stable to more strong electronic interaction and robust coordination. However, fabrication of SACs from carbonaceous precursor usually attains a random distribution of pyridinic and pyrrolic Ns. By controlling the nature of the N species, the catalytic performance can be significantly improved. Ha et al. demonstrated that lysozyme-modified Co-ZIF-8 selectively forms pyridinic Ns ligated Co SAs.[126] Other processes for the synthesis of carbon confined SACs include localized thermal treatment with laser and photochemical trapping of SAs in freeze-dried precursor,[127,128] while the gas transport approach and solid diffusion synthesis utilized evaporation of metal precursor at high temperature and subsequent trapping in growing carbonaceous networks.[129,130] Direct carbonizations of CN coordinated isolated metals were also used for the synthesis of M-N_x-C catalysts.[70,131] Chemical structure modification of carbon support with certain functional groups followed by decoration of SAs is also employed for the SACs fabrication.[132,133] Bakandritsos et al. used highly functionalized cyanographene for the decoration of mixed valence state Cu SA which cooperatively catalyzes oxidative coupling of amines with almost 99% selectivity.[134] Besides these chemical routes, physical methods such as ball milling, atomic layer deposition (ALD),[135,136] and flame spray pyrolysis (FSP)[137] are also utilized for the fabrication of SACs.[138] Ball milling utilizing high impact and localized heating to implant SA species in support is envisioned to make SACs on a commercial scale. However, the drawback of asymmetric size distribution, chemical structure alteration (phase change) of support, poor control over SA's coordination site, and inability to use impact-sensitive materials limits their applicability.[139,140] On the other hand, ALD provides uniform distribution of SAs with a possibility of multiple atom decoration for the synergic interaction.[136] Unfortunately, the slow deposition rate on limited surfaces, the requirement of specific instrumental conditions, and the inability to control over deposition of SA on specific sites are a few drawbacks. Similarly, FSP displayed limited application due to agglomeration and nonuniformity.[137] The arc discharge method can be used for the synthesis of SACs directly from high melting point metals to form SACs and single atom alloys (SAAs).[141] A more versatile approach frequently used for the synthesis of SACs and SAA is galvanic replacement (GR), which utilizes the electrochemical potential

https://doi.org/10.1021/acsnano.2c02464
ACS Nano XXXX, XXX, XXX−XXX

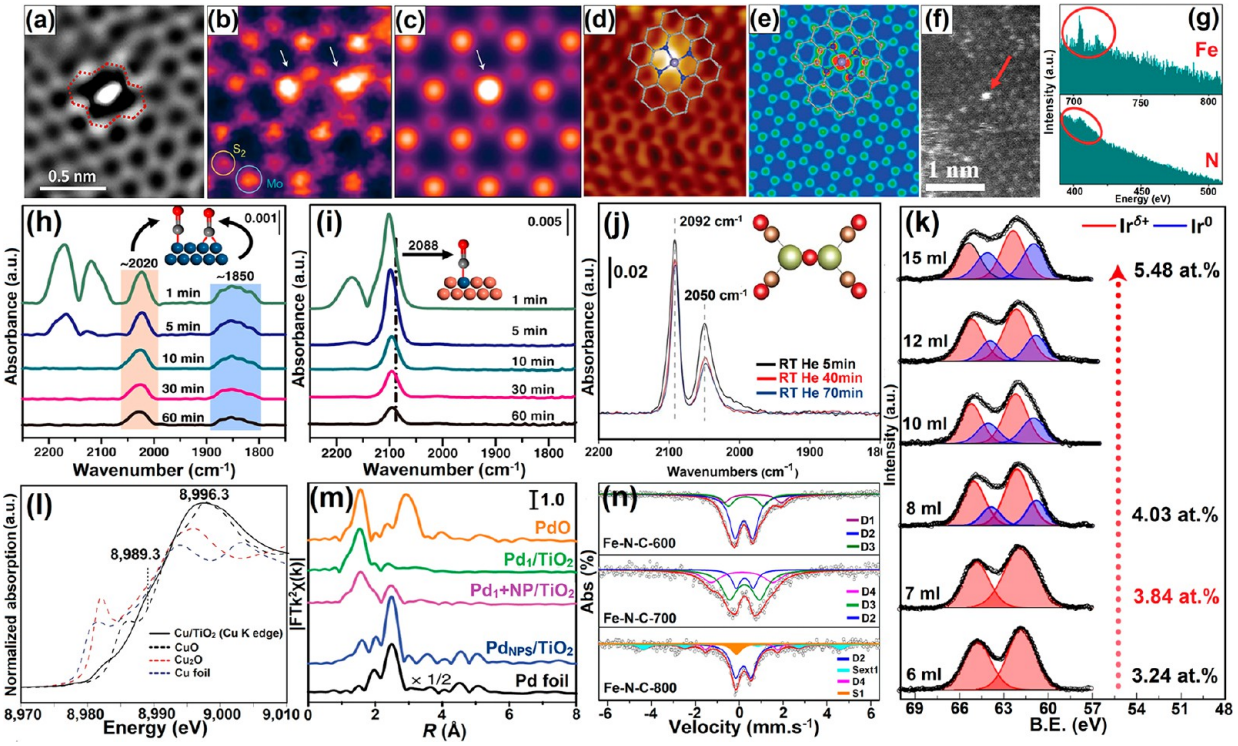

Figure 5. Various techniques employed for the characterization of SACs. (a) HADDF-STEM image of A-Ni@DG, Reprinted with permission from ref 154. Copyright 2018 Elsevier. (b) HAADF-STEM image of Co−$^{S}MoS_2$, showing two bright contrast sites in the MoS_2 monolayer and (c) HAADF image simulation. Reprinted with permission from ref 155. Copyright 2017 Springer Nature. (d) Low-temperature STM image of FeN_4/GN-2.7 and (e) simulated STM image. (f) HAADF-STEM images of FeN_4/GN-2.7. (g) EELS spectra of Fe and N from the bright dots. Reprinted with permission under a Creative Commons CC BY-NC 4.0 License from ref 158. Copyright 2015 AAAS. In situ CO-DRIFTS spectra of (h) Pt/MMO and (i) PtCu−SAA, as a function of time. Reprinted with permission under a Creative Commons CC-BY License from ref 145. Copyright 2019 Springer Nature. (j) In situ DRIFT spectra of Ir DHCs in He flow 5, 40, and 70 min after CO adsorption. Reprinted with permission under a Creative Commons CC-BY License from ref 160. Copyright 2018 PNAS. (k) Deconvolution of the Ir 4f spectra for Ir−N−C-6, Ir−N−C-7, Ir−N−C-8, Ir−N−C-10, Ir−N−C-12, and Ir−N−C-15 catalysts. Reprinted with permission from ref 123. Copyright 2021 Springer Nature. (l) Cu K-edge XANES spectra of Cu/TiO_2. Reprinted with permission from ref 165. Copyright 2019 Springer Nature. (m) R-spaced FT-EXAFS spectra of Pd_1/TiO_2, PdNPs/TiO_2 and Pd_1 + NPs/TiO_2. Reprinted with permission under a Creative Commons CC-BY License from ref 170. Copyright 2020 Springer Nature. (n) ^{57}Fe Mössbauer spectra of the Fe−N−C-600/700/800 samples. Reprinted with permission from ref 173. Copyright 2017 American Chemical Society.

difference between two metals/metal ions for the deposition.[142,143] In principle, when a metal ion with high reduction potential (noble metals) meets another metal with less reduction potential, the metal with lower reduction potential gets oxidize followed by dissolution in solution, resulting in reduced noble metal deposit on the surface.[144] Zhang et al. synthesized a PtCu SAA by galvanic deposition of Pt on CuMgAl-MMO (mixed metal oxide) surface which demonstrated a high conversion (99.6%) and selectivity (99.2%) for the glycerol hydrogenolysis to 1,2-propanediol.[145] Compared to physical methods, electrochemical approach is compelling due to better control over dispersion, fast synthesis, compact electrochemical cell design, and possibility for structural and chemical state manipulations.[146] Zhang et al. displayed Ir SA deposition on $Co(OH)_2$ nanosheets loaded on glassy carbon both in anodic and cathodic depositions.[147] A detailed mechanism speculated that the $IrCl_3$ precursor was transformed to $IrCl_3^+$ and $Ir(OH)_6^{2-}$ during cathodic and anodic deposition and finally reduce/oxidized at the $Co(OH)_2$ support. Additionally, Ir SAs were also deposited on $Co_{0.8}Fe_{0.2}Se_2$ nanosheets both anodically and cathodically, which can reach a current density of 10 mA cm^{-2} at 1.39 V in a two-electrode cell. The versatility of the process was tested on other materials and was also found to maintain similar atomic distribution. Conclusively, the synthesis of stable, high density SAs cooperatively working with other metal centers and support offering a better control over the coordination environment are the key synthetic challenges which need to be dealt with in near future.

4. CHARACTERIZATION OF SACS

The presence of atomically distributed species on catalytic support was deliberated back in the petrochemical industry where catalysts prepared by WI method with a dilute concentration of metal display high activity.[148] In 2003, the observance of unusual activity of Au NPs free CeO_2 surface with cationic Au and Pt species for water gas shift reaction contemplated the presence of SACs.[44] However, due to the limited resolution and contrast of high-resolution transmission electron microscopy, imaging SAs was not successful until the development of spherical aberration correctors with better beam alignment. For the first time, Tao Zhang confirmed the presence of a SA entity supported on FeO_x using aberration-corrected high-angle annular dark-field imaging-scanning transmission electron microscopy (AC-HAADF-STEM).[46] The SACs characterization techniques can be broadly divided into two subdomains: (1) imaging, which includes direct observation of SAs, i.e., AC-HAADF-STEM and scanning

https://doi.org/10.1021/acsnano.2c02464
ACS Nano XXXX, XXX, XXX−XXX

tunneling microscopy (STM) and (2) spectroscopic techniques, which provide auxiliary evidence of their presence and chemical environment, i.e., X-ray absorption spectroscopy (XAS), electron energy loss spectroscopy (EELS), CO-DRIFT, Fourier-transform infrared spectroscopy (FTIR), X-ray photoelectron spectroscopy (XPS), energy-dispersive X-ray spectroscopy, and Mössbauer spectra.[65,149] HAADF-STEM utilizes an annular detector to collect scattered electrons around the beam at a very high angle. Due to the collection of more electrons, the signal intensity and concomitantly the image quality are higher compared to conventional TEM dark-field imaging using an objective aperture. Since numbers of scatter electrons are dependent on atomic number (Z), the HAADF-STEM can distinguish atomic number change (Z-contrast imaging). Additionally, the electron beam passes through in HAADF-STEM, allowing to perform EELS simultaneously. The imaging of heavy SAs on light crystalline materials is straightforward due to the large Z-contrast difference. However, lighter SAs and heavy metal oxide supports (e.g., Fe@WO_3, Co-doped WO_3) pose significant challenges and can be visualized if the lighter atoms replace the heavier atoms and can be observed as a low contrast point.[150] If both support and SAs are in a similar atomic range, only the adsorbed SAs can be imaged, and the rest remains indistinguishable. By measuring the distance in the intensity profile of HAADF, it is possible to propose atomic numbers and differentiate between two different SAs.[151] Visualization of SAs in 2D/layered materials such as graphene and MoS_2 with few layers of thickness is much easier.[121,152] It must be noted that 2D materials do not have long-range crystallinity or periodicity (i.e., carbon), the lattice planes of supporting materials cannot be imaged, and the image quality remains poor due to uneven surface.[153] For example, g-C_3N_4 with plenty of intersheet hydrogen bonding between heptazine unit loses crystallinity. In contrast, Zhang et al. showed atomically dispersed Ni catalyst on defected graphene (A-Ni@DG) (Figure 5a).[154] Due to its crystalline nature, the lattice plane in graphene was visible where N was centered in the pyridinic N constituted Ni-N_4 cavity. In another example, Co atoms situated on Mo atop sites were imaged and simultaneously confirmed by simulation of DFT optimized structure (Figure 5b,c).[155] The low molecular weight materials and 2D sheets are prone to beam damage and imaging should be performed at low acceleration voltage. STM utilizes the quantum tunneling phenomena between the sample and the tip, and the resulting variation in tip current is translated into the form of an image. STM can scan the surface of samples in 10 pm depth resolution and can provide direct evidence of the presence of SA.[156,157] STM has its challenges such as the requirement of stable and clean surfaces, atomic/subclustered tips for better resolution, and an oscillation-free environment. Compared to inorganic crystalline thin films, STM imaging on 2D materials is easy and informative. Deng et al. displayed Fe-N_4(pyridinic) units embedded in a graphene network using STM that complied with simulated STM images (Figure 5d,e).[158] Further, EELS spectroscopy, which collects secondary electrons from the materials, can give information about the chemical environment and oxidation state. The EELS spectrum of bright spots and nearby areas in STEM images displayed Fe L edge and C K edge energy loss signals, validating the Fe species surrounded by N atoms (Figure 5f,g). DRIFTS spectroscopy in the presence of CO as a probe expands the indirect evidence of SA sites as CO binds differently in SACs compared to nanoparticulate materials.[159] Usually, linear single-site binding of CO is preferred on SA sites due to the unavailability of the adjacent site, while NPs prefer bridging CO adsorption along with a small fraction of linear bonding. For example, DRIFTS of Pt NPs displayed vibration bands of both Pt-CO(linear) and Pt_2-CO (bridged), while only one vibrational band was observed for atomically dispersed Pt SA on Cu as SAA catalyst (Figure 5h,i).[145] Linear coordination of two CO molecules on the same atom is also possible; however, it does not introduce bridged binding in the system due to the separation of metal centers. This idea is useful to differentiate DSACs that have a bridging atom as a spacer (prefer linear binding) and DSACs without a spacer element, which shows both linear and bridging binding (Figure 5j).[160] XPS allows determination of oxidation state change of SAs and comparison with metal NPs which can be used for the optimized synthesis/reaction temperature and identification of SAs agglomeration at a particular concentration/temperature.[161] Usually, SA exists in ionic form in supporting materials which permits them to form stable bonding with support via covalent metal−support interaction. At higher metal concentration or during the reaction, SAs tend to agglomerate, and the resulting metallic species exists in a zerovalent state. For instance, Xia et al. showed Ir-N-C catalysts with Ir in a +4 state and a maximum ∼3.84 at% loading can be achieved, after that the metallic species Pt^0 due to the formation of NPs emerges (Figure 5k).[123]

XAS including X-ray absorption near edge structure (XANES) and extended X-ray absorption fine structure (EXAFS) is the most powerful tool for the characterization of SACs which provide information on valence state, coordination environments and bonding pattern.[162,163] XANES originated from the excitation of core electrons to the higher energy unfilled molecular orbitals and continuum resonances which provide information about the oxidation state and coordination geometry. The XANES spectra in comparison with standards are used as a fingerprint to provide the valence state. Roughly, the absorption edge shifted by ∼2 eV with each oxidation state change.[164] For example, XANES spectra of Cu SA on TiO_2 were compared with standard Cu samples which display the edge overlapped with CuO showing a 2+ oxidation state (Figure 5l).[165] The careful evaluation of pre-edge region shape and intensity can provide significant information about electronic structure and coordination geometry. For example, the 1s → 3d transition is forbidden in symmetric octahedron coordination, while slight distortion from this geometry increases the 1s → 3d transition, leading to an increased pre-edge intensity. We refer the reader to the reference materials for an in-depth understanding of the topic.[164,166−169] EXAFS arises from the electronic excitation of an element in a continuum and when the resulting electron wave interacts with nearby atoms, and it provides information about the coordination and bond length. For SACs, the absence of M-M peak confirms SA identity, while in comparison with other models/standard materials, the bonding pattern can be determined. For example, in Figure 5m, the Pd_1/TiO_2 shows only one peak corresponding to Pd−O bonding, while peaks for Pd−O−Pd (in PdO NPs) and Pd−Pd (Pd metal) were absent, validating the existence of SA.[170] ^{57}Fe Mössbauer spectroscopy with high sensitivity and spectral resolution is a powerful technique which can differentiate between various Fe species and provide insight of coordination and electronic state.[171,172] For instance, ^{57}Fe Mössbauer spectra of Fe-N-C samples prepared at different annealing

https://doi.org/10.1021/acsnano.2c02464
ACS Nano XXXX, XXX, XXX−XXX

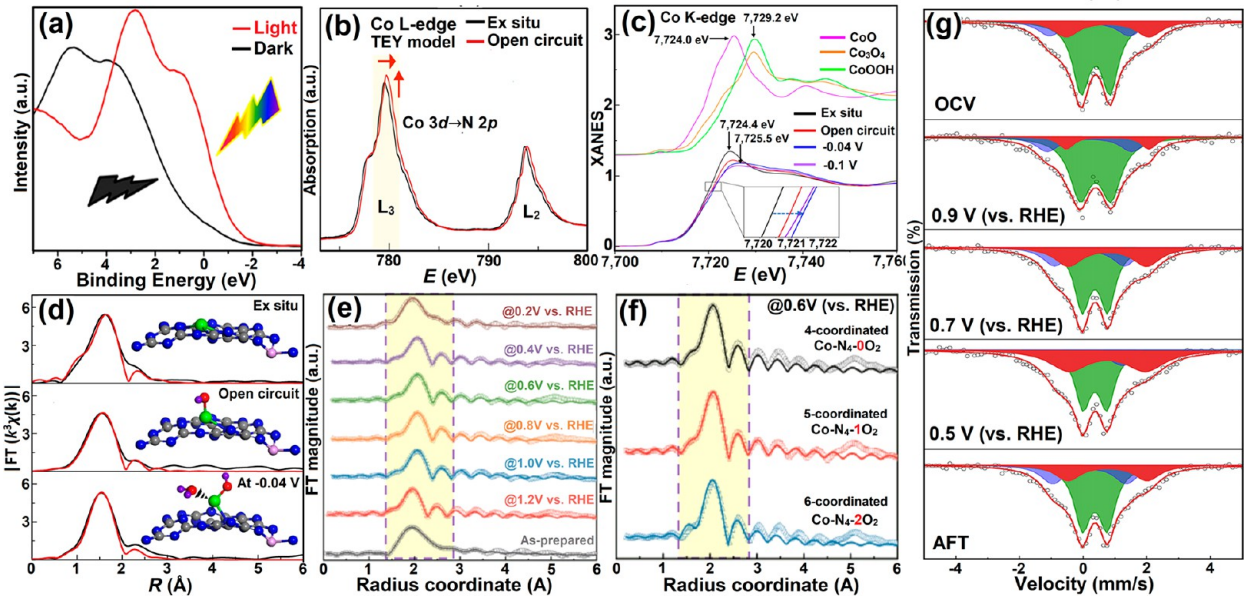

Figure 6. In situ physicochemical characterization of SACs. (a) XPS VB spectra of S−Pt−C_3N_4 under light and dark. Reprinted with permission from ref 176. Copyright 2020 Wiley VCH. (b) Co L-edge XANES spectra of the ex situ catalyst and under the open-circuit condition (total electron yield, TEY). (c) Operando Co K-edge XANES spectra of Co_1/PCN, at different applied voltages from the open-circuit condition to −0.1 V during HER and the XANES data of the reference standards of CoO, Co_3O_4, and CoOOH. (d) First-shell fitting of EXAFS spectra of Co_1/PCN sample under ex situ and open-circuit conditions and at −0.04 V vs RHE. Reprinted with permission from ref 182. Copyright 2019 Springer Nature. (e) The phase-corrected FT-EXAFS (k^3-weighted) of Co−N_4/C was obtained at various operando biases. (f) The EXAFS spectrum, which was obtained under a bias of 0.6 V (vs RHE), is fitted with three different models. Reprinted with permission under a Creative Commons CC-BY License from ref 183. Copyright 2020 Springer Nature. (g) Operando ^{57}Fe Mossbauer spectra for ^{57}Fe enriched Fe-NC-S recorded at an OCV, 0.9, 0.7, 0.5 V (vs RHE), and after ORR (at 0.5 V vs RHE) in O_2-saturated 1 M KOH at room temperature. The green, blue, and red doublets are assigned to LS $Fe^{II}N_4/O_2$−$Fe^{II}N_5$, MS $Fe^{II}N_4$, and HS $Fe_{II}N_5/O_2$−$Fe^{II}N_4$, respectively. Reprinted with permission from ref 184. Copyright 2020 Elsevier.

temperatures display the absence of sextet and singlet peaks at 600 and 700 °C, while one sextet and one singlet were present for the Fe-N-C 800 °C sample, suggesting the transformation of SA cationic species to Fe^0 NPs (Figure 5n).[173]

Besides ex situ characterizations of SACs, in situ/operando characterizations are also covered to develop a better understanding of the active sites, structural change, coordination behaviors, and electronic transitions which help to elucidate mechanism and reaction kinetics.[174,175] In situ characterization of SACs also helps to build models for theoretical studies which provide a roadmap for developing robust and active catalytic systems. The elementary tools frequently used for the characterization of SACs during the reaction are UV−vis, DRIFT (with probe or reactant), and Raman. Though UV−vis, DRIFT, and Raman do not provide direct evidence of coordination/electronic change, they are useful to understand the electronic transition and functional groups ligation/detachment during the reaction. For example, Zhang et al. employed synchronous illumination diffuse reflectance Fourier transform infrared spectroscopy to understand the vibrational feature of Pt-C_3N_4 SACs.[176] Under dark conditions, Pt^{2+} remained coordinated to N atoms in the heptazine cavity; however, under illumination conditions, the Pt−N bond cleaves due to the transfer of electrons from C_3N_4 to Pt^{2+} which results in increased signal intensity of C−N heterocycle. In situ XPS provides more tangible information on valence state change, charge transfer, and even the bonding state of SAs during the reaction. Nguyen et al. used in situ AP-XPS studies to know the chemical state of bimetallic Pt_1Co_m SACs during the catalytic hydrogenation of NO with H_2 at various temperatures.[177] As per their observation, the most active catalysts deposited on reduced Co_3O_4 (0.1 at% Pt/Co_3O_4, 0.5 at% Pt/Co_3O_4) via Pt−O−Co bonding (EXAFS) showed no change in 317.0 eV peak at higher temperature (300 °C), demonstrating ionic Pt species remain stable on support, while 0.5 at% Pt/SiO_2 displayed a signal corresponding to Pt^0 under identical conditions, suggesting a support stabilized ionic Pt thus maintaining catalytic performance during the reductive environment. On some occasions, in situ XPS can reveal auxiliary information otherwise evaded in operando XAS. For instance, Hülsey et al. found that negligible change in the oxidation state of Rh_1/NPTA was observed in operando XAS, while the in situ XPS displayed W $4f_{7/2}$ peak shifted from 36.1 to 35.6 eV, probing the role of support in CO oxidation.[175] Using SI-XPS valence band (VB) spectra, Zhang et al. also found that during irradiation, the Pt-C_3N_4 SAC displayed negative shift spectra due to the transformation of Pt^{2+} to Pt^0 and cleavage of Pt−N bond which increases the reduction ability of C_3N_4 scaffold (Figure 6a).[176] In situ TEM/STM allows visualization of SAs during the reaction or under thermal treatment. With the advent of environmental TEM (ETEM), characterization of the structural evolution of SACs under gaseous and operational conditions becomes possible. Wei et al. investigated the transformation mechanism of Pd, Pt, and Au-NPs (Pd-NPs@ZIF-8) to SACs above 900 °C using ETEM, where they demonstrate sintering and atomization coexisted during NP-to-SA transformation.[178] Operando XAS (XANES and EXAFS) is a versatile and reliable technique to determine the geometric and electronic structures of SACs during the reaction and probe the mechanism.[179] In situ XAS is widely used in electrochemistry to probe the mechanism of the reaction.[90,180,181] Cao et al. used operando X-ray

https://doi.org/10.1021/acsnano.2c02464
ACS Nano XXXX, XXX, XXX−XXX

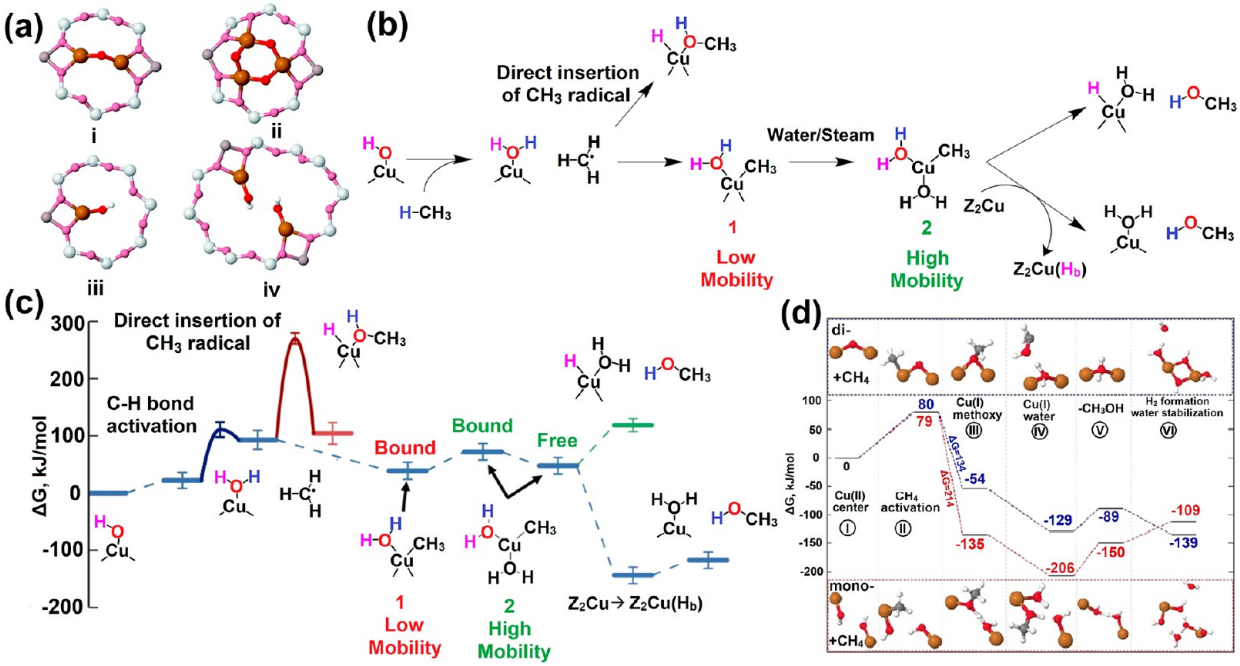

Figure 7. (a) Chemical structure of various copper-oxo active species (i) bent mono-(μ-oxo)dicupric site, $[Cu_2O]^{2+}$,[85] (ii) trinuclear copper oxygen clusters $[Cu_3(\mu\text{-}O)_3]^{2+}$,[84] (iii) $[Cu^{II}OH]^+$,[219] and (iv) bis(dihydroxy)dicopper.[219] Reprinted with permission under a Creative Commons CC-BY 3.0 License from ref 188. Copyright 2020 Royal Society of Chemistry. (b) Reaction scheme for partial CH_4 oxidation to CH_3OH for 8MR-$[CuOH]^+$ active site in Cu-CHA. (c) Free energy diagram for partial CH_4 oxidation to CH_3OH for the 8MR-$[CuOH]^+$ active site in Cu-CHA. The direct insertion of CH_3 radical into Cu-H_2O has a barrier of 175 kJ/mol and is unfavorable (red curve). Z_2Cu (H_b) refers to the addition of a Brønsted hydrogen to an adjacent 2Al/Cu(II) site (Z_2Cu). Reprinted with permission from ref 218. Copyright 2016 American Chemical Society. (d) Calculated reaction profiles and the corresponding intermediates of the anaerobic oxidation of methane to methanol for the CuMOR systems based on copper monomers (red lines) and dimers (blue lines). Reprinted with permission from ref 219. Copyright 2018 Wiley-VCH.

spectroscopy to unveil the nature of the Co active site in Co_1–N_4 sites embedded phosphorized CN (Co_1/PCN) SACs under HER conditions.[182] Soft XAS analysis of Co_1/PCN on Co L-edge displayed an increased peak intensity and higher energy peak shift (~0.2 eV) at OCV and applied bias, suggesting an increased valence state due to the O/OH adsorption lowering the electron density on Co 3d state (Figure 6b). Operando XANES spectra of Co_1/PCN at the Co K-edge at an open-circuit voltage (OCV) were shifted toward a higher energy by ~0.6 eV at the cathodic potentials (−0.04 and −0.1 V vs RHE), exhibiting an increase in valence state during applied potential (Figure 6c). By fitting XANES of pristine catalysts and catalysts under the applied bias of −0.04 V, they calculated that the oxidation state of Co was changed from +2.02 to +2.40. Furthermore, k^3-weighted EXAFS spectra for Co_1/PCN displayed a low-R shift from 1.63 to 1.56 Å for Co–O/N peaks (Figure 6d). The fitting of EXAFS displayed four Co–N coordination for the ex situ sample, which changed to two-fold Co–N coordination (R = 2.01 Å) plus one Co–O coordination (R = 2.08 Å) under OCV, demonstrating adsorption of oxo-group from the electrolyte. Under applied bias during HER, an additional Co–O coordination appeared implying adsorption of a water molecule in the Volmer step. In another study, Lien et al. investigated the coordination environment of a biomimetic Co–N_x/C catalysts (pyrolyzed vitamin B12) using operando EXAFS during oxygen reduction reaction (ORR) (Figure 6e,f).[183] Based on operando EXAFS analysis under applied bias followed by fitting, the authors proposed that five (Co–N_4-1O_2) and six (Co–N_4-2O_2) coordinated species dominated during the OCV and applied voltage (0.6 V vs RHE) conditions. In situ Mössbauer spectroscopy is a highly sensitive technique to elucidate the oxidation electron spin configuration and coordination environment which can identify the SACs intermediate state and probe the reaction mechanism. Li et al. studied the local chemical environment change of a series of Fe graphenic catalysts (Fe-ZIF, Fe-ZIF-S, and Fe-NC-S) during the ORR (Figure 6g).[184] The measurement of the isomer shift (IS) and quadrupole splitting (QS) demonstrates the decreased D3 content and an increase in the relative D1 content, due to the adsorption of O_2 on the D3 site resulting in the formation of O_2–$Fe^{II}N_5$ intermediate. Furthermore, the IS shift from 0.77 to 0.39 mm s^{-1} depicts an overlap between the Fe 3d orbital and O antibonding π^* orbitals, resulting into shortened Fe–N bond lengths and movement of Fe^{2+} inside the N–$Fe^{II}N_4$ plane in O_2^-–$Fe^{II}N_5$. Other in situ approaches sporadically used to investigate SACs reaction mechanism are in situ EPR, mass spectrometry, SERS, and in situ NMR.[149,185]

5. SACS SUPPORTED ON MICRO/MESOPOROUS SILICA (ZSM-5)

5.1. Transition-Metal SACs on Micro/Mesoporous Silica (ZSM-5). When SA are supported on the oxide support, SA can coordinate with surface oxygen moieties to form the M_1-O_x entity. These M_1-O_x entities due to differential electronegativity exhibit polarization and displayed Lewis acidity and basicity, respectively. These localized electrostatic fields on polarized catalysts' counterparts can induce electrostatic $CH_3^{\delta-}$-$H^{\delta+}$ polarization of methane, weakening the C–H bond followed by homolytic dissociation. Based on DFT

https://doi.org/10.1021/acsnano.2c02464
ACS Nano XXXX, XXX, XXX−XXX

calculations, Gao et al. studied SACs with different metal centers (Pd, Pt, Ni, Rh) supported on Al_2O_3 to screen the best catalysts to promote catalytic oxidation of CH_4.[186] Their observation suggests that the Ni atom with d^9 configuration can make stable bonding with methane and lowers the activation energy for further transformation. They also found that O-terminated Al_2O_3 (0001) has a strong coupling with the metal (0.23 eV for Ni). Indeed, Pt and Ni have been found to display higher catalytic performance experimentally; however, strong binding also promotes deep dehydrogenation and overoxidation of the product.[157] Compared to other metals, Cu-based catalysts have higher activation energies to cleave the C−H bond. However, resistance to deep dehydrogenation/overoxidation makes them a suitable choice to fabricate a SAC. Among the various materials investigated for CH_4 oxidation, alumino-silicates-based zeolites secured the top position due to their well-defined porous structure which can provide a specific coordination site to host metals (iron, Cu etc.) imitating natural enzymatic systems. Many elements such as W, Mo, Re, Cr, Fe, etc. on zeolites either in nanoparticulate form or dispersed monodiatomic species in cages forming hypervalent state with oxygen has been reported for CH_4OR.[187] Since the first report on the Cu entrapped zeolite for the CH_4 oxidation to CH_3OH, numerous zeolite-based systems have been developed demonstrating superior CH_4OR performance.[83] A detailed account of Cu-based CH_4OR catalysts hosted in various zeolitic frameworks, their catalytic activity, and mechanism is beautifully summarized by a review article by Newton et al.[188] Various Cu exchanged zeolitic frameworks such as MOR, CHA, ZSM-5, and MAZ, etc. have been demonstrated for CH_4OR.[189] The zeolite cavity size is crucial in determining the activity and even selectivity of such systems. Usually, it is believed that for the product formation, the ring size must be higher than six. The Cu species in zeolites can be present in either monomeric (mono(μ-oxo)) and dimeric form (bis μ-oxo dicopper) (Figure 7a). Initial investigation on Cu-ZSM-5 coupled using EXAFS, XANES, IR, and DFT demonstrates that bis(μ-oxo)dicopper was present in the ZSM framework which goes in a reductive-oxidation ($Cu^I \cdots Cu^I \rightarrow Cu_2^+\text{-}O_2\text{-}Cu^{2+}$) catalytic cycle during the oxidation of NO.[190] Unlike iron and other transition-metal-based catalysts which can form high valent M═O species, Cu undergoes a Cu^{II}/Cu^I cycles during CH_4OR on zeolite support. However, formation of high valent Cu^{III}═O species has also been proposed in synthetics and natural enzymatic systems.[191,192] Yoshizawa et al. based on DFT proposed a mechanism for methane hydroxylation in MMO involving a Cu^{III}−oxo reactive species.[193] Similarly, $[Cu_3(\mu\text{-}O)_3]^{2+}$, di($\mu$-oxo)-$Cu^{II}Cu^{III}$, ($\mu$-oxo)($\mu$-hydroxo)$Cu^{II}Cu^{III}$, and Cu^{III}−O-Cu^{III} species with high-valent Cu^{III} have been identified to involve in CH_4OR.[194−196] Other studies using Cu for catalytic C−C/C−X (X: heteroatoms) bond formation/oxidation also speculate that Cu^I/Cu^{III} redox cycles might be possible where a hypervalent Cu^{III}═O species is formed which by reductive elimination finally produces an initial Cu^I state.[197−200] Such a mechanism is also reported for computational studies of monooxygenase enzymatic systems.[201,202] However, isolation of Cu^{III} complexes and Cu^{III} species on support/matrix is reported by many.[203] For example, Elias et al. demonstrated the synthesis of aliovalent Cu^{2+} and Cu^{3+} on a ceria matrix which can catalyze CO oxidation.[204] However, due to the lack of evidence, the involvement of hypervalent Cu in CH_4OR is debatable. DiMucci et al. carried out XAS and DFT studies on various Cu^{III} metal catalysts and demonstrated that metal−ligand bonding in high-valent d^8 Cu^{III} species is extremely covalent due to the inverted ligand field.[205] Cu K-edge and $L_{2,3}$-edge display no signature features for the Cu^{III} oxidation state, thus indicating ligand involvement in catalysis rather than high-valent Cu^{III}. Narsimhan et al. reported Cu dimeric centers in Cu-exchanged mordenite (Cu-MOR) can promote CH_4 oxidation to CH_3OH using CO as an oxidant.[206] Experimental mechanism evaluations using MAS NMR, EPR, and UV−vis demonstrate the formation of CH_3O groups on Cu centers which can be migrated to Bronsted acid sites where carbonylation takes place. Interestingly, the exchange of acidic sites with Na in Cu-NaMOR significantly reduces the C_2 yield. The Si/Al ratio greatly influences the yield of the product discussed at the end of this section. Even in some cases, trimeric ($[Cu_3(\mu\text{-}O)_3]^{2+}$) was reported as an active center (Figure 7a).[84] For example, based on DFT calculations, Li et al. found that trinuclear oxygenated $[Cu_3(\mu\text{-}O)_3]^{2+}$ clusters are preferentially stabilized in the ZSM framework and in contrast to dimeric species provide a lower energy direct conversion path for CH_4 conversion.[207] However, which one is the real catalytic center is highly debatable.[84] Numerous reports on zeolite-supported copper catalysts show extremely high selectivity of methanol using O_2 or H_2O oxidants due to the involvement of the $Cu^{2+}-Cu^{+}-Cu^{2+}$ cycle.[208−210] Sushkevich et al. demonstrated that copper-exchanged mordenite zeolite (CuMOR) with Cu−O−Cu core can convert CH_4 to CH_3OH using water as a soft oxidant reaching a yield of 0.204 mol_{CH_3OH}/mol_{Cu} in the zeolite with associated selectivity of 97%.[211] Reaction with isotopically labeled $H_2{}^{18}O$ suggests oxygen exchange to Cu sites, while XANES demonstrates the formation of Cu^I sites and back oxidation to Cu^{II} by water. Time-resolved in situ FTIR spectroscopy using pyridine as probe molecule suggests C−H bond cleavage coincides with methoxy and Brønsted acid site formation. However, considering the thermodynamics limitation, Periana debated the role of water as an oxidant.[212]

Monomeric and dimeric Cu stabilization has been reported in both large and small membered ring zeolites; however, zeolites with small pore/cage such as CHA-type zeolites (Cu-SSZ-13 and Cu-SAPO-34) are found to produce CH_3OH selectively. Dinh et al. using in situ XAS reported the formation of $[Cu-O-Cu]^{2+}$ moieties in SSZ-13 zeolites via proton-aided diffusion of hydrated Cu ions which promotes CH_4OR to CH3OH oxidation.[213] The Cu loadings (Cu/cage < 0.3) and high Al content (Si/Al > 30) were crucial to forming $[Cu-O-Cu]^{2+}$ species while avoiding Cu_xO_y nanoclusters formation. A recent study on Cu-BEA zeolites with D_2O as isotopic tracer demonstrates that H_2O can build a high-speed proton transfer bridge between the generated moieties of CH_3^- and OH^- over the evolved mono(μ-oxo) dicopper ($[Cu-O-Cu]^{2+}$) active site, resulting in improved selectivity/activity.[214] Monomeric copper species have been also found to be active/selective for CH_4OR. In a recent work, Sun et al. showed particulate-MMO (pMMO) mimicked Cu−CHA zeolite can achieve an astonishing methanol space-time yield of 543 mmol/molCu/h with selectivity up to 91%. The in situ FTIR and UV−vis spectroscopy demonstrates the transformation of Cu^{2+} to Cu^+ and the active role of water and O_2 in the replenishing of catalytic centers.[215] They also demonstrated that both mono and dimeric Cu were active in CH_4 activation. However, Sushkevich compared the activity of mono and dimeric centers

https://doi.org/10.1021/acsnano.2c02464
ACS Nano XXXX, XXX, XXX−XXX

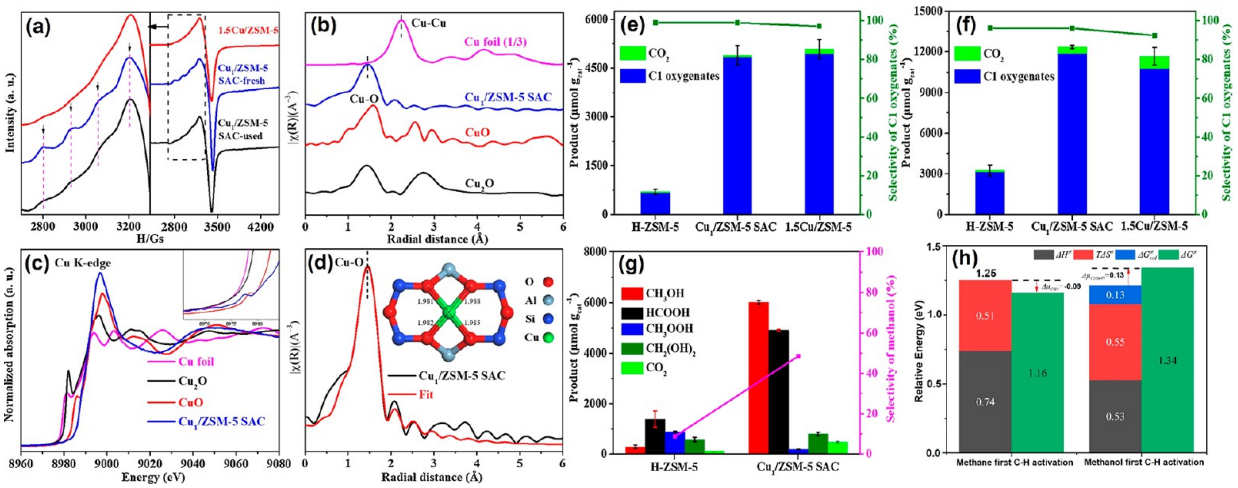

Figure 8. Chemical state and coordination information on Cu_1/ZSM-5 SAC. (a) EPR of 1.5 Cu/ZSM-5, fresh and used Cu_1/ZSM-5 SACs. (b) k^2-weighted $\mu(k)$ function of EXAFS spectra. (c) Copper K edge XANES spectra. Inset: pre-edge region of XANES. (d) EXAFS fitting curve for Cu_1/ZSM-5 SAC. Inset: the proposed coordination environment of the Cu_1-O_4 entity. Catalytic performances of Cu/ZSM-5 samples for direct methane oxidation (DOM). Productivity of DOM on pure H-ZSM-5, Cu_1/ZSM-5 SAC, and 1.5Cu/ZSM-5 at (e) 50 °C and (f) 70 °C. (g) Product distribution and selectivity of DOM on Cu_1/ZSM-5 SAC and pure H-ZSM-5 at 70 °C (d). Reaction conditions: 28 mg catalysts dispersed in 10 mL of 0.51 M H_2O_2 aqueous solution, 30 bar CH_4 for 30 min. Calculated activation free energies $\Delta G^{\neq}$ of C−H bond breaking of CH_4 and CH_3OH. For each free energy barrier, $\Delta H^{\neq}$, $T\Delta S^{\neq}$, $\Delta G^{\neq}_{sol}$ denote the enthalpy, entropy, and solvation free energy contribution to the free energy barrier. $\Delta G^{\neq}_{sol}$ was calculated with reference to 1 mol/L CH_3OH solution, corresponding to the partial pressure of gaseous CH_3OH of 0.01 bar. $\Delta\mu$ corresponds to the pressure and concentration influence on the free energy barrier when the reaction proceeded to 30 min at 323 K: 30 bar CH_4, 100 μmol CH_3OH/10 mL H_2O at 323 K. Reprinted with permission from ref 222. Copyright 2021 Elsevier.

based on kinetic and spectroscopic studies and demonstrated that monomeric species were relatively slow for CH_4 oxidation.[216] Motoki et al. demonstrated that Cu-containing SSZ-13 as CHA-type zeolite catalysts (Cu-CHA) can afford direct CH_3OH formation from CH_4 oxidation with almost 100% selectivity.[217] To elucidate the selective origin of CH_3OH in small-cage size zeolites, Kulkarni et al. based on DFT calculations suggest that monocopper ($[Cu^{II}OH]^+$) species in Cu-exchanged SSZ-13 zeolite's eight-membered ring (8MR) can provide an alternative route for methane oxidation compared to $[Cu-O-Cu]^{2+}$ sites.[218] Three possible Cu species are identified $[CuOO]^+$, $[CuO]^+$, and $[CuOH]^+$, and the energy barrier for C−H activation was found to be 155, 49, and 110 kJ/mol for $[CuOO]^+$, $[CuO]^+$, and $[CuOH]^+$, respectively. Due to a high-energy barrier, $[CuOO]^+$ was excluded. Compared to 6MR−Cu−H2O, the 8MR−Cu−H_2O was found to be more stable. For a high temperature and water partial pressure, $[CuOH]^+$ was found to remain as a major contributor (<11%) and CuO exists in a negligible amount. Due to the low-energy barrier, CH_4 binds with $[CuOH]^+$ yielding Cu−H_2O and a •CH_3 radical (Figure 7b,c). The possibility of direct insertion of CH_3 radical in Cu bonded H_2O molecule can be excluded due to the high activation energy barrier (75 kJ/mol). However, the addition of the CH_3 radical to the same Cu atom is energetically favorable due to the negligible barrier for the $[Cu-H_2O-CH_3]^+$ species. The formed $[Cu-H_2O-CH_3]^+$ cannot be directly converted to CH_3OH due to the higher-energy barrier and remains attached to the 8MR framework. Considering the presence of water and addition of one water molecule demonstrate that $[Cu-2(H_2O)-CH_3]^+$ became mobile and diffuses in zeolite framework after detaching from zeolite, the observed phenomenon is consistent with geometry optimizations, which show $[Cu-2(H_2O)-CH_3]^+$ species is ∼22.6 kJ/mol more favorable compared to species bound with zeolite framework. Finally, a proton abstraction from mobile Cu-hydrated species by adjacent Cu site yields methanol. Further, they evaluated the Si/Al ratio and found that at Si/Al ratio of 5, the kinetics remains the same; however, the probability of forming two "paired" Al atoms in the 6MR was increased. Suskevich et al. also confirmed that higher Si/Al ratio favors the formation of isolated Cu species which provide better methanol yield per Cu (Figure 7d).[219] However, sluggish water reactivation reaction reduces stability and regeneration by releasing molecular hydrogen. On the other hand, samples with lower Si/Al ratio with dimeric and oligomeric Cu species favor an energetically less costly release of hydrogen. CH_4-TPD with in situ XANES demonstrates that Cu-MOR samples with low Si/Al ratio reduces at 400 K, while CuMOR(46) with high Si/Al ratio demonstrates a gradual reduction up to a temperature of 600 K, suggesting monomeric Cu species were less active toward methane. Further, methane-reacted samples after anaerobic oxidation show generation of hydrogen in contrast to Cu monomeric samples which were active only under aerobic (O_2) condition. DFT comparison considering stabilization of two Cu monomeric units in 12MR and one Cu−O−Cu dimeric unit in 8MR demonstrates similar CH_4 activation steps in both monomers and the dimer, while higher stabilization of the methoxy species was achieved for monomeric species (214 kJ mol^{-1} vs 134 kJ mol^{-1} for the dimer). Despite favorable stabilization, the presence of more hydrogen bonds and larger distance between two Cu makes the process energy intensive. The addition of three extra water molecules to stabilize the structural model exhibited the release of hydrogen possessing higher free energy for monomeric species, while the corresponding energy profile for dimers decreased possibly due to the formation of a very stable bis(dihydroxy)dicopper sites. For the dimer, the stabilization after release was much easier, suggesting better regeneration compared to monomers.

https://doi.org/10.1021/acsnano.2c02464
ACS Nano XXXX, XXX, XXX−XXX

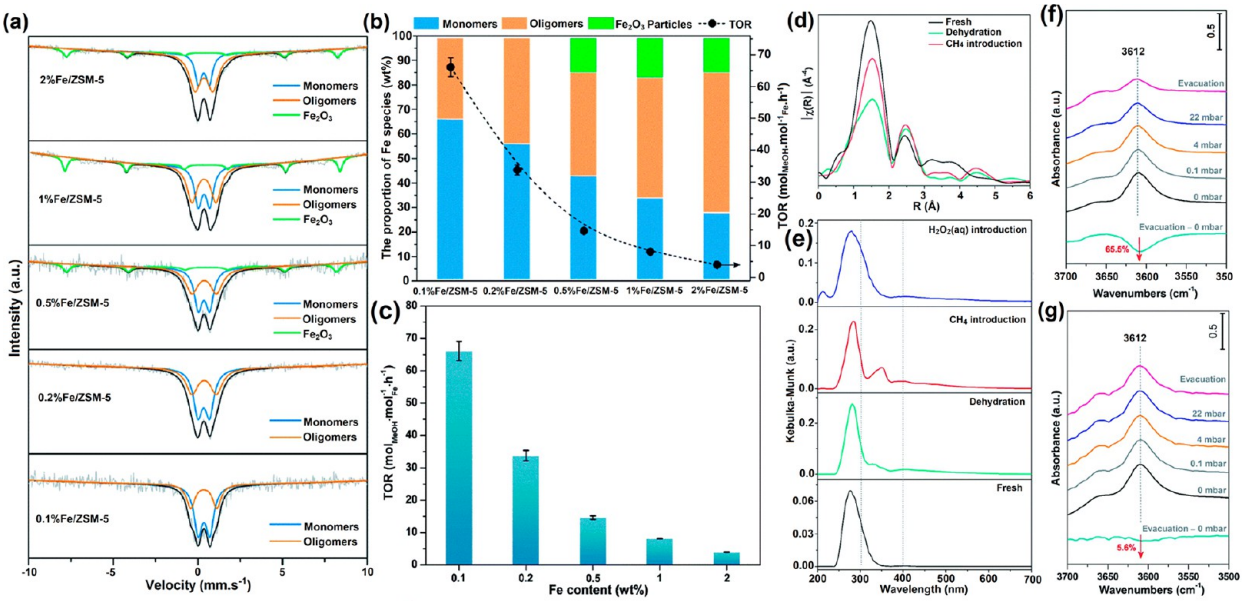

Figure 9. Effect of different Fe species on CH_4 oxidation activity. (a) ^{57}Fe Mössbauer spectra of the Fe/ZSM-5 zeolites with different Fe loadings obtained at ambient temperature. (b) The relative proportion of different Fe species in different Fe/ZSM-5 zeolites with the apparent TORs of five Fe/ZSM-5 zeolites. (c) TOR values of various Fe/ZSM-5 catalysts with different Fe content. (Reaction conditions: T = 50 °C, P_{CH4} = 30 bar, 0.5 M H_2O_2 aqueous solution, catalyst mass = 0.3 g, rpm = 1500, V = 80 mL, t = 30 min, the deviation bar is determined from running three additional repeats. In situ characterization results from in situ EXAFS, in situ UV−vis DR and in situ FT-IR. (d) In situ Fe K-edge EXAFS spectra of the 0.1% Fe/ZSM-5 at 50 °C with different treatments. (e) In situ UV−vis diffuse reflectance (DR) spectra of the 0.1% Fe/ZSM-5 at 50 °C with different treatments (fresh: the fresh catalyst; dehydration: treated by dehydration at 300 °C; CH_4 introduction: methane introduction at 50 °C; H_2O_2(aq) introduction: with a few droplets of 0.5 M H_2O_2 aqueous solution). (f and g) In situ FT-IR spectra of methane absorption bands in the −OH vibration region over the parent H-ZSM-5 and 0.1% Fe/ZSM-5 at 50 °C, respectively. Reprinted with permission from ref 228. Copyright 2021 Royal Society of Chemistry.

Considering the debatable role of mono and di-Cu species in CH_4 activation, it is essential to identify the activity of each component. However, the study of Cu species in caged zeolite systems is challenging. Meyet et al. synthesized isolated Cu^{II} sites by thermolysis of monomeric Cu^{II} siloxide molecular precursor [Cu(OSi(O*t*Bu)$_3$)$_2$(TMEDA)] on Al support which also provides a similar Si/Al coordination environment as present in zeolite frameworks.[220] Similarly, an oxygen-bridged dimeric Cu was also prepared for the comparison. The isolated mononuclear species demonstrated superior reactivity for CH_4OR yielding CH_3OH with >80% selectivity. XAS confirms the presence of Cu in the 2+ oxidation state, which was further validated by UV−vis absorption band at 900 nm due to the d−d transition of d^9 Cu^{II} species. The EXAFS spectra show the first-shell peak with an average of three oxygens, while the second shell peak can be fitted for one atom (Si/Al). A similar pattern was observed for dimeric Cu species. The catalytic performance evaluation yielded 11% CH_3OH per/Cu, which corresponds to 22% of such sites for the two-electron process. In-situ XAS demonstrates that 27% of the total Cu^{II} was reduced to Cu^{I} consistent with the 22% number obtained from CH_4 yield. Additionally, in situ EPR spectra demonstrate a decrease in signal intensity and 23% of Cu^{II} becomes EPR-silent due to the reduction of Cu^{II} to Cu^{I} which excludes the formation of antiferromagnetically coupled bridged μ-oxo Cu dimer and Cu oxide clusters. These observations suggested that dimeric/trimeric species and the presence of crystalline metal are not the ultimate necessity for the CH_4OR. XAS (XANES and EXAFS) is a widely used technique to characterize Cu-based zeolites; however, the identification of Cu^{II}-bis-μ-oxo and Cu^{II}-mono-μ-oxo sites, trimers $Cu_3O_3^{2+}$, and CuOH remains challenging due to similar first- and second-shell scattering and an almost identical Si/Al environment.[221] They demonstrated with careful measurement that the long k-range at cryogenic temperatures can improve the quality of fitting, while WT allows discrimination between various species. Inspired by these findings, Tang et al. synthesized a Cu isolated SA decorated H-ZSM-5 (SiO_2/Al_2O_3 = 25) catalysts possessing Cu_1-O_4 entities.[222] EPR spectra of Cu_1/ZSM-5 demonstrate a quartet EPR fine structure, suggesting signals were not uninterrupted by neighboring Cu atoms evidencing the presence of isolated centers (Figure 8a). The EXAFS spectra of Cu_1/ZSM-5 displayed a signal at 1.46 Å and peaks corresponding to Cu−Cu and Cu−O−Cu were absent, validating the atomic distribution of the copper on the surface of ZSM-5 (Figure 8b). XANES analysis shows peaks at 8977 eV due to 1s to 3d transition, while the shoulder peak for CuO at 8986 eV due to 1s to $4p_z$ transition was absent, suggesting bivalent Cu in planar geometry coordinated to 4 O atoms (Figure 8c,d). The yield of total oxygenates using Cu_1/ZSM-5 was 4800 μmol g_{cat}^{-1} (75% methanol selectivity) within 30 min compared to 680 μmol g_{cat}^{-1} in 30 min for the H-ZSM-5 (Figure 8e). When the temperature was increased from 50 to 70 °C, the yield of C1 oxygenates was increased to 12000 μmol g_{cat}^{-1} within 30 min, though the methanol selectivity was significantly decreased and formic acid was almost equally dominated product (Figure 8f,g). Generally, Fe impurities are present in commercial ZSM-5 which might be involved in enhanced activity due to synergistic Cu−Fe promoted reactions. To confirm the activity arose due to Cu sites, Fe free ZSM-5 decorated with Cu was investigated which demonstrated

https://doi.org/10.1021/acsnano.2c02464
ACS Nano XXXX, XXX, XXX−XXX

almost identical activity as commercial ZSM-5. DFT studies on Cu bonded to two Si^{4+} and two Al^{3+} sites displayed C−H bond scissoring at the Cu−O ion pair followed by interaction of formed CH_3* with H_2O_2 to form CH_3O* and finally CH_3OH. Interestingly, the first C−H bond cleavage energy for methane was lower than methanol due to better solvation of CH_3OH, and high translational and rotational entropy loss avoids the reabsorption of methanol (Figure 8h).

Nature's enzymatic transformation of methane to oxygenates under anaerobic conditions is usually promoted by MMO containing Fe-oxo and Cu-oxo active sites.[223−226] To mimic the natural architecture, several metal-containing zeolite catalysts with distinct metal-oxo species have been designed which demonstrate enzyme-like reactivity for methane oxidation to methanol and other oxygenates.[220,227] Unfortunately, controlling the oxidation degree remains a challenge and overoxidation products are usually dominated in such reactions. Low-temperature methane oxidation under an ambient environment has been reported in H_2O_2-based heterogeneous systems, containing metal-supported zeolites catalysts.[194,227] Dinuclear Fe-oxo species were proposed as active species based on ex situ experiments; however, the role of mononuclear species cannot be ruled out. Since most of the studies were in ex situ environments, it is highly debatable to determine the exact nature of catalytic sites. To understand the role of mononuclear iron sites, Yu et al. synthesized a series of Fe/ZSM-5 catalysts via the WI method with different Fe contents (0.1−2% Fe) and concomitantly different active species (i.e., mononuclear, oligonuclear clusters and metal oxide nanoparticles) were obtained. FE-SEM and XRD spectra of 0.1% Fe/ZSM-5 catalyst show no nanoparticles or diffraction peaks for iron suggesting the subnanometer size of Fe. While few nanoparticles (10−50 nm) were visible for high metal-containing catalysts (0.5−2.0%). UV−vis diffuse reflectance spectra of 0.1% Fe/ZSM-5 displayed one prominent peak at 278 nm assigned to mononuclear Fe^{3+} species in octahedral coordination, while 0.5% Fe/ZSM-5, 1% Fe/ZSM-5, and 2% Fe/ZSM-5 displayed peaks at >300 nm and >400 nm corroborated to oligomeric Fe_xO_y and Fe_2O_3 nanoparticles, respectively. A similar pattern was observed in H_2-TPD, where only one reduction peak was observed for 0.1% Fe/ZSM-5 at 503 °C due to monomeric Fe^{3+} species, while 0.2% Fe/ZSM-5 and 0.5% Fe/ZSM-5 demonstrated a reduction peak at 455 °C for oligomeric Fe_xO_y clusters. Further increments in Fe content in 1% Fe/ZSM-5 and 2% Fe/ZSM-5 lead to the evolution of three peaks at 395, 427, and 473 °C due to oligomeric Fe_xO_y and Fe_2O_3. AC-HAADF images further verify the presence of monomeric species in 0.1% Fe/ZSM-5. To gain further insight into the nature of iron species, ^{57}Fe Mössbauer spectroscopy was employed. The ^{57}Fe Mössbauer spectra of 0.1% Fe/ZSM-5 demonstrated two doublet components with an isomeric shift of IS ∼ 0.35 mm s^{-1} originated from Fe^{3+} oxidation state and QS ∼ 0.70 mm s^{-1} suggesting octahedral coordination of Fe^{3+} species (Figure 9a). The sextet components with IS = 0.36−0.38 mm s^{-1} and QS = 0.22−0.29 mm s^{-1} in ^{57}Fe Mössbauer spectra of 0.5% Fe/ZSM-5, 1% Fe/ZSM-5, and 2% Fe/ZSM-5 suggest presence of Fe_2O_3 nanoparticles. As the Fe content of Fe/ZSM-5 was increased from 0.1% to 2.0%, the monomeric Fe^{3+} species decreases from 66% to 28%, respectively (Figure 9b). Using pressurized methane (30 bar) and 0.5 M H_2O_2 oxidant a turnover rate (TOR) of 66 mol_{MeOH} mol_{Fe}^{-1} h^{-1} was obtained for 0.1% Fe/ZSM-5 catalyst which was significantly higher than other high-concentration Fe/ZSM-5 catalysts (Figure 9c). Based on the determined Fe species population from ^{57}Fe Mössbauer spectra TOR of mononuclear, dinuclear/oligomers and Fe_2O_3 was found to be 91 mol_{MeOH} mol_{Fe}^{-1} h^{-1}, 18 mol_{MeOH} mol_{Fe}^{-1} h^{-1}, and 210 mol_{MeOH} mol_{Fe}^{-1} h^{-1}, respectively, demonstrating mononuclear Fe^{3+} species were most active for the methane to methanol formation. In situ FT-EXAFS of fresh 0.1% Fe/ZSM-5 demonstrates the main peak components at 1.5 Å for octahedral species which after dehydration show a Fe−O peak at ∼1.91 Å (Figure 9d). The introduction of CH_4 followed by data fitting suggests the formation of Fe−C species providing evidence of C−H bond activation by Fe−C interaction. In situ UV−vis spectra of 0.1% Fe/ZSM-5 after dehydration give a band at ∼328 nm which upon introduction of CH_4 transformed into an intense band centered at ∼350 nm, suggesting gas-phase CH_4 can strongly interact with the Fe species and induce a partial agglomeration. Interestingly, after the addition of H_2O_2 aqueous solution, the absorption band corresponding to oligomeric cluster at ∼300−400 nm disappeared, demonstrating Fe species revert to monomeric phase in the presence of aqueous H_2O_2 to activate methane (Figure 9e). Time-resolved in situ FTIR spectra of H-ZSM-5 and 0.1% Fe/ZSM-5 at 50 °C after absorption of methane followed by desorption show decreased intensity of −OH vibration at 3612 cm^{-1} for pristine H-ZSM-5 (−65.5%) compared to 0.1% Fe/ZSM-5 (−5.6%), suggesting less effective interaction between methane and ZSM-5 after addition of Fe (Figure 9f,g). Products identification using 2D ^{1}H−^{13}C heteronuclear multiple quantum correlation demonstrates crossed peaks 3.34/49, 3.85/65, 5.03/93 and 8.25/167 (^{1}H/^{13}C) assigned to CH_3OH, CH_3OOH, $HOCH_2OOH$, and HCOOH.

Developing strong oxidation catalysts which can break the energy-intensive C−H bond of methane while preventing overoxidation of product from converting to waste CO_2 are two paradoxical prerequisites for successful conversion of CH_4 to oxygenates. Iron-based catalysts, due to the formation of biomimetic hypervalent Fe^{IV}=O state like sMMO and cytochrome P450 metallozymes displayed excellent performance in methane oxidation. In a recent report, Zhang et al. demonstrated that iron salt can promote efficient oxidation of CH_4 and HCOOH was a major product (33273.5 $\mu mol/g_{cat}$), while CH_3OH (1972.2 $\mu mol/g_{cat}$) was the second dominant product.[229] The Fe^{IV}=O was a reactive species, and the role of counterion was crucial, as compared to nitrate and bromide anions, the chloride was found to significantly enhance the performance. Many heterogeneous Fe-based zeolite supported catalysts such as Fe-ZSM-5[230−232] and Fe@MFI[233] have been reported for the CH_4OR.[187] Like Cu-based zeolites, the nature of catalytic centers remains elusive and monomeric, and dimeric $\mu[Fe_2(\mu_2\text{-}OH)_2(OH)_2\text{-}(H_2O)_2]^{2+}$ type species have been reported. Using in situ resonance-enhanced Raman spectroscopy, Hammon et al. demonstrated the presence of Fe−O(H)−Fe core and a Fe^{III}−OOH intermediate activation with H_2O_2.[234] A recent report by Wu et al. showed that Fe/ZSM-5 possessing $[Fe^{(III)}-(\mu O)_2-Fe^{(III)}-(OH)_2]$ active sites can afford a 100% selectivity for C_2 products (CH_3COOH) using CO and H_2O_2 as an oxidant at 30 °C.[235] Theoretical studies suggest the CH_3 radical can easily react with surface adsorbed *CO and *OH species forming CH_3COOH. In another study, a detailed DFT calculation on $[(H_2O)_2-Fe(III)-(\mu O)_2-Fe(III)-(H_2O)_2]^{2+}$ extra framework cluster on ZSM zeolites displayed that three possible CH_4OR

https://doi.org/10.1021/acsnano.2c02464
ACS Nano XXXX, XXX, XXX−XXX

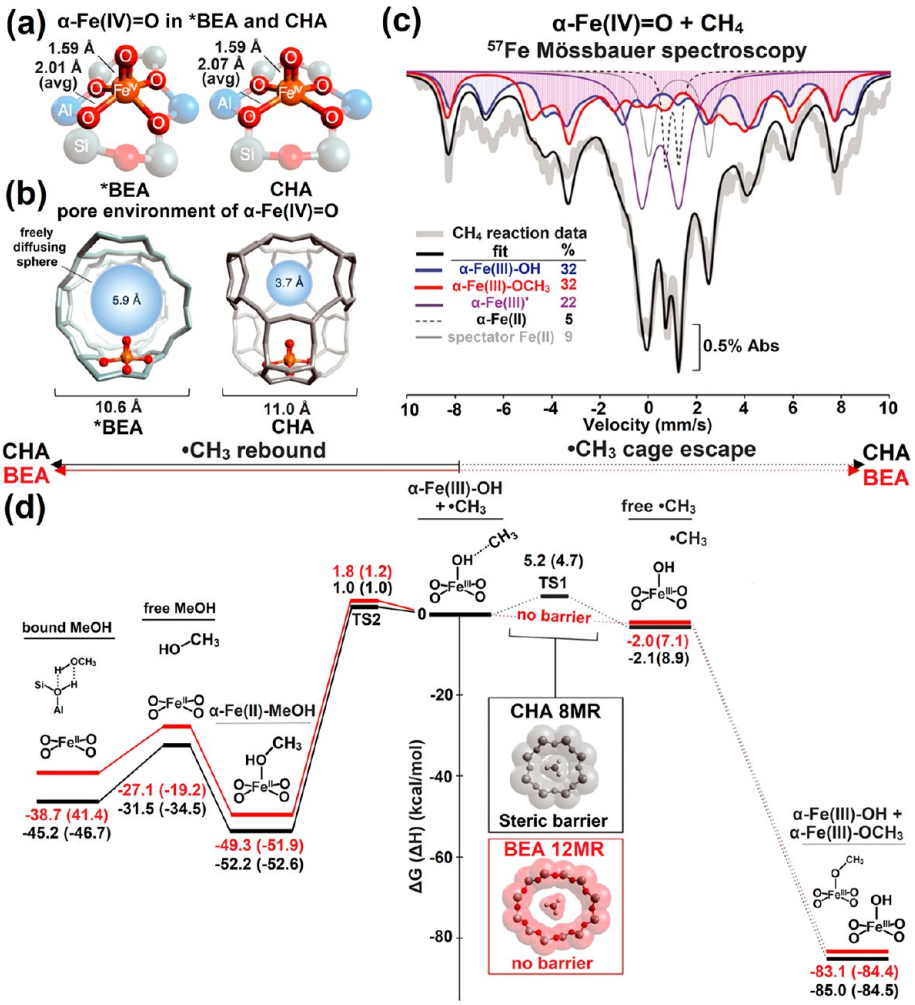

Figure 10. Local environments of α-Fe(IV)═O sites in *BEA and CHA. (a) Comparison of first coordination spheres, with bond lengths from spectroscopically calibrated DFT models.[241−243] (b) Comparison of α-Fe(IV)═O pore environments in *BEA and CHA. Identification of Fe(III) species after H_2 and CH_4 reactions with Fe-*BEA. ^{57}Fe Mössbauer spectrum of α-Fe(IV)═O in Fe-*BEA at 6 K. The blue trace shows the Mössbauer signal from α-Fe(III)−OH; the red trace shows the Mössbauer signal from α-Fe(III)-OCH_3. Comparison of reaction coordinates for *BEA (red) and CHA (black) after H atom abstraction. The reaction coordinates for radical rebound (left) and cage escape (right) are shown. Free energy changes (Δ*G* at 300 K, Δ*H* in parentheses) are given relative to the α-Fe(III)−OH···CH_3 vdW complex produced during H atom abstraction from CH_4 by α-Fe(IV)═O. The insets show how the vdW surface of an 8MR of CHA compares to that of a 12MR of *BEA, illustrating how the constricted CHA 8MR creates a steric barrier for radical escape from the CHA active site (TS1). Reprinted with permission from ref 244. Copyright 2021 AAAS.

pathways exist: (1) heterolytic and (2) homolytic methane dissociation and (3) Fenton-type reaction involving free OH radicals.[236] Despite, the high-energy barrier of the homo/heterolytic route compared to the Fenton reaction, these routes are favored. CH_4 and H_2O_2 compete for the same Fe sites, and due to favorable oxidation of H_2O_2 over CH_4, the product yield remains low. On the contrary, Fang et al., based on DFT and spectroscopic analysis, demonstrated that monomeric species can form •OH and •OOH resulting in the formation of CH_3COOH, while dimeric species produce CH_3OH via •OH radicals.[237] Yu et al. also showed, three synthesis routes named incipient wetness impregnation (IWI), liquid ion-exchange (IE), and solid-state ion-exchange (SSIE) for the synthesis of Fe-ZSM-5 among which SSIE had the highest (71%) population of monomeric species as determined by ^{57}Fe Mössbauer spectroscopy.[238] Compared to IWI and IE samples, the Fe/ZSM-5_{SSE} yielded the highest CH_3OH productivity and selectivity demonstrating the direct role of monomeric species. Like Cu-based zeolites, the Fe species entrapped in small cage zeolites such as 6MR cavity of BEA, CHA, FER, and MOR displayed better selectivity for methanol. The Fe/Al ratio is also extremely important to maintain the monomeric distribution. For example, Loberee et al. found that Fe/Al ratios higher than 0.56 led to the formation of FeO_x species, while $Fe^{3+}(OH^-)_2$ species prevailed below this ratio.[239] DFT studies also verified the preferential stabilization of monomeric Fe^{2+} in a six-membered ring (6MR) of SSZ-13 zeolite with proximal Al's which were more active than dimeric species for partial CH_4 oxidation.[240] The mononuclear species in Fe-zeolites forms square pyramidal high-spin (S = 2) α-Fe(IV)═O intermediate via O transfer that can abstract protons from the substrate due to a constrained coordination geometry imposed by the zeolite lattice. Unfortunately, the catalytic oxidation of methane remains poor due to the radical escape and absence of a closed catalytic cycle. In natural enzymatic systems, active sites embedded in the well-defined pocket of ligand pockets can direct precise control over radical recombination without

https://doi.org/10.1021/acsnano.2c02464
ACS Nano XXXX, XXX, XXX−XXX

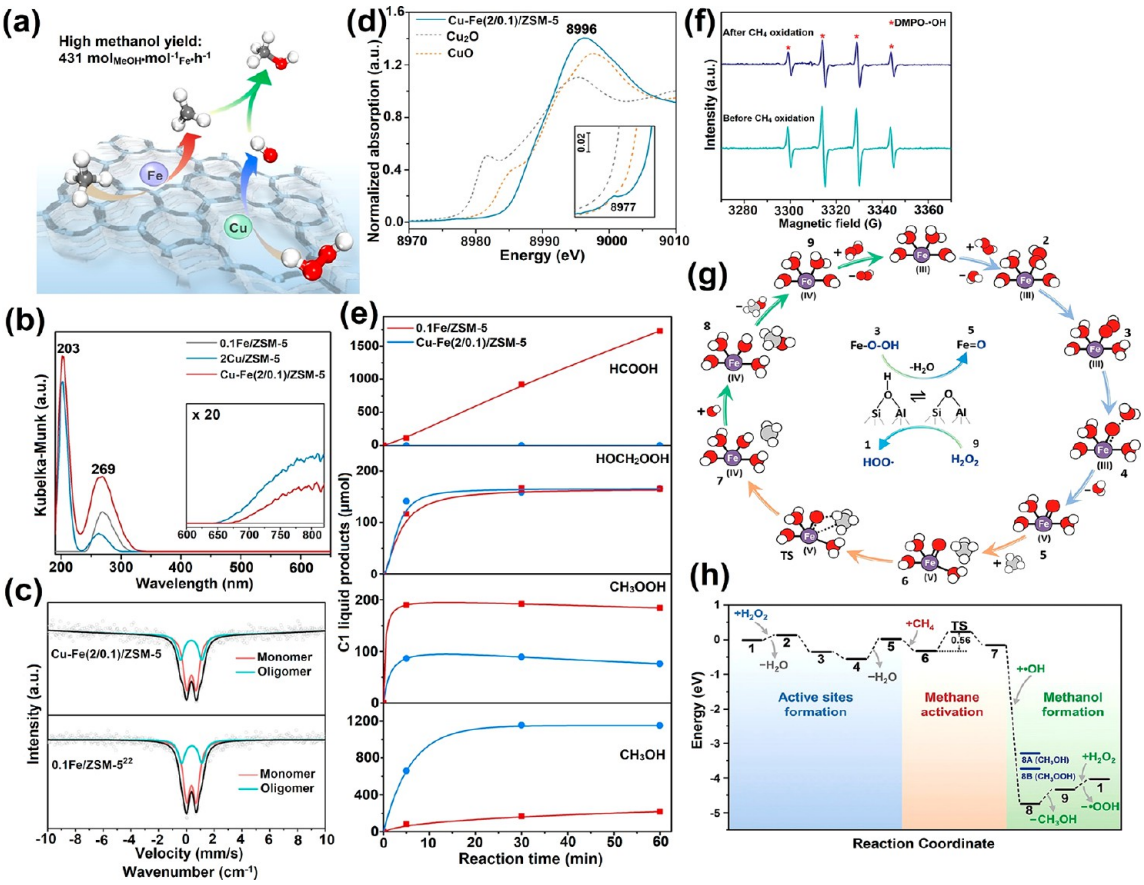

Figure 11. (a) General schematics of CH_4 oxidation on Cu−Fe ZSM-5 catalysts. (b) UV−vis DR spectra of the different catalysts. (c) ^{57}Fe Mössbauer spectra at 298 K in air for 0.1Fe/ZSM-5[228] and Cu−Fe(2/0.1)/ZSM-5 samples. (d) Cu K-edge XANES spectrum of the Cu−Fe(2/0.1)/ZSM-5 catalyst. (e) Time-online profile for the reaction products of CH_4 oxidation over the 0.1Fe/ZSM-5 and Cu−Fe(2/0.1)/ZSM-5 catalysts. (f) EPR trapping experiment with 5,5-dimethylpyrroline-*N*-oxide over the Cu−Fe(2/0.1)/ZSM-5 catalyst with H_2O_2 as the oxidant. (g) Proposed reaction scheme of reaction pathway for direct CH_4 oxidation to CH_3OH over Cu−Fe(2/0.1)/ZSM-5 using H_2O_2 as the oxidant. Red, purple, gray, and white balls represent O, Fe, C, and H atoms, respectively. (h) DFT-simulated pathway on the mononuclear Fe^{3+} species in zeolite ZSM-5 for the oxidation of CH_4 to CH_3OH using H_2O_2, illustrating the thermodynamic feasibility of the proposed mechanism. Reprinted with permission from ref 255. Copyright 2021 American Chemical Society.

radical escaping and thus preventing the deactivation mechanism. Similarly, controlling the size of the zeolite pore can exert similar effects and allow better control over reactivity/selectivity. Studies reveal that regardless of the quite similar chemical environment of α-Fe(IV)═O in chabazite (CHA) and zeolite beta (*BEA), they displayed different reactivity toward CH_4OR.[241−243] Snyder et al. speculated that cavity size must be playing a crucial role to decide reactivity.[244] The α-Fe(IV)═O sites in *BEA are constituted of a large 12-membered ring (12MR) of SiO_4 tetrahedra, while in CHA α-Fe(IV)═O, it is encased in a cage-like pore environment. Despite the similar cage dimension, the entrance to α-Fe(IV)═O sites in CHA are controlled by an 8MR. Figure 10a displays that for CHA, the maximum van der Waals (vdW) diameter of a molecule that can freely diffuse out of this constricted aperture is 3.7 Å, compared to 5.9 Å for *BEA. This reveals that the diffusion of CH_4, which has a larger vdW diameter than 3.7 Å [4.1 to 4.2 Å],[245] should be hindered in CHA but not *BEA. To evaluate the effect of cage size *BEA (Si/Al = 12.3, 0.30 wt % Fe) and CHA (Si/Al = 8.9, 0.24 wt % Fe) with monomeric Fe species, distributions were studied by Mössbauer spectroscopy. Fresh samples displayed almost identical signature peaks. However, after α-Fe(IV)═O sites were exposed to CH_4, the Mössbauer signal for *BEA was significantly diminished (α-Fe(II) ∼ 4%) demonstrating the presence of randomly oxidize Fe species, while for CHA, almost ∼37 Fe(II) were recovered after the reaction. The product yield was almost identical for the fresh samples; however, during the first and second cycle, the yield of CHA was almost ∼50% and ∼40% higher than that of *BEA (considering the ∼74% and ∼91% concentration of α-Fe(IV)═O for CHA, *BEA). The H_2 treatment of α-Fe(IV)═O in *BEA followed by Mössbauer spectroscopy demonstrated 61% α-Fe(III)−OH along with 17% signals from relaxing α-Fe(III)−OH′ species. Resonance Raman (rR) spectra displayed enhanced Raman vibration at 735 cm^{-1} assigned to α-Fe(III)−OH. After CH_4 treatment, the Raman spectra of *BEA demonstrated formation of deactivated Fe(III)-OCH_3 species by the reaction of CH_3 with remote α-Fe(IV)═O sites. The Mössbauer spectra after CH_4 treatment show a conversion of α-Fe(IV)═O to a 1:1 mixture of α-Fe(III)-OCH_3 and α-Fe(III)−OH, while form CHA, the contribution of α-Fe(III)−OH and α-Fe(III)-OCH_3] was ∼4:3 and almost 40% α-Fe(II) species were regenerated (Figure 10b). DFT calculation, for 12MR and 8MR channel modeled for *BEA and CHA, showed no barrier to CH_3 radical escape in *BEA. Additionally, CH_3 radical can freely react to remote α-Fe(IV)═O resulting in deactivated α-

https://doi.org/10.1021/acsnano.2c02464
ACS Nano XXXX, XXX, XXX−XXX

Fe(III)-OCH_3 and equivalent of α-Fe(III)−OH (Figure 10c). The obtained results were consistent with finding in Mössbauer and rR showing equal contribution of the two components. As expected, for CHA, an energy barrier of 5.2 kcal/mol for CH_3 escape was calculated. Despite the difference in cage path, their radical rebound mechanisms were similar to a low-energy barrier resulting in α-Fe(II) [α-Fe(II)−CH_3OH]. The released ∼50 kcal/mol in this step drive desorption of CH_3OH and regenerating α-Fe(II). Due to small pore in CHA, the CH_3 radical recombines with α-Fe(III)−OH to form CH_3OH and revert the α-Fe(III)−OH site to reduced α-Fe(II) state.

Despite high yield in some cases, the use of toxic CO and expensive H_2O_2 is undesirable, and overoxidation of the products remains a challenge. Copper species have been reported to prevent overoxidation of the oxygenates, and methanol is usually the dominant product. For instance, Hutching et al. reported a Cu−Fe/ZSM-5 catalyst that can selectively convert CH_4 to CH_3OH using H_2O_2 as an oxidant reaching a TOR of 31 mol_{MeOH} $mol^{-1}{}_{Fe}$ h^{-1} and 85% selectivity.[246] Despite the obvious observation of enhanced oxygenates selectivity, the role of Cu species remains elusive. It is believed that Cu species control the population of •OH radicals impeding the further oxidation of CH_3OH to formic acid.[247] Several studies have been conducted on copper exchanged zeolites (CuMFI, CuMOR, CuFAU, CuMAZ, and CuCHA) to know the role of copper in CH_4 to CH_3OH formation.[248,249] Detailed studies suggest the formation of oxo copper monomers, dimers, bis-μ-oxo and mono-μ-oxo states depending upon the structural topological feature, chemical composition (Si/Al ratio), copper concentration, and nature of counterions present on zeolite surface.[250] Based on the FTIR, DRIFT, and NMR studies on Cu exchanged zeolites, it can be confirmed that Cu^{II} sites are reduced to Cu^{I} during the reaction and methoxy, dimethyl ether species were bonded to Cu^{I} and Brønsted acid sites.[251] Suskevich et al. investigated the intermediate species in detail using NMR and suggest that CH_4 oxidation on activated Cu follows the formation and stabilization of CH_3OH on Brønsted acid sites, which was also confirmed in subsequent works indicating the transfer of methoxy from Cu sites to Brønsted acid sites.[248] Compared to copper-oxo oligomers (di/trimer), mono-μ-oxo species due to the absence of hydrogen atoms, the reaction with methane leads to the generation of free Brønsted acid sites and reduced Cu^{I}, and the resulting methoxy can migrate to Brønsted acid sites. In another study, Dyballa used $^{1}H-^{13}C$ cross-polarization (CP) MAS NMR and $^{1}H-^{13}C$ heteronuclear correlation (HECTOR) spectroscopy to evaluate the chemical nature of Cu sites and methanol formation mechanism on Cu exchanged mordenite (MOR).[252] It was found that surface methoxy groups (SMGs) were located on Brønsted sites preventing further oxidation. H-form with plenty of Brønsted sites is more active than Na-MOR, and activity can be further increased by tuning the n_{Si}/n_{Al} while keeping alternate Cu and Brønsted sites distribution. Despite these observations, many studies demonstrated that Cu also promotes the •OH radicals' generation. For instance, Sun et al. investigated the role of Cu^0, Cu^+, and Cu^{2+} dominant species supported on silica (Cu@SiO_2-R200) for the H_2O_2 to •OH radicals' generation, which demonstrates that Cu^+ species were the most active.[253] In situ DRIFT using CO as a probe molecule and XANES were used to confirm the presence of Cu^+ species, while DFT calculations suggest that adsorption energy of H_2O_2 on Cu_2O (Cu^+) was higher compared to Cu and CuO. Another study also demonstrates the accelerated generation of •OH radicals on Cu/ZSM-5 catalyst in Fenton-type reactions due to Cu^+/Cu^{2+} catalytic cycle.[254] From these speculations, it can be anticipated that Cu species help in •OH radical generation while at the same time stabilizing the CH_4 oxidation intermediates cooperatively with support to avoid over oxidation of the products. Yu et al. synthesized the Cu−Fe/ZSM-5 catalyst by varying the amount of Cu (0.1−3 wt %) to probe the role of Cu species on the product selectivity and the optimal concentration of Cu species require to maintain product selectivity (Figure 11a).[255] The Cu−Fe(2/0.1)/ZSM-5 catalyst demonstrated a maximum methanol yield of 215.6 mol/mol_{Fe} with an associated TOR of 431 h^{-1}. When Fe species were deposited on trace Fe free silicalite-1, the reaction was still catalyzed, while Cu/silicalite-1 does not show any activity substantiating Fe was the main catalytic species. UV−vis spectra of Cu−Fe(2/0.1)/ZSM-5 showed two peaks for Cu^{2+} (203 nm) and Fe^{3+}/Cu^+ (269 nm), while no peak for oligomeric Fe/Cu species was observed in 300−450 nm spectral range suggesting monomeric distribution (Figure 11b). The STEM mapping and UV−vis also demonstrate a nominal clustering of Cu in the form of CuO as evident from explicitly small absorption band around 600 nm. Quantitative determination of Fe species in 0.1Fe/ZSM-5 and Cu−Fe(2/0.1)/ZSM-5 using ^{57}Fe Mössbauer spectroscopy displayed a doublet with IS = 0.36 and QS = 0.69−0.70 mm/s ascribed to the dominant monomeric Fe^{3+} species in an octahedral coordination, while another doublet with IS = 0.34−0.38 and QS = 1.47−1.55 mm/s originated from oligomeric Fe_xO_y species (Figure 11c). Interestingly, the population of isolated Fe^{3+} species for Cu−Fe(2/0.1)/ZSM-5 was increased to 71% compared to 66% for 0.1Fe/ZSM-5. The pre-edge feature at 8977 eV in Cu K-edge XANES spectrum of Cu−Fe(2/0.1)/ZSM-5 with intensive white line feature at 8996 eV suggests the presence of Cu^{2+} species coordinated to H_2O/OH ligands (Figure 11d), while EXAFS spectra suggest four coordination with a Cu−O distance of 1.95 Å. Fe K-edge XANES spectra Cu−Fe(2/0.1)/ZSM-5 validate the presence of Fe^{3+} species. The presence of two Fe−O shells in EXAFS with a Fe−O distance of 1.89 and 2.05 Å with a coordination number 2 and 4 were corroborated to Fe−O−Al and Fe−OH/H_2O, respectively, evidencing the presence of monomeric Fe complex $[(HO)_2-Fe(III)-(H_2O)_2]^+$. The CH_4 oxidation in the presence of 0.1Fe/ZSM-5 catalysts mainly produces HCOOH with a CH_3OOH intermediate, while under identical conditions, CH_3OH was the main product for Cu−Fe(2/0.1)/ZSM-5 suggesting two reaction pathways catalyzed by •OOH and •OH species. Control experiments using CH_3OOH as a reactant and 0.1Fe/ZSM-5 and Cu−Fe(2/0.1)/ZSM-5 catalysts produce only formic acid (Figure 11e). No trace of methanol was observed, demonstrating CH_3OH was not produced from CH_3OOH oxidation. Furthermore, EPR spectra of Cu−Fe(2/0.1)/ZSM-5 displayed an increase •OH signals intensity compared to 0.1Fe/ZSM-5, indicating that Cu were the main species facilitating the •OH formation. Interestingly, after the addition of CH_4 in the H_2O_2 and Cu−Fe(2/0.1)/ZSM-5 catalysts systems, the •OH signals intensity were significantly decreased with increased CH_3OH yield (Figure 11f). However, no EPR signals corresponding to •CH_3 radicals were detected, demonstrating •CH_3 species were immediately captured by •OH radicals to generate CH_3OH. DFT calculation to evaluate the mechanism of

https://doi.org/10.1021/acsnano.2c02464
ACS Nano XXXX, XXX, XXX−XXX

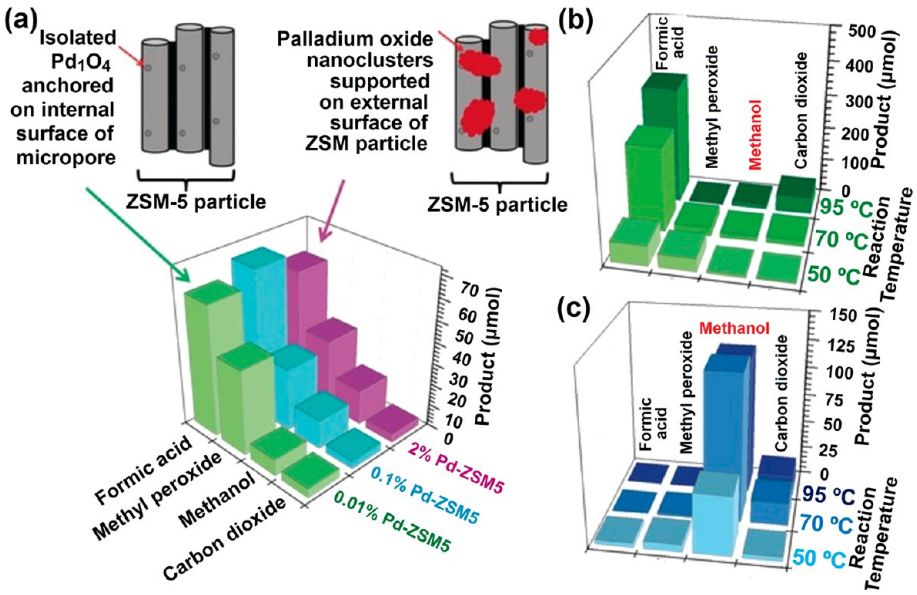

Figure 12. (a) Yields of products of transformation of CH_4 catalyzed by 0.01, 0.10, and 2.0 wt % Pd/ZSM-5 for methane partial oxidation at 50 °C. Catalytic performance of (b) 0.01 wt % Pd/ZSM-5 at 50, 70, and 95 °C and (c) 0.01 wt % Pd/ZSM-5 loaded with 2 wt % CuO at 50, 70, and 95 °C. The plotted yields of products formed on 28 mg 0.01 wt %Pd/ZSM-5 or 0.01 wt %Pd/ZSM-5 loaded with 2.0 wt %CuO are the values after subtraction of the yields of the products formed on 28 mg ZSM-5 (without Pd sites) under the same catalytic conditions. Reprinted with permission from ref 269. Copyright 2016 Wiley VCH.

reaction demonstrates that H_2O_2 replace coordinated water from hydrated $[(HO)_2-Fe(III)-(H_2O)_2]^+$ complex followed by transfer of H^+ to the adjacent − OH ligand (Figure 11g,h). The resulting Fe−OOH bond was cleaved by adjacent Brønsted acid sites to form hypervalent Fe(V)═O species. In the subsequent steps, the homolytic CH_3−H bond cleavage and integration of •CH_3 radical and a Fe coordinated −OH ligand take place producing CH_3OH. It is worthy to note that the introduction of Cu species in Cu−Fe(2/0.1)/ZSM-5 significantly reduced the energy barrier of the H_2O_2 dissociation to generate •OH radicals (0.08 eV) compared to Cu−Fe(2/0.1)/ZSM-5, providing populated concentration of •OH to react immediately with •CH_3 radicals.

5.2. Noble Metal SACs on Micro/Mesoporous Silica (ZSM-5). Currently, methane to methanol formation technology relies on the conversion of methane to the syn-gas mixture by SMR followed by conversion to methanol (FT process). The overall thermodynamic efficiency of these reactions is just 65% and required a high operating temperature (800−1000 °C) consuming almost 25% of the natural gas feed.[256] Direct methane conversion (DMC) can solve such issues, where C−H bond activation using benign oxidants and catalysts can be achieved at low temperature (and even room temperature). The earliest patent by Dowden and Walker at Imperial Chemical utilized $Fe_2O_3(MoO_3)_3$ catalysts that can afford an 869 g kg^{-1} h^{-1} of methanol,[257] after that several catalysts such as V_2O_5/SiO_2, Fe-ZSM5, etc., were introduced.[258,259] Compared to gas-phase oxidation, liquid-phase oxidation of methane is more appealing due to less complicated reactor design, less operating cost/easy handling and better catalysts dispersion which can achieve the higher catalytic activity. Initial studies on C−H bond activation of methane at room temperature, using H_2SO_4 and $HgSO_4$[260] followed by using bipyrimidyl Pt^{II} complex[261] to form CH_4OSO_3H paved the way to develop more efficient catalysts. Though aqueous phase oxidation of methane to methanol was reported long back in 1969 on H_2PtCl_4 catalyst,[262] the report by Neumann on aqueous phase oxidation of methane to methanol under mild aerobic conditions (50−60 °C, 0.1−0.2 MPa of O_2) using bipyrimidinylplatium-polyoxometalate ($H_5PV_2Mo_{10}O_{40}$) fueled the DMC research.[263] Later, aqueous phase oxidation of methane to methanol was matured by the pioneering work of Hutchings, where he developed numbers of Cu/Fe supported ZSM catalysts. He demonstrated that like MMO, these supported catalysts possess a μ-oxo dimeric form that facilitates the C−H bond scissoring.[246] Numerous heterogeneous supported systems with noble and non-noble metal, metal−organic framework (MOF), and polyoxometalate have been developed for DMC using O_2/H_2O_2 oxidant. Sorokin et al. demonstrated the homogeneous iron phthalocyanine dimer (μ-nitrido form) can afford a TON of 209 in the presence of H_2O_2 oxidant.[264] Even after such advancements, the DMC faces the dilemma of high selectivity and poor recyclability in homogeneous catalysts while easy recycling and poor catalytic activity/selectivity of supported catalysts. Noble metal-based catalysts are still at the top in terms of conversion rate.[265] For instance, Hutchings's prior work on TiO_2-supported Au−Pd nanocluster catalysts demonstrated excellent activity improvement for the direct conversion of methane to methanol using H_2O_2 as an oxidant.[266] However, in most of the bulk nanoparticles-based supported catalysts, almost 80% of atoms remain unexposed in bulk medium requiring high loading. For example, the loading of Au−Pd as high as 1−5% was required to maintain a significant oxidation rate, while the methanol selectivity remains below 50%. Noble metal-based SACs due to innate activity, high numbers of exposed catalytic sites, less proneness for deactivation, and heterogenized form with high selectivity like in homogeneous counterparts demonstrated the potential to materialize the DMC technology.[267,268] Tao's group demonstrated atomically dispersed Pd SA (Pd_1O_4 single sites) stapled on the internal surface of ZSM-5 silica micropores facilitates the oxidation of methane (Figure

https://doi.org/10.1021/acsnano.2c02464
ACS Nano XXXX, XXX, XXX−XXX

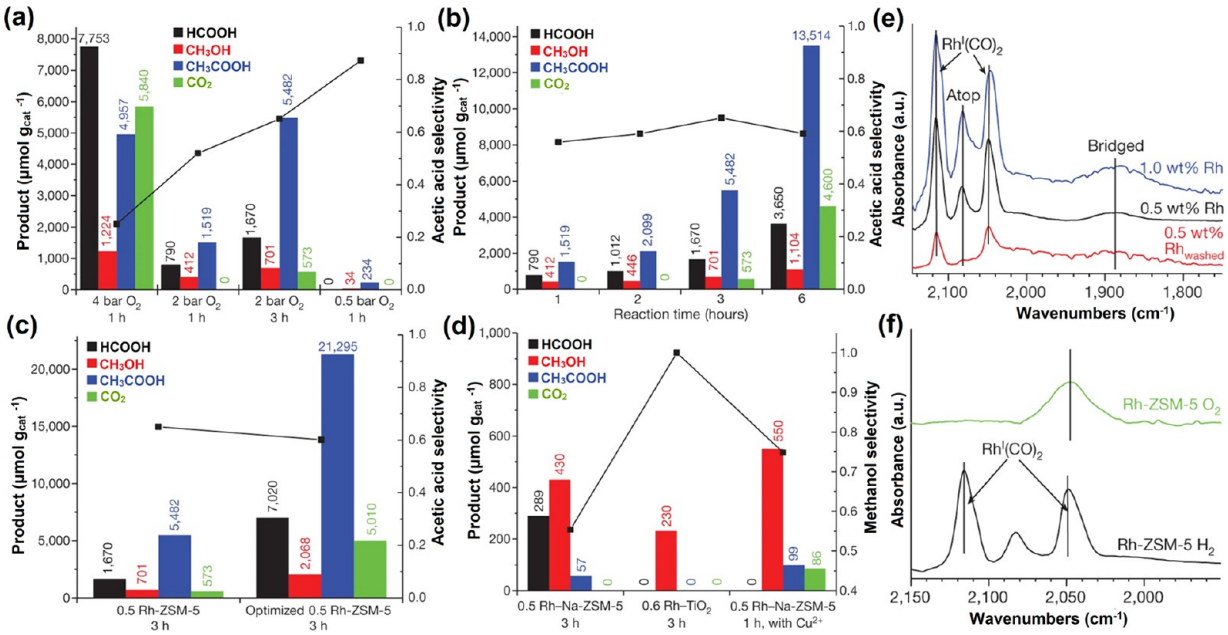

Figure 13. Catalytic performance of supported Rh catalysts in the conversion of CH_4 to oxygenates. (a−c) Product yields and acetic acid selectivity for 0.5 wt % Rh-ZSM-5 with varying PO_2 and reaction time (a); 0.5 wt % Rh-ZSM-5 at 2 bar O_2 with varying reaction time (b); and 0.5 wt % Rh-ZSM-5 and optimized 0.5 wt % Rh-ZSM-5 at 2 bar O_2 and 3 h reaction time (c). (d) Product yields and methanol selectivity for 0.5 wt % Rh-Na-ZSM-5 with and without Cu^{2+} and on 0.6 wt % rhodium/titanium dioxide, at 2 bar O_2 and varying reaction time. Reaction conditions: 20 mg catalyst, 0.5−4 bar O_2, 5 bar CO, 20 bar CH_4, 20 mL of water, 0.5−6 h reaction time, 150 °C reaction temperature. (e) CO-DRIFTS spectra of 1.0 wt % Rh-ZSM-5, 0.5 wt % Rh-ZSM-5 and 0.5 wt % Rh-ZSM-5_{washed}; an additional washing step was applied to the latter sample before the hydrogen reduction step to remove Rh species from the external surface of the zeolite. (f) CO-DRIFTS spectra of 0.5 wt % Rh-ZSM-5 (bottom trace) and 0.5 wt % Rh-ZSM-5 calcined in the air (top trace). Reprinted with permission from ref 284. Copyright 2020 Springer Nature.

12).[269] The singly dispersed Pd_1O_4/ZSM-5 was prepared using IWI method by injecting $Pd(NO_3)_2$ solution in evacuated ZSM-5 powder. As the concentration of Pd precursor and method of dispersion was extremely important, a series of samples with a Pd loading of 0.01, 0.04, and 2 wt % were prepared for comparison. The absence of any agglomerated particles in TEM images and absence of signals corresponding to Pd−O in XPS/XRD spectra suggest the monatomic distribution of Pd at low concentrations. Furthermore, EXAFS spectra of 0.01 wt % Pd did not show any peak due to low concentration, while 0.04 wt % Pd loading on ZSM-5 displayed a sharp peak for monatomic Pd−O species. No metal-to-metal interaction peak (Pd−Pd bonds 2.58 Å in metallic Pd) or Pd−O−Pd (in bulk PdO) peak was observed which further verifies the presence of isolated Pd centers. The determined coordination number of 4.12 ± 0.49 ensures absence of any bent mono(μ-oxo)dipalladium structure corroborating singly dispersed Pd_1O_4 coordinated species in ZSM-5. The methane catalytic oxidation experiments using 0.01 wt % Pd/ZSM-5 at 50 °C afford 111.91 μmol total yield of formic acid, methyl peroxide, methanol, and CO_2, while the product yield for identical concentration of Pd deposited on SiO_2 and Al_2O_3 nanoparticles was significantly lower. Furthermore, the catalytic activity of 0.01 wt % Pd/ZSM-5, 0.04 wt % Pd/ZSM-5 and 2 wt % Pd/ZSM-5 was found to be almost similar (Figure 12a). These observations suggest that only SA Pd distinctively coordinated in ZSM-5 cavities were able to activate C−H bond, while Pd atoms decorated outside the cavity were completely inactive for DMC. Though, enhanced reaction temperature (95 °C) promotes the conversion rate, the formic acid remains a dominate product due to the overoxidation of methanol by excess H_2O_2 (Figure 12b). To prevent the oxidation of the formed methanol, CuO was used to dissociate excess H_2O_2 that shifted the selectivity toward methanol formation. Under optimized reaction conditions, using 2 wt % CuO and 0.01 wt % Pd/ZSM-5, the methanol selectivities of 78.48, 85.46, and 86.35% were obtained at 50, 70, and 95 °C, respectively (Figure 12c). The maximum TOF value for 0.01 wt % Pd/ZSM-5 at 95 °C was calculated to be 2.33 CH_3OH molecules on a Pd_1O_4 site per second.

Methane can not only oxidize to the same carbon number oxygenates but can also produce high carbon number chemicals, using suitable coupling agents. The self-coupling of methane to ethane and other higher hydrocarbons has been reported at a higher temperature.[270,271] Direct conversion of methane to acetic acid has attracted significant attention due to the wide use of CH_3COOH as commodity chemicals such as vinyl acetate, acetate esters (ethylene-vinyl acetate, ethyl acetate, etc.).[272] Global CH_3COOH production was 9.07 million tons in 2020 and is expected to increase up to 11.85 million tons by 2026.[273] Direct acetic acid production from methane oxidation can suppress energetics and the cost of currently used multistep conversion methane to syngas (CO and H_2) followed by methanol and acetic acid formation via carbonylation with CO ($CH_4 \rightarrow CO/H_2 \rightarrow CH_3OH + CO \rightarrow 2CH_3COOH$). Usually, methane activation to acetic acid can also be promoted by coupling with CO and O_2 by the following reaction: $2CH_4 + 2CO + O_2 \rightarrow 2CH_3COOH$. However, some reports demonstrated that CO species originated via the oxidation of CH_3OH can also produce acetic acid.[274] For example, Periana et al. reported concen-

https://doi.org/10.1021/acsnano.2c02464
ACS Nano XXXX, XXX, XXX−XXX

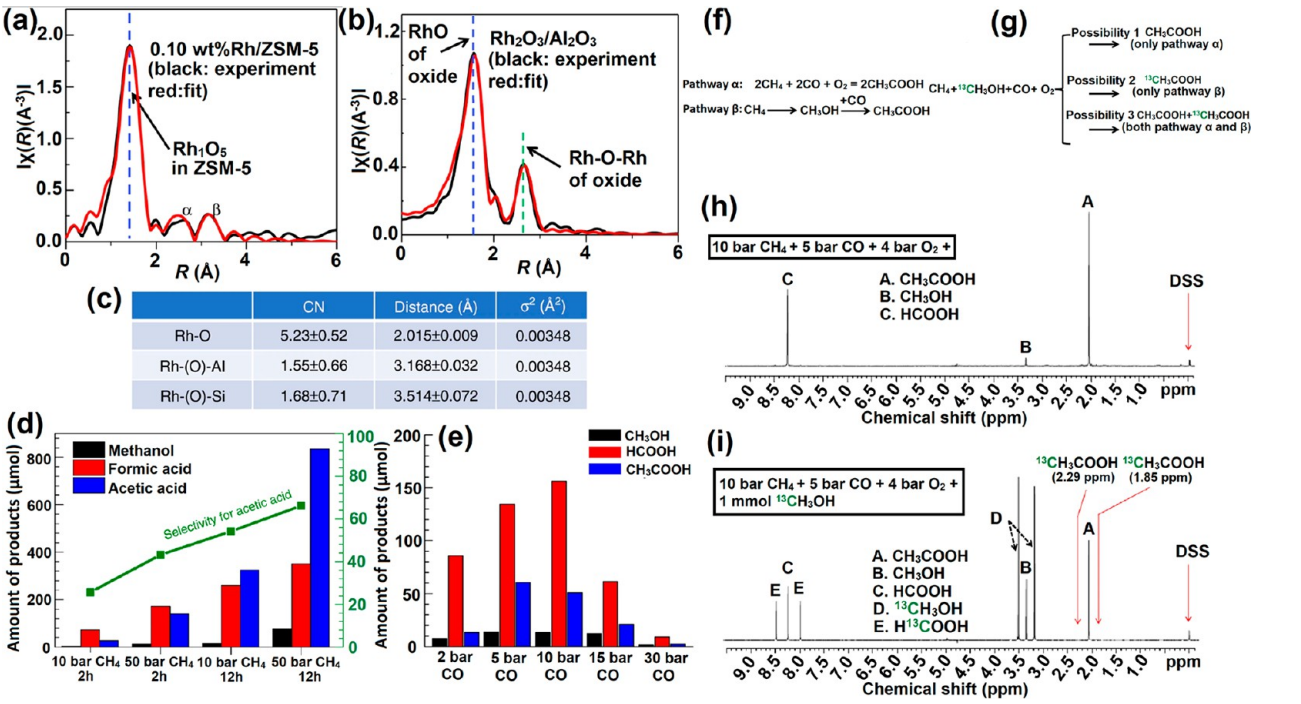

Figure 14. (a) r-space of Rh K-edge of experimental and calculated data of the k^2-weighted Rh K-edge EXAFS spectra of used 0.10 wt %Rh/ZSM-5. (b) r-space of Rh K-edge of experimental and calculated data of the k^2-weighted Rh K-edge EXAFS spectra of Rh_2O_3 NPs supported on Al_2O_3. (c) Coordination number and bond length on average of the used 0.10 wt %Rh/ZSM-5. (d) Catalytic performance of 0.10 wt % Rh/ZSM-5. Yields of methanol, formic acid, and acetic acid in the chemical transformation of CH_4 at 150 °C in aqueous solutions at different pressures of CO (e) 50 bar CH_4, 8 bar O_2, and different pressure of CO at 150 °C for 1.5 h. Isotope studies for elucidating whether acetic acid could be formed through coupling methanol with CO. (f) Two potential pathways *α* and *β* for production of acetic acid. In pathway *α*, CH_3OH is not an intermediate compound for formation of CH_3COOH, and in pathway *β*, CH_3OH is an intermediate compound for formation of CH_3COOH. (g) Potential catalytic products formed from 0.10 wt %Rh/ZSM-5 in the mixture of $^{13}CH_3OH$ and H_2O in solution under a mixture of CH_4, CO, and O_2 if the transformation of CH_4, CO, and O_2 follows pathway *α*, *β*, or both *α* and *β*. (h) NMR spectra of the products formed from 28 mg of 0.10 wt %Rh/ZSM-5 after reaction in 10 bar CH_4, 5 bar CO, and 4 bar O_2 at 150 °C for 1 h; there was no isotope-labeled methanol, $^{13}CH_3OH$ added to the rector before this catalysis test. (i) NMR spectra of the products formed from 28 mg of 0.10 wt %Rh/ZSM-5 after reaction in 10 bar CH_4, 5 bar CO, and 4 bar O_2 at 150 °C for 1 h; notably, 1.0 mmol $^{13}CH_3OH$ was added to H_2O before this catalysis test. Reprinted with permission under a Creative Commons CC-BY License from ref 285. Copyright 2018 Springer Nature.

trated H_2SO_4 and Pd salts promote methane activation to form acetic acid and methanol (82 mM and 38 mM respectively) with a 90% acetic acid selectivity without any external CO/CO_2.[275] Other cheaper calcium, vanadium-based catalysts have also been used for the carbonylation/carboxylation (CO/CO_2) of methane using O_2/H_2O_2, but the requirement of harsh acids such as CF_3COOH (TFA), $K_2S_2O_8$, high pressure, and poor product yield remains a challenge to meets large scale production.[276−279] Initial studies demonstrated Rh-based catalysts are highly active for methane carbonylation to CH_3COOH due to the stabilization of Rh-carbonyl species formed via CO insertion.[280] However, homogeneous system and bulk-supported nanoparticulate suffers from the drawbacks of recycling and the requirement of high metal loading. MOFs with more exposed catalytic centers displayed enhanced performance for CH_4 to CH_3COOH conversion.[281] ZSM-5 supported transition metals with a fine distribution of the metal centers have also been investigated for CH_4 oxidation. For example, copper-exchanged mordenite (Cu-MOR) can promote oxidation carbonylation of methoxy species.[282,283] Detailed mechanism studies using isotopically labeled $^{13}CH_4$, ^{13}CO, and $^{18}O_2$ followed by CP MAS NMR displayed that carbonylation reaction predominantly takes place in the 8MR pockets of MOR. Interestingly, studies suggest that Cu^{II}−O−Cu^{II} sites were active for the oxidation of methane to methoxy species; however, carbonylation takes place on acid sites located in the 8MR pockets.[206] Reducing the size of metal counterpart to atomic regime followed by decoration in hierarchical nanoporous supports can minimize the usage of expensive metal while ameliorating the catalytic activity due to the tuning of coordination environment. Flytzani-Stephanopoulos displayed that isolated Rh atoms embellished on nanoporous ZSM-5 can promote DMC to acetic acid and methanol with an optimized yield of 22000 and 230 μmol g^{-1}cat and 60−100% selectivity (Figure 13).[284] The catalyst was prepared by deposition of Rh in NH_4-ZSM-5 nanopores by IWI followed by annealing in 5% H_2 at 550 °C. The developed materials were washed several times to remove any additional nanoparticles. The atomically distributed entities and absence of any metal−metal clustering were confirmed by using EXAFS. The presence of two vibration peaks at 2116 and 2049 cm^{-1} in DRIFTS due to the symmetrical and asymmetrical stretching of dicarbonyl CO bonded to isolated mononuclear $Rh^I(CO)_2$ further validates the presence of SA Rh species (Figure 13e,f). The annealing of materials under H_2 and washing step after the synthesis of the catalyst were essential as unwashed samples displayed atop CO binding peaks at 2082 cm^{-1}. The catalytic performance evaluation using water suspended catalysts in pressurized CH_4, CO, and

https://doi.org/10.1021/acsnano.2c02464
ACS Nano XXXX, XXX, XXX−XXX

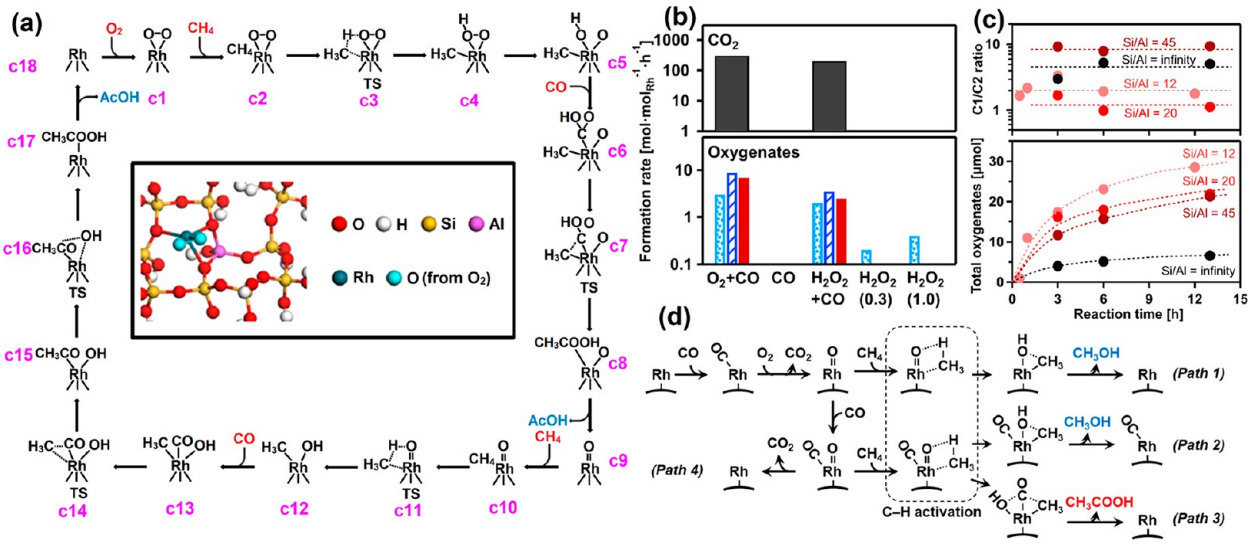

Figure 15. (a) Minimum-energy paths and reaction schematic for the formation of acetic acid from CH_4, CO, and O_2 on Rh_1O_5/ZSM-5. The formation of acetic acid is illustrated in a catalytic cycle starting with the singly dispersed Rh_1O_5 site. Reprinted with permission under a Creative Commons CC-BY License from ref 285. Copyright 2018 Springer Nature. (b) Products oxygenate (bottom) and CO_2 (top) formation rates over Rh-ZSM-5 using gaseous O_2 or H_2O_2 as an oxidant with/without CO. In the bar graph (bottom), the left bar with light-blue dots, the middle bar with blue stripes, and the right bar with filled red indicate methanol, formic acid, and acetic acid, respectively. (c) Changes in total oxygenate amounts with reaction time over Rh-ZSM-5 with different Si/Al ratios of 12 (light-red circles), 20 (red circles), 45 (brown circles), and pure silica (black circles), and the C1/C2 ratios (top). (d) C−H activation with the help of surface O species over bare or CO-coordinated Rh and subsequent oxygenate formation. Reprinted with permission from ref 287. Copyright 2022 Elsevier.

O_2 was performed at different temperatures. The ideal temperature at which the reaction start was 110 °C and the reaction yield reached optimum at 150 °C. Further, temperature increments reduce the product yield due to the overoxidation of reaction products to CO_2. High O_2 pressure (4 bar) was detrimental for the reaction, and high yield was afforded at 2 bar O_2 pressure and 6 h reaction (Figure 13a,b). Optimized particle-free catalysts demonstrated excellent selectivity for the acetic acid product at 0.5 bar pressure and 3 h reaction time (Figure 13c). To know the trajectory of the reaction, isotopic labeling experiments using ^{13}CO demonstrate insertion of CO in Rh−CH_3 to from Rh−$COCH_3$ species. However, acidic H-ZSM-5 support was essential to produce acetic acid and Na-ZSM-5 and TiO_2 decorated Rh SACs could not produce any acetic acid (Figure 13d).

SACs not only enhance the activity and selectivity but can also activate specific reactions due to the undercoordinated metal environment and ensemble effect of support. For example, Tang et al. demonstrated that Rh_1O_5 supported on ZSM-5 can promote methane oxidation to CH_3COOH and CH_3OH, while Rh metal particles supported on ZSM-5 were almost inactive for DMC.[285] To achieve this goal, they synthesized isolated Rh_1O_5 single sites coordinated in the inner pore of ZSM-5 by following a similar IWI method as reported for Pd_1O_4 using Brønsted acid sites containing H-ZSM-5.[285] The absence of any XPS signal in 0.10 wt %Rh/ZSM-5 catalysts and the presence of Rh in ICP-AES analysis evidenced that Rh was decorated inside the pores. EXAFS r-space spectrum of Rh K-edge demonstrated the coordination of Rh atom was 5.23 ± 0.52 in 0.10 wt %Rh/ZSM-5 (Figure 14a). The absence of Rh−Rh peak in 0.10 wt %Rh/ZSM-5 excludes the possibility of any clustering, while overlapped first shell with Rh_2O_3 nanoparticles and absence of second Rh_2O_3 shell peak at 2.60 Å illustrate lack of any metal oxide (Rh−O−Rh) nanoclusters (Figure 14a,b). After peak fitting, the small peak (α) at about 2.7 Å and β peak at 3.3 Å were assigned to Rh−O−Al and Rh−O−Si, respectively. The EXAFS results suggest each Rh atom was bonded with at least five oxygen atoms (Figure 14c). The catalytic reaction at 150 °C, using a mixture of CH_4, CO, and O_2 with 0.10 wt %Rh/ZSM-5 catalysts followed by product identification using NMR gave peaks at δ = 2.08, 8.28, and 3.33 ppm for acetic acid, formic acid, and methanol, respectively. Enhancing the Rh concentration to 0.50 wt % in 0.5 wt %Rh/ZSM-5 does not enhance the catalytic performance, substantiating the extra Rh outside the pores was not active for the CH_4 oxidation and does not contribute to the reaction. Control experiments using Rh deposited on SiO_2 and Al_2O_3 and Rh^{3+} only cannot even achieve yield in micromole decades regime. The maximum activity using 0.10 wt %Rh/ZSM-5 was found to be 0.10 CH_3COOH molecules on a Rh_1O_5 site per second with an associated selectivity of ∼70% (Figure 14d). To evaluate the role of O_2 and CO in the transformation of CH_4 to CH_3COOH, the reaction was performed by varying the pressure of O_2 and CO. As the O_2 and CO pressure was raised, an enhancement in the product conversion was observed. However, a further increase in pressure drops the product conversion due to coverage of all Rh sites with O_2 and CO (Figure 14e). These observations suggest that O_2 and CO_2 play a crucial role in methane transformation. Isotopic labeling experiments using ^{13}CO and unlabeled CH_4 gave $CH_3{}^{13}COOH$ or $H^{13}COOH$ as predominant products verifying carboxylic carbon of the products came from CO. Similarly, when $^{13}CH_4$ was used as a reactant, the NMR signals corresponding to $^{13}CH_3COOH$ and $^{13}CH_3OH$ were much higher than contrast experiments, validating methyl groups were originated from CH_4 oxidation. The CH_3COOH might be produced either by direct coupling of CH_4 with CO (pathway α) or the oxidation of CH_4 to CH_3OH followed by carbonylation (pathway β) (Figure 14f,g). To verify which

https://doi.org/10.1021/acsnano.2c02464
ACS Nano XXXX, XXX, XXX−XXX

route was followed, $^{13}CH_3OH$ was used as a reactant which does not produce any $^{13}CH_3COOH$ or $CH_3{}^{13}COOH$, demonstrating β-pathway was highly improbable and CH_4 activation proceeds through direct carbonylation of methane (Figure 14h,i). DFT calculations were run on the optimized structure by considering the EXAFS results in which three coordination sites of Rh were bonded with oxygen atoms of the substrate and two coordination sites were bound with an O_2 molecule (Figure 15a c1). The Rh atom binds to the ZSM-5 network by replacing one Al site and preferred ten membered ring channels. Isotopic labeling experiments demonstrate, C−H bond scissoring and CO insertion to form CH_3COOH. The reaction of Rh_1O_5 followed by C−H bond activation results in a transient state with methyl and hydroxyl adsorbed on the Rh atom (c2−c4). In the subsequent step, CO can insert into the Rh−O bond of Rh−O−H, forming a COOH which can react with CH_3 to form weakly bonded CH_3COOH (c7−c8). After desorption of CH_3COOH, the formed Rh═O can further activate C−H activation of the second CH_4 forming Rh coordinated CH_3 and OH (c9−c12). Again, CO insertion followed by CH_3COOH desorption and O_2 activation regenerates the penta-coordinated catalytic centers.

The CO-assisted CH_4 transformation over Cu and Rh-based catalysts were investigated before and most of the reports isolate CH_3COOH as a dominating product in the absence of O_2/H_2O. The mechanistic detail of methane carbonylation over zeolite support with metals has been proposed which suggests that alcohol formed during the reaction adsorbs on Brønsted acid sites and generates methoxy species which reacting with CO form an acylium cation which finally gets quenched by water to form acetic acid. Initial evidence of such a mechanism comes from the study of Blasco where they used in operando IR spectroscopy and in situ MAS NMR spectroscopy to study the mechanism of CH_3OH carbonylation over H-mordenite.[286] Other studies on Cu-exchanged zeolites demonstrate a Koch-type carbonylation mechanism where methoxy group formed on Cu sites migrated to Brønsted acid sites of zeolite followed by CO insertion and hydrolysis of the acyl group yield CH_3COOH. Narsimhan et al. showed CH_4 oxidation on Cu-exchanged zeolite and MOR zeolite which demonstrated that the Bronsted acid site in the 8MR pocket facilitates migration of methoxy group from oxidation site to carbonylation site.[206] Other transition and noble metal-based catalysts have also been reported to yield CH_3COOH from carbonylation of CH_4. For example, Moteki et al. screened Fe, Co, Ni, Cu, Ru, Rh, Pd, Ir, and Pt modified ZSM-5 catalysts for oxidative carbonylation of CH_4, of which Rh demonstrated the highest activity (Figure 15b−d).[287] They performed a series of experiments using CH_3OH, HCOOH, CH_3COOH, and CH_3CHO as a reactant in the presence of CO and O_2 to identify the course of the reaction. The CH_3OH can be oxidized to HCOOH, while CO_2 was a major product. Similarly, by using HCOOH, CO_2 was observed as the sole product demonstrating overoxidation. Considering the possibility of CH_3CHO formation, it was also used as a reactant that yielded CH_3COOH within a short time which was quite stable and does not form CO_2. Based on these observations, it can be speculated that two reaction pathways exist leading to the formation of different oxidation products. In another study, they also investigated the importance of O_2 in CO-assisted CH_4 conversion (Figure 15b). First, they introduced CO and O_2 mixture in a reactor followed by heating and removal of gas. In the second step, the CH_4 and CO were introduced and made to react together. In this case, stochiometric CH_3OH and CH_3COOH were observed as the main products. No product was observed if only CH_4 and CO were only used. These observations suggest that Rh═O species were formed from CO and O_2 in the initial step by following the reaction CO + O_2 + Rh-zeolite → CO_2 + O═Rh-zeolite. The use of H_2O_2 as an oxidant with CO resulted in a comparable product as with CO and O_2, suggesting O_2 is a crucial oxidant during the reaction and H_2O_2 was not formed in situ via WGS reaction. When the ratio of Si/Al was reduced to 12 and 20, the C_2 product ratio was decreased suggesting acidic sites (Al sites) facilitating C_2 formation (Figure 15c). Similarly, removal of the acidic site by titration reduces the C_2 product yield but does not completely hinder C_2 products substantiating another route for C_2 product formation that exists via Rh sites. Based on these observations, a reaction mechanism was proposed in which CO and O_2 form M═O species and CH_4 can bind to this via CH_3−M−OH formation (Figure 15d). This intermediate can directly react with H_2O to form CH_3OH or combine with CO to facilitate carbonylation yield CH_3COOH end product. Though, the presence of mono and diatomic species is believed to improve the CO-assisted CH_3COOH production. However, a recent report by Qi et al. demonstrated that Au nanoparticles supported on ZSM-5 can selectively convert CH_4 to CH_3OH and CH_3COOH.[288] Interestingly, no other coreductant was needed, and only oxygen can promote the reaction between 120 and 240 °C suggesting an alternative route. These results created ambiguity about the real active centers and oxidants and should be further explored.

Apart from the above-mentioned noble metal catalysts, a combination of noble metal and non-noble metal can galvanize the performance of CH_4OR catalysts. The additive effect of CuO species on the catalytic performance of Pd/ZSM-5 catalysts has been already discussed in the previous sections.[269] However, the combination of two noble metals in the presence of Cu species in the same catalyst system is not clear. To elucidate the effect of each component, Li et al. investigated a trimetallic IrCuPd-ZSM-5 SACs system for the CH_4OR.[289] The 1.39 wt % $Ir_1Cu_1Pd_{0.1}$-ZSM-5 catalyst was prepared by sequential WI approach, with an atomic ratio of Ir: Cu: Pd is 1:1:0.1. The reaction was carried out by using CO and O_2 as a source of in situ H_2O_2 production confirmed by titrimetric analysis with $TiOSO_4$. The activity of 1.0 wt % Ir-ZSM-5 (340 μmol $g_{cat}{}^{-1}$) was dramatically increased by adding Pd, reaching a C1 oxygenates yield of 2954 μmol $g_{cat}{}^{-1}$ for 1.06 wt % $Ir_1Pd_{0.1}$-ZSM-5. However, formic acid remains a dominating product with a 14% selectivity for CH_3OH due to the overoxidation of CH_4. Interestingly, trimetallic 1.33 wt % $Ir_1Cu_1Pd_{0.1}$-ZSM-5 SACs can reach an 80% selectivity with a ∼1200 μmol $g_{cat}{}^{-1}$, or ∼23.4 mol_{CH_3OH} $mol_{Ir}{}^{-1}$. The in situ DRIFT spectra in the presence of CO and CH_4 depict the formation of Ir(CO)(O) structure on SA sites during the reaction, while atop Ir_2 > CO signals remain unchanged suggesting the direct participation of SA species in CH_4 activation.

Based on the above discussions, it can be concluded that transition metal-based Cu-zeolite catalysts are highly selective for the CH_3OH generation; however, their performance remains poor in terms of product yield. Despite many dedicated studies, the role of mono and dimeric sites remains

https://doi.org/10.1021/acsnano.2c02464
ACS Nano XXXX, XXX, XXX−XXX

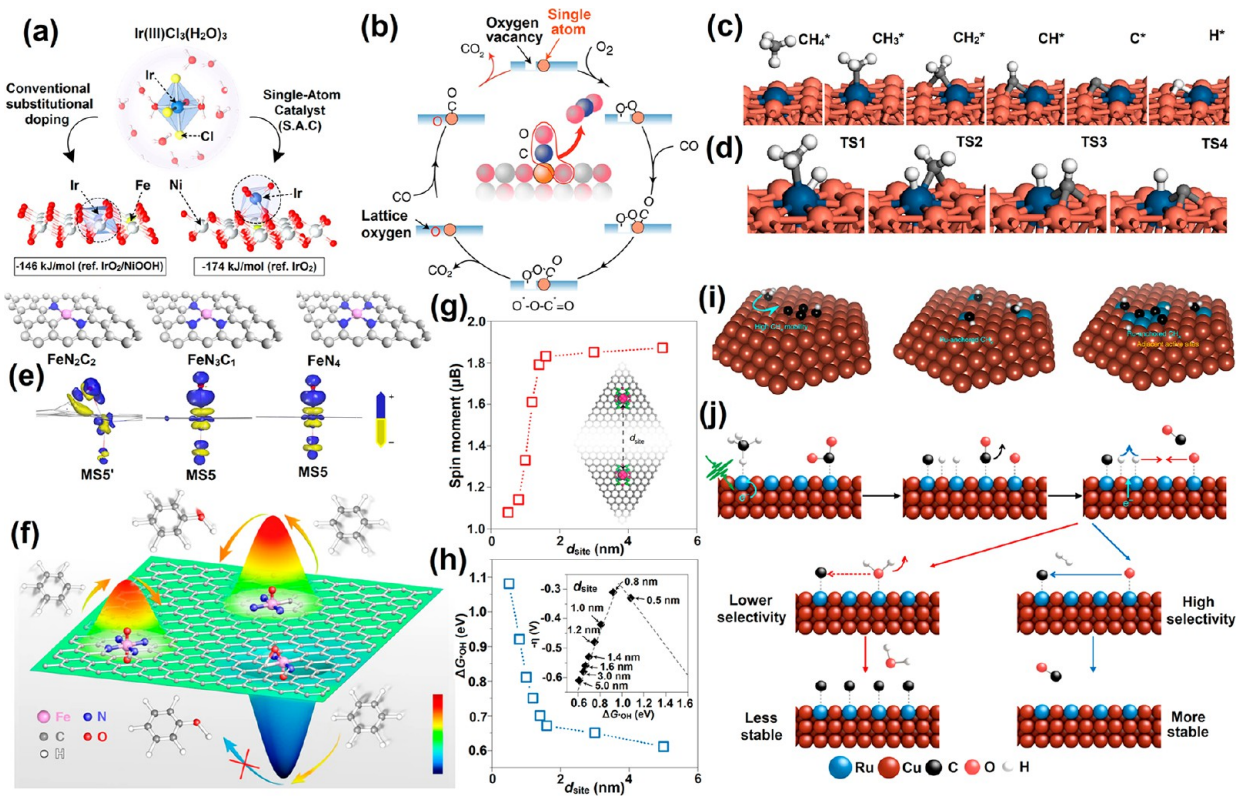

Figure 16. (a) Chemicals structure of NiFeIr SAC. The conventional in-layer substitution of Ni^{4+} by Ir^{4+} (NiFeIr) is compared to a more preferred single IrO_6 octahedron bonded to NiFe layer in SAC configuration (NiFeIr SAC). Reprinted with permission under a Creative Commons CC-BY-NC-ND 4.0 License from ref 298. Copyright 2021 PNAS. (b) Experimental and DFT simulated CO oxidation paths in MvK type reaction that leads to the formation and replenishment of oxygen vacancies proposed for Pt_1/FeO_x,[46] Au_1/FeO_x,[299] Pt_1/CeO_2,[300−302] Pt_1/TiO_2,[303] and Au_1/CeO_2.[304] Reprinted with permission from ref 305. Copyright 2019 Springer Nature. (c and d) Comparison of the reaction pathways between pure and Pt/Cu SAA surfaces. The comparison shows that Pt/Cu(111) SAAs have intermediate C−H scission barriers but beneficial Cu-like reaction energies, such that the SAA can perform C−H activation without carbon deposition. Optimized configurations from DFT for the most stable adsorptions of C_xH_y species on the Pt/Cu(111) SAA surface. Reprinted with permission from ref 157. Copyright 2018 Springer Nature. (e) Chemical structure and PDOS and charge density differences analyses of $Fe-N_xC_y$ (x = 2−4). Calculated charge density differences of O═Fe═O on $Fe-N_xC_y$ SAs/N−C catalysts. (f) The coordination effect of SA $Fe-N_xC_y$ catalytic sites on benzene oxidation. Reprinted with permission under a Creative Commons CC-BY License from ref 312. Copyright 2019 Springer Nature. (g) DFT-calculated on-site magnetic moments of Fe atoms interacting with neighboring sites with different d_{site} values (h) The d_{site}-dependent ΔG_{*OH} obtained by DFT calculations. Inset: volcano plot of calculated overpotentials for the ORR against ΔG_{*OH}. Reprinted with permission from ref 172. Copyright 2021 Springer Nature. (i) Schematics of the compositional dependence of the Cu_xRu_y photocatalyst with respect to coke resistance: pure Cu, low Ru loading and high Ru loading (left to right) (j) Schematics of enhanced selectivity and stability in photocatalysis via the DIET mechanism. Reprinted with permission from ref 322. Copyright 2020 Springer Nature.

elusive, and the presence of unsymmetric sites further raise a concern about the exact reaction mechanism. On the other hand, Fe-based catalysts with a hypervalent $Fe^{(IV)}$═O intermediate state were found highly active but remain highly unselective. Integrating Cu species in Fe-based catalysts to control oxidation rate and regulating the cavity size to prevent radical rebound are found encouraging. Noble metal (especially Rh) on ZSM-5 delivers a higher yield and, in some instances, can generate in situ H_2O_2 from H_2 and O_2 thus excluding the need for external oxidants. Further, the possibility of direct production of C_2 product (CH_3COOH) using CO as an oxidant widens the scope of zeolites-based catalysts.

6. THE ROLE OF SUPPORT: METAL SUPPORT INTERACTION

Support plays a vital role in the stabilization of SAs via coordination and also governs the reactivity/selectivity of SACs. The stabilization of a metal center on support via strong metal−support interaction (SMSI) depends highly on the availability of coordination ligand on support and effective orbital overlap between the metal and ligand.[290] The SMSI provides specific reactivity and prevents high-temperature sintering of catalysts. For example, 0.5% Fe©SiO_2 with an atomic distribution of iron species stays active up to 1293 K during the nonoxidative dehydrogenation of methane to aromatics.[291] Various approaches for the stabilization of SACs are to bind with a surface functional group, confinement in defects/vacancies, the substitution of support atom by a galvanic process, etc. In defect-rich materials, SA can occupy various defective sites such as steps, corners, and vacancies. Liu et al. investigated the stability of Au SA on various possible sites of CeO_2 and concluded that the stability of SAs decrease in the following order: vacancy > steps > oxygen vacancy > perfect (defect-free) surface.[42] However, it is not universal, and various other factors such as surface reducibility, nature of ligand and surrounding environment of the support are equally

https://doi.org/10.1021/acsnano.2c02464
ACS Nano XXXX, XXX, XXX−XXX

important. Practically, the synthesis of SA on defect-rich sites usually creates a mixture of SA sites distributed in various defects states. Due to different coordination environments, these SA sites can provide alternative reaction paths which compromise the selectivity and/or activity.[292] Thus, controlling the coordination environment of SA sites on the support is very essential.[293,294] The electronic interaction between SAs and support via electronic charge transfer/redistribution can shift the d-band electronic density and concomitantly the Fermi level, availing more electronic states for effective interaction to ameliorate a particular reaction (ensemble effect).[295,296] Studies demonstrated that merely changing the support can lead to an entirely different reaction product from using the same metal and reactant.[71] Such an intriguing phenomenon is evolved due to different coordination interactions between the SA and support. The EXAFS and XANES analyses usually reveal the presence of under coordinated SAs on support which demonstrate the charge transfer between metal and support. These under-coordinated sites also avail coordination of specific reactants. Li et al. demonstrated that Pt SA bonded with Co_3O_4 displayed enhanced performance for H_2 evolution compared to Pt supported on CeO_2 and ZrO_2.[297] The increased white line intensity in XANES and higher frequency of M-CO vibration in DRIFT displayed decreased 5d state electrons. The decreased 5d state suggests SMSI originated due to more electronic charge transfer from Pt to Co_3O_4 support stabilizing Pt^{4+} centers. The incorporation of SA on a specific site significantly influences the chemical charge and coordination patterns and concomitantly governs the stability and chemical reactivity. Zheng et al. found that Ir SA stabilization on NiFeOOH layered structure (NiFe) can accommodate two positions: (1) a conventional in-layer substitutional doping of Ir^{4+} replacing Ni^{4+} (NiFeIr) and (2) single IrO_6 octahedron bonded directly to the NiFe layer (atop) (Figure 16a).[298] The second configuration was found to be 28 kJ/mol more stable than the conventional model and displayed excellent performance for the OER. Interestingly, XAS evaluated +5.3 as the oxidation state of Ir in NiFeIr due to three OH in the coordination sphere compared to +4 for conventional three O bonded NiFeIr. The enhanced OER performance was attributed to the high oxidation state, multiple oxygen bonds at the NiFe layer, and effective interaction with the nearby solvent. Indeed, the specific activity of SA species supported on zeolite-based catalysts is because of the specific coordination of SAs with Al atoms, thus, changing the Si/Al ratio widely influences the nature of catalytic centers.

Easily reducible metal oxides such as TiO_2 and CeO_2 along with moderately reducible oxides such as CoO_x, MnO, NiO, CuO, and ZnO are ideal support to pin the SAs centers.[119] The generated defect states under a reducing environment not only provide coordination sites for SA but can also serve as reaction centers to synergistically catalyze a specific reaction. For instance, numerous SACs fabricated on a reducible surface such as Pt_1/FeO_x,[46] Au_1/FeO_x,[299] Pt_1/CeO_2,[300−302] Pt_1/TiO_2,[303] and Au_1/CeO_2[304] have shown specific reactivity for the CO oxidation due to the involvement of oxygen vacancies. The detailed mechanism supports the Mars van Krevelen (MvK) type mechanism where support lattice oxygen can also generate CO_2.[305] In general vacancies in the vicinity of isolated metal center adsorb O_2 molecule and form O_v-SA bonded O−O species in which CO insertion talks place to forming (O*−O−C*═O) intermediate. The release of CO leaves the metal center and the lattice oxygen to further react with another CO and finally produce CO_2 and surface vacancies (Figure 16b). The MvK type mechanism has also been reported for nonoxidative coupling of CH_4 to alkene and aromatics on iron supported silica catalysts (Fe©SiO_2).[306] Since, SiO_2 has less reducibility, usually carbon substituted SiO_2 is believed to promote the reaction. In gas-phase •CH_3 radical generation followed by coupling and dehydrogenation was proposed to produce unsaturated alkene/aromatics.[291] Further theoretical investigation reveals that C−H activation proceeds via a quasi-MvK mechanism via the formation of metal adsorbed •CH_3 and C−H species followed by •CH_3 migration to an adjacent carbon. Finally, ethylene is formed by abstraction of lattice carbon leaving a C vacancy which is regenerated by abstraction of C from another CH_4 molecule with the liberation of H_2. The classical example of metal−support interaction is presented by Fu et al. where Pt SA stabilized on reduced TiO_2 can promote selective hydrodeoxygenation-reduction of furfuryl alcohol to 2-methylfuran.[307] The selective reduction of the C−O bond in unsaturated aldehyde/alcohol is challenging because nanoparticulate metal catalysts also reduced the C═C bond-forming saturated alkanes. Previous studies indicated that O vacancies in oxide support can cleave the C−O bond via the reverse MvK mechanism and O abstraction can fill vacant O state. The resulting product is repelled by the oxide surface thus preventing ring chemistry. The vacancies can be replenished by simultaneous reduction with H_2 to generate H_2O; however, there should be an equilibrium between O vacancies filling and replenishing. The addition of noble metal on oxides supports is found to decrease the reduction temperature and can replenish vacancies at a lower temperature. However, unselective reduction remains a challenge, whereas SA centers on the other hand can direct selective hydrogenation. Considering these points, it was postulated that integration of SAs on the reducible surface can induce C−O scissoring and replenishing of vacancies at a lower temperature while maintaining selectivity for reduction. To validate the hypothesis, 0.04% Pt decorated on (101) TiO_2 was synthesized which can perfom selective reduction of furfuryl alcohol to 2-methylfuran at 160 °C, under H_2.

Nevertheless, the nondefect stabilization of SA species on the inorganic crystal is also not uncommon. The demonstration of high-temperature promoted evaporation of PtO_2 species from bulk nanoparticles followed by deposition in the atomic state on defect-free FeO_x substrate due to strong CMSI opens the door for nondefect stabilization of SAs.[119] For example, Liu et al. stabilized Ru SA on $MgAl_{1.2}Fe_{0.8}O_4$ support by anti-Ostwald ripening RuO_2 powders at high temperature.[308] In recent years, SAAs containing isolated metal SA on another metal have shown intrigued properties in the electrocatalysis field which are believed to be due to the generation of modulated electronic structure by orbital mixing and Fermi level adjustment.[143] The strong MSI facilitates synergistic stabilization of intermediate species (*O_2, H*, etc.) on support and SA species that ameliorate the catalytic properties. Besides electrocatalysis, SAA has also been investigated for thermo/photocatalytic applications. Marcinkowski et al. showed that Pt/Cu SAAs can activate C−H bonds to carry out complete oxidation without coking.[157] Figure 16c,d displays the C−H activation/dissociation of *H from intermediate species and associated transition states which demonstrated the participation of both Pt SA and Cu C−H bond scissoring. The calculated energy of the

https://doi.org/10.1021/acsnano.2c02464
ACS Nano XXXX, XXX, XXX−XXX

intermediates and transition state demonstrate that Pt(111) has a low-energy barrier, however leads to coke deposition due to the exothermic reaction coordinate. On the other hand, the Pt/Cu(111) SAA provides intermediate energy barrier heights compared to the two pure metals.

Compared to inorganic crystals, controlling the coordination pattern in carbon-based M-N_x-C catalysts is relatively easy.[309] The type of nitrogen that coordinates with the metal center also regulates the charge distribution on the latter which conversely affects the catalytic activity/selectivity. For example, MN_4 catalysts in which metal is coordinated to pyridinic Ns have a more stable configuration than pyrrolic, thus displaying better performance in ORR.[126] Similarly, the numbers of N atoms directly coordinated to the metal center are crucial to attaining a specific coordination environment. Depending upon the nature of the reaction, under N-coordinated M-N_x-C ($x < 4$) can either boost or hinder the reaction. For example, under N-coordinated, Ni-N_3-C[310] and W-N_2-C_2[311] can boost the CO_2RR and NRR reactions. On the other hand, under N-coordinated M-N_x-C_x catalysts were found to be less active for oxidation reactions. Pan et al. compared various Fe-N_xC_y (Fe-N_4, Fe-N_3C_1, and FeN_2C_2) catalysts for oxidation of benzene to phenol and found that Fe−N_4 species were most active while Fe-N_2C_2 was least active (Figure 16e,f).[312] Since, the formation of hypervalent Fe═O and O═Fe═O is essential for oxidation, the energy profile and coordination geometry of these systems were calculated. The Fe-N_2C_2 shows a low-energy intermediate (MS5′) with a −2.36 eV energy decrease relative to the normal O═Fe═O species resulting in the deactivation of Fe−N_2C_2 by the generation of the O═Fe═O species. The energy barrier for mono Fe═O species formation was found to be higher than O═Fe═O, and oxidation was expected to proceed via dioxo Fe state. Apart from the nature of bonding, the distance between isolated atomic centers is also important. He et al. demonstrated that density and distance between isolated metal centers can be regulated by using metalloporphyrin and tetraphenylporphyrin (TPP) and catalysts can afford regioselective hydrogenation of terminal alkynes.[121] However, how the distance between these atoms in graphene scaffold influence the reactivity remains elusive. To understand, the impact of atomic distance in electrocatalytic ORR, Jin et al. prepared a series of Fe-N_4-C catalysts with an atomic spacing of 0.5, 0.7, 0.9, 1.2, 1.9, 2.6, 3.2, 4.6, 5.2, and 7.8 nm (Figure 16g,h).[172] ORR results displayed that the intersite distance (d_{site}) between Fe centers with <1.2 nm increased the ORR reaching a maximum at 0.7 nm and then decreasing to 0.5 nm. These findings raise the question if there is any communication between two atoms at a short distance. To know the answer, Mössbauer spectroscopy was used which demonstrates decreasing the intersite distance from 1.9 and 0.5 nm increases the population of high-spin $Fe^{(III)}$-N_4 (highly active species for the ORR) from 56% and 63%. Further, DFT calculations illustrated on-site magnetic moment were weak above 1.6 nm and drastically decreased after that and were consistent with the experimental findings (Figure 16g). The density of state calculation also reveals that as two Fe centers approach closer, the d_{z^2} and adsorbate p_z orbital overlap, effectively allowing a higher degree of filling for the e_g electron which was also evident from increased free energy (ΔG_{*OH}) when the intersite distance was less than 1.6 nm (Figure 16h).

Besides electronic and coordination interaction, the support can alleviate the performance due to photocatalytic charge generation. Many examples of photoactive SACs supported on light-responsive materials have been demonstrated for CH_4OR and various other applications which will be discussed further in the following sections.[313] The photogenerated charge in the support can interact with the metal center, and the extent of interaction depends upon coordination, redox behavior, and affinity to the adsorbate. In contrast to the conventional photocatalytic system, plasmonic photocatalysis which includes interband electronic excitation of metal above the Fermi level and generation of hot electrons and holes to drive photocatalytic reaction has gained momentum due to longer wavelength operability.[314,315] Despite significant research, these catalysts have not reached their potential due to the less populated concentration of charge carriers.[316] Alloying bi/trimetallic systems are envisaged to troubleshoot this problem; however, carriers' annihilation at interface/second metal reduces quantum efficiency.[317−319] SAA on the other hand can overcome this barrier due to synergistic electronic structure manipulation and extraction of charge by point metal centers reducing bulk recombination.[320,321] Regardless of the high promise, a handful of reports are available in this direction which should be explored in the future. In a benchmark report, Zhou et al. synthesized a Cu−single atom and Ru surface alloy (Cu_xRu_y) plasmonic photocatalysts by varying the concentration of Ru (Figure 16i,j).[322] Interestingly, compared to other plasmonic photocatalysts, surface plasmons of earth-abundant Cu[323] were utilized to activate the C−H bond of CH_4. When used for CH_4 photoreforming using CO_2, the $Cu_{19.9}Ru_{0.2}$ catalysts can reach a conversion rate of ∼275 μmol CH_4 g^{-1} s^{-1} almost ∼5 times higher than thermal reforming of CH_4 at 1000 K. Mechanism evaluation with experimental findings and quantum mechanical studies displayed that O and H can diffuse freely on Cu(111) surface with barriers of 0.33 and 0.14 eV preventing RWGS, while, higher C^{ads} (2 eV) confine adsorbed C to Ru site minimizing coking (Figure 16i). The SA Ru can capture electrons from plasmon excited Cu(111) and bind with CH_4 and CO_2 which upon C−H and C−O bond scissoring form adsorbed Cads and O^{ads} species. The mobile O^{ads} can react with Ru adsorbed C forming CO (Figure 16j).

Since the high activity and selectivity in SACs are due to cooperative interaction between support and SAs sites, it is imperative to choose appropriate supporting material.[297,324] The SAs sites coordinate with support materials followed by coordination via the charge transfer process which stabilizes isolated atoms. The bond strength, coordination number, free coordination/undercoordinated sites after stabilizations, and nature of nearby active sites, etc., are factors that govern the activity and selectivity.[305,325] Experimental studies for CH_4OR demonstrate the significant role of support in substrate activation to stabilization of intermediate state.[326] For example, Pd and Rh SAs supported on SiO_2 were inactive for C−H bond activation, while ZSM-5 supported SAs demonstrate significant activity due to Al/Si coordination and Lewis acid sites. Similarly, Rh SA stabilized on ZrO_2 can divert the product selectivity toward methanol compared to acetic acid/formic acid in ZSM-5 supported SACs.[285] Theoretical study using DFT is a vital tool that can be implemented to predict the nature of catalytic sites, the interaction of substrate to these sites and neighboring acidic/basic sites. Harrath et al. theoretically investigated CH_4 activation on ZrO_2 supported Rh_1, Pd_1, Ir_1, and Pt_1 SACs using H_2O_2 as an oxidant.[327] The H_2O_2 adsorption on Rh_1/ZrO_2 and Pd_1/ZrO_2 proceeds via homolytic dissociation of H_2O_2 followed by adsorption of O_2

https://doi.org/10.1021/acsnano.2c02464
ACS Nano XXXX, XXX, XXX−XXX

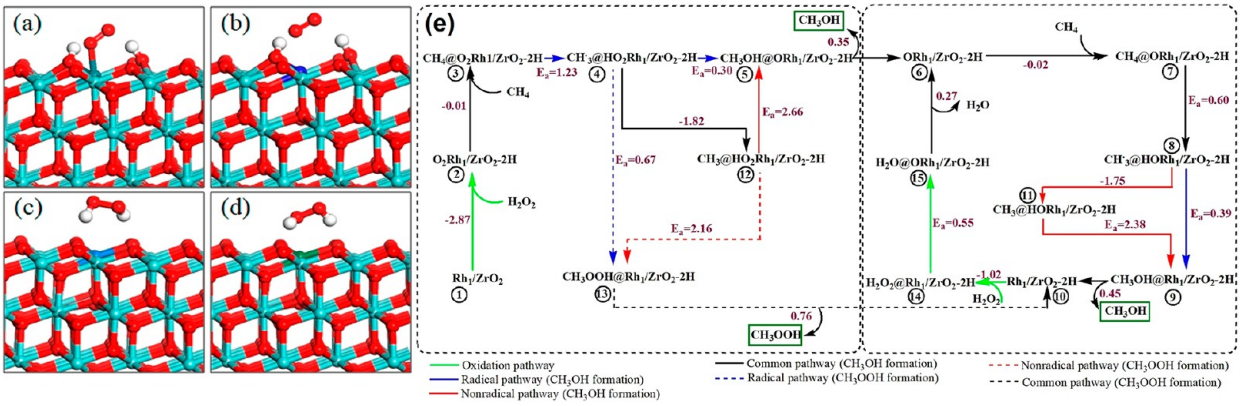

Figure 17. Preferred H_2O_2 adsorption configurations on (a) Rh_1/ZrO_2, (b) Pd_1/ZrO_2, (c) Ir_1/ZrO_2, and (d) Pt_1/ZrO_2. Reaction network for conversion of methane on the Rh_1/ZrO_2 SAC. Reprinted with permission from ref 327. Copyright 2019 American Chemical Society.

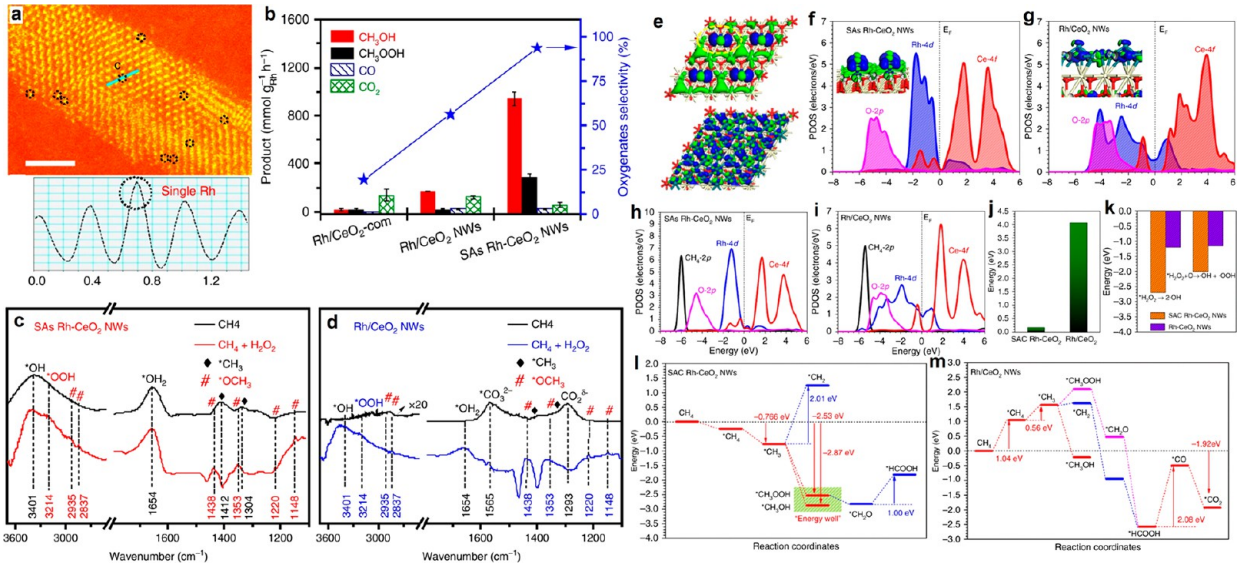

Figure 18. (a) AC-HAADF/STEM image in temperature color of the SAs Rh-CeO_2 NWs. The isolated Rh atoms are marked with black circles and the intensity profile recorded from the line in the panel. (b) The yield and selectivity of oxygenates from Rh/CeO_2-com, Rh/CeO_2 NWs, and SAs Rh-CeO_2 NWs. Reaction conditions: P_{CH_4}: 0.5 MPa, H_2O_2: 20 mL (1 M), T: 50 °C, reaction time: 1 h, and catalyst weight: 10 mg. In situ CH_4-DRIFTS measurements on (c) SAs Rh-CeO_2 NWs and (d) Rh/CeO_2 NWs. (e) The real spatial contour plots for bonding and antibonding orbitals near E_F for SAs Rh-CeO_2 NWs and Rh/CeO_2 NWs. (f) The PDOS of SAs Rh-CeO_2 NWs surface. (g) The PDOS of Rh/CeO_2 NWs surface. (h) The PDOS of CH_4 adsorption on SAs Rh-CeO_2 NWs surface. (i) The PDOS of CH_4 adsorption on Rh/CeO_2 NWs surface. (j) Energy comparison of [O] desorption from CeO_2 on SAs Rh-CeO_2 NWs and Rh/CeO_2 NWs. (k) The reaction energy comparison of generating radicals. (l) Reaction paths and energy profile of DMC over SAs Rh-CeO_2 NWs. (m) Reaction paths and energy profile of DMC over the Rh/CeO_2 NWs. Reprinted with permission under a Creative Commons CC-BY License from ref 331. Copyright 2020 Springer Nature.

on the surface, while Ir_1/ZrO_2 and Pt_1/ZrO_2 can just afford molecular adsorption (Figure 17a,d). The O_2 formed by dissociative adsorption in Pd_1/ZrO_2 desorbs spontaneously due to entropic contribution while Rh_1/ZrO_2 displayed a robust binding. These findings suggest that Rh_1/ZrO_2 can initiate selective C−H bond activation due to the adsorption of H_2O_2. The formed O_2Rh/ZrO_2-2H can cleave the C−H bond by proton abstraction with an associated energy barrier of 1.23 eV to generate •CH_3 radical leaving hydrogenated HOO-Rh sites (Figure 17e). In the next step, •CH_3 radical reacts with the HOO-Rh site to produce CH_3OH (0.30) as a major product compared to CH_3OOH (0.67 eV). The nonradical pathway involving *CH_3 radical to form CH_3OH or CH_3OOH on the HOO-Rh site was highly unfavorable due to the large energy barrier of 2.66 or 2.16 eV. Once the first produced CH_3OH is desorbed, the second CH_4 activation on ORh/ZrO_2-2H site requires only 0.60 eV activation energy for the generation of •CH_3 radical and finally producing CH_3OH with a barrier of 0.39 eV. Interestingly, the Rh site is reoxidized to the ORh site by H_2O_2, instead of the O_2Rh sites excluding the probability of formation of CH_3OOH. The hydrogenation of surface support produces ZrO_2-2H with surrounding hydroxyl groups which block the formation of the O_2M sites. Finally, a different combination of metal centers was investigated which demonstrates that Fe_1 sites can block the *OCH_3 formation, thus will be the most active catalysts.

6.1. SACs Supported on CeO_2. SA binds with support materials followed by charge redistribution between support and SAs and few undercoordinated sites remain available for the reaction providing exceptional activity/selectivity to SACs.

https://doi.org/10.1021/acsnano.2c02464
ACS Nano XXXX, XXX, XXX−XXX

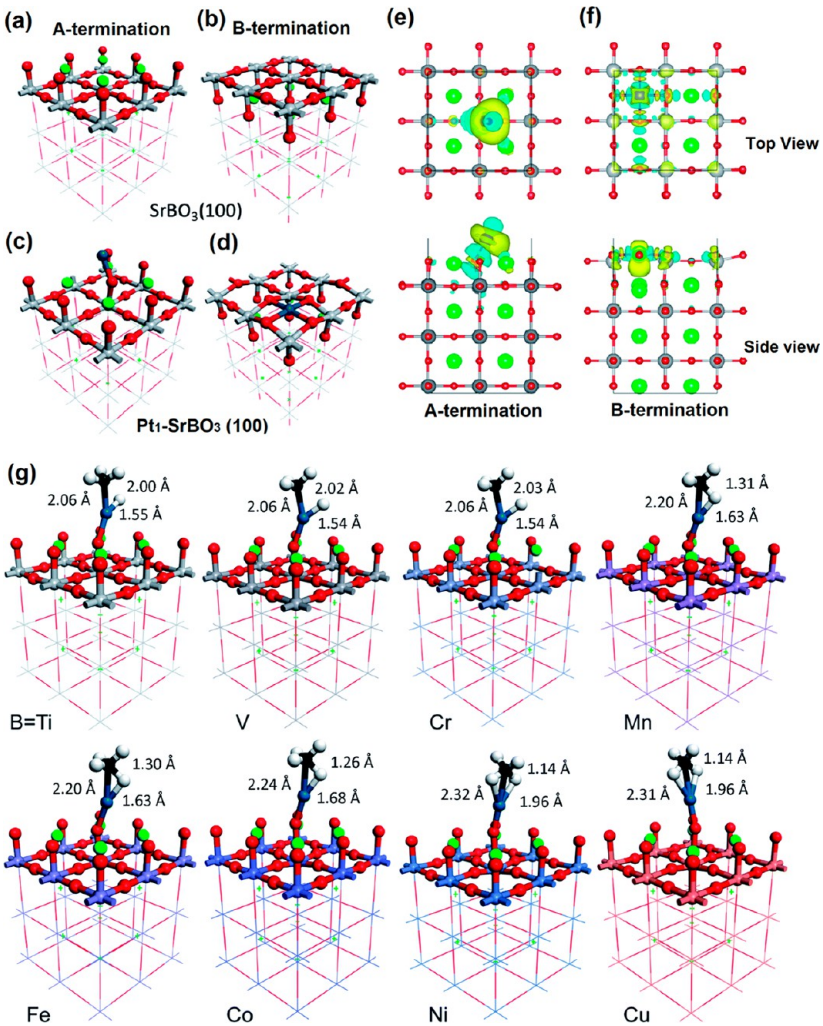

Figure 19. Typical structures of $SrBO_3(100)$ and $Pt_1-SrBO_3(100)$: (a) $SrBO_3(100)$ A-termination; (b) $SrBO_3(100)$ B-termination; (c) Pt_1 on $SrBO_3(100)$ A-termination; (d) Pt_1 on $SrBO_3(100)$ B-termination. Color code: O, red; Sr, green; B, gray; Pt, blue. Charge density difference plots of $Pt_1-SrTiO_3(100)$: (e) A-termination and (f) B-termination. Blue denotes depletion of electron density, while yellow represents accumulation. Color code: O, red; Sr, green; Ti, gray. Pt_1 is at the center of the charge transfer. The iso-surface value is equal to 0.0038 e $Å^{-3}$. (g) Optimized geometry of CH_4 adsorption on $Pt_1-SrBO_3(100)$ A-termination. Color code: O, red; Sr, green; Pt, blue; C, black; H, white; B, varies. Key bond distances are also given for the C−H bond being activated: Pt−C (left), Pt−H (lower right), and C−H (upper right). Reprinted with permission from ref 334. Copyright 2020 Royal Society of Chemistry.

Using appropriate supporting materials is of utmost importance to optimize the catalytic performance. The coordination environment and the electronic state of SAs can be significantly altered on different supporting materials. The resulting configuration provides opportunities for tuning SA sites to drive specific reactions. Sometimes, varying the support can influence the activation energy and reaction coordinates resulting in different product distribution and activity. For instance, in the previous examples when Rh was supported on Si and Al sites of ZSM-5 via O bridging (Rh−O−Si and Rh−O−Al), acetic acid and formic acid were dominant products. However, Kwon et al. demonstrated when Rh SA was supported on ZrO_2, methanol was the dominant product.[328] EXAFS spectra of Rh/ZrO_2 SAC demonstrate CN of Rh was 4.9 in contrast to 5.23 ± 0.52 for ZSM bounded Rh atom. Further, XANES spectra show increased white line intensity due to a more oxidic state. Unfortunately, the product selectivity remains poor (∼70%) due to the differential decomposition of methyl hydroperoxide and H_2O_2. CeO_2 is a better alternative supporting material because it can generate a defect-rich state by the reduction in the H_2 environment. Sadly, the reduction of CeO_2 support at elevated temperature also promotes agglomeration and results in the deactivation of active centers in an oxidative environment.[329] Interestingly, Nei et al. demonstrated that steam-treated (hydrothermally aged) Pt/CeO_2 catalysts can maintain atomic distribution of Pt even at high temperature (750 °C) which was attributed to redistribution of oxygen vacancies from the CeO_2 bulk to the $CeO_2(111)$ surface and formation of stable $O_{lattice}[H]$ in the vicinity of Pt center.[301] Kye et al. demonstrated the synthesis of SA Pt supported on TiO_2 (1 wt % Pt/CeO_2) by WI method which can promote CH_4 oxidation using CO as an oxidant at 300 °C yielding CH_3OH as the main product.[330] However, high reaction temperature and less activity/selectivity remain challenging. To overcome the drawbacks of low catalytic performance and selectivity of Rh-based SACs in DMC, Bai et al. decorated Rh SA centers on the CeO_2 nanowires support using an in situ hydrothermal deposition approach.[331] The atomically dispersed Rh species were discerned via aberration-corrected high-angle annular dark-field scanning transmission

https://doi.org/10.1021/acsnano.2c02464
ACS Nano XXXX, XXX, XXX−XXX

electron microscopy (AC-HAADF/STEM) (Figure 18a). The Rh $3d_{5/2}$ XPS peak shifting toward high energy value and increased concentration of Ce^{3+} species suggest electron transfer from Rh to CeO_2 support and strong synergistic interaction. The presence of an atomic state without any metal−metal or metal oxide clustering was ensured by EXAFS and XANES spectra. DRIFTS spectra using CO as a probe (CO-DRIFT) at 50 °C displayed a broad absorption peak due to low CO coverage and the presence of partially oxidized states (Figure 18c,d). As the temperature was raised at 150 °C, signature geminal dicarbonyl absorption peak (at 2101 and 2030 cm^{-1}) for SA centers appeared, while Rh-CeO_2 NWs (Rh NPs) displayed CO bridge adsorption only attainable for the nanoparticles. When used for the CH_4OR using H_2O_2 as an oxidant, the SA Rh-CeO_2 NWs can afford a yield of 940.3 and 291.4 mmol g_{Rh}^{-1} h^{-1}, for CH_3OH and CH_3OOH, respectively, which was a magnitude higher than control Rh-CeO_2 NWs and Rh/CeO_2-com (Figure 18b). The maximum selectivity and yield of total oxygenates reached up to 93.9% and 1231.7 mmol g_{Rh}^{-1} h^{-1} at 50 °C. Optimization studies suggest, 50 °C and 1 M H_2O_2 concentrations were ideal while changing CH_4 pressure does not influence much the oxygenates product yield. EPR spectra of reaction product using DMPO trap agent demonstrate the presence of •OH, •OOH and •CH_3 peaks. The in situ DRIFTS of SAs Rh-CeO_2 NWs catalysts depict the signals of C−H stretch, *OCH_3, *OH, *OH_2, and *OOH, while for the Rh-CeO_2 NWs catalysts, only strong signals for CO_3^{2-} and *$CO_2^{\delta-}$ were observed at 1589 and 1293 cm^{-1}. CH_4 temperature-programmed surface reaction (TPSR) spectra of CeO_2 does not give any peak due to its inactivity to activate CH_4, while SAs Rh-CeO_2 NWs displayed a clear peak for CH_4, CO, CO_2, and H_2O validating the direct role of Rh sites in the activation of methane molecule. DFT calculated real spatial orbital distribution of SAs Rh-CeO_2 NWs displayed the concentrated electron-rich features of SA Rh compared to Rh nanoclusters suggesting Rh SA possesses superior reaction priority (Figure 18e). Projected density of states (PDOS) of SAs Rh@CeO_2 displayed coupling between Rh-4d and Ce-4d, while strong coupling was observed in broad Rh-4d bands and O-2p and Ce-4f band of CeO_2 (Figure 18f−i). The relatively small distance between Rh-4d and O-2p bands on Rh/CeO_2 NWs and a strong coupling between CH_4 and local O atoms lead to the overbinding effect that increases energy barriers for the consecutive dehydrogenation of CH_4. The energy profile also verifies the flexible coordination of the O atom with a minimal energy barrier of 0.16 eV compared to 4.06 eV for the Rh/CeO_2 NWs. The energetics of •OH and •OOH radicals generation were favorable for the SAs Rh@CeO_2 catalysts (Figure 18j,k). The downhill reaction coordinates for the formation of CH_3OH and CH_3OOH and spontaneous adsorption and C−H bond activation demonstrate a high electronic activity and feasibility of the process. Interestingly, HCOOH formation using SAs Rh@CeO_2 NWs imposed a 1 eV additional energy barrier which suppresses overoxidation of CH_3OOH (Figure 18l,m).

6.2. SACs Supported on Perovskite Oxides. Most of the SACs investigated for the CH_4 activation are SAs stabilized on metal oxides such as FeO_x, Al_2O_3, TiO_2, and CeO_2 or graphene support. However, new support materials with tunable chemical and electronic environments can open the path to developing new SACs with more exciting properties. Perovskite oxide with a general formula ABO_3 might provide several A and B site combinations to manipulate SACs properties.[73,332] Indeed, perovskite oxides with various facets and terminations have been widely explored in catalysis to understand the structure−activity selectivity relationships.[333] Wan et al. studied the Pt_1 SA site on Sr-based perovskite ($SrBO_3$) by varying the B sites (Ti, V, Cr, Mn, Fe, Co, Ni, Cu) to understand the mechanism of CH_4 activation on various multimetallic planes and termination.[334] The $SrBO_3$ with the most stable 100 facets can have two terminations: (1) A-termination exposes the SrO layer and (b) B-termination exposes the BO_2 layer. DFT calculations suggest that Pt_1 on A-termination sites settles on top of a surface oxygen atom, while, on B-termination, it prefers to occupy a hollow site and coordinates with four O (Figure 19a−d). The Pt_1 adsorption on $SrBO_3$ by varying B sites shows that adsorption energies remain unchanged for A-termination sites and increase for B-termination sites in the order Ti < V < Cr < Mn < Fe < Co < Ni < Cu reaching maximum for $SrCuO_3$ (−9.22 eV). The O-vacancy formation energy was decreased from Ti to Cu suggesting a more reducible surface and more active surface to strongly interact with Pt atoms. Interestingly, the Bader charge distribution on Pt_1 seated on A-termination was negative with a minimum value for Cu, while B-termination lead to a positive charge on the Pt atom. The calculation of surface charge density by using $SrTiO_3$ (100) as a model displays that Pt_1 situated at A-termination sites can extract charge from underneath O atoms as seen in Figure 19e. With Pt atom in B-termination sites, the charge from Pt is transferred to Ti atoms (Figure 19f). The observed effect was explainable due to the polar surface of $SrTiO_3$ with positively charged SrO A-termination (+0.31 V) and negatively charged TiO_2 B-termination (−0.31 eV). The CH_4 adsorption on Pt_1−$SrBO_3$ (100) B-termination was found to be physisorption while chemisorption was mainly favored at A-termination (Figure 19g). The optimized geometry of the adsorbed CH_4 exhibits that dissociative adsorption followed for early transition metals, i.e., $SrTiO_3$, $SrVO_3$, and $SrCrO_3$, while Cu, Mn, etc., displayed bonding with two C−H with bond elongation. The PDOS of Pt_1 on $SrTiO_3$(100) A-termination sites show that empty 6s and 6p states (especially p_z) were just above the Fermi level and can work as an electron acceptor to weaken the C−H bond. However, due to the filled p_z state sp states were the prime acceptor. The absence of empty sp states was responsible for the weak CH_4 physisorption of CH_3 on B-termination sites. Based on these observations, the authors concluded that Pt_1 on $SrVO_3$(100) was the most promising to achieve both chemisorption and activation as Pt_1 has almost equal stability on the A and B terminations on these sites.

6.3. SACs Supported on ZrO_2. Numerous noble and non-noble metal-based catalysts have been investigated for the oxidation of methane to oxygenates.[335] Due to similarity with bioenzymes MMO, the variable oxidation state 3d metals and their oxides are proven to be efficient catalysts. For example, Fe and Cu deposited on zeolites are found to promote the C−H bond activation of methane.[64,336] Apart from that, noble metal-based catalysts especially Au/Pd-based alloy system has been widely investigated. For example, Ab Rahim et al. found that Au/Pd alloy can promote C−H bond activation by using H_2 and O_2 as in situ sources of H_2O_2 at 90 °C and pressurize conditions. However, initial CH_3OH selectivity remains only 19% with a maximum TOF of 25 h^{-1} for oxygenates.[266] Later, Au/Pd nanoparticle alloys supported on various supports such as TiO_2, CeO_2, etc. have been employed for in situ H_2O_2

https://doi.org/10.1021/acsnano.2c02464
ACS Nano XXXX, XXX, XXX−XXX

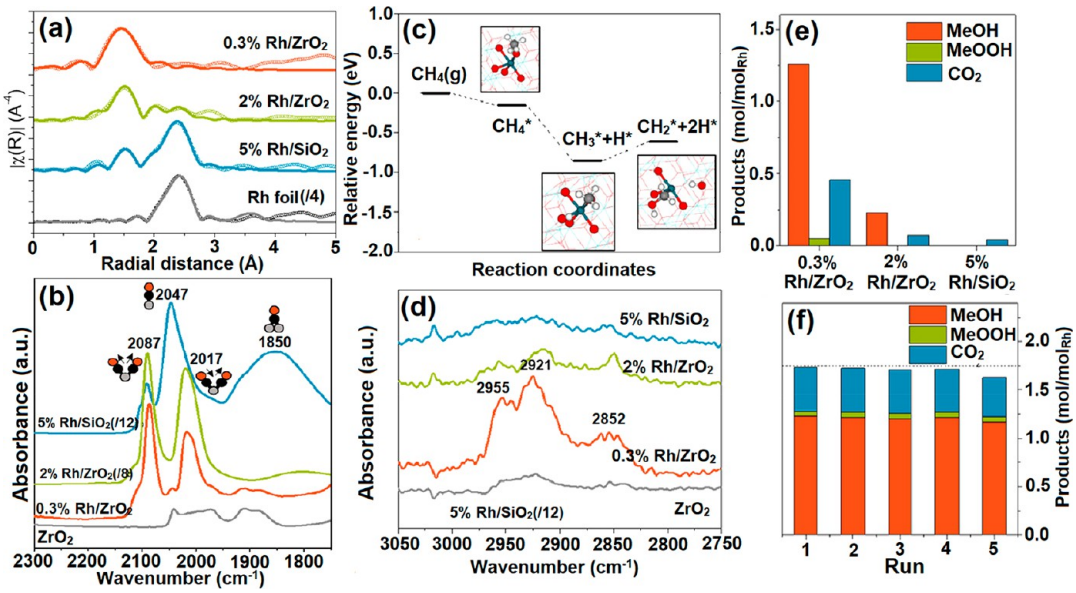

Figure 20. (a) Rh K edge k^3-weighted FT-EXAFS spectra of the 0.3 wt % Rh/ZrO_2, 2 wt % Rh/ZrO_2, 5 wt % Rh/SiO_2, and Rh foil. Dots, experimental data; lines, fitted results. (b) DRIFT spectra of CO molecules adsorbed on bare ZrO_2 support, 0.3 wt % Rh/ZrO_2, 2 wt % Rh/ZrO_2, and 5.0 wt % Rh/SiO_2 samples. (c) Energy diagram of CH_4 activation on the Rh_{Zr}-Hyd (4.3 OH/nm^2) model with optimized geometries of the intermediates. Inset figures: red balls indicate oxygen, cyan indicate zirconium, turquoise indicate rhodium, white indicate hydrogen, and gray indicate carbon. (d) DRIFT spectra of CH_4 adsorbed on bare ZrO_2, 0.3 wt % Rh/ZrO_2, 2 wt % Rh/ZrO_2, and 5 wt % Rh/SiO_2. The CH_4 adsorption was performed at 70 °C. (e) Direct methane oxidation results using H_2O_2 as an oxidant on the 0.3 wt % Rh/ZrO_2, 2 wt % Rh/ZrO_2, and 5 wt % Rh/SiO_2 catalysts. (f) Recyclability test results were performed with the 0.3 wt % Rh/ZrO_2 catalyst. Reaction condition: 30 bar of 95% CH_4/He, 70 °C, 1 h, 0.5 M H_2O_2, and catalyst 30 mg. Reprinted with permission from ref 328. Copyright 2017 American Chemical Society.

generated methane oxidation.[337] In such systems high pressure, extreme danger of explosive H_2 + O_2 mixture, and relatively low generation rate of H_2O_2 from H_2 and O_2 which can easily diffuse away from the active sites are the main challenges. Interestingly, theoretical investigations demonstrated that IrO_2 located at the top of the volcano curve can cleave the C−H bond at 150 K.[338] To validate the hypothesis, Yang et al. developed IrO_2/CuO catalysts in which electrophilic Ir^{4+} of IrO_2 facilitates C−H bond cleavage while CuO stabilizes the $-CH_3$ on oxygen sites to produce methanol in the end.[339] The limited selectivity for the methanol and the required high proportion of noble metals are another challenge to use such catalysts for methane oxidation. Contrarily, SACs require a much low concentration of metal to promote reaction and also improve the selectivity of products. Initial DFT calculations suggest that Pt clusters or under coordinated Rh can stabilize CH_3 to prohibit successive dehydrogenation. Kwon et al. synthesized Rh SACs supported on zirconia (ZrO_2) by WI method. EXAFS spectra of 0.3% Rh loaded ZrO_2 catalyst demonstrate a peak of Rh−O at 1.5 Å corresponded to 4.9 CN with neighboring oxygens (Figure 20a). As the concentration of Rh was increased, the Rh−Rh peak at 2.4 Å became prominent demonstrating that 0.3% Rh was optimum for the decoration of SACs. The absence of any particle in HAADF-TEM images and high white line intensity in the XANES spectra suggests the individual identity of Rh atoms with a more oxidic state, respectively. CO adsorption followed by DRIFT measurement demonstrates that 5 wt % Rh/SiO_2 show two peaks centered at 2047 and 1850 cm^{-1} for linear and bridged bonded CO. In the atomically distributed 0.3 wt % Rh/ZrO_2 sample, IR peaks for the linear CO disappeared while new peaks at 2087 and 2017 cm^{-1} for the symmetrical and asymmetrical stretch of geminal dicarbonyl (CO-Rh-CO) were observed (Figure 20b). Additionally, from the symmetric and asymmetric IR peaks area, the angle between two carbonyls was estimated to be ∼90°, 100°, and 120° for 0.3 wt % Rh/ZrO_2, $RhCl_3$ + ZrO_2, and 5 wt % Rh/SiO_2 samples indicating the dominance of isolated Rh species in 0.3 wt % Rh/ZrO_2 sample. The Rh $3d_{5/2}$ XPS peak at 309.4 eV for 0.3 wt % Rh/ZrO_2 suggests the oxidation state of Rh in between +3 and +4, which was further confirmed by the DFT model where Rh substitute Zr site on hydroxylated ZrO_2(101) surface demonstrated +3.7 oxidation state. The calculated relative energies of CH_x intermediates on the Rh_{Zr}-Hyd model displayed that adsorbed CH_3 intermediate (CH_3*) has the lowest energy and further dehydrogenation products CH_2 are not preferred due to high energy (Figure 20c). DRIFTS spectra of adsorbed methane on 0.3 wt % Rh/ZrO_2 show two IR bands due to the C−H stretch of a methoxy group (CH_3O−) and methyl groups verifying the DFT observation (Figure 20d). In contrast to metallic Rh, nanoparticles supported SiO_2 (5 wt % Rh/SiO_2) which afford overoxidized CO_2, atomically distributed 0.3 wt % Rh/ZrO_2 displayed dominant production of methanol and stability of the product distribution even after five catalytic cycles (Figure 20e,f). Further, compared to other metals such as Pd, Pt, and Ir, the Rh SACs displayed the highest activity, while among the various supporting materials such as CeO_2, TiO_2, SiO_2, and ZrO_2, the highest performance was observed for the ZrO_2 support. Lastly, when CH_4 and O_2 were reacted at 260 °C, ethane was produced, while no product was observed for the 5 wt % Rh/ZrO_2 suggesting Rh SAC can facilitate C−H bond activation.

6.3.1. Effect of ZrO_2 Surface Hydroxyl Groups on CH_4OR. Despite the Rh/ZrO_2 catalyst has demonstrated the enhanced performance of CH_4OR, the use of excessive H_2O_2 makes the

https://doi.org/10.1021/acsnano.2c02464
ACS Nano XXXX, XXX, XXX−XXX

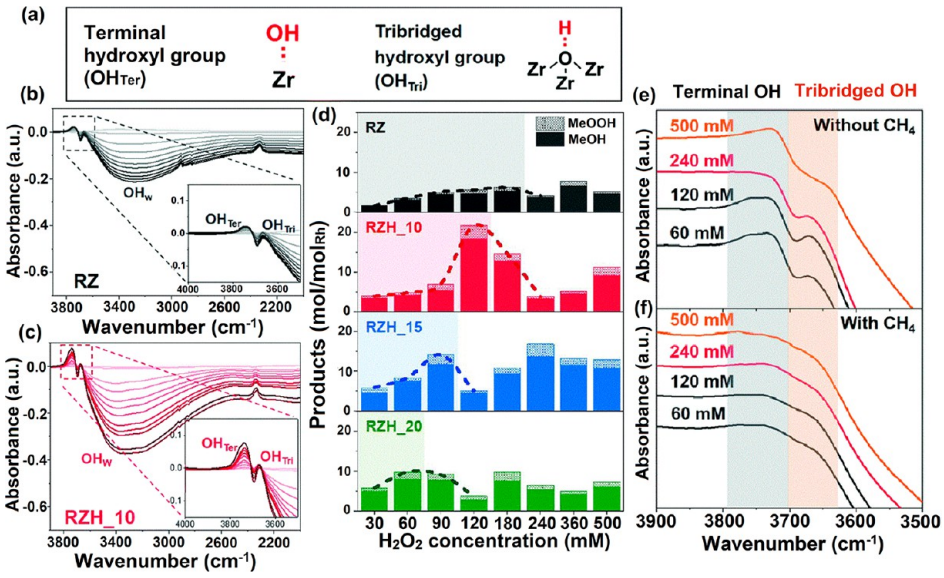

Figure 21. (a) The schemes of the terminal and tribridged hydroxyl groups. DRIFT spectra were obtained during dehydration at 300 °C for (b) RZ, (c) RZH_10. Evacuation time increased from 0 to 60 min as the color gets deeper. (d) Direct methane oxidation on RZ, RZH_10, RZH_15, and RZH_20 with different concentrations of H_2O_2. The reaction was performed at 30 bar of 95% CH_4/He, 2 bar of O_2 and 90 °C for 30 min using the catalyst 30 mg in 10 mL aqueous solution. (a) DRIFT spectra show the presence of surface hydroxyl groups without CH_4. (e) DRIFT spectra show the absence of surface hydroxyl groups after the reaction with CH_4. For all the reactions, RZH_10 was used. (f) Recycling test results. The productivity of CH_4 oxygenates was shown for fresh RZH_10 (fresh), the catalyst obtained after the first reaction (reuse), and the catalyst obtained after the second reaction followed by further hydrothermal treatment at 300 °C for 10 h (regenerated). Reprinted with permission from ref 341. Copyright 2020 Royal Society of Chemistry.

process costly due to the high market price of H_2O_2 compared to CH_3OH. The previous report on CH_4 oxidation using Fe supported TiO_2 displayed a minimum amount of H_2O_2 was required under light conditions.[340] Based on DFT, Harrath et al. displayed that H_2O_2 dissociatively adsorbed on the Rh_1/ZrO_2 catalyst forming O_2−Rh sites.[327] Hydrogenation of catalysts can suppress the overoxidation of CH_3OH to CH_3OOH and CO_2 due to the formation of hydrogenated oxide support (ZrO_2−2H), blocking the formation of neighboring O_2−Rh sites. These findings demonstrate that surface hydroxyl groups play an important role in suppressing the overoxidation of the product and can be tuned to get optimum products using minimum H_2O_2. To further explore the role of surface −OH groups on supporting materials, Kim et al. introduced the hydroxyl group in Rh_1/ZrO_2 catalysts by hydrothermal treatment at 300 °C for 10, 15, and 20 h (Figure 21).[341] The presence of two germinal peaks in CO-DRIFT spectra of Rh_1/ZrO_2 demonstrate SA identity was preserved after long hydrothermal treatment. Further, the peak area of the germinal peak corresponded to 90° angle binding in Rh_1/ZrO_2 verifying the presence of most of the Rh atoms in a SA state. TEM, XANES, EXAFS and XPS also validate SA Rh^{3+} species decorate of ZrO_2 support. The CH_4 DRIFT spectra of fresh Rh_1/ZrO_2 catalysts show three peaks at 2852 and 2955 (νC−H of $-OCH_3$) and 2921 cm^{-1} (νC−H of $-CH_3$) due to CH_4 cleavage and the intensity of the signal was significantly enhanced after the hydrothermal treatment suggesting −OH groups helping in CH_4 oxidation. Additionally, three DRIFT peaks for the terminal, tribridged, and surface-bound hydroxyl groups were used to monitor the chemical nature of surface bounded −OH groups. The tribridged hydroxyl group (OH_{Tri}) originated from hydrogen-bonded to lattice oxygen while OH connects with a Zr atom to produce form a terminal hydroxyl group (OH_{Ter}) (Figure 21a). Compared to tribridged OH_{Tri} and terminal OH_{Ter} groups which are stable up to 550−750 °C, the surface-bound −OH can be easily removed by the heating catalyst between 100 and 200 °C. The DRIFT spectra after heating the samples at 300 °C demonstrate the increased peak intensity of tribridged OH_{Tri} and terminal OH_{Ter} groups for hydrothermally treated samples (Figures 21b,c). The methane oxidation experiments demonstrate optimal yield for samples hydrothermally treated at 300 °C for 10h. Further, increasing the reaction time reduces the product yield which was due to the phase transition from tetragonal to monoclinic. The total oxygenates yield using hydrothermally treated Rh_1/ZrO_2_10 samples reach up to 21.7 mol mol_{Rh}^{-1} compared to fresh Rh_1/ZrO_2 RZ (7.7 mol mol_{Rh}^{-1}) with 120 mM of H_2O_2 and gaseous O_2 (Figure 21d). When H_2O_2 concentration was increased, the oxygenate yield was increased initially and reached a maximum followed by a drop. The concentration of H_2O_2 required to achieve maximum oxygenates decreased as hydrothermal treatment time was increased however oxygenates yield was relatively low compared to the 10 h sample. The DRIFT measurement using various concentration of H_2O_2 suggest as the H_2O_2 concentration was increased to 240 mM the terminal hydroxyl groups we removed while the tribridged hydroxyl group is slightly damaged (Figure 21e). Further recycling run after the reaction displayed significantly decreased catalytic activity which was resumed after hydrothermal treatment demonstrating −OH groups improve the catalytic performance.

6.4. SACs Supported on TiO_2 (Nonphotocatalytic CH_4OR). Numerous synthetic metal complexes based on iron, Mn, Cr, etc. have been reported for the C−H activation in the presence of oxygen or hydrogen peroxide. To imitate the functional activity of heme, Fe containing nanoclusters and SACs has been developed due to a similar coordination environment. Despite the significant progress, the Fe sites are

https://doi.org/10.1021/acsnano.2c02464
ACS Nano XXXX, XXX, XXX−XXX

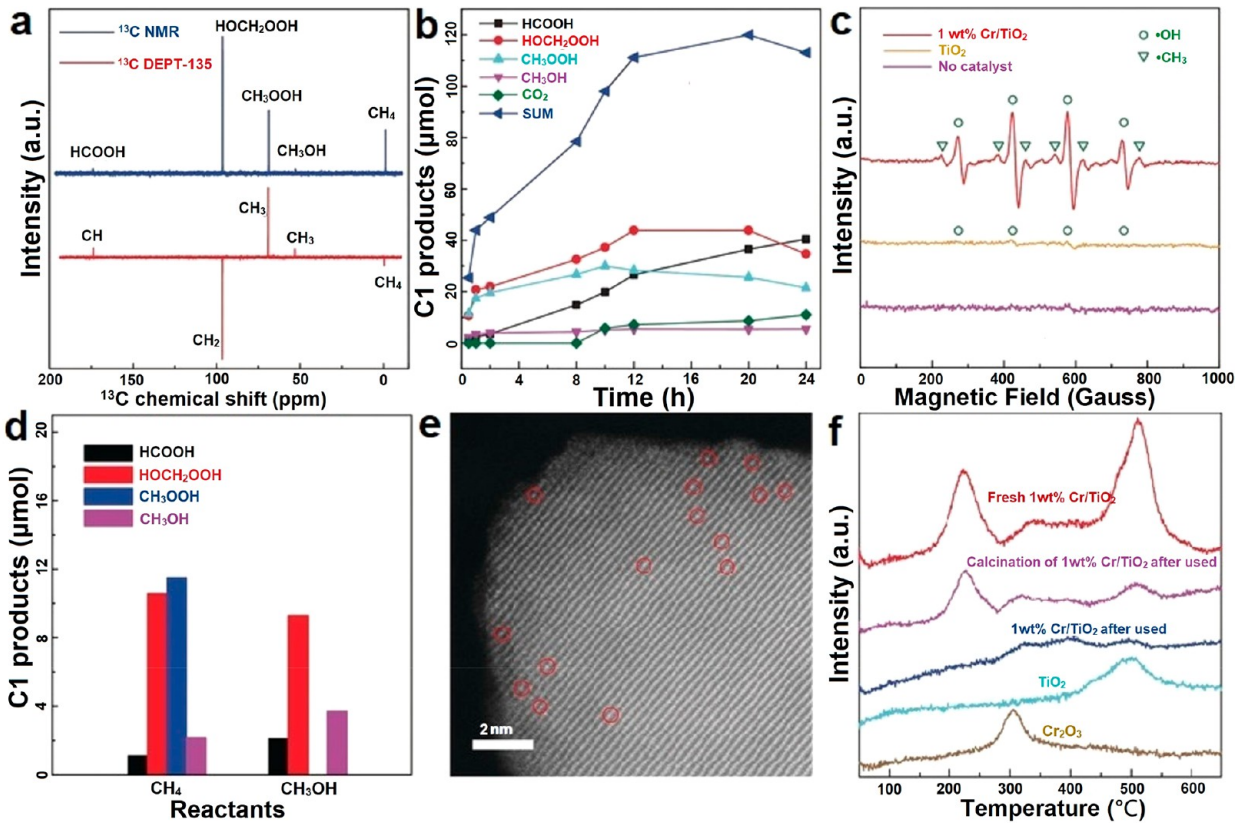

Figure 22. (a) ^{13}C NMR and ^{13}C DEPT-135 of oxygenated products in liquid phase with 1 wt % Cr/TiO_2 catalyst by using $^{13}CH_4$ as the reactant gas. (b) Catalytic performance of the 1 wt % Cr/TiO_2 catalysts for CH_4 oxidation with different reaction times. (c) EPR experiments with oxygenated products in the liquid phase with different catalysts. (d) Catalytic performance with CH_4 (3 MPa) and CH_3OH (ca. 15.8 μmol) as reactants over 1 wt % Cr/TiO_2. (e) HAADF-STEM image of 1 wt % Cr/TiO_2. The red circles show single Cr atoms in the matrix of TiO_2. (f) H_2-TPR results of catalysts. Reprinted with permission from ref 344. Copyright 2020 Wiley VCH.

vulnerable to deactivation during the redox cycle in the presence of strong oxidants. The deactivation and agglomeration can be minimized by adopting appropriate support materials stabilizing SAs via effective coordination. Oxide-based supports such as TiO_2, CeO_2, and ZrO_2 with easy reducibility are suitable candidates for the decoration of SAs as vacant sites can efficiently accommodate SAs. TiO_2 is a widely explored supporting and photoactive material for SA decoration. The better reducibility, formation of plenty of defect sites, possibility of controlling structural and exposed planes and large redox potential for photocatalytic activation of organics makes it an ideal candidate for various reactions including CH_4OR. TiO_2-based SACs have been used for both nonphotocatalytic and photocatalytic transformation of CH_4 to oxygenates. This section deals with the nonphotocatalytic TiO_2-based SACs for CH_4OR. A detailed description of the photocatalytic application is given in Section 8.1.

Despite, noble metal-based Rh_1/ZrO_2 SACs having demonstrated methane activation potential, the use of expensive/unselective H_2O_2 oxidant and side product formation is undesirable. On the other hand, AuPd/zeolite catalysts displayed in situ generations of H_2O_2 from O_2 and H_2 which can be used to promote CH_4 activation.[342] The introduction of additional CO in the reaction system can reduce H_2O to H_2 and can generate H_2O_2, thus excluding the use of an explosive H_2O_2 mixture. Considering these facts, Gu et al. synthesize Rh/TiO_2 SACs by deposition precipitation method which can promote selective oxidation of CH_4 to CH_3OH using CO and O_2 as oxidants.[343] The HAADF-STEM images show the atomic distribution for 0.2 wt % Rh loading while clustering was observed for higher (0.5 and 1.0 wt %) concentrations. CO-DRIFTS and XAS (XANES and EXAFS) also validate the isolated Rh sites dispersed on TiO_2. The Cu cations were used to maintain the low valence state of Rh in the reaction. Under optimized conditions, the methanol yield for the 0.2 Rh/TiO_2 reached up to 53 mol mol_{Rh}^{-1} while an unusual selectivity of 99% was achieved. The yield of products was increased by increasing temperatures reaching a maximum at 150 °C. Further, the yield of the product was increased by increasing the CH_4 (24 bar) and CO (5 bar) pressures while O_2 pressure higher than 2 bar has negligible influence on the activity. To validate that H_2O_2 was produced in situ from the reaction of CO and H_2O in a water gas shift reaction, colorimetric detection of H_2O_2 was done using $TiOSO_4$ reagent as per the following equation: $TiOSO_4 + H_2O_2 + H_2SO_4 \rightarrow H_2[Ti(O_2)(SO_4)_2] + H_2O$. The evolved H_2 from the reaction of water and CO was also measured which reacts with O_2 to form H_2O_2 as confirmed by EPR. The control experiment using only Rh/TiO_2, Cu/TiO_2 and $CuCl_2$ yielded negligible H_2O_2 demonstrating that the presence of Cu^{2+} cation was crucial for the transformation of CH_4 to CH_3OH. To probe the role of Cu in maintaining the low oxidations state of Rh catalysts EXAFS spectra of Rh/TiO_2 catalyst after the reaction was measured which displayed a reduced state. On the other hand, Cu_2O was also observed in EXAFS with Rh/TiO_2 while in the presence of O_2 and Rh/TiO_2, no Cu_2O was

https://doi.org/10.1021/acsnano.2c02464
ACS Nano XXXX, XXX, XXX−XXX

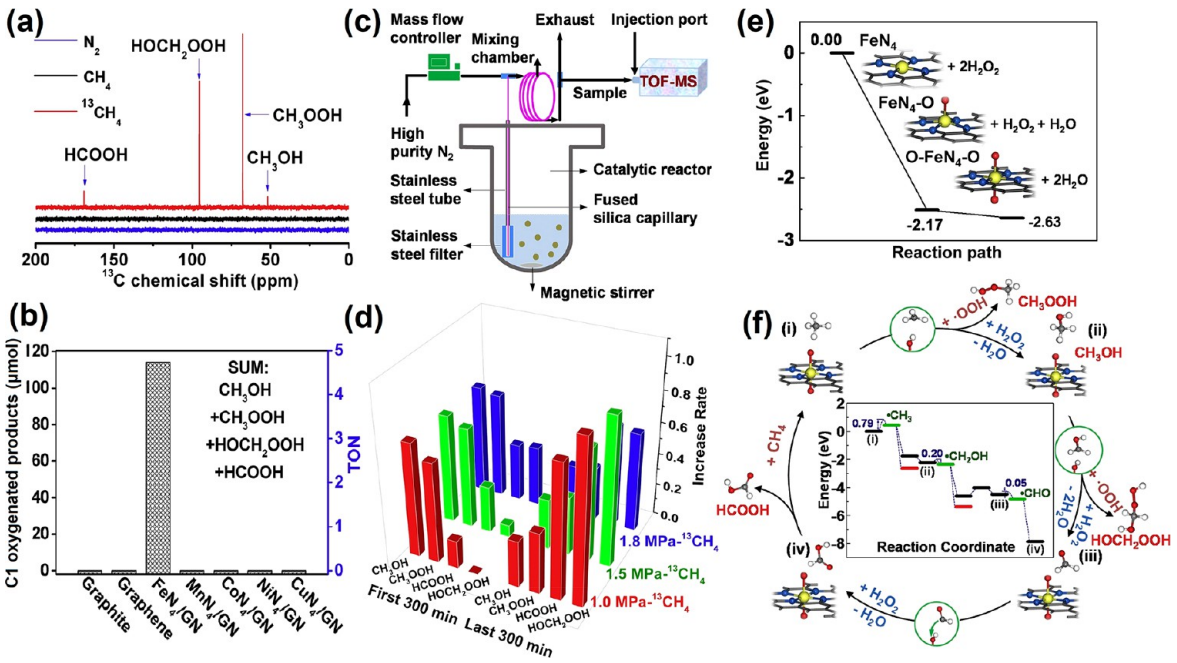

Figure 23. (a) ^{13}C NMR spectra obtained from N_2, CH_4, and $^{13}CH_4$ as reaction gas. (b) Catalytic performance of graphite, graphene, FeN_4/GN, and other metal-N_4/GN for CH_4 oxidation. Reaction conditions: 50 mg catalyst, 5 mL H_2O, 5 mL H_2O_2 (30%), and 2 MPa reaction gas in a stainless-steel autoclave containing a Teflon liner vessel (working volume, 50 mL) at 25 °C for 10 h. In operando characterizations for the evolution of liquid products over FeN_4/GN-2.7 (c) A scheme of the designed in operando TOF-MS. (d) The increase in the rate of the products at 0−600 min, corresponds to the relative intensity increment. Investigation of the reaction mechanism over FeN_4/GN (e) Transformation process of a FeN_4 center in H_2O_2 solution. The inset was the atomic structure model for each step. (f) Reaction pathway of methane conversion to CH_3OH, CH_3OOH, $HOCH_2OOH$, and HCOOH (the energy of reaction initiation was set as 0 eV) and reactants (black), intermediates (blue), products (green and red), and the activation energy of each step (unit, eV). Reprinted with permission from ref 349. Copyright 2018 Elsevier.

observed suggesting that Cu was reduced with in situ generated H_2 and then can act as a scavenger for Rh/TiO_2 reduction.

Even though the noble metal-based SAC displayed better performance, the relatively high cost put forth obstacles to its implementation. Another robust option is variable valency non-noble metals such as chromium, vanadium, etc. Shen et al. developed isolated chromium atom SACs supported on titanium dioxide nanoparticles (Cr_1/TiO_2) demonstrating an excellent methane conversion to yield C1 products such as CH_3OH, CH_3OOH, $HOCH_2OOH$, and HCOOH. After 20 h, an overall yield of C1 product was found to be 57.9 mol mol_{Cr}^{-1} with a C1 product selectivity of 93% using H_2O_2 as an oxidant at 50 °C and 3 MPa CH_4 pressure. Under identical conditions bulk Cr_2O_3 afforded only 2.6 μmol C1 oxygenated products after 1h, while SACs supported on other supports overperformed with a relatively higher product yield reaching the highest for Cr_1/TiO_2 (43.9%). ^{13}C NMR, ^{13}C DEPT-135 (distortionless enhancement by polarization transfer) spectra of products obtained by using isotopically labeled $^{13}CH_4$ demonstrate the presence of CH_3OH, $HOCH_2OOH$, CH_3OOH, and HCOOH (Figure 22a). Interestingly, the maximum C1 product yield was achieved in 20 h and thereafter the total product yield starts to diminish (Figure 22b). The EPR measurement using 1 wt % Cr/TiO_2 shows •CH_3 and •OH radicals generated through the C−H bond cleavage that can further react with Ti−OOH to produce CH_3OOH (Figure 22c). The •CH_3 and •OH also produce CH_3OH which oxidizes to $HOCH_2OOH$ and HCOOH after some time and is confirmed by using CH_3OH as reactant giving $HOCH_2OOH$ and HCOOH as end-product (Figure 22d). The presence of lonely Cr species was confirmed by AC-HAADF-STEM that shows bright spots corresponding to Cr atoms (Figure 22e). The HRXPS spectra of Cr_1TiO_2 gave two Cr $2p_{3/2}$ peaks at 586.4 and 588.4 eV suggesting chromium was present in Cr^{III} and Cr^{VI} mixed-valence states. Two reduction peaks at relatively low temperatures ca. 245 and 305 °C compared to bulk Cr_2O_3 in H_2-temperature-programmed reduction (H_2-TPR) validates the presence of Cr^{VI} and Cr^{III}, respectively (Figure 22f). After use, the catalysts lose significant activity and the Cr^{VI} peak almost disappeared which upon calcination re-emerged followed by regaining catalytic performance suggesting high-valent Cr^{VI} were the main bond cleavage catalytic centers.

It is evident from the above-mentioned discussion that an effective metal−support interaction which includes electronic charge redistribution, modulation of coordination/oxidation state and cooperative interaction with vicinal vacancies is the most important criteria to develop optimized SACs. Reducible/defect-rich surfaces allow better accommodation of the metal center and adsorption of the CH_4 substrate which can provide a low barrier reaction pathway to improve the catalytic activity. Alternatively, surface hydroxyl groups rich surface can not only reduce the H_2O_2 consumption but also suppress overoxidation of CH_4, thus producing the most desirable CH_3OH. The use of H_2O_2 can be excluded by noble metal Rh/TiO_2-based SACs which can directly use CO and O_2 as an oxidant to produce CH_3OH in the presence of a Cu cocatalyst. Variable transition metals that revert to an initial state in the catalytic cycle can further improve CH_4OR performance.

https://doi.org/10.1021/acsnano.2c02464
ACS Nano XXXX, XXX, XXX−XXX

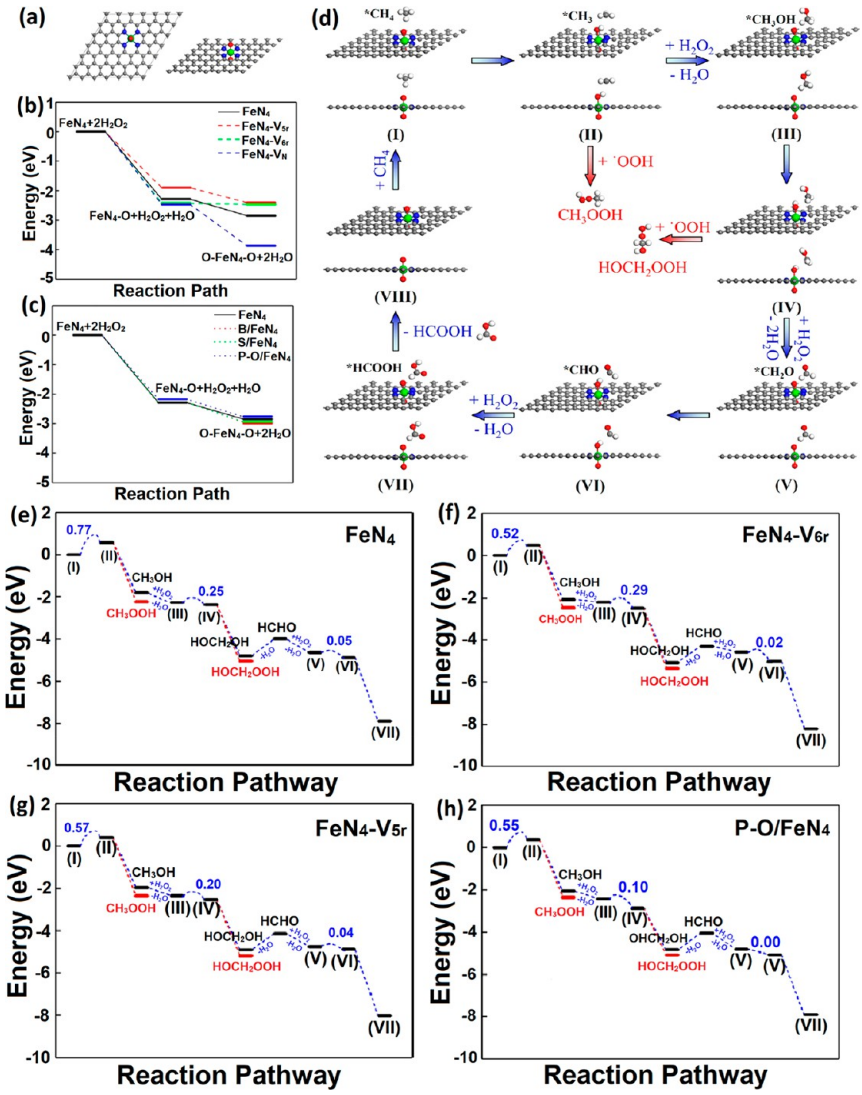

Figure 24. (a) Top and side views of optimized geometric structures of the oxidation processes of FeN_4 center to O−FeN_4−O structure by H_2O_2 on perfect FeN_4 catalyst. The free energy profiles of the oxidation processes of FeN_4 centers to O−FeN_4−O structures in H_2O_2 solution on (b) FeN_4 catalysts with various vacancies and (c) various doped FeN_4 catalysts. (d) The optimized geometric structures of methane conversion to C1 oxygenates on oxidized FeN_4−V_{5r} (the active center is O−FeN_4−O) along a radical pathway. The complete free energy profiles of methane conversion to C1 oxygenates on (e) perfect oxidized FeN_4, (f) oxidized FeN_4−V_{6r}, (g) oxidized FeN_4−V_{5r}, and (h) oxidized P−O/FeN_4. Reprinted with permission from ref 356. Copyright 2021 American Chemical Society.

7. SACS SUPPORTED ON 2D MATERIALS

7.1. MN_4 Graphenic SACs. The selective oxidation of methane in natural systems is promoted by Fe and Cu oxoclusters (Fe−O−Fe/Cu−O−Cu) containing MMO enzyme and two equivalents of reducing coenzymes. It is interesting to observe that nature adopted widely available transition metals for methane oxidation. Inspired by nature, several Cu/Fe supported on the high surface area support have been investigated. To date most active and selective methane oxidation catalysts reported are Cu/Fe supported on the ZSM-5 competing with MMO in the activity.[345,346] Unfortunately, the rate of oxidation for both natural enzymes and artificial catalysts is far below for commercial deployment. Additionally, the requirement of expensive H_2O_2 or N_2O terminal oxidants gravitates the commercial viability. Nevertheless, these nature-inspired protocols enlighten the way to find cheap and active methane oxidation catalysts.[347] Iron is the fourth most abundant element on the earth and is ideal to deploy on large-scale applications. The particle size plays a decisive role in catalytic activity. As the metal particle size is reduced to the nanoscale regime, the discretization of energy levels increases exponentially resulting in the separation of the HOMO and LUMO gap which influences energy distribution and concomitantly the catalytic properties. Further, the reduction of metal particle size to atomic level drastically increases the surface energy making them unstable in the isolated form. Therefore, supporting SA centers on the high surface area support such as porous carbon, silica, etc. is widely adopted for the fabrication of SAs catalysts. Recently, two-dimensional supports are gaining popularity for the fabrication of SACs due to their innate advantage of high surface area, effective interaction and synergistic effect.[86] Among the 2D family, graphene is an ideal choice to support lonely atoms due to its intriguing physicochemical properties and M-N_4 coordination stabilization which is not possible in other 2D systems. Numerous, cost-effective, and selective M−N_4 catalysts with Fe, Co, Ni, Zn, Mo, etc. as metal centers have been successfully developed and employed for various applications including thermal catalysis, biomass conversion, photocatalysis, electrocatalysts, fuel cell and energy storage applications.[348] Among the various elements, iron coordinated to nitrogen in N-graphene has displayed improved performance for various catalytic reactions. The remarkable activity of Fe−N_4 graphenic catalyst arises from the coordinatively unsaturated (CUS) iron sites which provide coordination sites for reactant molecules and also activate oxygen molecules

https://doi.org/10.1021/acsnano.2c02464
ACS Nano XXXX, XXX, XXX−XXX

via the formation of hypervalent Fe═O intermediate. Structurally, Fe−N_4 graphenic sites mimics catalytic sites found in the porphyrinic assembly of cytochrome P-450, nitrogenase, and MMO. Indeed, CUS iron has displayed higher catalytic activity compared to precious metals in many oxidative transformations. For example, Deng et al. synthesized Fe−N_4 graphenic (FeN_4/GN) structure via high energy ball milling of iron phthalocyanine (FePc) and graphene nanosheets (GNs) and first time undeniably prove the existence of Fe−N_4 entity using HAADF, EELS, and low-temperature STM.[158] The FeN_4/GN was found to actuate selective oxidation of benzene to phenol (another challenging $C_{aromatic}$-H activation reaction) even at low temperatures (0 °C). DFT and XANES studies reveal that Fe centers were sequentially oxidized to Fe═O/O═Fe═O moieties which can bind to C_6H_6 and form C_6H_5OH via the proton transfer step. Cui et al. investigated a series of M-N_4 graphene-based catalysts (M═Fe, Mn, Co, Ni, and Cu) for methane oxidation under mild conditions (Figure 23).[349] The O−FeN_4−O intermediate was an active center for the methane catalysis promoting the oxidation of methane via a radical pathway to produce CH_3OH, CH_3OOH, $HOCH_2OOH$, and HCOOH at room temperature (25 °C). The FeN_4/GN catalysts were prepared by adopting ball milling protocol using iron phthalocyanine and graphene and characterized with HAADF-STEM, XANES, and Fourier-transformed extended X-ray absorption fine structure (FT-EXAFS) confirming SA entities on graphene framework. The catalytic conversion of methane over FeN_4 catalysts was carried out in an autoclave using H_2O_2 as an oxidant. The produced products were analyzed by ^{1}H NMR, ^{13}C NMR, ^{13}C DEPT-135 (distortionless enhancement by polarization transfer), 2D ^{1}H−^{13}C heteronuclear multiple-quantum correlation, and TOF-MS demonstrating the presence of CH_3OH, CH_3OOH, $HOCH_2OOH$, and HCOOH. Under optimized conditions, a TOF of 0.47 h^{-1} was achieved. To validate the origin of products from the CH_4 oxidation instead of catalyst degradation, the reaction was also carried out under N_2, $^{12}CH_4$, and isotopically labeled $^{13}CH_4$, and products were analyzed by ^{13}C NMR. Control experiments using $^{13}CH_4$ followed by ^{13}C measurement demonstrate the products originated from the oxidation of CH_4 (Figure 23a). Additionally, among various metal centers such as Ni, Cu, Co, Mn, etc., only Fe demonstrated the catalytic activity (Figure 23b). The XAFS measurement after the reaction suggests the catalysts were still in a single atomic state. To investigate the reaction mechanism, in-operando TOF-MS with capillary to extract the product in real-time was used (Figure 23c). The product analysis demonstrates that initially CH_3OH and CH_3OOH were produced reaching a maximum at 300 min and after that $HOCH_2OOH$ was observed due to over oxidation of CH_3OH (Figure 23d). To validate that $HOCH_2OOH$ was produced from the CH_3OH oxidation, a reaction using isotopically labeled $^{13}CH_3OH$ was carried out which produces $HO^{13}CH_2OOH$ as a dominant product. DFT calculation reveals that H_2O_2 adsorption follows by absorption of O on Fe sites produces active O−FeN_4−O sites (Figure 23e). The concerted mechanism like in P450 which promotes hydroxylation on O−FeN_4−SH site was excluded due to the 1.91 eV energy barrier. A radical mechanism was followed in which C−H bond cleavage requires 0.79 eV to generate •CH_3 radicals. In the subsequent steps, •CH_3 radicals combined with hydroxyl and hydroperoxide radical to produce CH_3OH and CH_3OOH (Figure 23f).

7.2. Defects/Doping in MN_4 Graphene for Enhanced CH_4OR. Despite the exceptional capability of FeN_4/GN to activate the CH_4OR reaction compared to other elements on graphenic network which were almost inactive, the rate of oxygenates formation remains low.[349] After a 10 h reaction, only a tiny fraction of ca. 0.34% CH_4 was oxidized which renders the question, how to further improve the performance? Numerous studies suggest the introduction of defect state and heteroatom doping can significantly influence the charge distribution and concomitantly influence the nature of catalytic sites.[350−352] Defect-rich graphenic materials have been successfully employed for the ORR, OER, HER, CO_2RR, and N_2RR, etc.[353−355] To explore if defect states and heteroatom doping can further enhance the catalytic performance of FeN_4/GN, Tan et al. performed DFT studies on various models and found that C vacancies (FeN_4−V_{6r} and FeN_4−V_{5r}) and P dopant (P−O/FeN_4) adjacent to FeN_4 centers can significantly improve the catalytic activities of FeN_4 catalysts.[356] To simulate the vacancies rich model, C atoms adjacent to FeN_4 were removed from five and six-membered rings (FeN_4−V_{6r} and FeN_4−V_{5r}). N atom removal is also considered to create N vacancies (FeN_4−V_N). Additionally, heteroatoms such as B, S and P were introduced directly next to the N atom. The formation of O−FeN_4−O via H_2O_2 is the primary step that works as a catalytic center to further activate methane. The total energy decreases for FeN_4−V_{6r}, FeN_4−V_{5r}, and FeN_4−V_N adsorbs two O atoms were found to be 2.47, 2.40, and 3.87 eV, respectively suggesting O−FeN_4−O can be produced on both defect-free and defect-rich scaffold (Figure 24a−c). Based on the G_f and ΔG_a of the rate-determining C−H bond activation step, the methane activation rates for FeN_4−V_{6r} and FeN_4−V_{5r} were calculated to be 1.7×10^4 and 2.4×10^3 times higher than that of perfect FeN_4. The CH_4 activation on FeN_4−V_{6r} and FeN_4−V_{5r} models demonstrate C−H bond scissoring occurs at lower energy with an activation energy of 0.52 and 0.57 eV while FeN_4 requires significant high energy (0.77 eV) (Figure 24d,g). In the next free radical pathway, the energy barriers were below 0.3 eV suggesting the facile formation of oxygenates in subsequent steps. Among doped catalysts, P doped FeN_4 catalyst demonstrated optimum performance with a methane activation rate of 5.3×10^3 magnitudes higher compared to perfect FeN_4. The activation energy for the first C−H bond activation of methane using P−O/FeN_4 was also significantly low (0.55 eV) than FeN_4 (Figure 24h). These findings suggest graphene-based FeN_4 catalysts can be improved by introducing defects in the C_6 ring system.

7.3. MN_4 SACs Utilizing N_2O as an Oxidant for CH_4OR. Conventionally, O_2 and H_2O_2 are foreseen as inexpensive oxidant chemicals for methane oxidation. However, generating active oxygen species from oxygen itself is a big challenge due to high activation energy while H_2O_2 promotes nonstoichiometric oxidation products sacrificing the product's selectivity. Nitrous oxide (N_2O), a greenhouse gas 300 times more powerful than CO_2, can work as a terminal oxidant supplying oxygen and producing N_2 byproduct.[357,358] Besides the greenhouse effect, N_2O is also responsible for depleting the ozone layer in the stratosphere where it reacts with O_2 to produce NO_x (NO + NO_2) which are actual intermediates. Both anthropogenic and natural activities contribute to the N_2O is accumulation in the environment. Among natural sources, seafloor with oxygen-depleted zones (oxygen minimum/dead zones) accounts for 25% of N_2O emissions. While modern agricultural practices of using an excess of nitrogenous fertilizers account for over two-thirds of global N_2O emissions.[359−361] Some anaerobic bacteria can couple the oxidation of methane to denitrification process via the reduction of NO_3^- and NO_2^- through nitric oxide (NO) and/or N_2O which inspired the scientific community to use nitrogen oxides as an oxidant for CH_4OR.[362] Using N_2O as a terminal oxidant for methane oxidation can sequester two greenhouse gases producing value-added chemicals.[363] Arinaga et al. compiled various examples of alternative oxidant such as O_2, CO_2, N_2O, and S_2 which can be used for CH_4OR.[364] First-row transition metal oxide cations (MO^+) such as FeO^+ are found to promote oxidation of methane to methanol; however, the conversion and product selectivity remains poor to scale up.[365−367] Though CoO^+ has displayed a higher selectivity, reaction efficiency remains impoverished.[366,368] Many examples of metal (Cu, Fe) hosted zeolites using N_2O as oxidant has been reported in the lasted year.[369] Ipek et al. demonstrated Cu-SSZ-13 as a representative of CuCHA zeolite can produce CH_3OH with a rate of 13 μmol CH_3OH $g_{zeolite}^{-1}$ at 200 °C which was almost 1.5 times higher than the yield in O_2 (9.0 μmol CH_3OH $g_{zeolite}^{-1}$). They also investigated Cu-MOR under identical conditions which demonstrated a much lower yield attributed to smaller cavity size. Recently, Zhao et al. demonstrated that mono and polymeric iron sites incorporated in ferrierite (FER) zeolite via liquid IE and SSIE methods can catalyzed CH_3−H oxidation using N_2O as a terminal oxidant at 300−360 °C.[370] H_2-TPR followed by N_2O adsorption demonstrated the shift in desorption peak along with the emergence of a new peak around 220 °C demonstrating the presence of monatomic oxygen stabilized on

https://doi.org/10.1021/acsnano.2c02464
ACS Nano XXXX, XXX, XXX−XXX

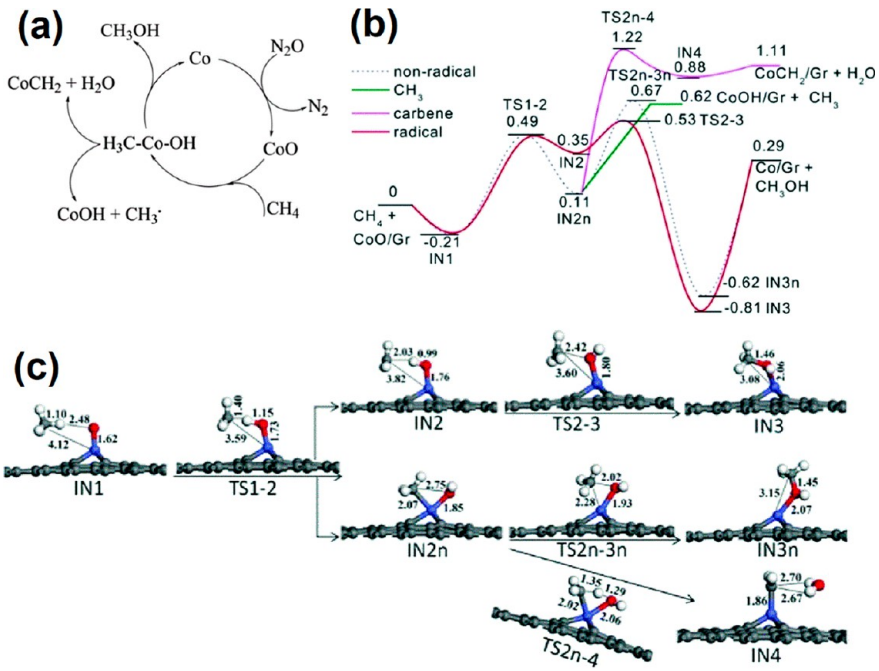

Figure 25. (a) Methane conversion catalyzed by Co/Gr, with N_2O as the oxidant (Gr is omitted for clarity). (b) The potential energy profiles (eV) for methane oxidation on CoO/Gr. (c) The species in the reaction process of methane oxidation on CoO/Gr. Reprinted with permission from ref 372. Copyright 2018 Royal Society of Chemistry.

Fe^{2+} species. Based on UV−vis, FTIR and TPD they concluded that monatomic species were dominant in the samples prepared by the wet ion-exchange method. N_2O TPD exhibited that single Fe site adsorption and decomposition of N_2O was prevailing thus giving a higher performance of Fe-FER-IE sample. Based on DFT calculation, Fellah et al. demonstrated that the Co-exchanged ZSM-5 cluster demonstrates a lower energy barrier for CH_4 to CH_3OH conversion compared to Fe-ZSM-5 (49 kcal/mol vs 53 kcal/mol).[371] Pinning a SA cobalt center on graphene can improve the conversion efficiency of methane oxidation due to the stabilization of the Co center and available specific surface area. Yuan et al. demonstrated that SA Co embedded in single vacancy graphene can uptake O from N_2O to form CoO, imitating metal oxide cation to promote oxidation of methane to methanol (Figure 25a).[372] DFT calculations suggest that the decomposition of N_2O on the Co/Gr surface is highly exothermic (1.54 eV) and require merely 0.1 eV energy input. While desorption of formed N_2 is also thermodynamically favored (0.1 eV) ensuring replenishing of catalysts surface. The oxidation of methane on resulting CoO/Gr catalysts can proceed via two routes: (1) radical and (2) nonradical route (Figure 25b,c). The reaction proceeds via adsorption of CH_4 on Co−O/Gr and formation of C−H···O intermediate (IN1) which proceeds to transition state TS1−2 and IN2/In2n in which H−O distances are shortened, and C−H distance is elongated. The elementary steps are exothermic by 0.29 eV, while the rate-limiting steps impose a low-energy barrier of 0.70 eV demonstrating that both radical and nonradical pathways can proceed to obtain methanol under mild conditions. The radical pathway is slightly more favorable due to the small energy barrier of the second elementary step (0.18 eV) than the nonradical pathway (0.56 eV). Further, the carbene formation through proton transfer to Co−OH (IN4 for short) followed by H_2O elimination is highly unfavorable due to associated energy-intensive high potential energy. Considering the Arrhenius empirical equation $k = A\exp(-E_a/RT)$, the calculated rate of methanol production through the radical pathway was found 6.5×10^{15} times faster than the carbene pathway.

Compared to bulk 3D crystals, M-N_4−C catalysts provide higher surface area, metal loading, facile synthesis/robust binding with four nitrogens. The access to the metal center from both side of MN_4 planes to form mono (M═O) and dioxo (O═M═O) centers allow efficient CH_4 oxidation, while the N-rich surface facilitates improved adsorption of the substrate. Fe−N_4 demonstrated the highest CH_4OR performance compared to other MN_4 metal centers due to the facile formation of hypervalent oxo-state. In contrast to conventional H_2O_2, N_2O might be a better oxidant for CH_4OR and Co−N_4 might be the best option because of low energy intermediate transition states. The performance of M-N_4 catalysts can be further ameliorated by vicinal doping and vacancies which stabilize CH_4 oxidation intermediate species.

8. PHOTOACTIVE SACS FOR CH_4OR

8.1. Metal Oxides Supported SACs. Apart from the high dissociation energy of the C−H bond (439.3 kJ mol^{-1}) for methane activation, controlling the overoxidation of methane remains a challenging task and a significant carbon loss as CO and CO_2. Conventional thermal catalysis usually produces a mixture of various oxygenates and required strong oxidants which further deteriorate the selectivity. Direct selective oxidation of CH_4 using O_2 under ambient conditions is a dream reaction. The fundamental challenge lies in overcoming the energy barrier of unyielding reaction between spin prohibited singlet CH_4 and triplet O_2.[153] Photocatalysis offers an efficient approach to drive thermodynamically nonspontaneous reactions under mild conditions.[373,374] Several oxides, sulfides, and carbonaceous semiconductors such as $KNbO_3$, Cu_2O, Bi_2WO_6, CdS, $BiVO_4$, g-C_3N_4, CeO_2, etc., either in pristine form or cocatalysts have been investigated for the photocatalytic methane oxidation in aerobic conditions; however, the quantum efficiency of mentioned systems remains too low.[373,375−380] Interestingly, zinc-based photocatalysts demonstrated a high affinity for CH_4 activation.[381] An early report by Li et al. on Zn-modified zeolite for the C−H activation of methane to ethane suggested that Zn^+ formed by in situ reductions with photogenerated electrons are key species activating the C−H bond.[382] Later, ZnO-based photocatalysts decorated with plasmonic or low bandgap cocatalysts were also investigated. Gas-phase photooxidation in

https://doi.org/10.1021/acsnano.2c02464
ACS Nano XXXX, XXX, XXX−XXX

the presence of oxygen usually affords CO_2/CO with negligible industrial relevance.[381] For example, 0.1 wt % Ag decorated ZnO can oxidize methane with 8% quantum efficiency at <400 nm producing futile CO_2 end-product.[383] Similarly, $H_3PW_{12}O_{40}$ heteropolyacids (HPW)-TiO_2 (P25) nanocomposite displayed CO as the main product with a quantum efficiency of 7.1% at 362 nm.[384] The mechanism evaluation suggests that superoxide radicals were the key species resulting in uncontrolled oxidation. Contrarily, when noble metals (Pd, Pt, Au, Ag) decorated ZnO was used as a photocatalyst under aqueous conditions and 0.1 MPa O_2 pressure liquids oxygenates such as CH_3OOH, CH_3OH, and HCHO were the main products reaching a total liquid products selectivity of ~95%.[385] The photogenerated hole assisted cleavage of C−H bond producing •CH_3 radical followed by reaction with mild •OOH radicals oxidant to produce liquid oxygenates. Even though the liquid oxygenates are economically feasible, in most of the reactions CH_3OOH remains a dominant product. Selective oxidation of CH_4 to methanol/formaldehyde is desirable to commercialize the process. Size reduction of catalysts in quantum size scale was found to enhance the catalytic selectivity. For example, $BiVO_4$ quantum-size nanoparticles were able to achieve selectivity of 96.6% and 86.7% for methanol and formaldehyde under the 300−600 nm wavelength spectrum.[386] Indeed, most of the product originated at a lower wavelength in this catalyst. Paradoxically, size reduction and concomitant enhancement in product selectivity come at the cost of compromised visible absorption resulting in poor reaction kinetics.

Among various semiconductor photocatalysts, TiO_2 is the most investigated photocatalytic material. The wide bandgap of TiO_2 (3.2 eV anatase) provides enough redox potential to drive oxidation/reduction reactions including photo/photoelectrochemical CO_2 reduction, water oxidation, organocatalysis, etc.[387] However, a major fraction of visible light remains unharvested and generated charge also get recombined resulting into poor efficiency. Various approaches such as metal doping, facet engineering, mixed-phase transformation, metal complexes anchoring, and nanohybrid formation with graphene/quantum dots and other macromolecular sensitizers were found to improve the photocatalytic performance.[388−390] For example, Su-Il In's research group reported reduced blue-titania sensitized with bimetallic Cu−Pt nanoparticles which can promote the reduction of CO_2 to C_{1-2} products (3.0 mmol g^{-1} methane and 0.15 mmol g^{-1} ethane) under AM1.5 irradiation reaching the Joule (sunlight) to Joule (fuel) photoconversion efficiency of 1%.[391] Another strategy to improve the photocatalytic performance of wide band gap catalysts is the decoration of nanoparticulate noble metal which can extend visible absorption and charge separation due to surface plasmon resonance (SPR) and electron capturing ability due to low work function. The nanosized plasmonic materials such as Au, Cu, Ag and TiN, etc. generate hot charge carriers (energetic electrons and holes) which can actuate several energy-demanding photoredox reactions. For instance, Vahidzadeh et al. reported that AuNPs embedded in a thin film of amorphous TiO_2 can inject hole holes in TiO_2 film which promotes PEC water oxidation.[392] Decoration of plasmonic nanoparticles on TiO_2 can not only improve the photocatalytic performance but can also control the product selectivity under different light irradiation. Zeng et al. found that periodically modulated TiO_2 nanotubes (PMTiNTs) photonic crystal modified with AuNPs demonstrates CH_4 as the main product under solar simulated light while formaldehyde was a dominating product when the catalyst was irradiated with solar simulated/and or UV and 550 nm light.[393] The unusual control of product selectivity was attributed to the establishment of the interband *Z*-scheme electron transfer mechanism. Even after these efforts, the performance of these catalysts remains far from real-world applications. Another approach to improve the visible light absorption, catalytic activity and even specificity of TiO_2-based materials is defect engineering. The first report by Chen et al.[394] on the synthesis of low bandgap black TiO_2 (~1.0 eV) with plenty of defects introduced by hydrogenation, geared the research in this direction.[395−397] The creation of point defects such as oxygen vacancies introduce subenergy gaps leading to an alternate path of excitation and relaxation.[398] Naldoni et al. reported a one-step reduction/crystallization synthesis of black TiO_2 exhibiting a bandgap of only 1.85 eV.[399] The structural characterizations reveal low-pressure hydrogenation favors Ti^{3+} and O vacancies compared to interstitial Ti ions under harsh conditions. After that several reports focused on various strategies of defect creation including chemical route and controlling nature of defects, photophysical characterization and photo/catalytic applications has emerged.[400401] In a recent study, Fornasiero group reported synthesis of O defect rich brookite TiO_2 nanorods via hydrogenation at 700 °C.[402] The thermal treatment under H_2 transforms anisotropic structure to irregular isotropic structure without distorting the crystal structure however oxygen vacancy point defects were introduced which were confirmed by UV−vis, Raman. When tested for the alcohol oxidation, the reduced brookite TiO_2 samples can reach a CH_3OH photooxidation rate of 99 mmol h^{-1} m^{-2} compared to pristine TiO_2 (27 mmol h^{-1} m^{-2}). The Pt photodeposited samples displayed the similar pattern for alcohol oxidation regardless of nonhomogeneous size distribution suggesting the key role of vacancies to promote reactions. The hydrogen evolution rate for platinized brookite samples was almost 18 times than pristine anisotropic sample. Interestingly, substrate specific activity was observed for the reduced brookite TiO_2 and methanol oxidation was predominant over ethanol and isopropanol. Detailed analysis of the sample with in situ PL demonstrate introduction of midgap state along with reduced lifetime of excited state implying enhance photoactivity. Synchrotron-based photoemission spectroscopy followed by DFT calculation suggest the specific activity for the methanol arised due to bound states between oxygen vacancies and large electron polarons.

The presence of defects on the surface of TiO_2 provides an opportunity to stabilize SACs which can form bonding with neighboring Ti atoms. Pan et al. demonstrated the defects confined growth on ultrasmall noble metal clusters on TiO_2 and speculated electrons transfer from vacancies to metal ion promoting stabilization of metal.[403] In another report Wan et al. demonstrated the formation of Au SACs on defect-rich TiO_2 nanosheets.[117] Detailed characterization including EXAFS, XANES, and EPR reveals that the Ti−Au−Ti bond was formed. Further, DFT studies suggest due to the reduced energy barrier for Ti−Au−Ti structure, the competitive adsorption can be avoided resulting in improved catalytic properties. Apart from reduction, various synthetic conditions can also introduce defects state in TiO_2. For example, Zhou et al. showed that anodic growth of TiO_2 nanotubes poses a considerable strain on tube walls ensuing the formation of the high density of Ti^{3+}-O_v surface defects.[404] Taking advantage of

https://doi.org/10.1021/acsnano.2c02464
ACS Nano XXXX, XXX, XXX−XXX

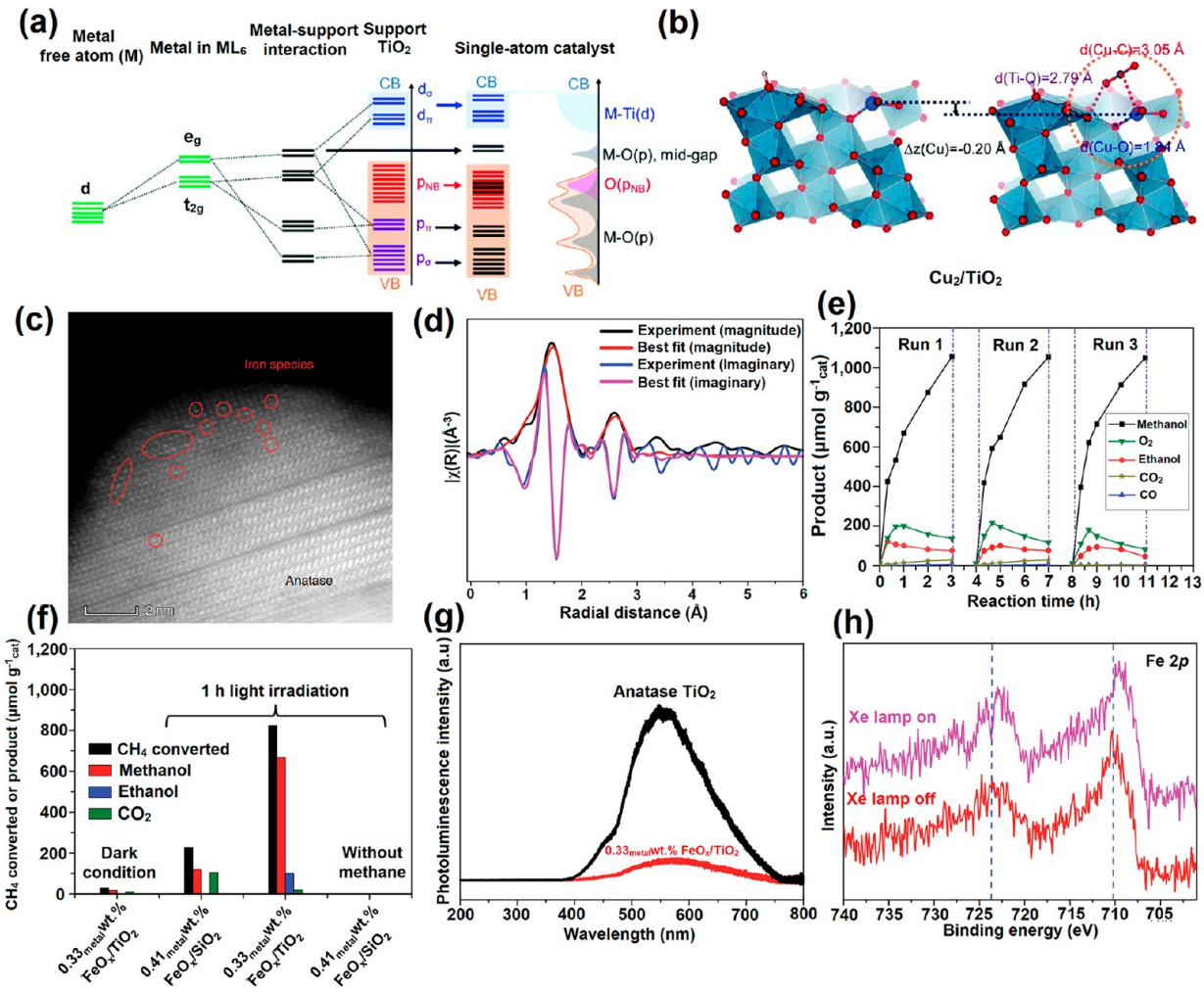

Figure 26. Enhanced surface reducibility of a SAC by electronic metal−support interfacial hybridization. (a) Schematic alignments of the d orbital splitting of a metal atom in a coordinate complex (left), the energy levels of the support material (middle) and their metal−support hybrid states based on ligand field theory (middle). (b) DFT optimized structure of Cu_2/TiO_{2-x}. Reprinted with permission from ref 405. Copyright 2022 Royal Society of Chemistry. (c) STEM image and (d) fitting details for iron K-edge EXAFS spectra of 0.33 $_{metal}$wt % FeO_x/TiO_2. (e) Three runs of CH_4 conversion by 0.33 $_{metal}$wt % FeO_x/TiO_2 under light irradiation operated at room temperature and atmospheric pressure. (f) CH_4 conversion amounts and product yields from a series of control experiments. Chemical and physical characterization of the TiO_2-based photocatalysts. (g) PL spectra of anatase TiO_2 and 0.33 $_{metal}$wt % FeO_x/TiO_2. (h) Fe 2p XPS spectra of 0.33 $_{metal}$wt % FeO_x/TiO_2 in the dark and under Xe lamp irradiation. Reprinted with permission from ref 340. Copyright 2018 Springer Nature.

defect-rich surface they pinned Ir SA sites by a simple impregnation approach. The resulting 0.58% IrSA TiO_2 catalyst displayed a turnover frequency of 4×10^6 h^{-1}. Interestingly, after the illumination, the SAs tend to agglomerate and the calculated SAs density was found to be 378134 SAs per μm^2 before and 18656 SAs per μm^2 after illumination. Despite the clustering of Ir centers, the catalytic activity remains almost stable that can be ascribed to the high activity of the SA site compared to the negligible performance of the nanoparticles. Compared to noble metal centers, the earth-abundant transition metals such as Cu, Fe and Ni, etc. are desirable candidates for fabricating SACs because of their low cost, high coordination number, variable valency and facile formation of M═O species. Like metallozymes where metal center's coordination environment with surrounding ligands has a significant impact on the activity/specificity, the catalytic performance of SACs is also governed by local atomic configuration on the supporting materials. The decoration of SAs on reducible oxide supports such as TiO_2, and CeO_2 affords the random distribution of SAs on various coordination sites that influence the degree of charge transfer between the interfaces. Due to the heterogeneity of these coordination sites, the investigation of the effect of these sites on activity remains ambiguous. To understand the role of the metal coordination environment on TiO_2 support, Lee et al. achieved site-specific stabilization of Cu SA in a Ti vacancy (Cu_1/TiO_2) which excludes coexistence of any other atomic configuration or subnanometric cluster which enabled investigation of the photocatalytic CO_2 reduction on a TiO_2 surface with atomic precision.[405] The study reveals that the CO_2 reduction activity was significantly boosted due to the formation of O vacancy in the vicinity of Cu atoms in Ti vacancies. Previously the same group also reported site-specific SA Cu/TiO_2 catalysts which can undergo a specific color change cycle under visible light irradiation during hydrogen evolution attributed to charge transfer from TiO_2 to the d band of isolated Cu atom.[165] Further, the presence of multiple adjacent Cu SAs facilitates CO_2-mediated cooperative charge relaxation and delocalization. The metal d-state in the MO_6 octahedron of TiO_2 generates e_g and t_{2g} states which overlap with oxygen's p

https://doi.org/10.1021/acsnano.2c02464
ACS Nano XXXX, XXX, XXX−XXX

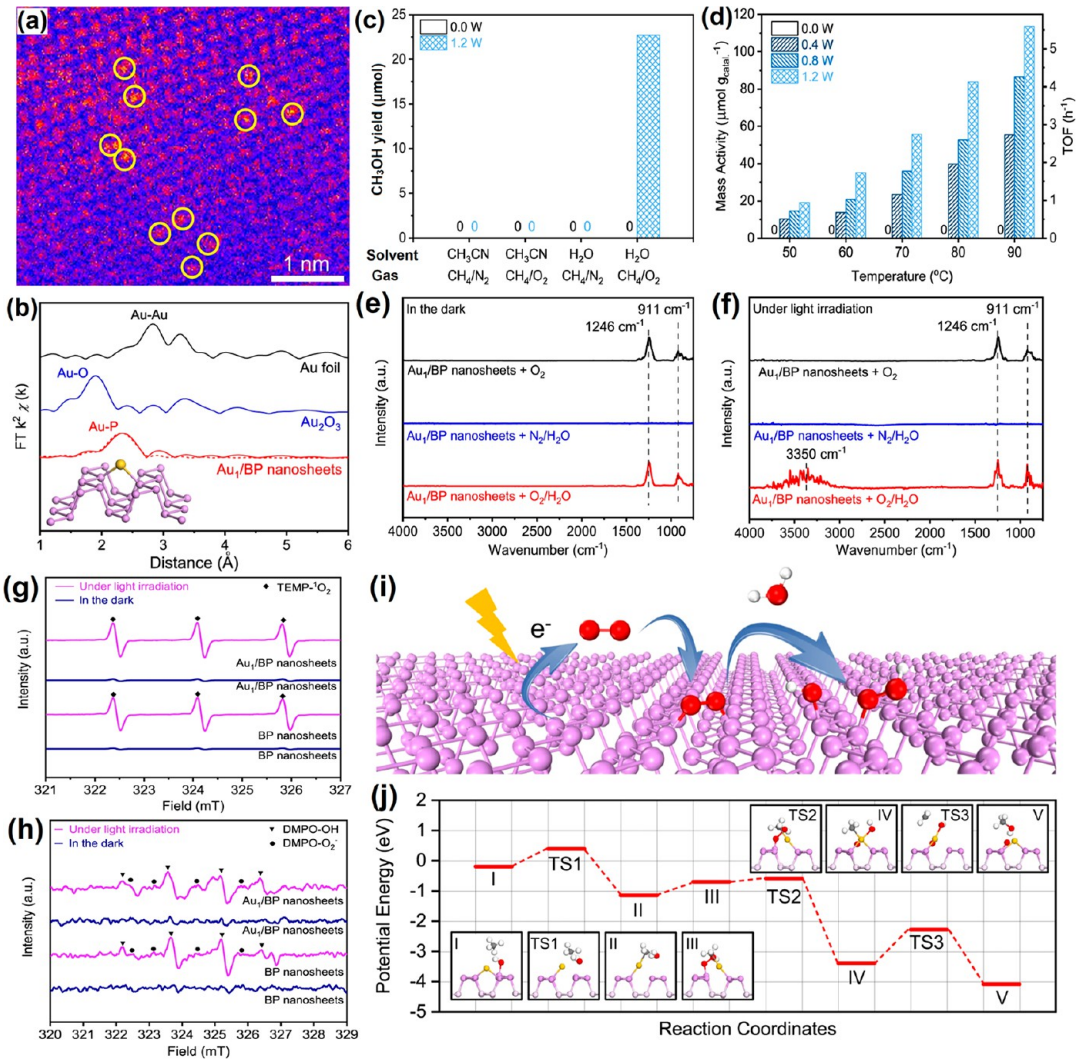

Figure 27. (a) HAADF-STEM image of Au_1/BP nanosheets with color-coded intensity. (b) EXAFS spectrum of Au_1/BP nanosheets, Au foil and Au_2O_3. The inset image shows a structural model of Au_1/BP nanosheets. (c) Comparison of methanol yields under different solvents and reactants at 90 °C for 2 h. (d) Mass activities and TOF numbers in 20 mL of water under 33 bar (CH_4:O_2 = 10:1) at different temperatures under different light powers with an irradiation area of 3.14 cm^2. In situ DRIFTS spectra of Au_1/BP nanosheets purged by 1 bar of different gases at 90 °C (e) in the dark and (f) under light irradiation. In situ ESR spectra of BP and Au_1/BP nanosheets under different conditions (g) in the presence of TEMP and (h) in the presence of DMPO. (i) Schematic illustration of oxygen activation on BP nanosheets. (j) Reaction path for partial oxidation of methane over Au_1/BP nanosheets under light irradiation. The inset images show the side views of the configurations. Reprinted with permission under a Creative Commons CC-BY License from ref 413. Copyright 2020 Springer Nature.

orbitals (p_σ and p_π) leaving nonbonded p states. The introduction of a Cu atom in a Ti vacancy leads to partial oxidation of an oxide anion (O^{2-}) which stabilizes the metal–support interface. The resulting configuration introduces midgap states above the Fermi level in Cu_1/TiO_2 making its surface vulnerable to reduction (Figure 26a). The surface reducibility of TiO_2 promotes the creation of O vacancies near Cu sites as demonstrated by −0.75 eV downhill energy for Cu_1/TiO_2 compared to pristine TiO_2 (+4.41 eV). The O vacancy containing Cu_1/TiO_2 can be represented as Cu_1/TiO_{2-x} where surface charge is balanced by protons. The photoexcited electrons are localized to the $d_{x^2-y^2}$ state of the Cu atom creating Cu^+ state which energetically favors reduction of CO_2. The CO_2 adsorbs on O vacancies near Cu followed by the formation of Cu−C state by Cu−O_4 square planar structure distortion. In the subsequent steps proton and electron transfer promotes the removal of O leading to M-CO which finally reduce to CH_4 in subsequent steps. To validate the obtained theoretical findings, the site-uniform Cu SAs containing TiO_2 hollow nanosphere were synthesized by template confined thermodynamic redistribution of SAs. The EELS spectra of pristine TiO_2 displayed Ti L_2 and L_3 edges with characteristics splitting due to e_g and t_{2g} energy gap which diminishes in Cu_1/TiO_2 suggesting the introduction of midgap state disturbed octahedral crystal field splitting. Further, the EELS spectrum at different sites displayed both two peak and two doublets splitting features respectively suggesting the coexistence of Ti^{3+} and Ti^{4+} states. The incorporation of Cu in the Ti vacant site was also confirmed by EXAFS which demonstrates a slightly undercoordinated (4.6−4.8) state compared to pristine TiO_2. The CO_2 to CH_4 formation rate of Cu_1/TiO_2 was found to be 416.9 ppm g^{-1} h^{-1} which was significantly higher than TiO_2, other M_1/TiO_2 and CuO nanoparticles decorated TiO_2 catalysts. To know the effect of

https://doi.org/10.1021/acsnano.2c02464
ACS Nano XXXX, XXX, XXX−XXX

neighboring atom in synergistic cooperative relaxation, an additional neighboring Cu atom was decorated (Cu_2/TiO_{2-x}) which indicates that a Cu single site and the nearby O vacancy offers an active binding pocket for bidentate binding of CO_2 while neighboring Cu can stabilize the d electrons by a charge delocalization through symmetrically matched d orbitals. This resulted in the distortion of the Cu−O_4 complex into a more symmetrical square planar (D_{4h}) structure that prevents charge localization on Cu maintaining the strong basicity of a Cu atom and binding pocket structure, required for chemical bond formation between CO_2 and Cu (Figure 26b).

Focusing on CH_4 oxidation, the photocatalytic process provides an advantage over thermal processes due to the generation of hydroxyl and superoxide radicals which can either directly attack CH_4 or produce secondary radical intermediate and H_2O_2. By controlling the nature of radical and H_2O_2 it is possible to get 100% selectivity as demonstrated in the following section. Despite, metal NPs decorated TiO_2 photocatalysts have been explored for the CH_4OR, there is only one report using TiO_2-based SACs photocatalysts and more work is needed in this direction. Since Fe-based SACs mimics natural enzymatic systems, anchoring Fe SA species on TiO_2 catalysts can provide significant achievement. Tang's group demonstrated that extremely nanosized Fe (FeOOH and Fe_2O_3) species supported on TiO_2 support were able to photocatalyze the selective oxidation (90% selectivity) of methane to methanol.[340] The FeO_x/TiO_2 samples were prepared by the WI method and used for the photocatalytic oxidation of CH_4. The STEM analysis reveals that optimized samples 0.33 $_{metal}$wt % FeO_x/TiO_2 displayed highly dispersed iron species including clusters and SA species (Figure 26c). XANES Fe K-edge spectra after fitting displayed that iron was mostly present as FeOOH with a small fraction of Fe_2O_3 species. Furthermore, EXAFS shows a major peak corresponding to the Fe−O shell with a minor Fe−Fe second-shell contribution which verified that FeOOH and Fe_2O_3 atomic to ultrasmall cluster form was present (Figure 26d). The samples 0.33 $_{metal}$wt % FeO_x/TiO_2 displayed highest CH_4OR performance (1.056 μmol g_{cat}^{-1} or 18 mol_{CH_3OH} $mole_{Fe}^{-1}$) and 90% selectivity while under identical conditions noble metal loaded TiO_2 (0.12 $_{metal}$wt % Au/TiO_2, 0.53 $_{metal}$wt %PdO_x/TiO_2 and 0.69 $_{metal}$wt %PtO/TiO_2,) displayed significant drop in catalytic activity (Figure 26e). To validate that the reaction was TiO_2 photocatalyst driven, 0.41 metalwt %FeO_x/SiO_2 was used which shows diminished product yield. The catalytic activity remains constant even after three recycle suggesting the stable nature of the catalyst (Figure 26f). The decreased PL intensity of 0.33 $_{metal}$wt % FeO_x/TiO_2 compared to pristine TiO_2 and shifted Fe 2p XPS peak toward lower binding energy suggesting better charge separation due to the capture of electrons via Fe species (Figure 26g,h).

8.2. Black Phosphorus Supported SACs. Decoration of SAs on low bandgap materials can translate a larger fraction of photogenerated charge carriers to drive a chemical reaction. Compared to bulk 3D materials, 2D materials can accommodate a large population of SA sites while providing a large surface area for substrate adsorption. BP, a 2D allotrope of phosphorus with a significantly small bandgap (0.3 eV), excellent carrier mobility, earth-abundant nature and p-type conductivity has attracted wide attention to be used in photocatalysis.[406,407] Interestingly, BP can be exfoliated to single layer to few layers sheets (called phosphorene) by solvent-assisted exfoliation using solvents such as dimethylformamide, dimethyl sulfoxide, *N*-methyl 2-pyrrolidone, ionic liquids, etc.[408−410] Due to the confinement effect, the theoretical band gap of single-layered BP sheets can be extended up to ∼2.1 nm.[411] The sp^3 hybridized phosphorene sheets have periodic out-of-plane P atoms which in the long-range provide 2D structure to BP nanosheets. These P atoms are easily oxidized under air/oxygen/water to form P−O and P═O dangling bonds. Similarly, P atoms can also coordinate with other metallic centers making them suitable candidates for the supporting SA centers.[412] Luo et al. synthesized gold SA decorated BP nanosheets (Au_1/BP nanosheets) by injecting $HAuCl_4$ precursor in exfoliated BP suspension.[413] The color mapped HAADF-STEM image of 0.2 wt % Au_1/BP nanosheets, displayed the atomic distribution of Au on the sheets (Figure 27a). When Au loading was increased to 1%, the nanoparticles with an average size of 6 nm were observed. The Au L_3-edge XANES spectra demonstrate the presence of Au in a mediate state between metallic Au and Au_2O_3 while EXAFS displayed a peak centered at 2.33 Å for double coordinated Au bridged with 2P atoms (Figure 27b). DRIFTS of Au_1/BP only shows linear absorption of CO probe molecule suggesting the presence of SA sites. Photocatalytic CH_4 oxidation under 33 bar pressures (CH_4:O_2 = 10:1) Au_1/BP nanosheets affords 22.7 μmol of methanol translated to methanol formation rate of 113.5 μmol g_{cat}^{-1}, with a TOF of 5.6 h^{-1}. (Figures 27c,d). The product formation rate was dependent on light intensity while the activation energy (E_a) of Au_1/BP nanosheets was almost independent of light intensity. They demonstrated significant stability and after 10 cycles about 205.2 μmol of methanol was observed with TOF ∼ 7%. The control experiments in the absence of O_2/light, using acetonitrile instead of water, using methanol as a reactant affords negligible reaction product suggesting water and O_2/light, were essential for the oxidation of methane to methanol. The detailed mechanism was evaluated using in situ DRIFTS. The DRIFTS spectra in the presence of O_2 demonstrated two peaks at 1246 and 911 cm^{-1} due to P═O and P−O−P stretch. However, in the presence of N_2/H_2O, no such peak was observed under dark or light conditions. When both O_2 and H_2O were present in the dark no significant difference was observed and only peaks for P═O and P−O−P were visible (Figure 27e). Interestingly, under light illumination, a sharp band around 3350 cm^{-1} appeared demonstrating the generation of hydroxyl groups (Figure 27f). Similarly, quasi-situ XPS displayed the only presence of P═O and P−O−P under dark while OH peaks were observed after the illumination. Further, EPR spectroscopy using DMPO and TEMP as trap agents suggest the formation of $^1O_2$, O_2^-, •OH, and P−OH species demonstrating the reaction was H_2O/O_2 driven (Figure 27g,h). Moreover, in situ DRIFTS in the presence of CH_4 after the O_2/H_2O activation of BP surface demonstrated the increased intensity of P−OH and CH_3*, while the peak intensity of CH_4 and P═O was significantly decreased, suggesting CH_4 generates CH_3* species by following reactions. (CH_4 + P═O → CH_3* + P−OH). Temperature-programmed surface reaction with mass spectroscopy (TSPR-MS) using isotope ^{18}O-labeled water ($H_2{}^{18}O$) shows the absence of any product without light. However, after illumination, $CH_3{}^{18}OH$, $CH_3{}^{16}OH$, $H_2{}^{18}O$, and $H_2{}^{16}O$ were observed, and no peak for CO_2 was observed. These observations suggest the reaction was O_2 and H_2O driven and required light for the activation. DFT studies confirm the formation of P═O and P−O−P

https://doi.org/10.1021/acsnano.2c02464
ACS Nano XXXX, XXX, XXX−XXX

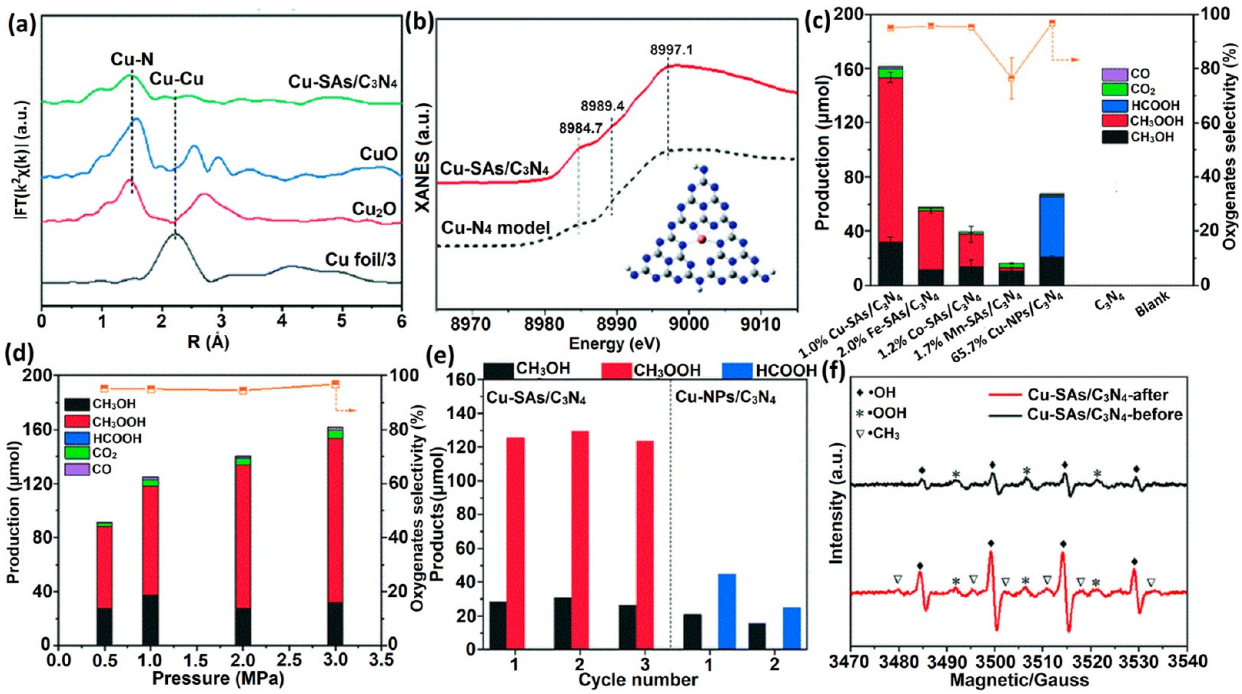

Figure 28. (a) FT of the Cu K-edge EXAFS spectra of Cu-SAs/C_3N_4, Cu foil, Cu_2O and CuO. (b) Cu K-edge XANES experimental spectra for Cu-SAs/C_3N_4 (red) and the calculated spectra for the proposed Cu−N_4 (black), Cu (orange-pink), N (blue), C (gray) and H (white). (c) Catalytic results over C_3N_4 and M/C_3N_4 catalysts at 3 MPa. (d) Effect of methane partial pressure on the Cu-SAs/C_3N_4 catalyst. (e) Recyclability tests over Cu-SAs/C_3N_4 and Cu-NPs/C_3N_4 catalysts. Reaction conditions: 5 h, 15 mL H_2O, 5 mL 40 wt % H_2O_2, 3 MPa and catalyst, 30 mg. (f) EPR experiments over Cu-SAs/C_3N_4 in the liquid phase. Reprinted with permission from ref 92. Copyright 2020 Royal Society of Chemistry.

species on Au_1/BP catalysts (Figure 27i). The surface adsorbed triplet $^3O_2$ after sequential electron and hole activation can form singlet $^1O_2$ which can react with H_2O to form OH* and HOO* and can be split into •OH radicals. The energy calculation of generation of CH_3OH by P−OH with CH_3* under dark conditions was calculated to be 2.18 eV, while under light this difference was just 1.15 eV suggesting the feasibility of reaction (Figure 27k). Further, theoretical results suggest the improved selectivity originated from the stabilization of CH_3* radicals by Au atom preventing further dehydrogenation by generating •OH radicals. Additionally, the energy barrier for methanol oxidation by P−OH and P═O species is 1.31 and 1.82 eV which is significantly higher than desorption energy, so, CH_3OH is preferably desorbed in water instead of further oxidation.

8.3. Carbon Nitride Supported SACs. Fabrication of SACs is often challenged by the aggregation of SAs on the supporting materials due to the large surface energies of single atomic metal sites. The stabilization of a SA on inorganic supports usually requires coordination sites present in the form of defects and vacancies, thus the concentration of SAs on inorganic supports is limited by the number of defects/vacancies.[414,415] The interaction of SAs with defects significantly influences the electronic structure and reactivity of the SACs.[416] For an effective interaction between a SA and support, the metal-oxide interaction should be stronger than the metal−metal interaction. Easily reducible metal−semiconductor oxides such as TiO_2, FeO_x, Cu_2O and CeO_2 are found to be suitable scaffolds for the fabrication of SACs.[305,324,417] Thermal/thermochemical treatment is the most common approach for enriching a crystal surface with defects/vacancies. For example, Cai et al. synthesized Pt SA on oxygen vacancy-rich TiO_2 using titanic acid nanotubes displaying enhanced activity for photo/electrochemical H_2 generation.[418] Apart from vacancies/defects, the edge and step defects have also been reported to anchor SAs on oxides supports. Specific planes exposed surfaces such as {001} of TiO_2 have also been focused to improve the performance of SA cocatalysts. For example, Wei et al. reported Pt/TiO_2-001 catalysts prepared by deposition precipitation method display 1156 times higher activity for H_2 generation than pristine TiO_2-001.[419] Such approaches usually afford a diluted metal concentration and come at the cost of sacrificed surface properties. Compared to bulk 3D crystals 2D materials are interesting due to their high specific surface area to accommodate large numbers of SA species. Numerous 2D materials such as MXenes, WS_2, MoS_2, etc., have been developed recently; however, controlling the chemical nature of vacancies is a challenge.[420−424] Though controlling the coordination environment of SAs in N doped graphene/carbon-based M-N_4-C catalysts is relatively easy but requires high-temperature synthesis and certain fractions get agglomerated on the carbonaceous scaffold which trade-off selectivity.[425,426] In recent years, graphitic CN (g-C_3N_4) with excellent thermal, chemical and photophysical stability has emerged as a potential photo/catalytic material for various reactions.[427−429] Due to the presence of plenty of secondary nitrogen's C_2N: of heptazine units (C_6N_7) and uncondensed NH/NH_2 groups, CN can promote metal-free organic transformation such as epoxidation, oxidation, three-component coupling under alkali-free conditions. Distinct from graphenic structure, CN possesses periodic in-plane cavities formed by three heptazine units bridged together with tertiary nitrogens. These cavities can accommodate SA centers and

https://doi.org/10.1021/acsnano.2c02464
ACS Nano XXXX, XXX, XXX−XXX

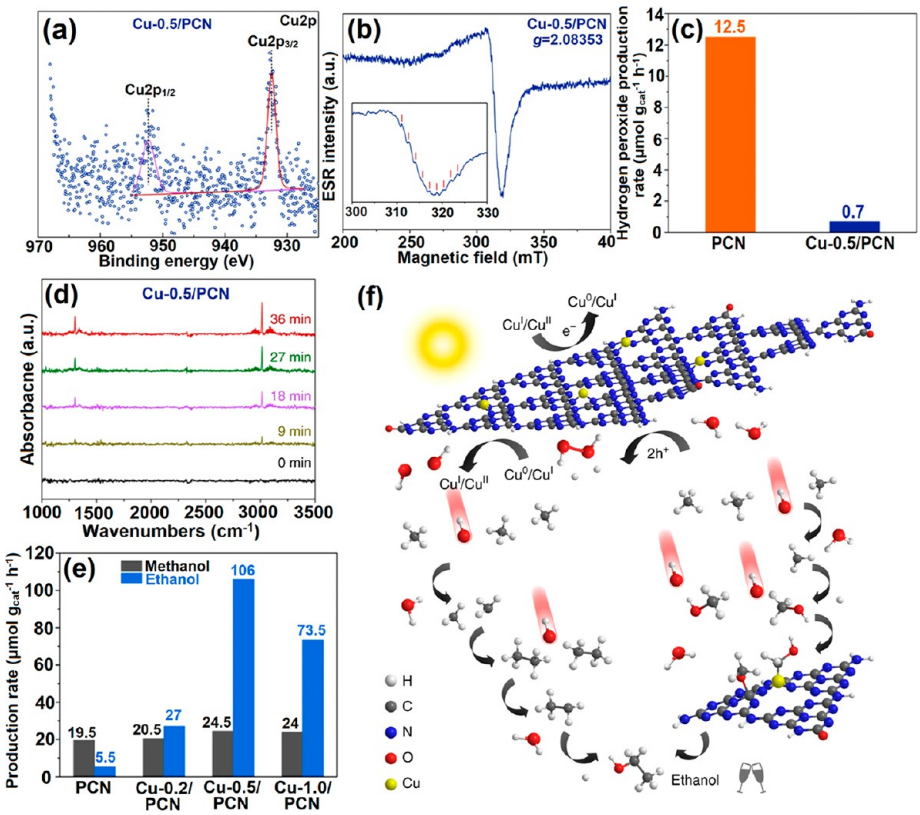

Figure 29. (a) Cu 2p XPS spectrum of Cu-0.5/PCN. (b) ESR spectrum of Cu-0.5/PCN (d) Photocatalytic anaerobic H_2O_2 production over PCN and Cu-0.5/PCN. (d) In situ IR spectra of methane adsorption on Cu-0.5/PCN. (e) Liquid products of methane conversion over PCN and Cu-X/PCN. (f) The hypothetic mechanism for photocatalytic anaerobic methane conversion over Cu-0.5/PCN. Reprinted with permission under a Creative Commons CC-BY License from ref 449. Copyright 2019 Springer Nature.

these atoms are stabilized via coordination with inner facing secondary nitrogens.[430,431] Due to the already available N coordination sites, the fabrication of SACs on CN support can be realized under mild conditions via deposition/in situ reduction approaches.[432,433] Assuming the periodic coordination of C_6N_7 units each vacancy is composed of one heptazine, thus, each C_6N_7 unit can accommodate one metal center reaching maximum possible occupancy. Though it is an idealized picture, as plenty of surfaces is not available in $\pi-\pi$ stacked sheets and uncondensed domains. The uncondensed domains are detrimental for photocatalytic processes as residual NH/NH_2 behaves as trap centers and also reduces the active area due to intersheets hydrogen bonding. Improving the surface area, crystallinity and tuning the cavity size of CN is an active area of research to improve the performance.[434] Numerous CN-based SACs have been reported for various applications such as photo/catalytic hydrogen evolution, CO_2 reduction, N_2 reduction reactions, CO oxidation, and biomass conversion.[435−438] Like copper-containing MMO enzyme, anchoring Cu atom in CN scaffold can promote efficient C−H activation of methane.[439,440] Wu et al. synthesized, copper SAs decorated CN catalysts Cu-SAs/C_3N_4 in the form of a Cu−N_4 moiety by using copper salts, melamine, and cyanuric acid complex (Cu−melamine−cyanuric complex) followed by thermal annealing at 550 °C for 4 h under Ar atmosphere.[92] The existence of isolated Cu SA entities was evident from AC-HAADF images and further supported by EXAFS demonstrating the absence of any Cu−Cu interaction (Figure 28a). EXAFS fitting for the first shell (Cu−N) suggests coordination number was 4. The Cu K-edge XANES spectrum demonstrates that the oxidation state of Cu was in between Cu_2O and CuO references ($Cu^{\delta+}$, $1 < \delta < 2$) suggesting partials charge transfer from Ns of CN to Cu^{2+}. Considering the Cu−N_4 coordination, the XANES spectrum obtained from the DFT model was coinciding with experimental results validating the Cu−N_4 structure (Figure 28b). When used as methane oxidation catalysts at room temperature in the presence of H_2O_2 oxidant, the Cu-SAs/C_3N_4 produce C1 oxygenates (CH_3OOH, CH_3OH and HCOOH) with a TOF of 6.7 h^{-1}, and the 95% C1 selectivity. Compared to other SACs such as Fe and Co, the Cu-SAs/C_3N_4 demonstrated the highest C1 products (153 μmol) after 5 h. Further, the activity of Cu-SAs/C_3N_4 was much higher compared to Cu nanoparticle decorated CN (CuNP@C_3N_4) (Figure 28c). Though, partial pressure does not have any influence on product selectivity, enhancing pressure increases product conversion (Figure 28d). The recycled catalysts displayed almost identical activity to the fresh one and no clustering/NP formation was observed after the reaction (Figure 28e). EPR spectra of the reaction mixture using 5,5-dimethyl-1-pyrroline-*N*-oxide (DMPO) spin-trap agent demonstrate the presence of •OH, •OOH and •CH_3 radical suggesting CH_3−H bond activation takes place by generated free radicals (Figure 28f).

Direct conversion of C_1 methane to C_2 products such as ethanol is an even more challenging reaction due to the involvement of C−H bond scissoring and C−C bond formations.[441,442] A handful of studies reported the direct conversion of methane to ethanol at low temperatures.[443,444] Wang et al. reported that cubic platinum (Pt) nanoparticles

https://doi.org/10.1021/acsnano.2c02464
ACS Nano XXXX, XXX, XXX−XXX

capped with $Cs_2[closo\text{-}B_{12}H_{12}]$ can directly convert CH_4 to C_2H_5OH with a very high selectivity ca. 97%. Under optimized conditions using H_2O_2 and O_2 as an oxidant, the yield of C_2H_5OH reached 148.41 mol kg_{cat}^{-1} h^{-1} at 50 °C.[445] Based on the presence of •CH_3 and •C_2H_5 radical's signal in EPR and DFT modeling, the authors concluded that •CH_3 radicals combined to generate C_2H_6 which was attacked by •OH radical to produce C_2H_5OH. In another study, Shen et al. used MMO-inspired biomimetic $CuFe_2O_4$-carbon nanotube catalyst to convert CH_4 to C_2H_5OH with 82% selectivity at 150 °C.[446] Electrocatalytic approach using Ni/NiO has also been applied to reach maximum Faradaic efficiency of 89% and ethanol yield of 25 μmol g_{NiO}^{-1} h^{-1} at 1.40 V vs RHE.[447] Some high-temperature reactions using Cu−Fe and Cu−Mn catalyst and CO_2 as a soft oxidant were also found to yield ethanol.[448] However, the mentioned processes either required temperature or electricity input and rely on expensive catalytic systems with low product yield. Photocatalytic conversion of CH_4 to oxygenates might be a solution; however, uncontrolled oxidation from generated •OH radicals leads to deep mineralization reducing the overall carbon efficiency. Photocatalytic generation of H_2O_2 followed by the production of •OH radicals in a Fenton-like process might be efficient, but only surface-bound species are mild enough to maintain selectivity. As previous studies on Cu-exchanged zeolites demonstrate that Cu sites prevent overoxidation of oxygenates, Cu-supported catalysts might enhance the product selectivity in photocatalysis. Zhou et al. demonstrated the synthesis of a pMMO type metalloenzyme catalyst by introducing Cu species into the cavity of polymeric CN (Figure 29).[449] The Cu-modified PCN can in situ produce H_2O_2 and •OH radical and generate C_2H_5OH as the main product with a yield of 106 μmol g_{cat}^{-1} h^{-1} under visible light. The Cu-X/PCN (where X is wt % of Cu) were prepared by thermal condensation of urea and $CuCl_2$. The optimized Cu-0.5/PCN sample does not show any sign of Cu nanoparticles in XRD and TEM substantiating the fine distribution of Cu species in PCN. The XPS spectra of Cu-0.5/PCN show two peak components assigned to Cu^I or Cu^0 species while Cu^{II} signals were obscured in the background (Figure 29a). ESR spectra of Cu-0.5/PCN displayed a Cu^{II} signature peak at g values 2.08 with nine hyperfine coupling peaks with equal spacing probably due to the partial delocalization of the unpaired electron spinning over two Cu centers (Figure 29b). These observations suggest a mixed-valence state of Cu in the catalysts. The band structure calculated from the Mott−Schottky measurement exhibit VB position for 0.5-Cu/PCN in between oxidation of H_2O to H_2O_2 and •OH substantiating the feasibility of two electrons mediated H_2O_2 production rather than direct •OH production. To validate that incorporation of Cu in PCN structure can facilitate in situ generations of H_2O_2 from water followed by localized generation of •OH radicals, the concentration of H_2O_2 was measured (Figure 29c). Using PCN as a photocatalyst, the H_2O_2 generation rate of 12.5 μmol g_{cat}^{-1} h^{-1} was achieved while 0.5Cu/PCN can afford only 0.7 μmol g_{cat}^{-1} h^{-1} production rate demonstrating H_2O_2 was degraded in the presence of Cu. The increased fluorescence intensity for 2-hydroxyterephthalic acid for 0.5Cu/PCN corroborates the generated H_2O_2 was in situ transformed to •OH radicals. Further, in situ FTIR on 0.5Cu/PCN after introducing methane exhibited two peaks centered at 3015 and 1304 cm^{-1} due to CH_4 adsorption (Figure 29d). Interestingly, the peak intensities were gradually increased for the 0.5Cu/PCN compared to PCN suggesting Cu benefits the adsorption of methane. Similarly, CH_4-TPD displayed a desorption peak around 250 °C while no desorption was observed in this range for PCN samples validating incorporation of Cu increase CH_4 adsorption on the catalyst's surface. The photocatalytic experiment demonstrates that 0.5Cu/PCN was highly active for the ethanol formation compared to pristine PCN and activity diminish as Cu content increased in 1.0Cu/PCN (Figure 29e). The XPS spectra of spent catalysts do not show any change suggesting photogenerated electrons can reduce the oxidized Cu species. The ethanol production was significantly dropped after the introduction of O_2 which was assumed due to the scavenging of electrons by O_2 to form superoxide radicals which also oxidize the generated product. Since the VB of Cu-0.5/PCN is not positive enough to oxidize H_2O into •OH, two-electron pathways of generation of H_2O_2 followed by decomposition to •OH radical was proposed. The oxidized Cu^{2+} species get reduced back to Cu^I by photogenerated electrons and maintain a mixed valence state. The •CH_3 radicals were generated by abstraction of a proton from CH_4 via •OH radicals. These methyl radicals can either react with another •OH radical to produce CH_3OH or might recombine to form ethane. The ethane is attacked by •OH radical to generate •C_2H_5 ethyl radicals which further react with water to form ethanol. However, as expected, this mechanism should lead to products with methanol as a dominating product. Control experiments using methanol reveal that more ethanol was produced using Cu-0.5/PCN if methane was not present in the system. The previous studies and current observations suggest a methane−methanol−ethanol pathway in which H abstraction from intermediate methanol by •OH generates *CH_2OH and *CH_3 groups. The coupling of *CH_2OH and *OCH_3 groups and methoxy groups on the adjacent C sites produce C_2H_5OH or ethyl radical which finally form ethanol by combining with •OH radical (Figure 29f).

$$CH_3OH + \bullet OH \rightarrow {}^*CH_2OH + H_2O$$

$$CH_3OH + \bullet OH \rightarrow {}^*OCH_3 + H_2O$$

$$^*CH_2OH + {}^*OCH_3 \rightarrow C_2H_5OH + {}^*O$$

$$^*CH_3 + {}^*OCH_3 \rightarrow \bullet CH_2CH_3 + {}^*OH$$

$$^*O + \bullet H + \bullet H \rightarrow H_2O$$

$$^*OH + \bullet H \rightarrow H_2O$$

As mentioned in previous sections, enzymatic systems are composed of mono and/or dimeric Cu/Fe species working synergistically to excel in the CH_4 oxidations. Like natural systems, two atomic sites working cooperatively can be decorated on an active support to amplify the catalytic performance. Compared to SACs which solely rely on the coordination environment of metal centers and metal−support interaction, DSACs can achieve cooperative interaction between two metal centers/support and also effectively stabilize reaction intermediate on two sites. Further, due to the presence of another metal in the first or second coordination shell, the local geometry and charge density can be modulated for the flexible adsorption configuration of reaction intermediates to optimize a specific reaction.[95,450] DSACs can be either homonuclear or heteronuclear and the

https://doi.org/10.1021/acsnano.2c02464
ACS Nano XXXX, XXX, XXX−XXX

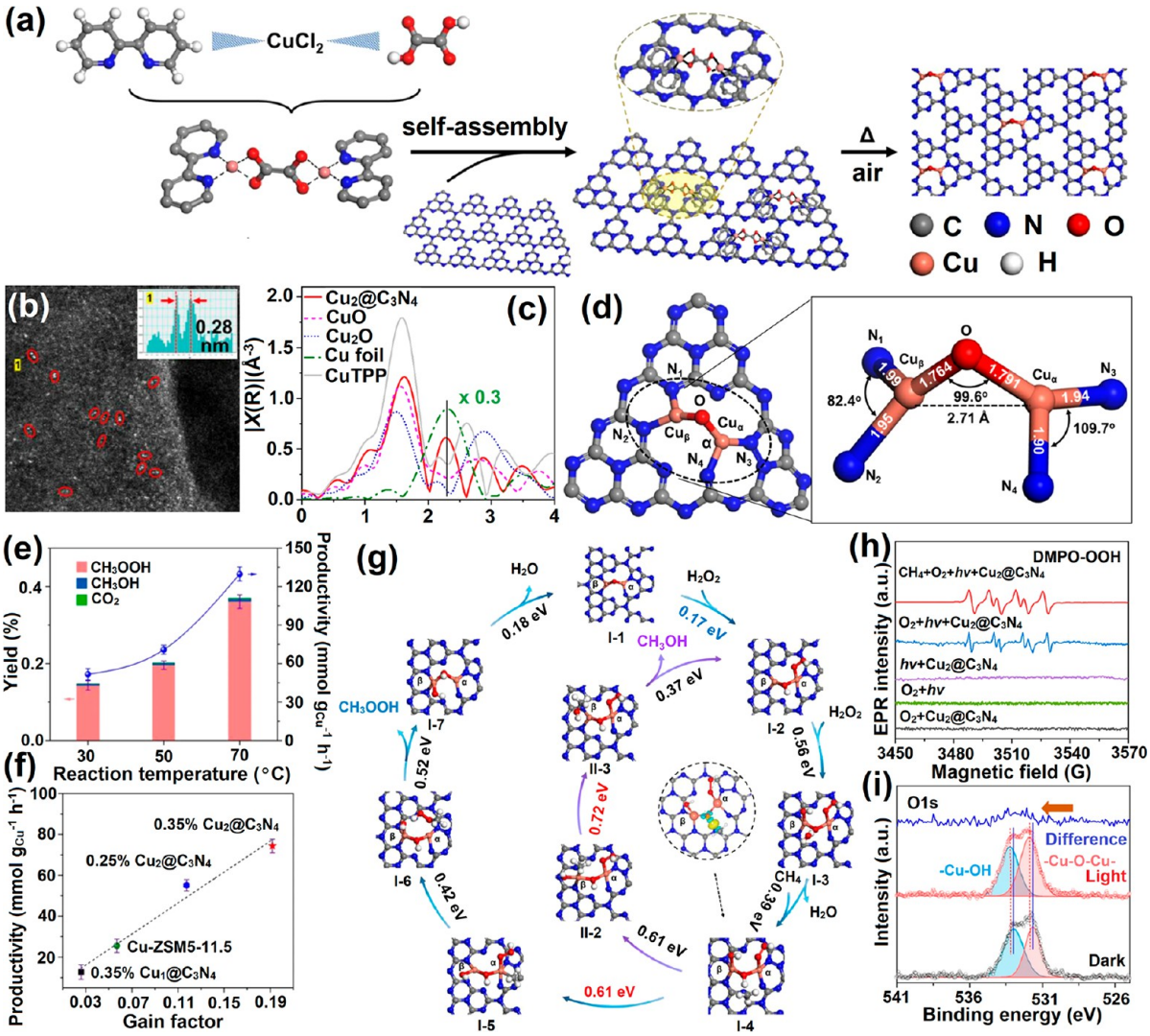

Figure 30. (a) Synthesis of the $Cu_2@C_3N_4$. (b) HAADF-STEM images of $Cu_2@C_3N_4$, insets showing line-scan intensity profiles of Cu dimers. (c) k^2-weighted EXAFS spectra at the Cu K-edge, with Cu foil, Cu_2O, CuO, and Cu-TPP. (d) The simulated structure model of dicopper-oxo center and geometric parameters of the dicopper-oxo center determined for $Cu_2@C_3N_4$. (e) Yields and productivity of methyl oxygenates at different reaction temperatures. (f) correlation between productivity of methyl oxygenates and gain factor for different catalysts. (g) Simulated pathways for the reaction between CH_4 with H_2O_2 on the $Cu_2@C_3N_4$ catalysts, with the middle inset illustrating the electron distribution of the CH_4 molecule being activated on the bridging oxygen site. (h) EPR spectra recorded for various control experiments using DMPO (i) In situ irradiation XPS spectra collected in the O 1s region. Reprinted with permission under a Creative Commons CC-BY License from ref 96. Copyright 2022 Springer Nature.

metal centers in DSACs can be either connected directly with M-M interaction or with a bridging nonmetal atom (as in pMMO). Although the nonmetal bridged DSACs have less intense M-M interaction, they ensure spatial distance to improve better intermediate stabilization. For example, Yang et al. demonstrated the synthesis of W_1Mo_1−NG DSACs in which W and Mo centers were connected via bridging O atoms and can achieve Pt-like activity/stability attributed to electron delocalization in W-O-Mo-O-C configuration.[451] Among the reported DSACs, M_1M_2-N_x-C are most common due to easy synthesis. However, their applications are mainly limited to electrocatalysis.[452−454] However, other options which can provide better catalytic/photocatalytic properties should be explored.

In recent years, g-C_3N_4 has emerged as an ideal supporting material due to its physicochemical properties, availability of numerous sites for coordination, precise control over coordination and the possibility of getting higher loading in C_6N_7 vacant sites. DSACs can be synthesized by using sequential coprecipitation/deposition, using precursors with two metal centers, MOFs and metal coordinated COF and controlling the support site to ensure the vicinity of two SAs. The most efficient strategy to synthesize DSACs is using a precursor which already has an M-M or M-O-M arrangement followed by the removal of ligand which leaves a naked pattern of molecule coordinating with supporting materials. For example, Tian et al. demonstrated the synthesis of Fe_2/mpg-C_3N_4 DSACs using bis(dicarbonylcyclopentadienyliron) ($Fe_2O_4C_{14}H_{10}$) followed by the removal of organic ligand.[455] The Fe_2/mpg-C_3N_4 demonstrate almost 90% conversion of stilbene to stilbene oxide while under identical conditions Fe_1/mpg-C_3N_4 was almost inactive.

In another example, Yang et al. demonstrated the synthesis of copper diatomic species on defected g-C_3N_4 ($Cu_2@C_3N_4$-

https://doi.org/10.1021/acsnano.2c02464
ACS Nano XXXX, XXX, XXX−XXX

Table 2. Experimentally Devised SACs Used for the CH_4OR to Oxygenates[a]

s. no.	catalysts	support	metal content	coordination/CN	oxidant	pressure/temperature	yield/TOR	selectivity	ref
1	Cu_1/ZSM-5	ZSM-5	0.34 wt %	$Cu_1-O_4/4$	0.5 M H_2O_2	30 bar/50 °C/70 °C	C_1 oxygenates- 4800 μmol g_{cat}^{-1} at 50 °C C_1 oxygenates-12000 μmol g_{cat}^{-1} at 70 °C within 30 min	C_1 oxygenates-99% at 50 °C CH_3OH-79% at 50 °C	222
2	Cu-CHA-T(0.5)	CHA zeolites	4.3 wt %	–	O_2 + CO	$CH_4/CO/O_2$-2.0/0.5/0.2 MPa/150 °C	CH_3OH-21 μmol g_{cat}^{-1} h^{-1}	CH_3OH-100%	217
3	monomeric Cu^{II} sites supported on alumina (1-a_{700})	Al_2O_3-Si/Al bridge	0.46 wt %	Cu−O/3 Cu−O−Si/Al/1.1	synthetic air	CH_4-6 bar/200 °C	CH_3OH-8.5 (μmol g^{-1}) 11.3 CH_3OH per Cu (%)	CH_3OH->80%	220
4	0.1% Fe/ZSM-5	ZSM-5	0.1%	Fe−O 6.0 ± 0.3 Fe−Fe 0.8 ± 0.4/mononuclear Fe^{3+}	0.5 M H_2O_2	30 bar/50 °C	CH_3OH-177 μmol CH_3OOH- 248 μmol $HOCH_2OOH$-191 μmol HCOOH- 431 μmol after 30 min CH_3OH-TOR-66 mol_{MeOH} mol_{Fe}^{-1} h^{-1}	C_1 oxygenates-97%	228
5	Fe/ZSM-5_{SSIE}	ZSM-5	~0.5 wt %	–	0.5 M H_2O_2	CH_4-30 bar/50 °C	CH_3OH-120 mol/mol_{Fe}	CH_3OH-96%	238
6	Cu−Fe(2/0.1)/ZSM-5 catalyst	ZSM-5	Cu-2% Fe-0.1%	Cu−O/4 Fe−O/2 (Fe−O−Al) Fe−O/4 (Fe−OH/H_2O) $[(HO)_2-Fe(III)-(H_2O)_2]^+$ coordinated with zeolite framework	0.5 M H_2O_2	30 bar/70 °C	CH_3OH- 215.6 mol/mol_{Fe} CH_3OOH-16.6 $HOCH_2OOH$-29.7 TOR-431 molMeOH mol^{-1} Fe h^{-1} TOR-431 h^{-1}	CH_3OH-80%	255
7	Pd_1O_4@ZSM-5 + 2 wt % CuO	ZSM-5	0.01 + 2 wt % CuO	$Pd_1O_4/4$	5 mM H_2O_2	30 bar/50, 70, 95 °C	C_1 products-66.64/151.41/127.55 μmol/28 mg_{cat} at 50/70/95 °C CH_3OH- 52.3/129.41/110.14 μmol/28 mg_{cat} at 50/70/95 °C HCOOH-4.00/0/0 μmol/28 mg_{cat} at 50/70/95 °C CH_3OOH-6.52/1.8/0.21 μmol/28 $mg_{cat.}$ at 50/70/95 °C after 30 min	CH_3OH-78.48/85.46/86.35% (50/70/95 °C)	269
8	Rh-ZSM-5	ZSM-5	0.5 wt %	Rh−O/3.6 ± 0.6	O_2	150 °C	CH_3COOH-22000 μmol $g^{-1}_{cat.}$ after 3 h CH_3OH- 230 μmol $g^{-1}_{cat.}$ after 3 h	CH_3COOH-92%	284
9	Rh/ZSM-5	ZSM-5	0.10 wt %	$Rh_1O_5/5$ Rh−O/5.23 ± 0.52 Rh−(O)−AI/1.55 ± 0.66 Rh−(O)−Si/1.68 ± 0.71	O_2	($CH_4/CO/O_2$ = 10/5/2) bar/150 °C	C_{1-2} oxygenates- 226.1 μmol/28 $mg_{cat.\,h}^{-1}$ CH_3OH-14.0 μmol/28 $mg_{cat.\,h}^{-1}$ HCOOH-153.4 μmol/28 $mg_{cat.\,h}^{-1}$ CH_3COOH-58.7 μmol/28 $mg_{cat.\,h}^{-1}$	CH_3COOH-~70%	285
10	0.2 wt % Rh-dB-ZSM-5	ZSM-5	0.2 wt %	–	O_2 + CO	$CH_4/CO/O_2$-0.3/0.1/0.05 MPa/150 °C	C_1 oxygenates-8513 μmol g_{cat}^{-1} CH_3COOH-13000 μmol g_{cat}^{-1}	–	457
11	$Ir_1Cu_1Pd_{0.1}$-ZSM-5	ZSM-5	total metal content-1.39 wt %	Ir−O/4.20 ± 0.6	O_2 + CO	$CH_4/CO/O_2$-20/5/4 bar 150 °C	CH_3OH ~ 1200 μmol g_{cat}^{-1} ~23.4 mol_{CH3OH}/mol_{Ir}	CH_3OH-80%	289
12	SAs Rh-CeO_2 NWs	CeO_2 NWs	0.29%	–	1 mol L^{-1} H_2O_2	0.5 MPa/50 °C	C_1 oxygenates-~1231.7 mmol g_{Rh}^{-1} h^{-1} CH_3OH-940.3 mmol g_{Rh}^{-1} h^{-1} CH_3OOH-291.4 mmol g_{Rh}^{-1} h^{-1}	C_1 oxygenates-93.9%	331
13	Rh/ZrO_2	ZrO_2	0.3 wt %	Rh−O/4.9	0.5 M H_2O_2	30 bar (95% CH_4 and 5% He)/70 °C	CH_3OH-1.07 μmol/μmol_{Rh} CH_3OOH-0.24 μmol/μmol_{Rh} CO_2-0.36 μmol/μmol_{Rh}	–	328
14	Rh_1/ZrO_2	ZrO_2	0.3 wt %	–	120 mM H_2O_2 + 2 bar O_2/90 °C	30 bar of 95/5% CH_4/He	C_1 oxygenates-21.7 mol mol_{Rh}^{-1}	–	341

https://doi.org/10.1021/acsnano.2c02464
ACS Nano XXXX, XXX, XXX−XXX

Table 2. continued

s. no.	catalysts	support	metal content	coordination/CN	oxidant	pressure/temperature	yield/TOR	selectivity	ref
15	Pt/CeO_2	CeO_2	1 wt %	–	CO	CH_4/CO 20/20 bar/300 °C	CH_3OH-6.27 mmol/g Pt	CH_3OH-95%	330
16	0.33 wt % FeO_x/TiO_2	TiO_2	0.33 metal wt %	Fe−O/6.2 ± 0.6 Fe−Fe/2.9 ± 0.2	8 μmol H_2O_2 in 10 mL of water	20% CH_4 in Ar/atmospheric pressure/photocatalytic	CH_3OH-1.056 μmol g_{cat}^{-1}	CH_3OH-90%	340
17	1.0 Rh/TiO_2	TiO_2	1.0 wt %	Rh−O/3.2 Rh−Rh/2.8	O_2 + CO	$CH_4/CO/O_2$-23/5/3 bar/150 °C	CH_3OH-5.2 mmol g_{cat}^{-1} -53 mol mol_{Rh}^{-1} after 1 h	CH_3OH-99%	343
18	Cr/TiO_2	TiO_2	1 wt %	–	0.5 mL H_2O_2 (30%), 9.5 mL DI water	3 MPa/50 °C	C_1 oxygenates-43.9 μmol/10 $mg_{cat.}$ CH_3OH-3.4/10 $mg_{cat.}$ CH_3OOH-17.5/10 $mg_{cat.}$ $HOCH_2OOH$-20.8/10 $mg_{cat.}$ HCOOH-2.2 μmol/10 $mg_{cat.}$ after 1 h	C_1 oxygenates-93%	344
19	Pd_x-def-In_2O_3	In_2O_3	0.1%	–	O_2	19/1 CH_4/O_2, photocatalytic	C_1 oxygenates-179.7 μmol/20 mg_{cat} after 3 h	C_1 oxygenates-80.4%	458
20	Co/SiO_2	SiO_2	0.1 wt %	–	O_2/H_2O	0.1 MPa ($CH_4/O_2/N_2/H_2O$ = 48/2/50/10)/400 °C	HCHO-6.07 μmol g^{-1} h^{-1} CH_3OH-0.76 μmol g^{-1} h^{-1}	C_1 products-100%	459
21	FeN_4/GN-2.7	N-doped graphene	2.7 wt %	Fe−N/4	5 mL H_2O, 5 mL H_2O_2 (30%)	2 MPa/25 °C	CH_3OH-5.60 μmol/50 $mg_{cat.}$ CH_3OOH-41.40 μmol/50 $mg_{cat.}$ $HOCH_2OOH$-31.46 μmol/50 $mg_{cat.}$ HCOOH-35.54 μmol/50 $mg_{cat.}$ after 10 h TOF-0.47 h^{-1} C_1 oxygenates-	C_1 oxygenates-94%	349
22	Au_1/BP	black phosphorus	0.2 wt %	Au−P/2	H_2O	33 bar (CH_4/O_2 = 10:1)/90 °C/photocatalysis	113.5 μmol g_{catal}^{-1}	CH_3OH->99%	413
23	Cu-SAs/C_3N_4	carbon nitride (C_3N_4)	1.0 wt %	Cu−N/4	5 mL 40 wt % H_2O_2	3 MPa/photocatalytic	C_1 oxygenates-153 μmol after 5 h TOF-11 h^{-1} C_1 oxygenates	C_1 oxygenates-95%	92
24	Cu-0.5/PCN	polymeric carbon nitride	0.5	–	water-in situ generated H_2O_2	CH_4/N_2-10/90 mL min^{-1}/photocatalytic	C_2H_5OH-106 μmol g_{cat}^{-1} h^{-1}	–	449
25	Cu_2@C_3N_4-D	defected C_3N_4	0.38 wt %	Cu−C/N-3.3 ± 0.4	0.5 M H_2O_2	95%CH_4/5%Ar/3 MPa/50 °C	STY-4878 μmol g_{cat}^{-1} h^{-1} CH_3OH-91 μmol g_{cat}^{-1} h^{-1} CH_3OOH-611 μmol g_{cat}^{-1} h^{-1} $OHCH_2OOH$-4176 μmol g_{cat}^{-1} h^{-1}	–	456
26	Cu_2@C_3N_4	C_3N_4	0.35 wt %	Cu−O/1.25 ± 0.20	0.2 mM H_2O_2	(i) 0.1 MP CH_4/photocatalytic	(i) C_1 oxygenates-51.6 mmol g_{Cu}^{-1} h^{-1} at 30 °C, −129.7 mmol g_{Cu}^{-1} h^{-1} at 50 °C after 30 min	C_1 oxygenates->98% selectivity	96
				Cu−N/1.84 ± 0.29 Cu−Cu/0.88 ± 0.15		(ii) P_{O_2} = 0.5 MP, P_{CH_4} = 1 MPa/photocatalytic	(ii) 1399.3 mmol g_{Cu}^{-1} h^{-1} (10.1% conversion) photocatalytic		

[a]Catalysts containing dimeric/oligomeric species on zeolites are not included.

https://doi.org/10.1021/acsnano.2c02464
ACS Nano XXXX, XXX, XXX−XXX

D) by a photodeposition process which can reach a space-time yield (STY) of 4878 μmol g_{cat}^{-1} h^{-1} and TOF of 83 h^{-1} for C1-oxygenates that was 300% higher than that of single atomic catalysts.[456] Interestingly, in contrast to the above-mentioned examples, two Cu were not connected directly and has a 2.5 Å spacing. XAS, XPS, and DFT analysis reveal that one Cu was bonded to three Ns in the heptazine framework cavity while another Cu occupied N vacancies and coordinates with two carbons and one nitrogen. Experimental mechanism investigation using EPR demonstrates the presence of •OH, •OOH and •CH_3 radicals indicating that H_2O_2 and CH_4 both are activated on the surface of $Cu_2@C_3N_4$-D. DFT calculation exhibits that CH_4OR on monatomic $Cu_1@C_3N_4$-D proceeds via the attack of H_2O_2 on Cu to form Cu−O adsorption of CH_4 on O atoms and finally C−H dissociation to CH_3OH, CH_3OOH, $OHCH_2OOH$. While in the case of $Cu_2@C_3N_4$-D, it can directly adsorb on the Cu site and dissociates into Cu-CH_3 and Cu−H (neighboring Cu) which finally reacts with H_2O_2/H_2O to form oxygenates.

In contrast to spaced dual Cu atom sites, Xie et al. reported the synthesis of oxo dicopper sites (Cu−O−Cu) in a C_3N_4 scaffold mimicking natural pMMO structure (Figure 30).[96] For the synthesis of $Cu_2@C_3N_4$ catalysts a "precursor-preselected" approach was used where $[Cu_2(bpy)_2(\mu\text{-ox})]Cl_2$ was immobilized on C_3N_4 followed by the removal of ligands at 250 °C in the air (Figure 30a). HAADF-STEM displayed dimeric copper moieties with 2.8 (±0.2 Å) spacing which was less than $[Cu_2(bpy)_2(\mu\text{-ox})]Cl_2$ precursor suggesting the reorganization of Cu centers on C_3N_4 after the removal of ligands (Figure 30b). The Cu K edge XANES spectrum of $Cu_2@C_3N_4$ substantiates an oxidation state between +1 to +2 and no spectral match with Cu_2O and CuO overruled the presence of Cu in a mixed-valence state. EXAFS validates that Cu was connected with a bridging O and the bond length was calculated to be 1.76 and 1.79 Å with a Cu−O−Cu angle of 99.6° (Figure 30c,d). Thermocatalytic oxidation of methane in the presence of 0.2 mM of H_2O_2 and 0.1 MPa of CH_4 yielded 0.14% oxygenates (dominantly CH_3OOH) within 30 min at 30 °C. When the temperature was raised to 70 °C the oxygenates yield was significantly improved reaching 0.37% (129.7 mmol g_{Cu}^{-1} h^{-1}) (Figure 30e). To evaluate the catalyst's stability, five recycling studies were performed which demonstrated no change in the product yield and the Cu−O−Cu structure remains intact. The comparative studies using monomeric $Cu_1@C_3N_4$ afforded only 0.03% oxygenates yield while Cu-ZSM5 (Si/Al-11.5, Cu/Al- 0.51) gave a relatively low oxygenate yield (25.5 mmol g_{Cu}^{-1} h^{-1}) compared to $Cu_2@C_3N_4$ (74.4 mmol g_{Cu}^{-1} h^{-1}) (Figure 30f) These observations suggest that specific coordination and collaborative effect of C_3N_4 must be responsible for the enhanced performance. DFT studies suggest that reaction initiates with the adsorption of H_2O_2 on Cu_α forming Cu-OOH and bridging O adsorbed H species (Figure 30g). The adsorption of a second H_2O_2 on the Cu_β site generates Cu−OH species while OH combines with bridging O ligated H to form water, freeing O sites. In the subsequent steps, CH_4 adsorb on bridging O and undergoes heterolytic cleavage to form O adsorbed H and $-CH_3$ group. The migration of the $-CH_3$ group on Cu_α or Cu_β sites followed by a combination with OOH and OH species generates CH_3OOH and CH_3OH. Interestingly, the calculated energy barrier for $*CH_3 + *OH \rightarrow *CH_3OH$ was 0.72 eV which was higher than $*CH_3 + *OOH \rightarrow *CH_3OOH$ (0.52 eV) thus favoring the formation of CH_3OOH which was also observed in experimental results.

Since the thermocatalytic process requires the use of external H_2O_2 as an oxidant, the potential of $Cu_2@C_3N_4$ for photocatalytic in situ CH_4 oxidation was also investigated. In the photocatalytic process, O_2 can generate •OH and •OOH ROS which can substitute the role of H_2O_2 in thermal reaction. Interestingly, using O_2 as an oxidant and light as an energy source, the CH_4 conversion rate reached almost 13.1% after 6 h. Again, CH_3OOH was a dominating product and total oxygenates selectivity was 98.9%. Under optimized conditions (P_{O2} = 0.5 MPa and P_{CH4} = 1 MPa) the methyl oxygenates productivity of 1399.3 mmol g_{Cu}^{-1} h^{-1} was obtained which is the highest reported activity for any catalytic system under benign conditions. The generation of ROS was further validated by EPR which shows signature peaks for •OOH radicals (Figure 30h). In situ XPS spectra for O 1s and Cu 2p under light conditions exhibited a blue shift compared to light while N 1s spectra were red-shifted suggesting C_3N_4 transfer hole to Cu/O sites where CH_4 is activated, and the generated electrons reduced the O_2 to H_2O_2 (Figure 30i). The in situ generated H_2O_2 on C_3N_4 migrates to Cu oxo centers forming *OOH or *OH species to form CH_3OH and CH_3OOH.

Compared to thermocatalytic processes, photocatalytic processes can provide better catalytic selectivity due to generation of mild oxidative species. Bulk 3D photocatalysts with a wide bandgap are less selective because they generate energetic •OH radicals directly from water oxidation leading to random oxidation. 2D materials have been proven more appealing due to their photophysical properties and high surface area. Further, in situ generations of mild ROS which react with CH_4 and restricts deep mineralization thus enhancing the selectivity. Au supported on black P with almost complete visible absorption has demonstrated the highest CH_3OH selectivity as it generates mild •OH radical from triplet O_2 and water via P−OH intermediate. The possibility of generation of higher alcohols in Cu SA integrated C_3N_4 illustrates the feasibility of the photocatalytic process to directly utilize CH_4 for chemical productions. Multicentered dicopper oxo DSACs due to cooperative catalysis, better stabilization of reaction intermediates and tuning of coordination environment have emerged as a forefront candidate for CH_4OR. Indeed, to the present date, $Cu_2@C_3N_4$ catalysts have demonstrated the highest recorded CH_4 conversion rate. Table 2 summarizes the catalytic performance of various SACs used for the CH_4OR.

9. CONCLUSIONS AND FUTURE PERSPECTIVES

The catalytic conversion of earth warming methane to transportable liquid oxygenates can solve the issues of depleting energy and staggering global temperature. The fundamental challenge associated with CH_4OR is cleaving the first C−H bond which requires a significant amount of energy due to low electron affinity and the absence of dipole interaction in CH_4. Transition-metal-based nanoparticulate and homogeneous catalysts have demonstrated activity toward C−H bond activation. However, the cleavage of the first C−H bond leads to the formation of intermediate species which are prone to deep oxidation and spontaneously oxidize to CO_2. The antagonistic requirement of controlling the overoxidation to selectively form the methanol while sustaining the cogent reaction rate necessitates the search for efficient and selective catalysts. Methanotrophs using sMMO/pMMO metallozymes

https://doi.org/10.1021/acsnano.2c02464
ACS Nano XXXX, XXX, XXX−XXX

with bimetallic Cu/Fe μ-oxo centers and P450 with Fe containing heme centers can activate C−H via the formation of hypervalent metallic species (intermediate Q). Isolated SA species coordinated on active supporting materials mimic metallozymes to promote CH_4OR. The afforded activity arises due formation of hypervalent M(IV)═O species which can polarize the C−H bond and transfer the O atom. Further, generated methyl and methyl hydroxyl radicals are stabilized due to synergistic binding with SA sites and support followed by transfer of radical to support site. Fe-based mono and dimeric species in conjugation with Cu species as a methyl radical stabilizer on ordered ZSM-5 have displayed encouraging results to achieve selective oxidations of CH_4 at ambient temperature. Unfortunately, the reaction rate of Fe/Cu-based SACs remains far from the practicability, and further improvement is needed in the future. Noble metals including Rh, Pd and Ru-based SACs tagged on diverse supports including CeO_2, ZrO_2, and aluminosilicates boost confidence due to elevated reaction rate and stability. SACs confined on 2D supports such as graphene (M-N_4), transition-metal dichalcogenides, MXenes, metal oxides, etc., due to populated metal concentration, high specific surface area, and specific metal-2D support interaction are emerging frontier that will translate CH_4 to oxygenates. Despite the potential of SACs to exponentiate CH_4OR, unlike natural metallozymes, most of the SACs still required strong H_2O_2 oxidant and mild temperature. A handful of noble metal SACs can generate in situ H_2O_2 in perilous pressurized H_2 and O_2 conditions. For a sustainable deployment of CH_4 oxidation technology, the O_2 should be utilized as an oxidant, which is challenging due to the requirement of triplet to a singlet state transition and subsequent transfer to methane via C−H cleavage. Photocatalysis offers facile generation of singlet O_2 and •OH radicals which prevent uncontrolled oxidation to improve the selectivity. The primitive challenges are improving visible light absorption and nonannihilating charge separation. Newly discovered low bandgap elemental/mixed stoichiometric and C−N constituted 2D semiconductors are overcoming these impediments. Indeed, the highest selectivity for CH_4OR was reported by Au decorated BP SACs which can be further increased by doping/surface modification and decoration of multiple atomic sites. Pursuing CH_4OR with methyl radical coupling and carbonylation/carboxylation will be interesting to afford C_{2+} oxygenates omitting multistep synthesis. The Cu containing C_3N_4 has displayed direct upconversion of CH_4 to C_2H_5OH at room temperature and visible light irradiation that strengthens optimizm in the feasibility of the technology. Undoubtedly, initial success on SAC-mediated CH_4OR is stimulating; however, the sluggish reaction rate, low metal loading, the requirement of pressurized gas, use of expensive H_2O_2 oxidants, and limited recyclability should be overcome in near future. The viable solution will be screening appropriate SACs with optimized metal−support interaction by employing DFT (followed by actual performance evaluation) which can facilitate CH_4 adsorption, activation by molecular oxygen, stabilization of intermediates, and facile desorption of the intermediates. As per our observation, SACs/DSACs supported on photoactive 2D materials (BP and C_3N_4) have proven most successful candidates due to higher quantum efficiency and better control of ROS species to prevent deep mineralization. Despite DSACs with cooperatively associated metal centers have demonstrated record activity for CH_4OR in benign conditions, regulating the product distribution toward desirable CH_3OH is indispensably required. Furthermore, controlling the spatial distribution, coordination environment of SAs, and coupling two/or more metallic species for synergistic catalysis will be key steps to garnering the economic treasure from planet warming CH_4 gas.

AUTHOR INFORMATION

Corresponding Authors

Pawan Kumar − *Department of Chemical and Petroleum Engineering, University of Calgary, Calgary, Alberta T2N 1N4, Canada;* orcid.org/0000-0003-2804-9298; Email: pawan.kumar@ucalgary.ca

Md. Golam Kibria − *Department of Chemical and Petroleum Engineering, University of Calgary, Calgary, Alberta T2N 1N4, Canada;* orcid.org/0000-0003-3105-5576; Email: md.kibria@ucalgary.ca

Authors

Tareq A. Al-Attas − *Department of Chemical and Petroleum Engineering, University of Calgary, Calgary, Alberta T2N 1N4, Canada;* orcid.org/0000-0003-4305-735X

Jinguang Hu − *Department of Chemical and Petroleum Engineering, University of Calgary, Calgary, Alberta T2N 1N4, Canada;* orcid.org/0000-0001-8033-7102

Complete contact information is available at: https://pubs.acs.org/10.1021/acsnano.2c02464

Notes

The authors declare no competing financial interest.

ACKNOWLEDGMENTS

The authors would like to thank the Department of Chemical and Petroleum Engineering Schulich School of Engineering and the University of Calgary CFREF fund for financial assistance.

REFERENCES

(1) Fletcher, S. E. M.; Schaefer, H. Rising Methane: A New Climate Challenge. *Science* **2019**, *364*, 932−933.

(2) Hammitt, J. K. The Future Costs of Methane Emissions. *Nature* **2021**, *592*, 514−515.

(3) Crill, P. M.; Thornton, B. F. Whither Methane in the IPCC Process? *Nat. Clim. Change* **2017**, *7*, 678−680.

(4) Herndon, E. M. Permafrost Slowly Exhales Methane. *Nat. Clim. Change* **2018**, *8*, 273−274.

(5) Wessells, S.; Stern, L.; Kirby, S. USGS Gas Hydrates Lab. *United States Geological Survey Multimedia Gallery Video*, 2012. https://www.usgs.gov/media/videos/usgs-gas-hydrates-lab (accessed 2022-03-07).

(6) *IPCC, 2021, AR6 Climate Change 2021: The Physical Science Basis*; Masson-Delmotte, V., Zhai, P., Pirani, A., Connors, S. L., Péan, C., Berger, S., Caud, N., Chen, Y., Goldfarb, L., Gomis, M. I., Huang, M., Leitzell, K., Lonnoy, E., Matthews, J. B. R., Maycock, T. K., Waterfield, T., Yelekçi, O., Yu, R., Zhou, B., Eds.; Cambridge University Press: Cambridge, 2021.

(7) McGrawth, M. *BBC News, COP26: US and EU Announce Global Pledge to Slash Methane*. https://www.bbc.com/news/world-59137828 (accessed 2022-03-07).

(8) Saunois, M.; Jackson, R.; Bousquet, P.; Poulter, B.; Canadell, J. The Growing Role of Methane in Anthropogenic Climate Change. *Environ. Res. Lett.* **2016**, *11*, 120207.

(9) The Economist. *Those Who Worry About CO_2 Should Worry About Methane, Too*. https://www.economist.com/science-and-technology/2021/04/03/those-who-worry-about-co2-should-worry-about-methane-too (accessed 2022-03-07).

(10) Franz, R.; Uslamin, E. A.; Pidko, E. A. Challenges for the Utilization of Methane as a Chemical Feedstock. *Mendeleev Commun.* **2021**, *31*, 584−592.
(11) Sher Shah, M. S. A.; Oh, C.; Park, H.; Hwang, Y. J.; Ma, M.; Park, J. H. Catalytic Oxidation of Methane to Oxygenated Products: Recent Advancements and Prospects for Electrocatalytic and Photocatalytic Conversion at Low Temperatures. *Adv. Sci.* **2020**, *7*, 2001946.
(12) Upham, D. C.; Agarwal, V.; Khechfe, A.; Snodgrass, Z. R.; Gordon, M. J.; Metiu, H.; McFarland, E. W. Catalytic Molten Metals for the Direct Conversion of Methane to Hydrogen and Separable Carbon. *Science* **2017**, *358*, 917−921.
(13) Palmer, C.; Upham, D. C.; Smart, S.; Gordon, M. J.; Metiu, H.; McFarland, E. W. Dry Reforming of Methane Catalysed by Molten Metal Alloys. *Nat. Catal.* **2020**, *3*, 83−89.
(14) Kang, D.; Rahimi, N.; Gordon, M. J.; Metiu, H.; McFarland, E. W. Catalytic Methane Pyrolysis in Molten $MnCl_2$-KCl. *Appl. Catal., B* **2019**, *254*, 659−666.
(15) Fan, Z.; Weng, W.; Zhou, J.; Gu, D.; Xiao, W. Catalytic Decomposition of Methane to Produce Hydrogen: A Review. *J. Energy Chem.* **2021**, *58*, 415−430.
(16) Wang, X.; Wei, K.; Yan, S.; Wu, Y.; Kang, J.; Feng, P.; Wang, S.; Zhou, F.; Ling, Y. Efficient and Stable Conversion of Oxygen-Bearing Low-Concentration Coal Mine Methane by the Electrochemical Catalysis of SOFC Anode: From Pollutant to Clean Energy. *Appl. Catal., B* **2020**, *268*, 118413.
(17) Kye, S.; Kim, H. J.; Go, D.; Yang, B. C.; Shin, J. W.; Lee, S.; An, J. Ultralow-Loading Ruthenium Catalysts by Plasma-Enhanced Atomic Layer Deposition for a Solid Oxide Fuel Cell. *ACS Catal.* **2021**, *11*, 3523−3529.
(18) Schwach, P.; Pan, X.; Bao, X. Direct Conversion of Methane to Value-Added Chemicals Over Heterogeneous Catalysts: Challenges and Prospects. *Chem. Rev.* **2017**, *117*, 8497−8520.
(19) Meng, X.; Cui, X.; Rajan, N. P.; Yu, L.; Deng, D.; Bao, X. Direct Methane Conversion Under Mild Condition by Thermo-, Electro-, or Photocatalysis. *Chem.* **2019**, *5*, 2296−2325.
(20) Prajapati, A.; Collins, B. A.; Goodpaster, J. D.; Singh, M. R. Fundamental Insight into Electrochemical Oxidation of Methane Towards Methanol on Transition Metal Oxides. *Proc. Natl. Acad. Sci. U. S. A.* **2021**, *118*, e2023233118.
(21) Mostaghimi, A. H. B.; Al-Attas, T. A.; Kibria, M. G.; Siahrostami, S. A Review on Electrocatalytic Oxidation of Methane to Oxygenates. *J. Mater. Chem. A* **2020**, *8*, 15575−15590.
(22) Jang, J.; Shen, K.; Morales-Guio, C. G. Electrochemical Direct Partial Oxidation of Methane to Methanol. *Joule* **2019**, *3*, 2589−2593.
(23) Arnarson, L.; Schmidt, P. S.; Pandey, M.; Bagger, A.; Thygesen, K. S.; Stephens, I. E.; Rossmeisl, J. Fundamental Limitation of Electrocatalytic Methane Conversion to Methanol. *Phys. Chem. Chem. Phys.* **2018**, *20*, 11152−11159.
(24) Zhao, G.; Drewery, M.; Mackie, J.; Oliver, T.; Kennedy, E. M.; Stockenhuber, M. The Catalyzed Conversion of Methane to Value-Added Products. *Energy Technol.* **2020**, *8*, 1900665.
(25) Hu, J.; Shekhawat, D. *Direct Natural Gas Conversion to Value-added Chemicals*; CRC Press: Boca Raton, FL, 2020.
(26) Gunsalus, N. J.; Koppaka, A.; Park, S. H.; Bischof, S. M.; Hashiguchi, B. G.; Periana, R. A. Homogeneous Functionalization of Methane. *Chem. Rev.* **2017**, *117*, 8521−8573.
(27) Liu, Z.; Huang, E.; Orozco, I.; Liao, W.; Palomino, R. M.; Rui, N.; Duchoň, T.; Nemšák, S.; Grinter, D. C.; Mahapatra, M.; et al. Water-Promoted Interfacial Pathways in Methane Oxidation to Methanol on a CeO_2-Cu_2O Catalyst. *Science* **2020**, *368*, 513−517.
(28) Hu, A.; Chang, L.; Zuo, Z. Recent Advancement in Homogeneous Functionalizations of Methane. *Chin. Sci. Bull.* **2019**, *64*, 1878−1886.
(29) Kulkarni, A. R.; Zhao, Z.-J.; Siahrostami, S.; Nørskov, J. K.; Studt, F. Cation-Exchanged Zeolites for the Selective Oxidation of Methane to Methanol. *Catal. Sci. Technol.* **2018**, *8*, 114−123.
(30) Zhang, Q.; Yu, J.; Corma, A. Applications of Zeolites to C1 Chemistry: Recent Advances, Challenges, and Opportunities. *Adv. Mater.* **2020**, *32*, 2002927.
(31) Barona, M.; Snurr, R. Q. Exploring the Tunability of Trimetallic MOF Nodes for Partial Oxidation of Methane to Methanol. *ACS Appl. Mater. Interfaces* **2020**, *12*, 28217−28231.
(32) Li, Y.; Yu, J. Emerging Applications of Zeolites in Catalysis, Separation and Host−Guest Assembly. *Nat. Rev. Mater.* **2021**, *6*, 1156−1174.
(33) Berkowitz, J.; Greene, J.; Cho, H.; Ruscić, B. The Ionization Potentials of CH_4 and CD_4. *J. Chem. Phys.* **1987**, *86*, 674−676.
(34) Komornicki, A.; Dixon, D. A. Accurate Proton Affinities: Ab Initio Proton Binding Energies for N_2, CO, CO_2, and CH_4. *J. Chem. Phys.* **1992**, *97*, 1087−1094.
(35) Paganini, M. C.; Chiesa, M.; Martino, P.; Giamello, E.; Garrone, E. EPR Study of the Surface Basicity of Calcium Oxide. 2: The Interaction with Alkanes. *J. Phys. Chem. B* **2003**, *107*, 2575−2580.
(36) Taifan, W.; Baltrusaitis, J. CH_4 Conversion to Value Added Products: Potential, Limitations and Extensions of a Single Step Heterogeneous Catalysis. *Appl. Catal., B* **2016**, *198*, 525−547.
(37) Hiberty, P. C.; Cooper, D. L. Valence Bond Calculations of the Degree of Covalency in a C-X Bond: Application to CH_4 and CH_3Li. *J. Mol. Struc. Theochem.* **1988**, *169*, 437−446.
(38) Hammond, C.; Conrad, S.; Hermans, I. Oxidative Methane Upgrading. *ChemSusChem* **2012**, *5*, 1668−1686.
(39) Chen, Y.; Mu, X.; Luo, X.; Shi, K.; Yang, G.; Wu, T. Catalytic Conversion of Methane at Low Temperatures: A critical review. *Energy Technol.* **2020**, *8*, 1900750.
(40) Qin, L.; Guo, M.; Liu, Y.; Cheng, Z.; Fan, J. A.; Fan, L.-S. Enhanced Methane Conversion in Chemical Looping Partial Oxidation Systems Using a Copper Doping Modification. *Appl. Catal., B* **2018**, *235*, 143−149.
(41) Yasuda, S.; Osuga, R.; Kunitake, Y.; Kato, K.; Fukuoka, A.; Kobayashi, H.; Gao, M.; Hasegawa, J.-y.; Manabe, R.; Shima, H.; et al. Zeolite-Supported Ultra-Small Nickel as Catalyst for Selective Oxidation of Methane to Syngas. *Commun. Chem.* **2020**, *3*, 129.
(42) Liu, J.-C.; Wang, Y.-G.; Li, J. Toward Rational Design of Oxide-Supported Single-Atom Catalysts: Atomic Dispersion of Gold on Ceria. *J. Am. Chem. Soc.* **2017**, *139*, 6190−6199.
(43) Zhang, Q.; Guan, J. Single-Atom Catalysts for Electrocatalytic Applications. *Adv. Funct. Mater.* **2020**, *30* (31), 2000768.
(44) Fu, Q.; Saltsburg, H.; Flytzani-Stephanopoulos, M. Active Nonmetallic Au and Pt Species on Ceria-Based Water-Gas Shift Catalysts. *Science* **2003**, *301*, 935−938.
(45) Mitchell, S.; Pérez-Ramírez, J. Single Atom Catalysis: A Decade of Stunning Progress and the Promise for A Bright Future. *Nat. Commun.* **2020**, *11*, 4302.
(46) Qiao, B.; Wang, A.; Yang, X.; Allard, L. F.; Jiang, Z.; Cui, Y.; Liu, J.; Li, J.; Zhang, T. Single-Atom Catalysis of CO Oxidation Using Pt_1/FeO_x. *Nat. Chem.* **2011**, *3*, 634−641.
(47) Law ton, T. J.; Rosenzweig, A. C. Methane-Oxidizing Enzymes: An Upstream Problem in Biological Gas-to-Liquids Conversion. *J. Am. Chem. Soc.* **2016**, *138*, 9327−9340.
(48) Chang, W.-H.; Lin, H.-H.; Tsai, I.; Huang, S.-H.; Chung, S.-C.; Tu, I.; Yu, S.-F.; Chan, S. Copper Centers in the Cryo-EM Structure of Particulate Methane Monooxygenase Reveal the Catalytic Machinery of Methane Oxidation. *J. Am. Chem. Soc.* **2021**, *143*, 9922−9932.
(49) Tinberg, C. E.; Lippard, S. J. Dioxygen Activation in Soluble Methane Monooxygenase. *Acc. Chem. Res.* **2011**, *44*, 280−288.
(50) Kass, D.; Corona, T.; Warm, K.; Braun-Cula, B.; Kuhlmann, U.; Bill, E.; Mebs, S.; Swart, M.; Dau, H.; Haumann, M.; et al. Stoichiometric Formation of An Oxoiron (IV) Complex by a Soluble Methane Monooxygenase Type Activation of O_2 at an Iron (II)-Cyclam Center. *J. Am. Chem. Soc.* **2020**, *142*, 5924−5928.
(51) Koo, C. W.; Rosenzweig, A. C. Biochemistry of Aerobic Biological Methane Oxidation. *Chem. Soc. Rev.* **2021**, *50*, 3424−3436.

https://doi.org/10.1021/acsnano.2c02464
ACS Nano XXXX, XXX, XXX−XXX

(52) Pfleger, B. F. Microbes Paired for Biological Gas-to-Liquids (Bio-GTL) Process. *Proc. Natl. Acad. Sci. U. S. A.* **2016**, *113*, 3717−3719.
(53) Wang, S.; An, Z.; Wang, Z.-W. Bioconversion of Methane to Chemicals and Fuels by Methane-Oxidizing Bacteria. In *Advances in Bioenergy*; Yebo Li, S. K. K., Ed.; Elsevier: London, UK, 2020; Vol. *5*, pp 169−247.
(54) Miyagawa, K.; Isobe, H.; Shoji, M.; Kawakami, T.; Yamanaka, S.; Yamaguchi, K. A Three States Model for Hydrogen Abstraction Reactions with the Cytochrome P450 Compound I is Revisited. Isolobal and Isospin Analogy Among Fe(IV)═O, O═O and O. *J. Photochem. Photobiol., A* **2021**, *405*, 112902.
(55) Zilly, F. E.; Acevedo, J. P.; Augustyniak, W.; Deege, A.; Häusig, U. W.; Reetz, M. T. Tuning a P450 Enzyme for Methane Oxidation. *Angew. Chem., Int. Ed.* **2011**, *50*, 2720−2724.
(56) Fasan, R. Tuning P450 Enzymes as Oxidation Catalysts. *ACS Catal.* **2012**, *2*, 647−666.
(57) Chen, M. M.; Coelho, P. S.; Arnold, F. H. Utilizing Terminal Oxidants to Achieve P450-Catalyzed Oxidation of Methane. *Adv. Synth. Catal.* **2012**, *354*, 964−968.
(58) Nam, W. High-Valent Iron (IV)−Oxo Complexes of Heme and Non-Heme Ligands in Oxygenation Reactions. *Acc. Chem. Res.* **2007**, *40*, 522−531.
(59) Que, L.; Tolman, W. B. Biologically Inspired Oxidation Catalysis. *Nature* **2008**, *455*, 333−340.
(60) Zhang, X.; Huang, Z.; Ferrandon, M.; Yang, D.; Robison, L.; Li, P.; Wang, T. C.; Delferro, M.; Farha, O. K. Catalytic Chemoselective Functionalization of Methane in a Metal−Organic Framework. *Nat. Catal.* **2018**, *1*, 356−362.
(61) Osadchii, D. Y.; Olivos-Suarez, A. I.; Szécsényi, Á.; Li, G.; Nasalevich, M. A.; Dugulan, I. A.; Crespo, P. S.; Hensen, E. J.; Veber, S. L.; Fedin, M. V.; et al. Isolated Fe Sites in Metal Organic Frameworks Catalyze the Direct Conversion of Methane to Methanol. *ACS Catal.* **2018**, *8*, 5542−5548.
(62) Simons, M. C.; Prinslow, S. D.; Babucci, M.; Hoffman, A. S.; Hong, J.; Vitillo, J. G.; Bare, S. R.; Gates, B. C.; Lu, C. C.; Gagliardi, L.; et al. Beyond Radical Rebound: Methane Oxidation to Methanol Catalyzed by Iron Species in Metal−Organic Framework Nodes. *J. Am. Chem. Soc.* **2021**, *143*, 12165−12174.
(63) Baek, J.; Rungtaweevoranit, B.; Pei, X.; Park, M.; Fakra, S. C.; Liu, Y.-S.; Matheu, R.; Alshmimri, S. A.; Alshehri, S.; Trickett, C. A.; et al. Bioinspired Metal−Organic Framework Catalysts for Selective Methane Oxidation to Methanol. *J. Am. Chem. Soc.* **2018**, *140*, 18208−18216.
(64) Jiao, L.; Yan, H.; Wu, Y.; Gu, W.; Zhu, C.; Du, D.; Lin, Y. When Nanozymes Meet Single-Atom Catalysis. *Angew. Chem.* **2020**, *132*, 2585−2596.
(65) Kaiser, S. K.; Chen, Z.; Faust Akl, D.; Mitchell, S.; Pérez-Ramírez, J. Single-Atom Catalysts Across the Periodic Table. *Chem. Rev.* **2020**, *120*, 11703−11809.
(66) Wang, A.; Li, J.; Zhang, T. Heterogeneous Single-Atom Catalysis. *Nat. Rev. Chem.* **2018**, *2*, 65−81.
(67) Qi, K.; Chhowalla, M.; Voiry, D. Single Atom is Not Alone: Metal−Support Interactions in Single-Atom Catalysis. *Mater. Today* **2020**, *40*, 173−192.
(68) He, X.; He, Q.; Deng, Y.; Peng, M.; Chen, H.; Zhang, Y.; Yao, S.; Zhang, M.; Xiao, D.; Ma, D.; et al. A Versatile Route to Fabricate Single Atom Catalysts with High Chemoselectivity and Regioselectivity in Hydrogenation. *Nat. Commun.* **2019**, *10*, 3663.
(69) Bakandritsos, A.; Kadam, R. G.; Kumar, P.; Zoppellaro, G.; Medved', M.; Tuček, J.; Montini, T.; Tomanec, O.; Andrýsková, P.; Drahoš, B.; et al. Mixed-Valence Single-Atom Catalyst Derived from Functionalized Graphene. *Adv. Mater.* **2019**, *31*, 1900323.
(70) Gawande, M. B.; Fornasiero, P.; Zbořil, R. Carbon-Based Single-Atom Catalysts for Advanced Applications. *ACS Catal.* **2020**, *10*, 2231−2259.
(71) Yan, H.; Su, C.; He, J.; Chen, W. Single-Atom Catalysts and Their Applications in Organic Chemistry. *J. Mater. Chem. A* **2018**, *6*, 8793−8814.
(72) Chen, Y.; Ji, S.; Chen, C.; Peng, Q.; Wang, D.; Li, Y. Single-Atom Catalysts: Synthetic Strategies and Electrochemical Applications. *Joule* **2018**, *2*, 1242−1264.
(73) Zhang, L.; Filot, I. A.; Su, Y.-Q.; Liu, J.-X.; Hensen, E. J. Understanding the Impact of Defects on Catalytic CO Oxidation of $LaFeO_3$-Supported Rh, Pd, and Pt Single-Atom Catalysts. *J. Phys. Chem. C* **2019**, *123*, 7290−7298.
(74) Singh, B.; Sharma, V.; Gaikwad, R. P.; Fornasiero, P.; Zboril, R.; Gawande, M. B. Single-Atom Catalysts: A Sustainable Pathway for the Advanced Catalytic Applications. *Small* **2021**, *17*, 2006473.
(75) Zhao, C.; Xiong, C.; Liu, X.; Qiao, M.; Li, Z.; Yuan, T.; Wang, J.; Qu, Y.; Wang, X.; Zhou, F.; et al. Unraveling the Enzyme-Like Activity of Heterogeneous Single Atom Catalyst. *Chem. Commun.* **2019**, *55*, 2285−2288.
(76) Zhang, H.; Lu, X. F.; Wu, Z.-P.; Lou, X. W. D. Emerging Multifunctional Single-Atom Catalysts/Nanozymes. *ACS Cent. Sci.* **2020**, *6*, 1288−1301.
(77) Huang, L.; Chen, J.; Gan, L.; Wang, J.; Dong, S. Single-Atom Nanozymes. *Sci. Adv.* **2019**, *5*, eaav5490.
(78) Yang, H.; Shi, R.; Shang, L.; Zhang, T. Recent Advancements of Porphyrin-Like Single-Atom Catalysts: Synthesis and Applications. *Small Structures* **2021**, *2*, 2100007.
(79) Huo, M.; Wang, L.; Wang, Y.; Chen, Y.; Shi, J. Nanocatalytic Tumor Therapy by Single-Atom Catalysts. *ACS Nano* **2019**, *13*, 2643−2653.
(80) Kim, M. S.; Lee, J.; Kim, H. S.; Cho, A.; Shim, K. H.; Le, T. N.; An, S. S. A.; Han, J. W.; Kim, M. I.; Lee, J. Heme Cofactor-Resembling Fe−N Single Site Embedded Graphene as Nanozymes to Selectively Detect H_2O_2 with High Sensitivity. *Adv. Funct. Mater.* **2020**, *30*, 1905410.
(81) Ji, S.; Jiang, B.; Hao, H.; Chen, Y.; Dong, J.; Mao, Y.; Zhang, Z.; Gao, R.; Chen, W.; Zhang, R.; et al. Matching the Kinetics of Natural Enzymes with a Single-Atom Iron Nanozyme. *Nat. Catal.* **2021**, *4*, 407−417.
(82) Ravi, M.; Sushkevich, V. L.; Knorpp, A. J.; Newton, M. A.; Palagin, D.; Pinar, A. B.; Ranocchiari, M.; van Bokhoven, J. A. Misconceptions and Challenges in Methane-to-Methanol over Transition-Metal-Exchanged Zeolites. *Nat. Catal.* **2019**, *2*, 485−494.
(83) Groothaert, M. H.; Smeets, P. J.; Sels, B. F.; Jacobs, P. A.; Schoonheydt, R. A. Selective Oxidation of Methane by the Bis (μ-Oxo) Dicopper Core Stabilized on ZSM-5 and Mordenite Zeolites. *J. Am. Chem. Soc.* **2005**, *127*, 1394−1395.
(84) Grundner, S.; Markovits, M. A.; Li, G.; Tromp, M.; Pidko, E. A.; Hensen, E. J.; Jentys, A.; Sanchez-Sanchez, M.; Lercher, J. A. Single-Site Trinuclear Copper Oxygen Clusters in Mordenite for Selective Conversion of Methane to Methanol. *Nat. Commun.* **2015**, *6*, 7546.
(85) Woertink, J. S.; Smeets, P. J.; Groothaert, M. H.; Vance, M. A.; Sels, B. F.; Schoonheydt, R. A.; Solomon, E. I. A $[Cu_2O]^{2+}$ Core in Cu-ZSM-5, the Active Site in the Oxidation of Methane to Methanol. *Proc. Natl. Acad. Sci. U. S. A.* **2009**, *106*, 18908−18913.
(86) Gusmão, R.; Vesely, M.; Sofer, Z. k. Recent Developments on the Single Atom Supported at 2D Materials Beyond Graphene as Catalysts. *ACS Catal.* **2020**, *10*, 9634−9648.
(87) Zheng, X.; Li, P.; Dou, S.; Sun, W.; Pan, H.; Wang, D.; Li, Y. Non-Carbon-Supported Single-Atom Site Catalysts for Electrocatalysis. *Energy Environ. Sci.* **2021**, *14*, 2809−2858.
(88) Alam, K. M.; Kumar, P.; Kar, P.; Thakur, U. K.; Zeng, S.; Cui, K.; Shankar, K. Enhanced Charge Separation in gC_3N_4−BiOI Heterostructures for Visible Light Driven Photoelectrochemical Water Splitting. *Nanoscale Adv.* **2019**, *1*, 1460−1471.
(89) Chen, C.; Ou, W.; Yam, K. M.; Xi, S.; Zhao, X.; Chen, S.; Li, J.; Lyu, P.; Ma, L.; Du, Y.; et al. Zero-Valent Palladium Single-Atoms Catalysts Confined in Black Phosphorus for Efficient Semi-Hydrogenation. *Adv. Mater.* **2021**, *33*, 2008471.
(90) Feng, J.; Gao, H.; Zheng, L.; Chen, Z.; Zeng, S.; Jiang, C.; Dong, H.; Liu, L.; Zhang, S.; Zhang, X. A Mn-N_3 Single-Atom Catalyst Embedded in Graphitic Carbon Nitride for Efficient CO_2 Electroreduction. *Nat. Commun.* **2020**, *11*, 4341.

https://doi.org/10.1021/acsnano.2c02464
ACS Nano XXXX, XXX, XXX−XXX

(91) Zhang, P.; Sun, D.; Cho, A.; Weon, S.; Lee, S.; Lee, J.; Han, J. W.; Kim, D.-P.; Choi, W. Modified Carbon Nitride Nanozyme as Bifunctional Glucose Oxidase-Peroxidase for Metal-Free Bioinspired Cascade Photocatalysis. *Nat. Commun.* **2019**, *10*, 940.
(92) Wu, B.; Yang, R.; Shi, L.; Lin, T.; Yu, X.; Huang, M.; Gong, K.; Sun, F.; Jiang, Z.; Li, S.; et al. Cu Single-Atoms Embedded in Porous Carbon Nitride for Selective Oxidation of Methane to Oxygenates. *Chem. Commun.* **2020**, *56*, 14677−14680.
(93) Li, R.; Wang, D. Superiority of Dual-Atom Catalysts in Electrocatalysis: One Step Further Than Single-Atom Catalysts. *Adv. Energy Mater.* **2022**, *12*, 2103564.
(94) Wu, Y.; Ye, C.; Yu, L.; Liu, Y.; Huang, J.; Bi, J.; Xue, L.; Sun, J.; Yang, J.; Zhang, W.; et al. Soft Template-Directed Interlayer Confinement Synthesis of a Fe-Co Dual Single-Atom Catalyst for Zn-Air Batteries. *Energy Storage Mater.* **2022**, *45*, 805−813.
(95) Fu, J.; Dong, J.; Si, R.; Sun, K.; Zhang, J.; Li, M.; Yu, N.; Zhang, B.; Humphrey, M. G.; Fu, Q.; et al. Synergistic Effects for Enhanced Catalysis in a Dual Single-Atom Catalyst. *ACS Catal.* **2021**, *11*, 1952−1961.
(96) Xie, P.; Ding, J.; Yao, Z.; Pu, T.; Zhang, P.; Huang, Z.; Wang, C.; Zhang, J.; Zecher-Freeman, N.; Zong, H.; et al. Oxo Dicopper Anchored on Carbon Nitride for Selective Oxidation of Methane. *Nat. Commun.* **2022**, *13*, 1375.
(97) Jiao, L.; Ye, W.; Kang, Y.; Zhang, Y.; Xu, W.; Wu, Y.; Gu, W.; Song, W.; Xiong, Y.; Zhu, C. Atomically Dispersed N-Coordinated Fe-Fe Dual-Sites with Enhanced Enzyme-Like Activities. *Nano Res.* **2022**, *15*, 959−964.
(98) Park, D.; Lee, J. Biological Conversion of Methane to Methanol. *Korean J. Chem. Eng.* **2013**, *30*, 977−987.
(99) Huang, S.-P.; Shiota, Y.; Yoshizawa, K. DFT Study of the Mechanism for Methane Hydroxylation by Soluble Methane Monooxygenase (sMMO): Effects of Oxidation State, Spin State, and Coordination Number. *Dalton Trans.* **2013**, *42*, 1011−1023.
(100) Da Silva, J. C.; Pennifold, R. C.; Harvey, J. N.; Rocha, W. R. A Radical Rebound Mechanism for the Methane Oxidation Reaction Promoted by the Dicopper Center of a pMMO Enzyme: A Computational Perspective. *Dalton Trans.* **2016**, *45*, 2492−2504.
(101) Liu, X.; Wang, D.; Li, Y. Synthesis and Catalytic Properties of Bimetallic Nanomaterials with Various Architectures. *Nano Today* **2012**, *7*, 448−466.
(102) Cuenya, B. R.; Baeck, S.-H.; Jaramillo, T. F.; McFarland, E. W. Size-and Support-Dependent Electronic and Catalytic Properties of Au^0/Au^{3+} Nanoparticles Synthesized from Block Copolymer Micelles. *J. Am. Chem. Soc.* **2003**, *125*, 12928−12934.
(103) Zhang, Q.-F.; Chen, X.; Wang, L.-S. Toward Solution Syntheses of the Tetrahedral Au_{20} Pyramid and Atomically Precise Gold Nanoclusters with Uncoordinated Sites. *Acc. Chem. Res.* **2018**, *51*, 2159−2168.
(104) Yang, X.-F.; Wang, A.; Qiao, B.; Li, J.; Liu, J.; Zhang, T. Single-Atom Catalysts: A New Frontier in Heterogeneous Catalysis. *Acc. Chem. Res.* **2013**, *46*, 1740−1748.
(105) Lang, R.; Du, X.; Huang, Y.; Jiang, X.; Zhang, Q.; Guo, Y.; Liu, K.; Qiao, B.; Wang, A.; Zhang, T. Single-Atom Catalysts Based on the Metal−Oxide Interaction. *Chem. Rev.* **2020**, *120*, 11986−12043.
(106) Ji, S.; Chen, Y.; Wang, X.; Zhang, Z.; Wang, D.; Li, Y. Chemical Synthesis of Single Atomic Site Catalysts. *Chem. Rev.* **2020**, *120*, 11900−11955.
(107) Xi, J.; Jung, H. S.; Xu, Y.; Xiao, F.; Bae, J. W.; Wang, S. Synthesis Strategies, Catalytic Applications, and Performance Regulation of Single-Atom Catalysts. *Adv. Funct. Mater.* **2021**, *31*, 2008318.
(108) Lai, W. H.; Miao, Z.; Wang, Y. X.; Wang, J. Z.; Chou, S. L. Atomic-Local Environments of Single-Atom Catalysts: Synthesis, Electronic Structure, and Activity. *Adv. Energy Mater.* **2019**, *9*, 1900722.
(109) Guo, W.; Wang, Z.; Wang, X.; Wu, Y. General Design Concept for Single-Atom Catalysts toward Heterogeneous Catalysis. *Adv. Mater.* **2021**, *33*, 2004287.
(110) Wang, L.; Huang, L.; Liang, F.; Liu, S.; Wang, Y.; Zhang, H. Preparation, Characterization and Catalytic Performance of Single-Atom Catalysts. *Chin. J. Catal.* **2017**, *38*, 1528−1539.
(111) Ye, C.; Zhang, N.; Wang, D.; Li, Y. Single Atomic Site Catalysts: Synthesis, Characterization, and Applications. *Chem. Commun.* **2020**, *56*, 7687−7697.
(112) Li, P.; Wang, M.; Duan, X.; Zheng, L.; Cheng, X.; Zhang, Y.; Kuang, Y.; Li, Y.; Ma, Q.; Feng, Z.; et al. Boosting Oxygen Evolution of Single-Atomic Ruthenium Through Electronic Coupling with Cobalt-Iron Layered Double Hydroxides. *Nat. Commun.* **2019**, *10*, 1711.
(113) Liu, X.; Mateen, M.; Cheng, X.; Wu, D.; Zhang, J.; Cheong, W. C.; Liu, S. Constructing Atomic Co_1-N_4 Sites in 2D Polymeric Carbon Nitride for Boosting Photocatalytic Hydrogen Harvesting Under Visible Light. *Int. J. Hydrog. Energy* **2022**, *47*, 12592−12604.
(114) Wang, Z.; Xu, S.-M.; Xu, Y.; Tan, L.; Wang, X.; Zhao, Y.; Duan, H.; Song, Y.-F. Single Ru Atoms with Precise Coordination on A Monolayer Layered Double Hydroxide for Efficient Electro-oxidation Catalysis. *Chemical Sci.* **2019**, *10*, 378−384.
(115) Cao, W.; Lin, L.; Qi, H.; He, Q.; Wu, Z.; Wang, A.; Luo, W.; Zhang, T. In-Situ Synthesis of Single-Atom Ir by Utilizing Metal-Organic Frameworks: An Acid-Resistant Catalyst for Hydrogenation of Levulinic Acid to γ-Valerolactone. *J. Catal.* **2019**, *373*, 161−172.
(116) Liu, Y.; Li, Z.; Yu, Q.; Chen, Y.; Chai, Z.; Zhao, G.; Liu, S.; Cheong, W.-C.; Pan, Y.; Zhang, Q.; et al. A General Strategy for Fabricating Isolated Single Metal Atomic Site Catalysts in Y Zeolite. *J. Am. Chem. Soc.* **2019**, *141*, 9305−9311.
(117) Wan, J.; Chen, W.; Jia, C.; Zheng, L.; Dong, J.; Zheng, X.; Wang, Y.; Yan, W.; Chen, C.; Peng, Q.; et al. Defect Effects on TiO_2 Nanosheets: Stabilizing Single Atomic Site Au and Promoting Catalytic Properties. *Adv. Mater.* **2018**, *30*, 1705369.
(118) Ding, S.; Guo, Y.; Hülsey, M. J.; Zhang, B.; Asakura, H.; Liu, L.; Han, Y.; Gao, M.; Hasegawa, J.-y.; Qiao, B.; et al. Electrostatic Stabilization of Single-Atom Catalysts by Ionic Liquids. *Chem.* **2019**, *5*, 3207−3219.
(119) Lang, R.; Xi, W.; Liu, J.-C.; Cui, Y.-T.; Li, T.; Lee, A. F.; Chen, F.; Chen, Y.; Li, L.; Li, L.; et al. Non Defect-Stabilized Thermally Stable Single-Atom Catalyst. *Nat. Commun.* **2019**, *10*, 234.
(120) Zhao, L.; Zhang, Y.; Huang, L.-B.; Liu, X.-Z.; Zhang, Q.-H.; He, C.; Wu, Z.-Y.; Zhang, L.-J.; Wu, J.; Yang, W.; et al. Cascade Anchoring Strategy for General Mass Production of High-Loading Single-Atomic Metal-Nitrogen Catalysts. *Nat. Commun.* **2019**, *10*, 1278.
(121) He, X.; He, Q.; Deng, Y.; Peng, M.; Chen, H.; Zhang, Y.; Yao, S.; Zhang, M.; Xiao, D.; Ma, D.; et al. A Versatile Route to Fabricate Single Atom Catalysts with High Chemoselectivity and Regioselectivity in Hydrogenation. *Nat. Commun.* **2019**, *10*, 3663.
(122) Wu, J.; Zhou, H.; Li, Q.; Chen, M.; Wan, J.; Zhang, N.; Xiong, L.; Li, S.; Xia, B. Y.; Feng, G.; et al. Densely Populated Isolated Single Co-N Site for Efficient Oxygen Electrocatalysis. *Adv. Energy Mater.* **2019**, *9*, 1900149.
(123) Xia, C.; Qiu, Y.; Xia, Y.; Zhu, P.; King, G.; Zhang, X.; Wu, Z.; Kim, J. Y. T.; Cullen, D. A.; Zheng, D.; et al. General Synthesis of Single-Atom Catalysts with High Metal Loading Using Graphene Quantum Dots. *Nat. Chem.* **2021**, *13*, 887−894.
(124) Fan, K.; Li, Z.; Song, Y.; Xie, W.; Shao, M.; Wei, M. Confinement Synthesis Based on Layered Double Hydroxides: A New Strategy to Construct Single-Atom-Containing Integrated Electrodes. *Adv. Funct. Mater.* **2021**, *31*, 2008064.
(125) Wang, X.; Chen, W.; Zhang, L.; Yao, T.; Liu, W.; Lin, Y.; Ju, H.; Dong, J.; Zheng, L.; Yan, W.; et al. Uncoordinated Amine Groups of Metal−Organic Frameworks to Anchor Single Ru Sites as Chemoselective Catalysts Toward the Hydrogenation of Quinoline. *J. Am. Chem. Soc.* **2017**, *139*, 9419−9422.
(126) Ha, Y.; Fei, B.; Yan, X.; Xu, H.; Chen, Z.; Shi, L.; Fu, M.; Xu, W.; Wu, R. Atomically Dispersed Co-Pyridinic N-C for Superior Oxygen Reduction Reaction. *Adv. Energy Mater.* **2020**, *10*, 2002592.

https://doi.org/10.1021/acsnano.2c02464
ACS Nano XXXX, XXX, XXX−XXX

(127) Peng, Y.; Cao, J.; Sha, Y.; Yang, W.; Li, L.; Liu, Z. Laser Solid-Phase Synthesis of Single-Atom Catalysts. *Light Sci. Appl.* **2021**, *10*, 168.
(128) Wei, H.; Huang, K.; Wang, D.; Zhang, R.; Ge, B.; Ma, J.; Wen, B.; Zhang, S.; Li, Q.; Lei, M.; et al. Iced Photochemical Reduction to Synthesize Atomically Dispersed Metals by Suppressing Nanocrystal Growth. *Nat. Commun.* **2017**, *8*, 1490.
(129) Yang, Z.; Chen, B.; Chen, W.; Qu, Y.; Zhou, F.; Zhao, C.; Xu, Q.; Zhang, Q.; Duan, X.; Wu, Y. Directly Transforming Copper (I) Oxide Bulk into Isolated Single-Atom Copper Sites Catalyst Through Gas-Transport Approach. *Nat. Commun.* **2019**, *10*, 3734.
(130) Zhao, C.; Wang, Y.; Li, Z.; Chen, W.; Xu, Q.; He, D.; Xi, D.; Zhang, Q.; Yuan, T.; Qu, Y.; et al. Solid-Diffusion Synthesis of Single-Atom Catalysts Directly from Bulk Metal for Efficient CO_2 Reduction. *Joule* **2019**, *3*, 584−594.
(131) Xi, D.; Li, J.; Low, J.; Mao, K.; Long, R.; Li, J.; Dai, Z.; Shao, T.; Zhong, Y.; Li, Y.; et al. Limiting the Uncoordinated N Species in M−N_x Single-Atom Catalysts toward Electrocatalytic CO_2 Reduction in Broad Voltage Range. *Adv. Mater.* **2021**, 2104090.
(132) Ren, M.; Zhang, X.; Liu, Y.; Yang, G.; Qin, L.; Meng, J.; Guo, Y.; Yang, Y. Interlayer Palladium-Single-Atom-Coordinated Cyano-Group-Rich Graphitic Carbon Nitride for Enhanced Photocatalytic Hydrogen Production Performance. *ACS Catal.* **2022**, *12*, 5077−5093.
(133) Tan, H.; Gu, X.; Kong, P.; Lian, Z.; Li, B.; Zheng, Z. Cyano Group Modified Carbon Nitride with Enhanced Photoactivity for Selective Oxidation of Benzylamine. *Appl. Catal., B* **2019**, *242*, 67−75.
(134) Bakandritsos, A.; Kadam, R. G.; Kumar, P.; Zoppellaro, G.; Medveď, M.; Tuček, J.; Montini, T.; Tomanec, O.; Andrýsková, P.; Drahoš, B.; et al. Mixed-Valence Single-Atom Catalyst Derived from Functionalized Graphene. *Adv. Mater.* **2019**, *31*, 1900323.
(135) Zhang, L.; Banis, M. N.; Sun, X. Single-Atom Catalysts by the Atomic Layer Deposition Technique. *Natl. Sci. Rev.* **2018**, *5*, 628−630.
(136) Zhang, L.; Si, R.; Liu, H.; Chen, N.; Wang, Q.; Adair, K.; Wang, Z.; Chen, J.; Song, Z.; Li, J.; et al. Atomic Layer Deposited Pt-Ru Dual-Metal Dimers and Identifying Their Active Sites for Hydrogen Evolution Reaction. *Nat. Commun.* **2019**, *10*, 4936.
(137) Muravev, V.; Spezzati, G.; Su, Y.-Q.; Parastaev, A.; Chiang, F.-K.; Longo, A.; Escudero, C.; Kosinov, N.; Hensen, E. J. Interface Dynamics of Pd−CeO_2 Single-Atom Catalysts During CO Oxidation. *Nat. Catal.* **2021**, *4*, 469−478.
(138) Bi, W.; Hu, Y.; Jiang, H.; Yu, H.; Li, W.; Li, C. In-Situ Synthesized Surface N-Doped Pt/TiO_2 via Flame Spray Pyrolysis with Enhanced Thermal Stability for CO Catalytic Oxidation. *Appl. Surf. Sci.* **2019**, *481*, 360−368.
(139) Fei, H.; Dong, J.; Chen, D.; Hu, T.; Duan, X.; Shakir, I.; Huang, Y.; Duan, X. Single Atom Electrocatalysts Supported on Graphene or Graphene-Like Carbons. *Chem. Soc. Rev.* **2019**, *48*, 5207−5241.
(140) Deng, D.; Chen, X.; Yu, L.; Wu, X.; Liu, Q.; Liu, Y.; Yang, H.; Tian, H.; Hu, Y.; Du, P.; et al. A Single Iron Site Confined in a Graphene Matrix for the Catalytic Oxidation of Benzene at Room Temperature. *Sci. Adv.* **2015**, *1*, e1500462.
(141) Bi, Q.; Yuan, X.; Lu, Y.; Wang, D.; Huang, J.; Si, R.; Sui, M.; Huang, F. One-Step High-Temperature-Synthesized Single-Atom Platinum Catalyst for Efficient Selective Hydrogenation. *Research* **2020**, *2020*, 9140841.
(142) Zhang, T.; Walsh, A. G.; Yu, J.; Zhang, P. Single-Atom Alloy Catalysts: Structural Analysis, Electronic Properties and Catalytic Activities. *Chem. Soc. Rev.* **2021**, *50*, 569−588.
(143) Hannagan, R. T.; Giannakakis, G.; Flytzani-Stephanopoulos, M.; Sykes, E. C. H. Single-Atom Alloy Catalysis. *Chem. Rev.* **2020**, *120*, 12044−12088.
(144) Xia, X.; Wang, Y.; Ruditskiy, A.; Xia, Y. 25th Anniversary Article: Galvanic Replacement: A Simple and Versatile Route to Hollow Nanostructures with Tunable and Well-Controlled Properties. *Adv. Mater.* **2013**, *25*, 6313−6333.
(145) Zhang, X.; Cui, G.; Feng, H.; Chen, L.; Wang, H.; Wang, B.; Zhang, X.; Zheng, L.; Hong, S.; Wei, M. Platinum−Copper Single Atom Alloy Catalysts with High Performance Towards Glycerol Hydrogenolysis. *Nature Commun.* **2019**, *10*, 5812.
(146) Liu, J.-C.; Xiao, H.; Li, J. Constructing High-Loading Single-Atom/Cluster Catalysts via an Electrochemical Potential Window Strategy. *J. Am. Chem. Soc.* **2020**, *142*, 3375−3383.
(147) Zhang, Z.; Feng, C.; Liu, C.; Zuo, M.; Qin, L.; Yan, X.; Xing, Y.; Li, H.; Si, R.; Zhou, S.; et al. Electrochemical Deposition as a Universal Route for Fabricating Single-Atom Catalysts. *Nat. Commun.* **2020**, *11*, 1215.
(148) Patterson, W.; Rooney, J. Single Atom Sites and Hydrocarbon Reaction Mechanisms. *Catal. Today* **1992**, *12*, 113−129.
(149) Zhang, L.; Doyle-Davis, K.; Sun, X. Characterization of Supported Metal Single-Atom Catalysts. *Supported Metal Single Atom Catalysis*; Serp, P., Minh, D. P., Eds.; Wiley-VCH GmbH: Weinheim, Germany, 2022; pp 169−198.
(150) Liu, L.; Zhao, Y.; Wang, Y.; Zhang, Z.; Liu, J.; Wu, T.; Qin, W.; Liu, S.; Jia, B.; Wu, H.; et al. Single-Atom Co Doped in Ultrathin WO_3 Arrays for the Enhanced Hydrogen Evolution Reaction in a Wide pH Range. *ACS Appl. Mater. Interfaces* **2021**, *13*, 53915−53924.
(151) Ying, Y.; Luo, X.; Qiao, J.; Huang, H. More is Different:" Synergistic Effect and Structural Engineering in Double-Atom Catalysts. *Adv. Funct. Mater.* **2021**, *31*, 2007423.
(152) Chung, H. T.; Cullen, D. A.; Higgins, D.; Sneed, B. T.; Holby, E. F.; More, K. L.; Zelenay, P. Direct Atomic-Level Insight into the Active Sites of a High-Performance PGM-Free ORR Catalyst. *Science* **2017**, *357*, 479−484.
(153) Zhang, L. S.; Jiang, X. H.; Zhong, Z. A.; Tian, L.; Sun, Q.; Cui, Y. T.; Lu, X.; Zou, J. P.; Luo, S. L. Carbon Nitride Supported High-Loading Fe Single-Atom Catalyst for Activation of Peroxymonosulfate to Generate $^1O_2$ with 100% Selectivity. *Angew. Chem., Int. Ed.* **2021**, *60*, 21751−21755.
(154) Zhang, L.; Jia, Y.; Gao, G.; Yan, X.; Chen, N.; Chen, J.; Soo, M. T.; Wood, B.; Yang, D.; Du, A.; et al. Graphene Defects Trap Atomic Ni Species for Hydrogen and Oxygen Evolution Reactions. *Chem.* **2018**, *4*, 285−297.
(155) Liu, G.; Robertson, A. W.; Li, M. M.-J.; Kuo, W. C.; Darby, M. T.; Muhieddine, M. H.; Lin, Y.-C.; Suenaga, K.; Stamatakis, M.; Warner, J. H.; et al. MoS_2 Monolayer Catalyst Doped with Isolated Co Atoms for the Hydrodeoxygenation Reaction. *Nat. Chem.* **2017**, *9*, 810−816.
(156) Therrien, A. J.; Hensley, A. J.; Marcinkowski, M. D.; Zhang, R.; Lucci, F. R.; Coughlin, B.; Schilling, A. C.; McEwen, J.-S.; Sykes, E. C. H. An Atomic-Scale View of Single-Site Pt Catalysis for Low-Temperature CO Oxidation. *Nat. Catal.* **2018**, *1*, 192−198.
(157) Marcinkowski, M. D.; Darby, M. T.; Liu, J.; Wimble, J. M.; Lucci, F. R.; Lee, S.; Michaelides, A.; Flytzani-Stephanopoulos, M.; Stamatakis, M.; Sykes, E. C. H. Pt/Cu Single-Atom Alloys as Coke-Resistant Catalysts for Efficient C−H Activation. *Nat. Chem.* **2018**, *10*, 325.
(158) Deng, D.; Chen, X.; Yu, L.; Wu, X.; Liu, Q.; Liu, Y.; Yang, H.; Tian, H.; Hu, Y.; Du, P.; et al. A Single Iron Site Confined in a Graphene Matrix for the Catalytic Oxidation of Benzene at Room Temperature. *Sci. Adv.* **2015**, *1*, e1500462.
(159) Kottwitz, M.; Li, Y.; Wang, H.; Frenkel, A. I.; Nuzzo, R. G. Single Atom Catalysts: A Review of Characterization Methods. *Chemistry-Methods* **2021**, *1*, 278−294.
(160) Zhao, Y.; Yang, K. R.; Wang, Z.; Yan, X.; Cao, S.; Ye, Y.; Dong, Q.; Zhang, X.; Thorne, J. E.; Jin, L.; et al. Stable Iridium Dinuclear Heterogeneous Catalysts Supported on Metal-Oxide Substrate for Solar Water Oxidation. *Proc. Natl. Acad. Sci. U. S. A.* **2018**, *115*, 2902−2907.
(161) Yang, T.; Mao, X.; Zhang, Y.; Wu, X.; Wang, L.; Chu, M.; Pao, C.-W.; Yang, S.; Xu, Y.; Huang, X. Coordination Tailoring of Cu Single Sites on C_3N_4 Realizes Selective CO_2 Hydrogenation at Low Temperature. *Nat. Commun.* **2021**, *12*, 6022.
(162) Qiao, S.; He, Q.; Zhang, P.; Zhou, Y.; Chen, S.; Song, L.; Wei, S. Synchrotron-Radiation Spectroscopic Identification Towards

https://doi.org/10.1021/acsnano.2c02464
ACS Nano XXXX, XXX, XXX−XXX

Diverse Local Environments of Single-Atom Catalysts. *J. Mater. Chem. A* **2022**, *10*, 5771−5791.
(163) Shah, K.; Dai, R.; Mateen, M.; Hassan, Z.; Zhuang, Z.; Liu, C.; Israr, M.; Cheong, W. C.; Hu, B.; Tu, R.; et al. Cobalt Single Atom Incorporated in Ruthenium Oxide Sphere: A Robust Bifunctional Electrocatalyst for HER and OER. *Angew. Chem.* **2022**, *134*, e202114951.
(164) Van Bokhoven, J. A.; Lamberti, C. *X-ray Absorption and X-Ray Emission Spectroscopy: Theory and Applications*; John Wiley & Sons: Chichester, UK, 2016.
(165) Lee, B.-H.; Park, S.; Kim, M.; Sinha, A. K.; Lee, S. C.; Jung, E.; Chang, W. J.; Lee, K.-S.; Kim, J. H.; Cho, S.-P.; et al. Reversible and Cooperative Photoactivation of Single-Atom Cu/TiO_2 Photocatalysts. *Nat. Mater.* **2019**, *18*, 620−626.
(166) Singh, J.; Lamberti, C.; van Bokhoven, J. A. Advanced X-ray Absorption and Emission Spectroscopy: In Situ Catalytic Studies. *Chem. Soc. Rev.* **2010**, *39*, 4754−4766.
(167) Henderson, G. S.; De Groot, F. M.; Moulton, B. J. X-Ray Absorption Near-Edge Structure (XANES) Spectroscopy. *Rev. Mineral. Geochem.* **2014**, *78*, 75−138.
(168) Iwasawa, Y.; Asakura, K.; Tada, M. *XAFS Techniques for Catalysts, Nanomaterials, and Surfaces*; Springer International Publishing:Cham, Switzererland, 2017.
(169) Evans, J. *X-Ray Absorption Spectroscopy for the Chemical and Materials Sciences*; John Wiley & Sons: Chichester, UK, 2018.
(170) Kuai, L.; Chen, Z.; Liu, S.; Kan, E.; Yu, N.; Ren, Y.; Fang, C.; Li, X.; Li, Y.; Geng, B. Titania Supported Synergistic Palladium Single Atoms and Nanoparticles for Room Temperature Ketone and Aldehydes Hydrogenation. *Nat. Commun.* **2020**, *11*, 48.
(171) An, S.; Zhang, G.; Wang, T.; Zhang, W.; Li, K.; Song, C.; Miller, J. T.; Miao, S.; Wang, J.; Guo, X. High-Density Ultra-Small Clusters and Single-Atom Fe Sites Embedded in Graphitic Carbon Nitride (g-C_3N_4) for Highly Efficient Catalytic Advanced Oxidation Processes. *ACS Nano* **2018**, *12*, 9441−9450.
(172) Jin, Z.; Li, P.; Meng, Y.; Fang, Z.; Xiao, D.; Yu, G. Understanding the Inter-Site Distance Effect in Single-Atom Catalysts for Oxygen Electroreduction. *Nat. Catal.* **2021**, *4*, 615−622.
(173) Liu, W.; Zhang, L.; Liu, X.; Liu, X.; Yang, X.; Miao, S.; Wang, W.; Wang, A.; Zhang, T. Discriminating Catalytically Active FeN_x Species of Atomically Dispersed Fe−N−C Catalyst for Selective Oxidation of the C−H Bond. *J. Am. Chem. Soc.* **2017**, *139*, 10790−10798.
(174) Li, X.; Yang, X.; Zhang, J.; Huang, Y.; Liu, B. In Situ/Operando Techniques for Characterization of Single-Atom Catalysts. *ACS Catal.* **2019**, *9*, 2521−2531.
(175) Hülsey, M. J.; Zhang, B.; Ma, Z.; Asakura, H.; Do, D. A.; Chen, W.; Tanaka, T.; Zhang, P.; Wu, Z.; Yan, N. In Situ Spectroscopy-Guided Engineering of Rhodium Single-Atom Catalysts for CO Oxidation. *Nature Commun.* **2019**, *10*, 1330.
(176) Zhang, L.; Long, R.; Zhang, Y.; Duan, D.; Xiong, Y.; Zhang, Y.; Bi, Y. Direct Observation of Dynamic Bond Evolution in Single-Atom Pt/C_3N_4 Catalysts. *Angew. Chem.* **2020**, *132*, 6283−6288.
(177) Nguyen, L.; Zhang, S.; Wang, L.; Li, Y.; Yoshida, H.; Patlolla, A.; Takeda, S.; Frenkel, A. I.; Tao, F. Reduction of Nitric Oxide with Hydrogen on Catalysts of Singly Dispersed Bimetallic Sites Pt_1Co_m and Pd_1Co_n. *ACS Catal.* **2016**, *6*, 840−850.
(178) Wei, S.; Li, A.; Liu, J.-C.; Li, Z.; Chen, W.; Gong, Y.; Zhang, Q.; Cheong, W.-C.; Wang, Y.; Zheng, L.; et al. Direct Observation of Noble Metal Nanoparticles Transforming to Thermally Stable Single Atoms. *Nat. Nanotechnol.* **2018**, *13*, 856−861.
(179) Fang, L.; Seifert, S.; Winans, R. E.; Li, T. Operando XAS/SAXS: Guiding Design of Single-Atom and Subnanocluster Catalysts. *Small Methods* **2021**, *5*, 2001194.
(180) Tong, M.; Sun, F.; Xie, Y.; Wang, Y.; Yang, Y.; Tian, C.; Wang, L.; Fu, H. Operando Cooperated Catalytic Mechanism of Atomically Dispersed Cu−N_4 and Zn−N_4 for Promoting Oxygen Reduction Reaction. *Angew. Chem., Int. Ed.* **2021**, *60*, 14005−14012.
(181) Timoshenko, J.; Roldan Cuenya, B. In Situ/Operando Electrocatalyst Characterization by X-Ray Absorption Spectroscopy. *Chem. Rev.* **2021**, *121*, 882−961.
(182) Cao, L.; Luo, Q.; Liu, W.; Lin, Y.; Liu, X.; Cao, Y.; Zhang, W.; Wu, Y.; Yang, J.; Yao, T.; et al. Identification of Single-Atom Active Sites in Carbon-Based Cobalt Catalysts During Electrocatalytic Hydrogen Evolution. *Nat. Catal.* **2019**, *2*, 134−141.
(183) Lien, H.-T.; Chang, S.-T.; Chen, P.-T.; Wong, D. P.; Chang, Y.-C.; Lu, Y.-R.; Dong, C.-L.; Wang, C.-H.; Chen, K.-H.; Chen, L.-C. Probing the Active Site in Single-Atom Oxygen Reduction Catalysts via Operando X-Ray and Electrochemical Spectroscopy. *Nat. Commun.* **2020**, *11*, 4233.
(184) Li, X.; Cao, C.-S.; Hung, S.-F.; Lu, Y.-R.; Cai, W.; Rykov, A. I.; Miao, S.; Xi, S.; Yang, H.; Hu, Z.; et al. Identification of the Electronic and Structural Dynamics of Catalytic Centers in Single-Fe-Atom Material. *Chem.* **2020**, *6*, 3440−3454.
(185) Samantaray, M. K.; D'Elia, V.; Pump, E.; Falivene, L.; Harb, M.; Ould Chikh, S.; Cavallo, L.; Basset, J.-M. The Comparison Between Single Atom Catalysis and Surface Organometallic Catalysis. *Chem. Rev.* **2020**, *120*, 734−813.
(186) Gao, F.; Gao, S.; Meng, S. Screening Single-Atom Catalysts for Methane Activation: α−Al_2O_3 (0001)-Supported Ni. *Phys. Rev. Mater.* **2017**, *1*, 035801.
(187) Kiani, D.; Sourav, S.; Tang, Y.; Baltrusaitis, J.; Wachs, I. E. Methane Activation by ZSM-5-Supported Transition Metal Centers. *Chem. Soc. Rev.* **2021**, *50*, 1251−1268.
(188) Newton, M. A.; Knorpp, A. J.; Sushkevich, V. L.; Palagin, D.; Van Bokhoven, J. A. Active Sites and Mechanisms in the Direct Conversion of Methane to Methanol Using Cu in Zeolitic Hosts: A Critical Examination. *Chem. Soc. Rev.* **2020**, *49*, 1449−1486.
(189) Park, M. B.; Ahn, S. H.; Mansouri, A.; Ranocchiari, M.; van Bokhoven, J. A. Comparative Study of Diverse Copper Zeolites for the Conversion of Methane into Methanol. *ChemCatChem.* **2017**, *9*, 3705−3713.
(190) Groothaert, M. H.; van Bokhoven, J. A.; Battiston, A. A.; Weckhuysen, B. M.; Schoonheydt, R. A. Bis (μ-Oxo) Dicopper in Cu-ZSM-5 and its Role in the Decomposition of NO: A Combined In Situ XAFS, UV−Vis−Near-IR, and Kinetic Study. *J. Am. Chem. Soc.* **2003**, *125*, 7629−7640.
(191) Citek, C.; Gary, J. B.; Wasinger, E. C.; Stack, T. D. P. Chemical Plausibility of Cu(III) with Biological Ligation in pMMO. *J. Am. Chem. Soc.* **2015**, *137*, 6991−6994.
(192) Citek, C.; Lin, B.-L.; Phelps, T. E.; Wasinger, E. C.; Stack, T. D. P. Primary Amine Stabilization of a Dicopper (III) Bis (μ-Oxo) Species: Modeling the Ligation in pMMO. *J. Am. Chem. Soc.* **2014**, *136*, 14405−14408.
(193) Yoshizawa, K.; Shiota, Y. Conversion of Methane to Methanol at the Mononuclear and Dinuclear Copper Sites of Particulate Methane Monooxygenase (pMMO): A DFT and QM/MM Study. *J. Am. Chem. Soc.* **2006**, *128*, 9873−9881.
(194) Vogiatzis, K. D.; Li, G.; Hensen, E. J.; Gagliardi, L.; Pidko, E. A. Electronic Structure of the $[Cu_3(\mu\text{-}O)_3]^{2+}$ Cluster in Mordenite Zeolite and Its Effects on the Methane to Methanol Oxidation. *J. Phys. Chem. C* **2017**, *121*, 22295−22302.
(195) Shiota, Y.; Juhász, G.; Yoshizawa, K. Role of Tyrosine Residue in Methane Activation at the Dicopper Site of Particulate Methane Monooxygenase: A Density Functional Theory Study. *Inorg. Chem.* **2013**, *52*, 7907−7917.
(196) Shiota, Y.; Yoshizawa, K. Comparison of the Reactivity of Bis (μ-oxo) CuIICuIII and CuIIICuIII Species to Methane. *Inorg. Chem.* **2009**, *48*, 838−845.
(197) Paeth, M.; Tyndall, S. B.; Chen, L.-Y.; Hong, J.-C.; Carson, W. P.; Liu, X.; Sun, X.; Liu, J.; Yang, K.; Hale, E. M.; et al. Csp^3−Csp^3 Bond-Forming Reductive Elimination from Well-Defined Copper (III) Complexes. *J. Am. Chem. Soc.* **2019**, *141*, 3153−3159.
(198) Tang, X.; Wu, W.; Zeng, W.; Jiang, H. Copper-Catalyzed Oxidative Carbon−Carbon and/or Carbon−Heteroatom Bond Formation with O_2 or Internal Oxidants. *Acc. Chem. Res.* **2018**, *51*, 1092−1105.

https://doi.org/10.1021/acsnano.2c02464
ACS Nano XXXX, XXX, XXX−XXX

(199) Zhao, B.; Peng, X.; Zhu, Y.; Ramirez, T. A.; Cornwall, R. G.; Shi, Y. Cu(I)-Catalyzed Diamination of Conjugated Dienes. Complementary Regioselectivity from Two Distinct Mechanistic Pathways Involving Cu(II) and Cu(III) Species. *J. Am. Chem. Soc.* **2011**, *133*, 20890−20900.

(200) Wang, L.; Xu, H.; Jiang, N.; Wang, Z.; Jiang, J.; Zhang, T. Trace Cupric Species Triggered Decomposition of Peroxymonosulfate and Degradation of Organic Pollutants: Cu(III) Being the Primary and Selective Intermediate Oxidant. *Environ. Sci. Technol.* **2020**, *54*, 4686−4694.

(201) Abad, E.; Rommel, J. B.; Kästner, J. Reaction Mechanism of the Bicopper Enzyme Peptidylglycine α-Hydroxylating Monooxygenase. *J. Biol. Chem.* **2014**, *289*, 13726−13738.

(202) Cao, L.; Caldararu, O.; Rosenzweig, A. C.; Ryde, U. Quantum Refinement Does Not Support Dinuclear Copper Sites in Crystal Structures of Particulate Methane Monooxygenase. *Angew. Chem., Int. Ed.* **2018**, *57*, 162−166.

(203) Ribas, X.; Jackson, D. A.; Donnadieu, B.; Mahía, J.; Parella, T.; Xifra, R.; Hedman, B.; Hodgson, K. O.; Llobet, A.; Stack, T. D. P. Aryl C-H Activation by CuII To Form an Organometallic Aryl−CuIII Species: A Novel Twist on Copper Disproportionation. *Angew. Chem., Int. Ed.* **2002**, *41*, 2991−2994.

(204) Elias, J. S.; Risch, M.; Giordano, L.; Mansour, A. N.; Shao-Horn, Y. Structure, Bonding, and Catalytic Activity of Monodisperse, Transition-Metal-Substituted CeO_2 Nanoparticles. *J. Am. Chem. Soc.* **2014**, *136*, 17193−17200.

(205) DiMucci, I. M.; Lukens, J. T.; Chatterjee, S.; Carsch, K. M.; Titus, C. J.; Lee, S. J.; Nordlund, D.; Betley, T. A.; MacMillan, S. N.; Lancaster, K. M. The Myth of d^8 Copper (III). *J. Am. Chem. Soc.* **2019**, *141*, 18508−18520.

(206) Narsimhan, K.; Michaelis, V. K.; Mathies, G.; Gunther, W. R.; Griffin, R. G.; Roman-Leshkov, Y. Methane to Acetic Acid Over Cu-Exchanged Zeolites: Mechanistic Insights from a Site-Specific Carbonylation Reaction. *J. Am. Chem. Soc.* **2015**, *137*, 1825−1832.

(207) Li, G.; Vassilev, P.; Sanchez-Sanchez, M.; Lercher, J. A.; Hensen, E. J.; Pidko, E. A. Stability and Reactivity of Copper Oxo-Clusters in ZSM-5 Zeolite for Selective Methane Oxidation to Methanol. *J. Catal.* **2016**, *338*, 305−312.

(208) Narsimhan, K.; Iyoki, K.; Dinh, K.; Román-Leshkov, Y. Catalytic Oxidation of Methane into Methanol Over Copper-Exchanged Zeolites with Oxygen at Low Temperature. *ACS Cent. Sci.* **2016**, *2*, 424−429.

(209) Wang, X.; Martin, N. M.; Nilsson, J.; Carlson, S.; Gustafson, J.; Skoglundh, M.; Carlsson, P.-A. Copper-Modified Zeolites and Silica for Conversion of Methane to Methanol. *Catalysts* **2018**, *8*, 545.

(210) Himes, R. A.; Karlin, K. D. A New Copper-Oxo Player in Methane Oxidation. *Proc. Natl. Acad. Sci. U. S. A.* **2009**, *106*, 18877−18878.

(211) Sushkevich, V. L.; Palagin, D.; Ranocchiari, M.; van Bokhoven, J. A. Selective Anaerobic Oxidation of Methane Enables Direct Synthesis of Methanol. *Science* **2017**, *356*, 523−527.

(212) Periana, R. A. Comment on "Selective Anaerobic Oxidation of Methane Enables Direct Synthesis of Methanol. *Science* **2017**, *358* (6360), aan5970 DOI: 10.1126/science.aan5970.

(213) Dinh, K. T.; Sullivan, M. M.; Narsimhan, K.; Serna, P.; Meyer, R. J.; Dincă, M.; Román-Leshkov, Y. Continuous Partial Oxidation of Methane to Methanol Catalyzed by Diffusion-Paired Copper Dimers in Copper-Exchanged Zeolites. *J. Am. Chem. Soc.* **2019**, *141*, 11641−11650.

(214) Xu, R.; Liu, N.; Dai, C.; Li, Y.; Zhang, J.; Wu, B.; Yu, G.; Chen, B. H_2O-Built Proton Transfer Bridge Enhances Continuous Methane Oxidation to Methanol over Cu-BEA Zeolite. *Angew. Chem.* **2021**, *133*, 16770−16776.

(215) Yang, J.; Du, X.; Qiao, B. Methane Oxidation to Methanol Over Copper-Containing Zeolite. *Chem.* **2021**, *7*, 2270−2272.

(216) Sushkevich, V. L.; Artsiusheuski, M.; Klose, D.; Jeschke, G.; van Bokhoven, J. A. Identification of Kinetic and Spectroscopic Signatures of Copper Sites for Direct Oxidation of Methane to Methanol. *Angew. Chem., Int. Ed.* **2021**, *60*, 15944−15953.

(217) Sogukkanli, S.; Moteki, T.; Ogura, M. Selective Methanol Formation via CO-Assisted Direct Partial Oxidation of Methane Over Copper-Containing CHA-Type Zeolites Prepared by One-Pot Synthesis. *Green Chem.* **2021**, *23*, 2148−2154.

(218) Kulkarni, A. R.; Zhao, Z.-J.; Siahrostami, S.; Nørskov, J. K.; Studt, F. Monocopper Active Site for Partial Methane Oxidation in Cu-Exchanged 8MR Zeolites. *ACS Catal.* **2016**, *6*, 6531−6536.

(219) Sushkevich, V. L.; Palagin, D.; van Bokhoven, J. A. The Effect of the Active-Site Structure on the Activity of Copper Mordenite in the Aerobic and Anaerobic Conversion of Methane into Methanol. *Angew. Chem.* **2018**, *130*, 9044−9048.

(220) Meyet, J.; Searles, K.; Newton, M. A.; Wörle, M.; van Bavel, A. P.; Horton, A. D.; van Bokhoven, J. A.; Copéret, C. Monomeric Copper (II) Sites Supported on Alumina Selectively Convert Methane to Methanol. *Angew. Chem.* **2019**, *131*, 9946−9950.

(221) Sushkevich, V. L.; Safonova, O. V.; Palagin, D.; Newton, M. A.; van Bokhoven, J. A. Structure of Copper Sites in Zeolites Examined by Fourier and Wavelet Transform Analysis of EXAFS. *Chem. Sci.* **2020**, *11*, 5299−5312.

(222) Tang, X.; Wang, L.; Yang, B.; Fei, C.; Yao, T.; Liu, W.; Lou, Y.; Dai, Q.; Cai, Y.; Cao, X.-M.; et al. Direct Oxidation of Methane to Oxygenates on Supported Single Cu Atom Catalyst. *Appl. Catal., B* **2021**, *285*, 119827.

(223) Szécsényi, Á.; Li, G.; Gascon, J.; Pidko, E. A. Unraveling Reaction Networks Behind the Catalytic Oxidation of Methane with H_2O_2 Over a Mixed-Metal MIL-53 (Al, Fe) MOF Catalyst. *Chem. Sci.* **2018**, *9*, 6765−6773.

(224) Park, M. B.; Park, E. D.; Ahn, W.-S. Recent Progress in Direct Conversion of Methane to Methanol Over Copper-Exchanged Zeolites. *Front. Chem.* **2019**, *7*, 514.

(225) Haynes, C. A.; Gonzalez, R. Rethinking Biological Activation of Methane and Conversion to Liquid Fuels. *Nat. Chem. Biol.* **2014**, *10*, 331−339.

(226) Liu, Y.; Chen, Y.; Yu, H.; Guan, F.; Hou, Z.; Cui, D.; Zhang, Y. Bimetallic Ni-Co Catalysts for Co-Production of Methane and Liquid Fuels from Syngas. *Catal. Today* **2021**, *369*, 167−174.

(227) Wang, V. C.-C.; Maji, S.; Chen, P. P.-Y.; Lee, H. K.; Yu, S. S.-F.; Chan, S. I. Alkane Oxidation: Methane Monooxygenases, Related Enzymes, and Their Biomimetics. *Chem. Rev.* **2017**, *117*, 8574−8621.

(228) Yu, T.; Li, Z.; Jones, W.; Liu, Y.; He, Q.; Song, W.; Du, P.; Yang, B.; An, H.; Farmer, D. M.; et al. Identifying Key Mononuclear Fe Species for Low-Temperature Methane Oxidation. *Chem. Sci.* **2021**, *12*, 3152−3160.

(229) Zhang, L.; Sun, Z.; Lang, J.; Hu, Y. H. Direct Conversion of Methane to Oxygenates Catalyzed by Iron (III) Chloride in Water at Near Ambient Temperature. *Int. J. Energy Res.* **2021**, *45*, 2581−2592.

(230) Pirngruber, G. D.; Roy, P. K.; Prins, R. The Role of Autoreduction and of Oxygen Mobility in N_2O Decomposition over Fe-ZSM-5. *J. Catal.* **2007**, *246*, 147−157.

(231) Sazama, P.; Sathu, N. K.; Tabor, E.; Wichterlová, B.; Sklenák, Š.; Sobalík, Z. Structure and Critical Function of Fe and Acid Sites in Fe-ZSM-5 in Propane Oxidative Dehydrogenation with N_2O and N_2O Decomposition. *J. Catal.* **2013**, *299*, 188−203.

(232) Kim, M. S.; Park, E. D. Aqueous-Phase Partial Oxidation of Methane with H_2O_2 over Fe-ZSM-5 Catalysts Prepared from Different Iron Precursors. *Microporous Mesoporous Mater.* **2021**, *324*, 111278.

(233) Yang, N.; Ren, Z.; Yang, C.; Wu, P.; Zeng, G. Direct Oxidation of CH_4 to HCOOH Over Extra-Framework Stabilized Fe@MFI Catalyst at Low Temperature. *Fuel* **2021**, *305*, 121624.

(234) Hammond, C.; Hermans, I.; Dimitratos, N. Biomimetic Oxidation with Fe-ZSM-5 and H_2O_2? Identification of an Active, Extra-Framework Binuclear Core and an Fe^{III}-OOH Intermediate with Resonance-Enhanced Raman Spectroscopy. *ChemCatChem.* **2015**, *7*, 434−440.

(235) Wu, B.; Lin, T.; Lu, Z.; Yu, X.; Huang, M.; Yang, R.; Wang, C.; Tian, C.; Li, J.; Sun, Y.; et al. Fe Binuclear Sites Convert Methane to Acetic Acid with Ultrahigh Selectivity. *Chem.* **2022**, DOI: 10.1016/j.chempr.2022.02.001.

(236) Szécsényi, Á.; Li, G.; Gascon, J.; Pidko, E. A. Mechanistic Complexity of Methane Oxidation with H_2O_2 by Single-Site Fe/ZSM-5 Catalyst. *ACS Catal.* **2018**, *8*, 7961−7972.
(237) Fang, Z.; Huang, M.; Liu, B.; Chen, J.; Jiang, F.; Xu, Y.; Liu, X. Insights into Fe Species Structure-Performance Relationship for Direct Methane Conversion Toward Oxygenates over Fe-MOR Catalysts. *ChemCatChem.* **2022**, DOI: 10.1002/cctc.202200218.
(238) Yu, T.; Su, Y.; Wang, A.; Weckhuysen, B. M.; Luo, W. Efficient Synthesis of Monomeric Fe Species in Zeolite ZSM-5 for the Low-Temperature Oxidation of Methane. *ChemCatChem.* **2021**, *13*, 2766−2770.
(239) Lobree, L. J.; Hwang, I.-C.; Reimer, J. A.; Bell, A. T. Investigations of the State of Fe in H−ZSM-5. *J. Catal.* **1999**, *186*, 242−253.
(240) Li, S.; Wang, Y.; Wu, T.; Schneider, W. F. First-Principles Analysis of Site-and Condition-Dependent Fe Speciation in SSZ-13 and Implications for Catalyst Optimization. *ACS Catal.* **2018**, *8*, 10119−10130.
(241) Snyder, B. E.; Vanelderen, P.; Bols, M. L.; Hallaert, S. D.; Böttger, L. H.; Ungur, L.; Pierloot, K.; Schoonheydt, R. A.; Sels, B. F.; Solomon, E. I. The Active Site of Low-Temperature Methane Hydroxylation in Iron-Containing Zeolites. *Nature* **2016**, *536*, 317−321.
(242) Snyder, B. E.; Böttger, L. H.; Bols, M. L.; Yan, J. J.; Rhoda, H. M.; Jacobs, A. B.; Hu, M. Y.; Zhao, J.; Alp, E. E.; Hedman, B.; et al. Structural Characterization of A Non-Heme Iron Active Site in Zeolites that Hydroxylates Methane. *Proc. Natl. Acad. Sci. U. S. A.* **2018**, *115*, 4565−4570.
(243) Bols, M. L.; Hallaert, S. D.; Snyder, B. E.; Devos, J.; Plessers, D.; Rhoda, H. M.; Dusselier, M.; Schoonheydt, R. A.; Pierloot, K.; Solomon, E. I.; et al. Spectroscopic Identification of the α-Fe/α-O Active Site in Fe-CHA Zeolite for the Low-Temperature Activation of the Methane C−H Bond. *J. Am. Chem. Soc.* **2018**, *140*, 12021−12032.
(244) Snyder, B. E.; Bols, M. L.; Rhoda, H. M.; Plessers, D.; Schoonheydt, R. A.; Sels, B. F.; Solomon, E. I. Cage Effects Control the Mechanism of Methane Hydroxylation in Zeolites. *Science* **2021**, *373*, 327−331.
(245) Kammeyer, C. W.; Whitman, D. R. Quantum Mechanical Calculation of Molecular Radii. I. Hydrides of Elements of Periodic Groups IV Through VII. *J. Chem. Phys.* **1972**, *56*, 4419−4421.
(246) Hammond, C.; Forde, M. M.; Ab Rahim, M. H.; Thetford, A.; He, Q.; Jenkins, R. L.; Dimitratos, N.; Lopez-Sanchez, J. A.; Dummer, N. F.; Murphy, D. M.; et al. Direct Catalytic Conversion of Methane to Methanol in An Aqueous Medium by Using Copper-Promoted Fe-ZSM-5. *Angew. Chem.* **2012**, *124*, 5219−5223.
(247) Dinh, K. T.; Sullivan, M. M.; Serna, P.; Meyer, R. J.; Dincă, M.; Román-Leshkov, Y. Viewpoint on the Partial Oxidation of Methane to Methanol Using Cu-and Fe-Exchanged Zeolites. *ACS Catal.* **2018**, *8*, 8306−8313.
(248) Sushkevich, V. L.; Verel, R.; van Bokhoven, J. A. Pathways of Methane Transformation over Copper-Exchanged Mordenite as Revealed by In Situ NMR and IR Spectroscopy. *Angew. Chem.* **2020**, *132*, 920−928.
(249) Sushkevich, V. L.; van Bokhoven, J. A. Kinetic Study and Effect of Water on Methane Oxidation to Methanol Over Copper-Exchanged Mordenite. *Catal. Sci. Technol.* **2020**, *10*, 382−390.
(250) Ravi, M.; Sushkevich, V. L.; Knorpp, A. J.; Newton, M. A.; Palagin, D.; Pinar, A. B.; Ranocchiari, M.; van Bokhoven, J. A. Misconceptions and Challenges in Methane-to-Methanol Over Transition-Metal-Exchanged Zeolites. *Nat. Catal.* **2019**, *2*, 485−494.
(251) Mahyuddin, M. H.; Shiota, Y.; Yoshizawa, K. Methane Selective Oxidation to Methanol by Metal-Exchanged Zeolites: A Review of Active Sites and Their Reactivity. *Catal. Sci. Technol.* **2019**, *9*, 1744−1768.
(252) Dyballa, M. M.; Thorshaug, K.; Pappas, D.; Borfecchia, E.; Kvande, K.; Bordiga, S.; Berlier, G.; Lazzarini, A.; Olsbye, U.; Beato, P.; et al. Zeolite Surface Methoxy Groups as Key Intermediates in the Stepwise Conversion of Methane to Methanol. *ChemCatChem.* **2019**, *11*, 5022−5026.
(253) Sun, Y.; Tian, P.; Ding, D.; Yang, Z.; Wang, W.; Xin, H.; Xu, J.; Han, Y.-F. Revealing the Active Species of Cu-Based Catalysts for Heterogeneous Fenton Reaction. *Appl. Catal., B* **2019**, *258*, 117985.
(254) Li, H.; Cheng, R.; Liu, Z.; Du, C. Waste control by waste: Fenton−Like Oxidation of Phenol over Cu Modified ZSM−5 from Coal Gangue. *Sci. Total Environ.* **2019**, *683*, 638−647.
(255) Yu, T.; Li, Z.; Lin, L.; Chu, S.; Su, Y.; Song, W.; Wang, A.; Weckhuysen, B. M.; Luo, W. Highly Selective Oxidation of Methane into Methanol over Cu-Promoted Monomeric Fe/ZSM-5. *ACS Catal.* **2021**, *11*, 6684−6691.
(256) Yuan, S.; Li, Y.; Peng, J.; Questell-Santiago, Y. M.; Akkiraju, K.; Giordano, L.; Zheng, D. J.; Bagi, S.; Román-Leshkov, Y.; Shao-Horn, Y. Conversion of Methane into Liquid Fuels-Bridging Thermal Catalysis with Electrocatalysis. *Adv. Energy Mater.* **2020**, *10*, 2002154.
(257) Dowden, D.; Walker, G. Oxygenated Hydrocarbons Production. Patent GB1244001A, 1971.
(258) Zhen, K.; Khan, M.; Mak, C.; Lewis, K.; Somorjai, G. Partial Oxidation of Methane with Nitrous Oxide Over V_2O_5.SiO_2 Catalyst. *J. Catal.* **1985**, *94*, 501−507.
(259) Michalkiewicz, B. Partial Oxidation of Methane to Formaldehyde and Methanol Using Molecular Oxygen Over Fe-ZSM-5. *Appl. Catal., A* **2004**, *277*, 147−153.
(260) Periana, R. A.; Taube, D. J.; Evitt, E. R.; Löffler, D. G.; Wentrcek, P. R.; Voss, G.; Masuda, T. A Mercury-Catalyzed, High-Yield System for the Oxidation of Methane to Methanol. *Science* **1993**, *259*, 340−343.
(261) Periana, R. A.; Taube, D. J.; Gamble, S.; Taube, H.; Satoh, T.; Fujii, H. Platinum Catalysts for the High-Yield Oxidation of Methane to a Methanol Derivative. *Science* **1998**, *280*, 560−564.
(262) Goldshleger, N.; Tyabin, M.; Shilov, A.; Shteinman, A. Activation of Saturated Hydrocarbons-Deuterium-Hydrogen Exchange in Solutions of Transition Metal Complexes. *Russ. J. Phys. Chem.* **1969**, *43*, 1222.
(263) Bar-Nahum, I.; Khenkin, A. M.; Neumann, R. Mild, Aqueous, Aerobic, Catalytic Oxidation of Methane to Methanol and Acetaldehyde Catalyzed by a Supported Bipyrimidinylplatinum−Polyoxometalate Hybrid Compound. *J. Am. Chem. Soc.* **2004**, *126*, 10236−10237.
(264) Sorokin, A.; Kudrik, E.; Alvarez, L.; Afanasiev, P.; Millet, J.; Bouchu, D. Oxidation of Methane and Ethylene in Water at Ambient Conditions. *Catal. Today* **2010**, *157*, 149−154.
(265) Monai, M.; Montini, T.; Gorte, R. J.; Fornasiero, P. Catalytic Oxidation of Methane: Pd and Beyond. *Eur. J. Inorg. Chem.* **2018**, *2018*, 2884−2893.
(266) Ab Rahim, M. H.; Forde, M. M.; Jenkins, R. L.; Hammond, C.; He, Q.; Dimitratos, N.; Lopez-Sanchez, J. A.; Carley, A. F.; Taylor, S. H.; Willock, D. J.; et al. Oxidation of Methane to Methanol with Hydrogen Peroxide using Supported Gold−Palladium Alloy Nanoparticles. *Angew. Chem., Int. Ed.* **2013**, *52*, 1280−1284.
(267) Friberg, I.; Clark, A. H.; Ho, P. H.; Sadokhina, N.; Smales, G. J.; Woo, J.; Auvray, X.; Ferri, D.; Nachtegaal, M.; Kröcher, O.; et al. Structure and Performance of Zeolite Supported Pd for Complete Methane Oxidation. *Catal. Today* **2021**, *382*, 3−12.
(268) Hou, Y.; Nagamatsu, S.; Asakura, K.; Fukuoka, A.; Kobayashi, H. Trace Mono-Atomically Dispersed Rhodium on Zeolite-Supported Cobalt Catalyst for the Efficient Methane Oxidation. *Commun. Chem.* **2018**, *1*, 41.
(269) Huang, W.; Zhang, S.; Tang, Y.; Li, Y.; Nguyen, L.; Li, Y.; Shan, J.; Xiao, D.; Gagne, R.; Frenkel, A. I.; et al. Low-Temperature Transformation of Methane to Methanol on Pd_1O_4 Single Sites Anchored on the Internal Surface of Microporous Silicate. *Angew. Chem.* **2016**, *128*, 13639−13643.
(270) Kwon, G.; Shin, D.; Jeong, H.; Sahoo, S. K.; Lee, J.; Kim, G.; Choi, J.; Kim, D. H.; Han, J. W.; Lee, H. Oxidative Methane Conversion to Ethane on Highly Oxidized Pd/CeO_2 Catalysts Below 400 °C. *ChemSusChem* **2020**, *13*, 677−681.
(271) Li, X.; Xie, J.; Rao, H.; Wang, C.; Tang, J. Platinum-and CuO_x-Decorated TiO_2 Photocatalyst for Oxidative Coupling of Methane to

C_2 Hydrocarbons in a Flow Reactor. *Angew. Chem.* **2020**, *132*, 19870−19875.
(272) Tu, C.; Nie, X.; Chen, J. G. Insight into Acetic Acid Synthesis from the Reaction of CH_4 and CO_2. *ACS Catal.* **2021**, *11*, 3384−3401.
(273) Mordor Intelligence. *Acetic Acid Market - Growth, Trends, COVID-19 Impact, and Forecasts (2021−2026) Technical Report*, 2021.
(274) Wu, J.-F.; Yu, S.-M.; Wang, W. D.; Fan, Y.-X.; Bai, S.; Zhang, C.-W.; Gao, Q.; Huang, J.; Wang, W. Mechanistic Insight into the Formation of Acetic Acid from the Direct Conversion of Methane and Carbon Dioxide on Zinc-Modified H−ZSM-5 Zeolite. *J. Am. Chem. Soc.* **2013**, *135*, 13567−13573.
(275) Periana, R. A.; Mironov, O.; Taube, D.; Bhalla, G.; Jones, C. Catalytic, Oxidative Condensation of CH_4 to CH_3COOH in One Step via CH Activation. *Science* **2003**, *301*, 814−818.
(276) Asadullah, M.; Kitamura, T.; Fujiwara, Y. Calcium-Catalyzed Selective and Quantitative Transformation of CH_4 and CO into Acetic Acid. *Angew. Chem., Int. Ed.* **2000**, *39*, 2475−2478.
(277) Nizova, G. V.; Shul'pin, G. B.; Nizova, G. V.; Suss-Fink, G.; Stanislas, S. Carboxylation of Methane with CO or CO_2 in Aqueous Solution Catalysed by Vanadium Complexes. *Chem. Commun.* **1998**, 1885−1886.
(278) Reis, P. M.; Silva, J. A.; Palavra, A. F.; Fraústo da Silva, J. J.; Kitamura, T.; Fujiwara, Y.; Pombeiro, A. J. Single-Pot Conversion of Methane into Acetic Acid in the Absence of CO and with Vanadium Catalysts Such as Amavadine. *Angew. Chem.* **2003**, *115*, 845−847.
(279) Kirillova, M. V.; Kuznetsov, M. L.; Reis, P. M.; da Silva, J. A.; Fraústo da Silva, J. J.; Pombeiro, A. J. Direct and Remarkably Efficient Conversion of Methane into Acetic Acid Catalyzed by Amavadine and Related Vanadium Complexes. A Synthetic and a Theoretical DFT Mechanistic Study. *J. Am. Chem. Soc.* **2007**, *129*, 10531−10545.
(280) Lin, M.; Sen, A. Direct Catalytic Conversion of Methane to Acetic Acid in an Aqueous Medium. *Nature* **1994**, *368*, 613−615.
(281) Phan, A.; Czaja, A. U.; Gándara, F.; Knobler, C. B.; Yaghi, O. M. Metal−Organic Frameworks of Vanadium as Catalysts for Conversion of Methane to Acetic Acid. *Inorg. Chem.* **2011**, *50*, 7388−7390.
(282) Rabie, A. M.; Betiha, M. A.; Park, S.-E. Direct Synthesis of Acetic Acid by Simultaneous Co-Activation of Methane and CO_2 over Cu-Exchanged ZSM-5 Catalysts. *Appl. Catal., B* **2017**, *215*, 50−59.
(283) Zhang, P.; Yang, X.; Hou, X.; Mi, J.; Yuan, Z.; Huang, J.; Stampfl, C. Active Sites and Mechanism of the Direct Conversion of Methane and Carbon Dioxide to Acetic Acid over the Zinc-Modified H-ZSM-5 Zeolite. *Catal. Sci. Technol.* **2019**, *9*, 6297−6307.
(284) Shan, J.; Li, M.; Allard, L. F.; Lee, S.; Flytzani-Stephanopoulos, M. Mild Oxidation of Methane to Methanol or Acetic Acid on Supported Isolated Rhodium Catalysts. *Nature* **2017**, *551*, 605−608.
(285) Tang, Y.; Li, Y.; Fung, V.; Jiang, D.-e.; Huang, W.; Zhang, S.; Iwasawa, Y.; Sakata, T.; Nguyen, L.; Zhang, X.; et al. Single Rhodium Atoms Anchored in Micropores for Efficient Transformation of Methane Under Mild Conditions. *Nat. Commun.* **2018**, *9*, 1231.
(286) Blasco, T.; Boronat, M.; Concepción, P.; Corma, A.; Law, D.; Vidal-Moya, J. A. Carbonylation of Methanol on Metal−Acid Zeolites: Evidence for a Mechanism Involving a Multisite Active Center. *Angew. Chem.* **2007**, *119*, 4012−4015.
(287) Moteki, T.; Tominaga, N.; Ogura, M. Mechanism Investigation and Product Selectivity Control on CO-Assisted Direct Conversion of Methane into C1 and C2 Oxygenates Catalyzed by Zeolite-Supported Rh. *Appl. Catal., B* **2022**, *300*, 120742.
(288) Qi, G.; Davies, T. E.; Nasrallah, A.; Sainna, M. A.; Howe, A. G.; Lewis, R. J.; Quesne, M.; Catlow, C. R. A.; Willock, D. J.; He, Q.; et al. Au-ZSM-5 Catalyses the Selective Oxidation of CH_4 to CH_3OH and CH_3COOH using O_2. *Nat. Catal.* **2022**, *5*, 45−54.
(289) Li, M.; Shan, J.; Giannakakis, G.; Ouyang, M.; Cao, S.; Lee, S.; Allard, L. F.; Flytzani-Stephanopoulos, M. Single-Step Selective Oxidation of Methane to Methanol in the Aqueous Phase on Iridium-Based Catalysts. *Appl. Catal., B* **2021**, *292*, 120124.
(290) Parkinson, G. S. Single-Atom Catalysis: How Structure Influences Catalytic Performance. *Catal. Lett.* **2019**, *149*, 1137−1146.
(291) Guo, X.; Fang, G.; Li, G.; Ma, H.; Fan, H.; Yu, L.; Ma, C.; Wu, X.; Deng, D.; Wei, M.; et al. Direct, Nonoxidative Conversion of Methane to Ethylene, Aromatics, and Hydrogen. *Science* **2014**, *344*, 616−619.
(292) Ma, X.; Liu, H.; Yang, W.; Mao, G.; Zheng, L.; Jiang, H.-L. Modulating Coordination Environment of Single-Atom Catalysts and Their Proximity to Photosensitive Units for Boosting MOF Photocatalysis. *J. Am. Chem. Soc.* **2021**, *143*, 12220−12229.
(293) Shi, Y.; Huang, W.-M.; Li, J.; Zhou, Y.; Li, Z.-Q.; Yin, Y.-C.; Xia, X.-H. Site-Specific Electrodeposition Enables Self-Terminating Growth of Atomically Dispersed Metal Catalysts. *Nat. Commun.* **2020**, *11*, 4558.
(294) Christopher, P. Single-Atom Catalysts: Are All Sites Created Equal? *ACS Energy Lett.* **2019**, *4*, 2249−2250.
(295) Qi, K.; Chhowalla, M.; Voiry, D. Single atom is not alone: Metal−Support Interactions in Single-Atom Catalysis. *Mater. Today* **2020**, *40*, 173−192.
(296) Shi, Y.; Ma, Z.-R.; Xiao, Y.-Y.; Yin, Y.-C.; Huang, W.-M.; Huang, Z.-C.; Zheng, Y.-Z.; Mu, F.-Y.; Huang, R.; Shi, G.-Y.; et al. Electronic Metal−Support Interaction Modulates Single-Atom Platinum Catalysis for Hydrogen Evolution Reaction. *Nat. Commun.* **2021**, *12*, 3021.
(297) Li, J.; Guan, Q.; Wu, H.; Liu, W.; Lin, Y.; Sun, Z.; Ye, X.; Zheng, X.; Pan, H.; Zhu, J.; et al. Highly Active and Stable Metal Single-Atom Catalysts Achieved by Strong Electronic Metal−Support Interactions. *J. Am. Chem. Soc.* **2019**, *141*, 14515−14519.
(298) Zheng, X.; Tang, J.; Gallo, A.; Torres, J. A. G.; Yu, X.; Athanitis, C. J.; Been, E. M.; Ercius, P.; Mao, H.; Fakra, S. C.; et al. Origin of Enhanced Water Oxidation Activity in An Iridium Single Atom Anchored on NiFe Oxyhydroxide Catalyst. *Proc. Natl. Acad. Sci. U. S. A.* **2021**, *118*, e2101817118.
(299) Qiao, B.; Liang, J.-X.; Wang, A.; Xu, C.-Q.; Li, J.; Zhang, T.; Liu, J. J. Ultrastable Single-Atom Gold Catalysts with Strong Covalent Metal-Support Interaction (CMSI). *Nano Res.* **2015**, *8*, 2913−2924.
(300) Wang, C.; Gu, X.-K.; Yan, H.; Lin, Y.; Li, J.; Liu, D.; Li, W.-X.; Lu, J. Water-Mediated Mars−van Krevelen Mechanism for CO Oxidation on Ceria-Supported Single-Atom Pt_1 Catalyst. *ACS Catal.* **2017**, *7*, 887−891.
(301) Nie, L.; Mei, D.; Xiong, H.; Peng, B.; Ren, Z.; Hernandez, X. I. P.; DeLaRiva, A.; Wang, M.; Engelhard, M. H.; Kovarik, L.; et al. Activation of Surface Lattice Oxygen in Single-Atom Pt/CeO_2 for Low-Temperature CO Oxidation. *Science* **2017**, *358*, 1419−1423.
(302) Chen, J.; Wanyan, Y.; Zeng, J.; Fang, H.; Li, Z.; Dong, Y.; Qin, R.; Wu, C.; Liu, D.; Wang, M.; et al. Surface Engineering Protocol to Obtain an Atomically Dispersed Pt/CeO_2 Catalyst with High Activity and Stability for CO Oxidation. *ACS Sustainable Chem. Eng.* **2018**, *6*, 14054−14062.
(303) DeRita, L.; Dai, S.; Lopez-Zepeda, K.; Pham, N.; Graham, G. W.; Pan, X.; Christopher, P. Catalyst Architecture for Stable Single Atom Dispersion Enables Site-Specific Spectroscopic and Reactivity Measurements of CO Adsorbed to Pt Atoms, Oxidized Pt Clusters, and Metallic Pt Clusters on TiO_2. *J. Am. Chem. Soc.* **2017**, *139*, 14150−14165.
(304) Wang, J.; Tan, H.; Yu, S.; Zhou, K. Morphological Effects of Gold Clusters on the Reactivity of Ceria Surface Oxygen. *ACS Catal.* **2015**, *5*, 2873−2881.
(305) Beniya, A.; Higashi, S. Towards Dense Single-Atom Catalysts for Future Automotive Applications. *Nat. Catal.* **2019**, *2*, 590−602.
(306) Liu, Y.; Liu, J. C.; Li, T. H.; Duan, Z. H.; Zhang, T. Y.; Yan, M.; Li, W. L.; Xiao, H.; Wang, Y. G.; Chang, C. R.; et al. Unravelling the Enigma of Nonoxidative Conversion of Methane on Iron Single-Atom Catalysts. *Angew. Chem.* **2020**, *132*, 18745−18749.
(307) Fu, J.; Lym, J.; Zheng, W.; Alexopoulos, K.; Mironenko, A. V.; Li, N.; Boscoboinik, J. A.; Su, D.; Weber, R. T.; Vlachos, D. G. C−O Bond Activation using Ultralow Loading of Noble Metal Catalysts on Moderately Reducible Oxides. *Nat. Catal.* **2020**, *3*, 446−453.
(308) Liu, K.; Zhao, X.; Ren, G.; Yang, T.; Ren, Y.; Lee, A. F.; Su, Y.; Pan, X.; Zhang, J.; Chen, Z.; et al. Strong Metal-Support Interaction

Promoted Scalable Production of Thermally Stable Single-Atom Catalysts. *Nat. Commun.* **2020**, *11*, 1263.
(309) Yang, Y.; Yang, Y.; Pei, Z.; Wu, K.-H.; Tan, C.; Wang, H.; Wei, L.; Mahmood, A.; Yan, C.; Dong, J.; et al. Recent Progress of Carbon-Supported Single-Atom Catalysts for Energy Conversion and Storage. *Matter* **2020**, *3*, 1442−1476.
(310) Zhang, Y.; Jiao, L.; Yang, W.; Xie, C.; Jiang, H. L. Rational Fabrication of Low-Coordinate Single-Atom Ni Electrocatalysts by MOFs for Highly Selective CO_2 Reduction. *Angew. Chem., Int. Ed.* **2021**, *60*, 7607−7611.
(311) Gu, Y.; Xi, B.; Tian, W.; Zhang, H.; Fu, Q.; Xiong, S. Boosting Selective Nitrogen Reduction via Geometric Coordination Engineering on Single-Tungsten-Atom Catalysts. *Adv. Mater.* **2021**, *33*, 2100429.
(312) Pan, Y.; Chen, Y.; Wu, K.; Chen, Z.; Liu, S.; Cao, X.; Cheong, W.-C.; Meng, T.; Luo, J.; Zheng, L.; et al. Regulating the Coordination Structure of Single-Atom Fe-N_xC_y Catalytic Sites for Benzene Oxidation. *Nat. Commun.* **2019**, *10*, 4290.
(313) Gao, C.; Low, J.; Long, R.; Kong, T.; Zhu, J.; Xiong, Y. Heterogeneous Single-Atom Photocatalysts: Fundamentals and Applications. *Chem. Rev.* **2020**, *120*, 12175−12216.
(314) Aslam, U.; Rao, V. G.; Chavez, S.; Linic, S. Catalytic Conversion of Solar to Chemical Energy on Plasmonic Metal Nanostructures. *Nat. Catal.* **2018**, *1*, 656−665.
(315) Li, S.; Miao, P.; Zhang, Y.; Wu, J.; Zhang, B.; Du, Y.; Han, X.; Sun, J.; Xu, P. Recent Advances in Plasmonic Nanostructures for Enhanced Photocatalysis and Electrocatalysis. *Adv. Mater.* **2021**, *33*, 2000086.
(316) Cortés, E.; Besteiro, L. V.; Alabastri, A.; Baldi, A.; Tagliabue, G.; Demetriadou, A.; Narang, P. Challenges in Plasmonic Catalysis. *ACS Nano* **2020**, *14*, 16202−16219.
(317) Valenti, M.; Venugopal, A.; Tordera, D.; Jonsson, M. P.; Biskos, G.; Schmidt-Ott, A.; Smith, W. A. Hot Carrier Generation and Extraction of Plasmonic Alloy Nanoparticles. *ACS Photonics* **2017**, *4*, 1146−1152.
(318) He, R.; Wang, Y.-C.; Wang, X.; Wang, Z.; Liu, G.; Zhou, W.; Wen, L.; Li, Q.; Wang, X.; Chen, X.; et al. Facile Synthesis of Pentacle Gold−Copper Alloy Nanocrystals and Their Plasmonic and Catalytic Properties. *Nat. Commun.* **2014**, *5*, 4327.
(319) Huang, L.; Zou, J.; Ye, J. Y.; Zhou, Z. Y.; Lin, Z.; Kang, X.; Jain, P. K.; Chen, S. Synergy between Plasmonic and Electrocatalytic Activation of Methanol Oxidation on Palladium−Silver Alloy Nanotubes. *Angew. Chem.* **2019**, *131*, 8886−8890.
(320) Greiner, M. T.; Jones, T.; Beeg, S.; Zwiener, L.; Scherzer, M.; Girgsdies, F.; Piccinin, S.; Armbrüster, M.; Knop-Gericke, A.; Schlögl, R. Free-Atom-Like d States in Single-Atom Alloy Catalysts. *Nat. Chem.* **2018**, *10*, 1008−1015.
(321) Han, L.; Zhang, L.; Wu, H.; Zu, H.; Cui, P.; Guo, J.; Guo, R.; Ye, J.; Zhu, J.; Zheng, X.; et al. Anchoring Pt Single Atoms on Te Nanowires for Plasmon-Enhanced Dehydrogenation of Formic Acid at Room Temperature. *Adv. Sci.* **2019**, *6*, 1900006.
(322) Zhou, L.; Martirez, J. M. P.; Finzel, J.; Zhang, C.; Swearer, D. F.; Tian, S.; Robatjazi, H.; Lou, M.; Dong, L.; Henderson, L.; et al. Light-Driven Methane Dry Reforming with Single Atomic Site Antenna-Reactor Plasmonic Photocatalysts. *Nat. Energy* **2020**, *5*, 61−70.
(323) Xin, Y.; Yu, K.; Zhang, L.; Yang, Y.; Yuan, H.; Li, H.; Wang, L.; Zeng, J. Copper-Based Plasmonic Catalysis: Recent Advances and Future Perspectives. *Adv. Mater.* **2021**, *33*, 2008145.
(324) Lustemberg, P. G.; Palomino, R. M.; Gutiérrez, R. A.; Grinter, D. C.; Vorokhta, M.; Liu, Z.; Ramírez, P. J.; Matolín, V.; Ganduglia-Pirovano, M. V. n.; Senanayake, S. D.; et al. Direct Conversion of Methane to Methanol on Ni-Ceria Surfaces: Metal−Support Interactions and Water-Enabled Catalytic Conversion by Site Blocking. *J. Am. Chem. Soc.* **2018**, *140*, 7681−7687.
(325) Li, X.; Rong, H.; Zhang, J.; Wang, D.; Li, Y. Modulating the Local Coordination Environment of Single-Atom Catalysts for Enhanced Catalytic Performance. *Nano Res.* **2020**, *13*, 1842−1855.
(326) Sun, Q.; Wang, N.; Yu, J. Advances in Catalytic Applications of Zeolite-Supported Metal Catalysts. *Adv. Mater.* **2021**, *33*, 2104442.
(327) Harrath, K.; Yu, X.; Xiao, H.; Li, J. The Key Role of Support Surface Hydrogenation in the CH_4 to CH_3OH Selective Oxidation by a ZrO_2-Supported Single-Atom Catalyst. *ACS Catal.* **2019**, *9*, 8903−8909.
(328) Kwon, Y.; Kim, T. Y.; Kwon, G.; Yi, J.; Lee, H. Selective Activation of Methane on Single-Atom Catalyst of Rhodium Dispersed on Zirconia for Direct Conversion. *J. Am. Chem. Soc.* **2017**, *139*, 17694−17699.
(329) Nunan, J. G.; Robota, H. J.; Cohn, M. J.; Bradley, S. A. Physicochemical Properties of Ce-Containing Three-Way Catalysts and the Effect of Ce on Catalyst Activity. *J. Catal.* **1992**, *133*, 309−324.
(330) Kye, S.-H.; Park, H. S.; Zhang, R.; Yang, H. J.; Lee, K. H.; Suh, H.; Kim, J.-G.; Kim, M. G.; Hwang, G. S.; Hur, N. H. Partial Oxidation of Methane to Methanol by Isolated Pt Catalyst Supported on a CeO_2 Nanoparticle. *J. Chem. Phys.* **2020**, *152*, 054715.
(331) Bai, S.; Liu, F.; Huang, B.; Li, F.; Lin, H.; Wu, T.; Sun, M.; Wu, J.; Shao, Q.; Xu, Y.; et al. High-Efficiency Direct Methane Conversion to Oxygenates on a Cerium Dioxide Nanowires Supported Rhodium Single-Atom Catalyst. *Nat. Commun.* **2020**, *11*, 954.
(332) Ji, Q.; Bi, L.; Zhang, J.; Cao, H.; Zhao, X. S. The Role of Oxygen Vacancies of ABO_3 Perovskite Oxides in the Oxygen Reduction Reaction. *Energy Environ. Sci.* **2020**, *13*, 1408−1428.
(333) Tian, C.; Zhang, H.; Zhu, X.; Lin, B.; Liu, X.; Chen, H.; Zhang, Y.; Mullins, D. R.; Abney, C. W.; Shakouri, M.; et al. A New Trick for an Old Support: Stabilizing Gold Single Atoms on $LaFeO_3$ Perovskite. *Appl. Catal., B* **2020**, *261*, 118178.
(334) Wan, Q.; Fung, V.; Lin, S.; Wu, Z.; Jiang, D.-e. Perovskite-Supported Pt Single Atoms for Methane Activation. *J. Mater. Chem. A* **2020**, *8*, 4362−4368.
(335) Agarwal, N.; Freakley, S. J.; McVicker, R. U.; Althahban, S. M.; Dimitratos, N.; He, Q.; Morgan, D. J.; Jenkins, R. L.; Willock, D. J.; Taylor, S. H.; et al. Aqueous Au-Pd Colloids Catalyze Selective CH_4 Oxidation to CH_3OH with O_2 Under Mild Conditions. *Science* **2017**, *358*, 223−227.
(336) Salvadeo, E.; Dubois, L.; Latour, J.-M. Trinuclear Copper Complexes as Biological Mimics: Ligand Designs and Reactivities. *Coord. Chem. Rev.* **2018**, *374*, 345−375.
(337) Williams, C.; Carter, J. H.; Dummer, N. F.; Chow, Y. K.; Morgan, D. J.; Yacob, S.; Serna, P.; Willock, D. J.; Meyer, R. J.; Taylor, S. H.; et al. Selective Oxidation of Methane to Methanol Using Supported AuPd Catalysts Prepared by Stabilizer-Free Sol-Immobilization. *ACS Catal.* **2018**, *8*, 2567−2576.
(338) Liang, Z.; Li, T.; Kim, M.; Asthagiri, A.; Weaver, J. F. Low-Temperature Activation of Methane on the IrO_2 (110) Surface. *Science* **2017**, *356*, 299−303.
(339) Yang, L.; Huang, J.; Ma, R.; You, R.; Zeng, H.; Rui, Z. Metal−Organic Framework-Derived IrO_2/CuO Catalyst for Selective Oxidation of Methane to Methanol. *ACS Energy Lett.* **2019**, *4*, 2945−2951.
(340) Xie, J.; Jin, R.; Li, A.; Bi, Y.; Ruan, Q.; Deng, Y.; Zhang, Y.; Yao, S.; Sankar, G.; Ma, D.; et al. Highly Selective Oxidation of Methane to Methanol at Ambient Conditions by Titanium Dioxide-Supported Iron Species. *Nat. Catal.* **2018**, *1*, 889−896.
(341) Kim, G.; Kwon, G.; Lee, H. The Role of Surface Hydroxyl Groups on a Single-Atomic Rh_1/ZrO_2 Catalyst for Direct Methane Oxidation. *Chem. Commun.* **2021**, *57*, 1671−1674.
(342) Jin, Z.; Wang, L.; Zuidema, E.; Mondal, K.; Zhang, M.; Zhang, J.; Wang, C.; Meng, X.; Yang, H.; Mesters, C.; et al. Hydrophobic Zeolite Modification for In Situ Peroxide Formation in Methane Oxidation to Methanol. *Science* **2020**, *367*, 193−197.
(343) Gu, F.; Qin, X.; Li, M.; Xu, Y.; Hong, S.; Ouyang, M.; Giannakakis, G.; Cao, S.; Peng, M.; Xie, J. Selective Catalytic Oxidation of Methane to Methanol in Aqueous Medium over Copper Cations Promoted by Atomically Dispersed Rhodium on TiO_2. *Angew. Chem., Int. Ed.* **2022**, *16*, e202201540.

https://doi.org/10.1021/acsnano.2c02464
ACS Nano XXXX, XXX, XXX−XXX

(344) Shen, Q.; Cao, C.; Huang, R.; Zhu, L.; Zhou, X.; Zhang, Q.; Gu, L.; Song, W. Single Chromium Atoms Supported on Titanium Dioxide Nanoparticles for Synergic Catalytic Methane Conversion Under Mild Conditions. *Angew. Chem.* **2020**, *132*, 1232−1235.
(345) Freakley, S. J.; Dimitratos, N.; Willock, D. J.; Taylor, S. H.; Kiely, C. J.; Hutchings, G. J. Methane Oxidation to Methanol in Water. *Acc. Chem. Res.* **2021**, *54*, 2614−2623.
(346) Ravi, M.; Ranocchiari, M.; van Bokhoven, J. A. The Direct Catalytic Oxidation of Methane to Methanol-A Critical Assessment. *Angew. Chem., Int. Ed.* **2017**, *56*, 16464−16483.
(347) Impeng, S.; Khongpracha, P.; Warakulwit, C.; Jansang, B.; Sirijaraensre, J.; Ehara, M.; Limtrakul, J. Direct Oxidation of Methane to Methanol on Fe−O Modified Graphene. *RSC Adv.* **2014**, *4*, 12572−12578.
(348) Singh, B.; Gawande, M. B.; Kute, A. D.; Varma, R. S.; Fornasiero, P.; McNeice, P.; Jagadeesh, R. V.; Beller, M.; Zbořil, R. Single-atom (Iron-Based) Catalysts: Synthesis and Applications. *Chem. Rev.* **2021**, *121* (21), 13620−13697.
(349) Cui, X.; Li, H.; Wang, Y.; Hu, Y.; Hua, L.; Li, H.; Han, X.; Liu, Q.; Yang, F.; He, L.; et al. Room-Temperature Methane Conversion by Graphene-Confined Single Iron Atoms. *Chem.* **2018**, *4*, 1902−1910.
(350) Zhao, S.; Li, M.; Han, M.; Xu, D.; Yang, J.; Lin, Y.; Shi, N. E.; Lu, Y.; Yang, R.; Liu, B.; et al. Defect-Rich Ni_3FeN Nanocrystals Anchored on N-Doped Graphene for Enhanced Electrocatalytic Oxygen Evolution. *Adv. Funct. Mater.* **2018**, *28*, 1706018.
(351) Zheng, F.; Ji, Y.; Dong, H.; Liu, C.; Chen, S.; Li, Y. Edge Effect Promotes Graphene-Confining Single-Atom Co−N_4 and Rh−N_4 for Bifunctional Oxygen Electrocatalysis. *J. Phys. Chem. C* **2022**, *126*, 30−39.
(352) Chen, F.; Wu, X. L.; Shi, C.; Lin, H.; Chen, J.; Shi, Y.; Wang, S.; Duan, X. Molecular Engineering toward Pyrrolic N-Rich M-N_4 (M= Cr, Mn, Fe, Co, Cu) Single-Atom Sites for Enhanced Heterogeneous Fenton-Like Reaction. *Adv. Funct. Mater.* **2021**, *31*, 2007877.
(353) Xia, W.; Tang, J.; Li, J.; Zhang, S.; Wu, K. C. W.; He, J.; Yamauchi, Y. Defect-Rich Graphene Nanomesh Produced by Thermal Exfoliation of Metal−Organic Frameworks for the Oxygen Reduction Reaction. *Angew. Chem.* **2019**, *131*, 13488−13493.
(354) Chen, X.; Peng, M.; Cai, X.; Chen, Y.; Jia, Z.; Deng, Y.; Mei, B.; Jiang, Z.; Xiao, D.; Wen, X.; et al. Regulating Coordination Number in Atomically Dispersed Pt Species on Defect-Rich Graphene for n-Butane Dehydrogenation Reaction. *Nat. Commun.* **2021**, *12*, 2664.
(355) Meng, F.; Peng, M.; Chen, Y.; Cai, X.; Huang, F.; Yang, L.; Liu, X.; Li, T.; Wen, X.; Wang, N.; et al. Defect-Rich Graphene Stabilized Atomically Dispersed Cu_3 Clusters with Enhanced Oxidase-Like Activity for Antibacterial Applications. *Appl. Catal., B* **2022**, *301*, 120826.
(356) Tan, X.; Tahini, H. A.; Smith, S. C. Defect Engineering in Graphene-Confined Single-Atom Iron Catalysts for Room-Temperature Methane Conversion. *J. Phys. Chem. C* **2021**, *125*, 12628−12635.
(357) Griffis, T. J.; Chen, Z.; Baker, J. M.; Wood, J. D.; Millet, D. B.; Lee, X.; Venterea, R. T.; Turner, P. A. Nitrous Oxide Emissions are Enhanced in a Warmer and Wetter World. *Proc. Natl. Acad. Sci. U. S. A.* **2017**, *114*, 12081−12085.
(358) Kweku, D. W.; Bismark, O.; Maxwell, A.; Desmond, K. A.; Danso, K. B.; Oti-Mensah, E. A.; Quachie, A. T.; Adormaa, B. B. Greenhouse Effect: Greenhouse Gases and Their Impact on Global Warming. *J. Sci. Res. Rep.* **2017**, *17*, 1−9.
(359) Reay, D. S.; Davidson, E. A.; Smith, K. A.; Smith, P.; Melillo, J. M.; Dentener, F.; Crutzen, P. J. Global Agriculture and Nitrous Oxide Emissions. *Nat. Clim. Change* **2012**, *2*, 410−416.
(360) Venterea, R. T.; Halvorson, A. D.; Kitchen, N.; Liebig, M. A.; Cavigelli, M. A.; Grosso, S. J. D.; Motavalli, P. P.; Nelson, K. A.; Spokas, K. A.; Singh, B. P.; et al. Challenges and Opportunities for Mitigating Nitrous Oxide Emissions from Fertilized Cropping Systems. *Front. Ecol. Environ.* **2012**, *10*, 562−570.
(361) Chu, X.; Qu, Y.; Zada, A.; Bai, L.; Li, Z.; Yang, F.; Zhao, L.; Zhang, G.; Sun, X.; Yang, Z. D.; et al. Ultrathin Phosphate-Modulated Co Phthalocyanine/g-C_3N_4 Heterojunction Photocatalysts with Single Co−N_4 (II) Sites for Efficient O_2 Activation. *Adv. Sci.* **2020**, *7*, 2001543.
(362) Ettwig, K. F.; Butler, M. K.; Le Paslier, D.; Pelletier, E.; Mangenot, S.; Kuypers, M. M.; Schreiber, F.; Dutilh, B. E.; Zedelius, J.; de Beer, D.; et al. Nitrite-Driven Anaerobic Methane Oxidation by Oxygenic Bacteria. *Nature* **2010**, *464*, 543−548.
(363) Prather, M. J.; Hsu, J. Coupling of Nitrous Oxide and Methane by Global Atmospheric Chemistry. *Science* **2010**, *330*, 952−954.
(364) Arinaga, A. M.; Ziegelski, M. C.; Marks, T. J. Alternative Oxidants for the Catalytic Oxidative Coupling of Methane. *Angew. Chem., Int. Ed.* **2021**, *60*, 10502−10515.
(365) Schröder, D.; Schwarz, H. FeO⊕ Activates Methane. *Angew. Chem., Int. Ed.* **1990**, *29*, 1433−1434.
(366) Yoshizawa, K.; Shiota, Y.; Yamabe, T. Methane−Methanol Conversion by MnO^+, FeO^+, and CoO^+: A Theoretical Study of Catalytic Selectivity. *J. Am. Chem. Soc.* **1998**, *120*, 564−572.
(367) Shiota, Y.; Yoshizawa, K. Methane-to-Methanol Conversion by First-Row Transition-Metal Oxide Ions: ScO^+, TiO^+, VO^+, CrO^+, MnO^+, FeO^+, CoO^+, NiO^+, and CuO^+. *J. Am. Chem. Soc.* **2000**, *122*, 12317−12326.
(368) Chen, Y.-M.; Clemmer, D.; Armentrout, P. Conversion of CH_4 to CH_3OH: Reactions of CoO^+ with CH_4 and D_2, Co^+ with CH_3OD and D_2O, and Co^+ (CH_3OD) with Xe. *J. Am. Chem. Soc.* **1994**, *116*, 7815−7826.
(369) Zecchina, A.; Rivallan, M.; Berlier, G.; Lamberti, C.; Ricchiardi, G. Structure and Nuclearity of Active Sites in Fe-Zeolites: Comparison with Iron Sites in Enzymes and Homogeneous Catalysts. *Phys. Chem. Chem. Phys.* **2007**, *9*, 3483−3499.
(370) Zhao, G.; Chodyko, K.; Benhelal, E.; Adesina, A.; Kennedy, E.; Stockenhuber, M. Methane Oxidation by N_2O over Fe-FER Catalysts Prepared by Different Methods: Nature of Active Iron Species, Stability of Surface Oxygen Species and Selectivity to Products. *J. Catal.* **2021**, *400*, 10−19.
(371) Fellah, M. F.; Onal, I. Direct Methane Oxidation to Methanol by N_2O on Fe-and Co-ZSM-5 Clusters With and Without Water: A Density Functional Theory Study. *J. Phys. Chem. C* **2010**, *114*, 3042−3051.
(372) Yuan, J.; Zhang, W.; Li, X.; Yang, J. A High Performance Catalyst for Methane Conversion to Methanol: Graphene Supported Single Atom Co. *Chem. Commun.* **2018**, *54*, 2284−2287.
(373) Li, Q.; Ouyang, Y.; Li, H.; Wang, L.; Zeng, J. Photocatalytic Conversion of Methane: Recent Advancements and Prospects. *Angew. Chem., Int. Ed.* **2022**, *61*, e202108069.
(374) Zhu, Z.; Guo, W.; Zhang, Y.; Pan, C.; Xu, J.; Zhu, Y.; Lou, Y. Research Progress on Methane Conversion Coupling Photocatalysis and Thermocatalysis. *Carbon Energy* **2021**, *3*, 519−540.
(375) Song, H.; Meng, X.; Wang, Z.-j.; Liu, H.; Ye, J. Solar-Energy-Mediated Methane Conversion. *Joule* **2019**, *3*, 1606−1636.
(376) Chen, X.; Li, Y.; Pan, X.; Cortie, D.; Huang, X.; Yi, Z. Photocatalytic Oxidation of Methane over Silver Decorated Zinc Oxide Nanocatalysts. *Nat. Commun.* **2016**, *7*, 12273.
(377) Huang, E.; Orozco, I.; Ramírez, P. J.; Liu, Z.; Zhang, F.; Mahapatra, M.; Nemšák, S. r.; Senanayake, S. D.; Rodriguez, J. A.; Liu, P. Selective Methane Oxidation to Methanol on ZnO/Cu2O/Cu (111) Catalysts: Multiple Site-Dependent Behaviors. *J. Am. Chem. Soc.* **2021**, *143*, 19018−19032.
(378) Yang, J.; Hao, J.; Wei, J.; Dai, J.; Li, Y. Visible-Light-Driven Selective Oxidation of Methane to Methanol on Amorphous FeOOH Coupled m-WO_3. *Fuel* **2020**, *266*, 117104.
(379) Hu, A.; Guo, J.-J.; Pan, H.; Zuo, Z. Selective Functionalization of Methane, Ethane, and Higher Alkanes by Cerium Photocatalysis. *Science* **2018**, *361*, 668−672.
(380) Yovanovich, M.; da Silva, A. J.; de Souza, R. F.; Ussui, V.; Neto, A. O.; Lazar, D. R. Conversion of Methane to Methanol using

https://doi.org/10.1021/acsnano.2c02464
ACS Nano XXXX, XXX, XXX−XXX

WO_3/TiO_2 Porous Photocatalyst. *Int. J. Electrochem. Sci.* **2021**, *16*, 210735.
(381) Li, Z.; Pan, X.; Yi, Z. Photocatalytic Oxidation of Methane over CuO-Decorated ZnO Nanocatalysts. *J. Mater. Chem. A* **2019**, *7*, 469−475.
(382) Li, L.; Li, G. D.; Yan, C.; Mu, X. Y.; Pan, X. L.; Zou, X. X.; Wang, K. X.; Chen, J. S. Efficient Sunlight-Driven Dehydrogenative Coupling of Methane to Ethane over a Zn^+-Modified Zeolite. *Angew. Chem., Int. Ed.* **2011**, *50*, 8299−8303.
(383) Cortie, D.; Yi, Z.; Chen, X.; Li, Y.; Pan, X.; Huang, X. Photocatalytic Oxidation of Methane over Silver Decorated Zinc Oxide Nanocatalysts. *Nat. Commun.* **2016**, *7*, 12273.
(384) Yu, X.; De Waele, V.; Löfberg, A.; Ordomsky, V.; Khodakov, A. Y. Selective Photocatalytic Conversion of Methane into Carbon Monoxide over Zinc-Heteropolyacid-Titania Nanocomposites. *Nat. Commun.* **2019**, *10*, 700.
(385) Song, H.; Meng, X.; Wang, S.; Zhou, W.; Wang, X.; Kako, T.; Ye, J. Direct and Selective Photocatalytic Oxidation of CH_4 to Oxygenates with O_2 on Cocatalysts/ZnO at Room Temperature in Water. *J. Am. Chem. Soc.* **2019**, *141*, 20507−20515.
(386) Fan, Y.; Zhou, W.; Qiu, X.; Li, H.; Jiang, Y.; Sun, Z.; Han, D.; Niu, L.; Tang, Z. Selective Photocatalytic Oxidation of Methane by Quantum-Sized Bismuth Vanadate. *Nat. Sustain.* **2021**, *4*, 509−515.
(387) Gong, E.; Ali, S.; Hiragond, C. B.; Kim, H. S.; Powar, N. S.; Kim, D.; Kim, H.; In, S.-I. Solar Fuels: Research and Development Strategies to Accelerate Photocatalytic CO_2 Conversion into Hydrocarbon Fuels. *Energy Environ. Sci.* **2022**, *15*, 880−937.
(388) Hiragond, C. B.; Lee, J.; Kim, H.; Jung, J.-W.; Cho, C.-H.; In, S.-I. A Novel N-Doped Graphene Oxide Enfolded Reduced Titania for Highly Stable and Selective Gas-Phase Photocatalytic CO_2 Reduction into CH_4: An In-Depth Study on the Interfacial Charge Transfer Mechanism. *Chem. Eng. J.* **2021**, *416*, 127978.
(389) Kumar, P.; Kar, P.; Manuel, A. P.; Zeng, S.; Thakur, U. K.; Alam, K. M.; Zhang, Y.; Kisslinger, R.; Cui, K.; Bernard, G. M.; et al. Noble Metal Free, Visible Light Driven Photocatalysis using TiO_2 Nanotube Arrays Sensitized by P-doped C_3N_4 Quantum Dots. *Adv. Opt. Mater.* **2020**, *8*, 1901275.
(390) Kar, P.; Zeng, S.; Zhang, Y.; Vahidzadeh, E.; Manuel, A.; Kisslinger, R.; Alam, K. M.; Thakur, U. K.; Mahdi, N.; Kumar, P.; et al. High Rate CO_2 Photoreduction using Flame Annealed TiO_2 Nanotubes. *Appl. Catal., B* **2019**, *243*, 522−536.
(391) Sorcar, S.; Hwang, Y.; Lee, J.; Kim, H.; Grimes, K. M.; Grimes, C. A.; Jung, J.-W.; Cho, C.-H.; Majima, T.; Hoffmann, M. R.; et al. CO_2, Water, and Sunlight to Hydrocarbon Fuels: A Sustained Sunlight to Fuel (Joule-to-Joule) Photoconversion Efficiency of 1%. *Energy Environ. Sci.* **2019**, *12*, 2685−2696.
(392) Vahidzadeh, E.; Zeng, S.; Alam, K. M.; Kumar, P.; Riddell, S.; Chaulagain, N.; Gusarov, S.; Kobryn, A. E.; Shankar, K. Harvesting Hot Holes in Plasmon-Coupled Ultrathin Photoanodes for High-Performance Photoelectrochemical Water Splitting. *ACS Appl. Mater. Interfaces* **2021**, *13*, 42741−42752.
(393) Zeng, S.; Vahidzadeh, E.; VanEssen, C. G.; Kar, P.; Kisslinger, R.; Goswami, A.; Zhang, Y.; Mahdi, N.; Riddell, S.; Kobryn, A. E.; et al. Optical Control of Selectivity of High Rate CO_2 Photoreduction via Interband-or Hot Electron Z-Scheme Reaction Pathways in Au-TiO_2 Plasmonic Photonic Crystal Photocatalyst. *Appl. Catal., B* **2020**, *267*, 118644.
(394) Chen, X.; Liu, L.; Yu, P. Y.; Mao, S. S. Increasing Solar Absorption for Photocatalysis with Black Hydrogenated Titanium Dioxide Nanocrystals. *Science* **2011**, *331*, 746−750.
(395) Laishram, D.; Shejale, K. P.; Gupta, R.; Sharma, R. K. Heterostructured HfO_2/TiO_2 Spherical Nanoparticles for Visible Photocatalytic Water Remediation. *Mater. Lett.* **2018**, *231*, 225−228.
(396) Lü, X.; Chen, A.; Luo, Y.; Lu, P.; Dai, Y.; Enriquez, E.; Dowden, P.; Xu, H.; Kotula, P. G.; Azad, A. K.; et al. Conducting Interface in Oxide Homojunction: Understanding of Superior Properties in Black TiO_2. *Nano Lett.* **2016**, *16*, 5751−5755.
(397) Ali-Löytty, H.; Hannula, M.; Saari, J.; Palmolahti, L.; Bhuskute, B. D.; Ulkuniemi, R.; Nyyssönen, T.; Lahtonen, K.; Valden, M. Diversity of TiO_2: Controlling the Molecular and Electronic Structure of Atomic-Layer-Deposited Black TiO_2. *ACS Appl. Mater. Interfaces* **2019**, *11*, 2758−2762.
(398) Tian, M.; Mahjouri-Samani, M.; Eres, G.; Sachan, R.; Yoon, M.; Chisholm, M. F.; Wang, K.; Puretzky, A. A.; Rouleau, C. M.; Geohegan, D. B.; et al. Structure and Formation Mechanism of Black TiO_2 Nanoparticles. *ACS Nano* **2015**, *9*, 10482−10488.
(399) Naldoni, A.; Allieta, M.; Santangelo, S.; Marelli, M.; Fabbri, F.; Cappelli, S.; Bianchi, C. L.; Psaro, R.; Dal Santo, V. Effect of Nature and Location of Defects on Bandgap Narrowing in Black TiO_2 Nanoparticles. *J. Am. Chem. Soc.* **2012**, *134*, 7600−7603.
(400) Naldoni, A.; Altomare, M.; Zoppellaro, G.; Liu, N.; Kment, S.; Zboril, R.; Schmuki, P. Photocatalysis with Reduced TiO_2: From Black TiO_2 to Cocatalyst-Free Hydrogen Production. *ACS Catal.* **2019**, *9*, 345−364.
(401) Di Valentin, C.; Pacchioni, G.; Selloni, A. Reduced and n-Type Doped TiO_2: Nature of Ti^{3+} Species. *J. Phys. Chem. C* **2009**, *113*, 20543−20552.
(402) Hejazi, S. H.; Shahrezaei, M.; Błoński, P.; Allieta, M.; Sheverdyaeva, P. M.; Moras, P.; Badura, Z.; Kalytchuk, S.; Mohammadi, E.; Zbořil, R.; et al. Defect Engineering over Anisotropic Brookite Toward Substrate-Specific Photo-Oxidation of Alcohols. *Chem. Catal.* **2022**, *2*, 1177.
(403) Pan, X.; Xu, Y.-J. Defect-Mediated Growth of Noble-Metal (Ag, Pt, and Pd) Nanoparticles on TiO_2 with Oxygen Vacancies for Photocatalytic Redox Reactions under Visible Light. *J. Phys. Chem. C* **2013**, *117*, 17996−18005.
(404) Zhou, X.; Hwang, I.; Tomanec, O.; Fehn, D.; Mazare, A.; Zboril, R.; Meyer, K.; Schmuki, P. Advanced Photocatalysts: Pinning Single Atom Co-Catalysts on Titania Nanotubes. *Adv. Funct. Mater.* **2021**, *31*, 2102843.
(405) Lee, B.-H.; Gong, E.; Kim, M.; Park, S.; Kim, H. R.; Lee, J.; Jung, E.; Lee, C. W.; Bok, J.; Jung, Y.; et al. Electronic Interaction Between Transition Metal Single-Atoms and Anatase TiO_2 Boosts CO_2 Photoreduction with H_2O. *Energy Environ. Sci.* **2022**, *15*, 601−609.
(406) Li, B.; Lai, C.; Zeng, G.; Huang, D.; Qin, L.; Zhang, M.; Cheng, M.; Liu, X.; Yi, H.; Zhou, C.; et al. Black Phosphorus, A Rising Star 2D Nanomaterial in the Post-Graphene Era: Synthesis, Properties, Modifications, and Photocatalysis Applications. *Small* **2019**, *15*, 1804565.
(407) Ling, X.; Wang, H.; Huang, S.; Xia, F.; Dresselhaus, M. S. The renaissance of black phosphorus. *Proc. Natl. Acad. Sci. U. S. A.* **2015**, *112*, 4523−4530.
(408) Brent, J. R.; Savjani, N.; Lewis, E. A.; Haigh, S. J.; Lewis, D. J.; O'Brien, P. Production of Few-Layer Phosphorene by Liquid Exfoliation of Black Phosphorus. *Chem. Commun.* **2014**, *50*, 13338−13341.
(409) Zhao, W.; Xue, Z.; Wang, J.; Jiang, J.; Zhao, X.; Mu, T. Large-Scale, Highly Efficient, and Green Liquid-Exfoliation of Black Phosphorus in Ionic Liquids. *ACS Appl. Mater. Interfaces* **2015**, *7*, 27608−27612.
(410) Yasaei, P.; Kumar, B.; Foroozan, T.; Wang, C.; Asadi, M.; Tuschel, D.; Indacochea, J. E.; Klie, R. F.; Salehi-Khojin, A. High-Quality Black Phosphorus Atomic Layers by Liquid-Phase Exfoliation. *Adv. Mater.* **2015**, *27*, 1887−1892.
(411) Batmunkh, M.; Bat-Erdene, M.; Shapter, J. G. Phosphorene and Phosphorene-Based Materials−Prospects for Future Applications. *Adv. Mater.* **2016**, *28*, 8586−8617.
(412) Wang, M.; Shi, H.; Tian, M.; Chen, R.; Shu, J.; Zhang, Q.; Wang, Y.; Li, C.; Wan, N.; Lei, S. Single Nickel Atom-Modified Phosphorene Nanosheets for Electrocatalytic CO_2 Reduction. *ACS Appl. Nano Mater.* **2021**, *4*, 11017−11030.
(413) Luo, L.; Luo, J.; Li, H.; Ren, F.; Zhang, Y.; Liu, A.; Li, W.-X.; Zeng, J. Water Enables Mild Oxidation of Methane to Methanol on Gold Single-Atom Catalysts. *Nat. Commun.* **2021**, *12*, 1218.
(414) Zhang, Y.; Guo, L.; Tao, L.; Lu, Y.; Wang, S. Defect-Based Single-Atom Electrocatalysts. *Small Methods* **2019**, *3*, 1800406.

https://doi.org/10.1021/acsnano.2c02464
ACS Nano XXXX, XXX, XXX−XXX

(415) Hejazi, S.; Mohajernia, S.; Osuagwu, B.; Zoppellaro, G.; Andryskova, P.; Tomanec, O.; Kment, S.; Zbořil, R.; Schmuki, P. On the Controlled Loading of Single Platinum Atoms as a Co-Catalyst on TiO_2 Anatase for Optimized Photocatalytic H_2 Generation. *Adv. Mater.* **2020**, *32*, 1908505.

(416) Jiang, D.; Yao, Y.; Li, T.; Wan, G.; Pereira-Hernández, X. I.; Lu, Y.; Tian, J.; Khivantsev, K.; Engelhard, M. H.; Sun, C.; et al. Tailoring the Local Environment of Platinum in Single-Atom Pt_1/CeO_2 Catalysts for Robust Low-Temperature CO Oxidation. *Angew. Chem., Int. Ed.* **2021**, *60*, 26054−26062.

(417) Liu, J.-C.; Tang, Y.; Wang, Y.-G.; Zhang, T.; Li, J. Theoretical Understanding of the Stability of Single-Atom Catalysts. *Natl. Sci. Rev.* **2018**, *5*, 638−641.

(418) Cai, S.; Wang, L.; Heng, S.; Li, H.; Bai, Y.; Dang, D.; Wang, Q.; Zhang, P.; He, C. Interaction of Single-Atom Platinum−Oxygen Vacancy Defects for the Boosted Photosplitting Water H_2 Evolution and CO_2 Photoreduction: Experimental and Theoretical Study. *J. Phys. Chem. C* **2020**, *124*, 24566−24579.

(419) Wei, T.; Zhu, Y.; Wu, Y.; An, X.; Liu, L.-M. Effect of Single-Atom Cocatalysts on the Activity of Faceted TiO_2 Photocatalysts. *Langmuir* **2019**, *35*, 391−397.

(420) Du, C.; Lin, H.; Lin, B.; Ma, Z.; Hou, T.; Tang, J.; Li, Y. MoS_2 Supported Single Platinum Atoms and Their Superior Catalytic Activity for CO Oxidation: A Density Functional Theory Study. *J. Mater. Chem. A* **2015**, *3*, 23113−23119.

(421) Meza, E.; Diaz, R. E.; Li, C. W. Solution-Phase Activation and Functionalization of Colloidal WS_2 Nanosheets with Ni Single Atoms. *ACS Nano* **2020**, *14*, 2238−2247.

(422) Lou, Y.; Zheng, Y.; Li, X.; Ta, N.; Xu, J.; Nie, Y.; Cho, K.; Liu, J. Pocketlike Active Site of Rh_1/MoS_2 Single-Atom Catalyst for Selective Crotonaldehyde Hydrogenation. *J. Am. Chem. Soc.* **2019**, *141*, 19289−19295.

(423) Lei, Y.; Butler, D.; Lucking, M. C.; Zhang, F.; Xia, T.; Fujisawa, K.; Granzier-Nakajima, T.; Cruz-Silva, R.; Endo, M.; Terrones, H.; et al. Single-Atom Doping of MoS_2 with Manganese Enables Ultrasensitive Detection of Dopamine: Experimental and Computational Approach. *Sci. Adv.* **2020**, *6*, eabc4250.

(424) Zhao, D.; Chen, Z.; Yang, W.; Liu, S.; Zhang, X.; Yu, Y.; Cheong, W.-C.; Zheng, L.; Ren, F.; Ying, G.; et al. MXene (Ti_3C_2) Vacancy-Confined Single-Atom Catalyst for Efficient Functionalization of CO_2. *J. Am. Chem. Soc.* **2019**, *141*, 4086−4093.

(425) Fei, H.; Dong, J.; Feng, Y.; Allen, C. S.; Wan, C.; Volosskiy, B.; Li, M.; Zhao, Z.; Wang, Y.; Sun, H.; et al. General Synthesis and Definitive Structural Identification of MN_4C_4 Single-Atom Catalysts with Tunable Electrocatalytic Activities. *Nat. Catal.* **2018**, *1*, 63−72.

(426) Yang, H.; Shang, L.; Zhang, Q.; Shi, R.; Waterhouse, G. I.; Gu, L.; Zhang, T. A Universal Ligand Mediated Method for Large Scale Synthesis of Transition Metal Single Atom Catalysts. *Nat. Commun.* **2019**, *10*, 4585.

(427) Kumar, P.; Laishram, D.; Sharma, R. K.; Vinu, A.; Hu, J.; Kibria, M. G. Boosting Photocatalytic Activity Using Carbon Nitride Based 2D/2D van der Waals Heterojunctions. *Chem. Mater.* **2021**, *33*, 9012−9092.

(428) Kumar, P.; Vahidzadeh, E.; Thakur, U. K.; Kar, P.; Alam, K. M.; Goswami, A.; Mahdi, N.; Cui, K.; Bernard, G. M.; Michaelis, V. K.; et al. C_3N_5: A Low Bandgap Semiconductor Containing An Azo-linked Carbon Nitride Framework for Photocatalytic, Photovoltaic and Adsorbent Applications. *J. Am. Chem. Soc.* **2019**, *141*, 5415−5436.

(429) Kessler, F. K.; Zheng, Y.; Schwarz, D.; Merschjann, C.; Schnick, W.; Wang, X.; Bojdys, M. J. Functional Carbon Nitride Materials-Design Strategies for Electrochemical Devices. *Nat. Rev. Mater.* **2017**, *2*, 17030.

(430) Teng, Z.; Zhang, Q.; Yang, H.; Kato, K.; Yang, W.; Lu, Y.-R.; Liu, S.; Wang, C.; Yamakata, A.; Su, C.; et al. Atomically Dispersed Antimony on Carbon Nitride for the Artificial Photosynthesis of Hydrogen Peroxide. *Nat. Catal.* **2021**, *4*, 374−384.

(431) Chen, Z.; Zhao, J.; Cabrera, C. R.; Chen, Z. Computational Screening of Efficient Single-Atom Catalysts Based on Graphitic Carbon Nitride (g-C_3N_4) for Nitrogen Electroreduction. *Small Methods* **2019**, *3*, 1800368.

(432) Chen, Z.; Vorobyeva, E.; Mitchell, S.; Fako, E.; López, N.; Collins, S. M.; Leary, R. K.; Midgley, P. A.; Hauert, R.; Pérez-Ramírez, J. Single-Atom Heterogeneous Catalysts Based on Distinct Carbon Nitride Scaffolds. *Natl. Sci. Rev.* **2018**, *5*, 642−652.

(433) Chen, Z.; Mitchell, S.; Vorobyeva, E.; Leary, R. K.; Hauert, R.; Furnival, T.; Ramasse, Q. M.; Thomas, J. M.; Midgley, P. A.; Dontsova, D.; et al. Stabilization of Single Metal Atoms on Graphitic Carbon Nitride. *Adv. Funct. Mater.* **2017**, *27*, 1605785.

(434) Kumar, P.; Boukherroub, R.; Shankar, K. Sunlight-Driven Water-Splitting Using Two-Dimensional Carbon Based Semiconductors. *J. Mater. Chem. A* **2018**, *6*, 12876−12931.

(435) Chu, C.; Zhu, Q.; Pan, Z.; Gupta, S.; Huang, D.; Du, Y.; Weon, S.; Wu, Y.; Muhich, C.; Stavitski, E.; et al. Spatially Separating Redox Centers on 2D Carbon Nitride with Cobalt Single Atom for Photocatalytic H_2O_2 Production. *Proc. Natl. Acad. Sci. U. S. A.* **2020**, *117*, 6376−6382.

(436) Zhang, W.; Peng, Q.; Shi, L.; Yao, Q.; Wang, X.; Yu, A.; Chen, Z.; Fu, Y. Merging Single-Atom-Dispersed Iron and Graphitic Carbon Nitride to a Joint Electronic System for High-Efficiency Photocatalytic Hydrogen Evolution. *Small* **2019**, *15*, 1905166.

(437) Sharma, P.; Kumar, S.; Tomanec, O.; Petr, M.; Zhu Chen, J.; Miller, J. T.; Varma, R. S.; Gawande, M. B.; Zbořil, R. Carbon Nitride-Based Ruthenium Single Atom Photocatalyst for CO_2 Reduction to Methanol. *Small* **2021**, *17* (16), 2006478.

(438) Zheng, M.; Xu, H.; Li, Y.; Ding, K.; Zhang, Y.; Sun, C.; Chen, W.; Lin, W. Electrocatalytic Nitrogen Reduction by Transition Metal Single-Atom Catalysts on Polymeric Carbon Nitride. *J. Phys. Chem. C* **2021**, *125*, 13880−13888.

(439) Wang, G.; Zhang, T.; Yu, W.; Si, R.; Liu, Y.; Zhao, Z. Modulating Location of Single Copper Atoms in Polymeric Carbon Nitride for Enhanced Photoredox Catalysis. *ACS Catal.* **2020**, *10*, 5715−5722.

(440) Yang, P.; Zuo, S.; Zhang, F.; Yu, B.; Guo, S.; Yu, X.; Zhao, Y.; Zhang, J.; Liu, Z. Carbon Nitride-Based Single-Atom Cu Catalysts for Highly Efficient Carboxylation of Alkynes with Atmospheric CO_2. *Ind. Eng. Chem. Res.* **2020**, *59*, 7327−7335.

(441) Farrell, B. L.; Igenegbai, V. O.; Linic, S. A Viewpoint on Direct Methane Conversion to Ethane and Ethylene using Oxidative Coupling on Solid Catalysts. *ACS Catal.* **2016**, *6*, 4340−4346.

(442) Levin, N.; Lengyel, J.; Eckhard, J. F.; Tschurl, M.; Heiz, U. Catalytic Non-Oxidative Coupling of Methane on $Ta_8O_2^+$. *J. Am. Chem. Soc.* **2020**, *142* (12), 5862−5869.

(443) Okolie, C.; Belhseine, Y. F.; Lyu, Y.; Yung, M. M.; Engelhard, M. H.; Kovarik, L.; Stavitski, E.; Sievers, C. Conversion of Methane into Methanol and Ethanol over Nickel Oxide on Ceria−Zirconia Catalysts in a Single Reactor. *Angew. Chem., Int. Ed.* **2017**, *56*, 13876−13881.

(444) Zhou, Y.; Wang, H.; Liu, X.; Qiao, S.; Shao, D.; Zhou, J.; Zhang, L.; Wang, W. Direct Piezocatalytic Conversion of Methane into Alcohols over Hydroxyapatite. *Nano Energy* **2021**, *79*, 105449.

(445) Wang, Z.; Liu, Y.; Zhang, H.; Zhou, X. Cubic Platinum Nanoparticles Capped with Cs_2[closo-$B_{12}H_{12}$] as an Effective Oxidation Catalyst for Converting Methane to Ethanol. *J. Colloid Interface Sci.* **2020**, *566*, 135−142.

(446) Shen, X.; Wu, D.; Fu, X.-Z.; Luo, J.-L. Highly Selective Conversion of Methane to Ethanol over $CuFe_2O_4$-Carbon Nanotube Catalysts at Low Temperature. *Chin. Chem. Lett.* **2022**, *33*, 390−393.

(447) Song, Y.; Zhao, Y.; Nan, G.; Chen, W.; Guo, Z.; Li, S.; Tang, Z.; Wei, W.; Sun, Y. Electrocatalytic Oxidation of Methane to Ethanol via NiO/Ni Interface. *Appl. Catal., B* **2020**, *270*, 118888.

(448) Abd El-Hafiz, D. R.; Sakr, A. A.-E.; Ebiad, M. A. Methane Bi-Reforming for Direct Ethanol Production over Smart Cu/Mn-Ferrite Catalysts. *Renew. Energy* **2021**, *167*, 236−247.

(449) Zhou, Y.; Zhang, L.; Wang, W. Direct Functionalization of Methane into Ethanol over Copper Modified Polymeric Carbon Nitride via Photocatalysis. *Nat. Commun.* **2019**, *10* (1), 506.

https://doi.org/10.1021/acsnano.2c02464
ACS Nano XXXX, XXX, XXX−XXX

(450) Shan, J.; Ye, C.; Jiang, Y.; Jaroniec, M.; Zheng, Y.; Qiao, S.-Z. Metal-Metal Interactions in Correlated Single-Atom Catalysts. *Sci. Adv.* **2022**, *8*, eabo0762.
(451) Yang, Y.; Qian, Y.; Li, H.; Zhang, Z.; Mu, Y.; Do, D.; Zhou, B.; Dong, J.; Yan, W.; Qin, Y.; et al. O-Coordinated W-Mo Dual-Atom Catalyst for pH-Universal Electrocatalytic Hydrogen Evolution. *Sci. Adv.* **2020**, *6*, eaba6586.
(452) Zhang, L.; Fischer, J. M. T. A.; Jia, Y.; Yan, X.; Xu, W.; Wang, X.; Chen, J.; Yang, D.; Liu, H.; Zhuang, L.; et al. Coordination of Atomic Co−Pt Coupling Species at Carbon Defects as Active Sites for Oxygen Reduction Reaction. *J. Am. Chem. Soc.* **2018**, *140*, 10757−10763.
(453) Zhou, Y.; Yang, W.; Utetiwabo, W.; Lian, Y.-m.; Yin, X.; Zhou, L.; Yu, P.; Chen, R.; Sun, S. Revealing of Active Sites and Catalytic Mechanism in N-Coordinated Fe, Ni Dual-Doped Carbon with Superior Acidic Oxygen Reduction than Single-Atom Catalyst. *J. Phys. Chem. Lett.* **2020**, *11*, 1404−1410.
(454) Zhang, W.; Chao, Y.; Zhang, W.; Zhou, J.; Lv, F.; Wang, K.; Lin, F.; Luo, H.; Li, J.; Tong, M.; et al. Emerging Dual-Atomic-Site Catalysts for Efficient Energy Catalysis. *Adv. Mater.* **2021**, *33*, 2102576.
(455) Tian, S.; Fu, Q.; Chen, W.; Feng, Q.; Chen, Z.; Zhang, J.; Cheong, W.-C.; Yu, R.; Gu, L.; Dong, J.; et al. Carbon Nitride Supported Fe_2 Cluster Catalysts with Superior Performance for Alkene Epoxidation. *Nat. Commun.* **2018**, *9*, 2353.
(456) Yang, N.; Zhao, Y.; Wu, P.; Liu, G.; Sun, F.; Ma, J.; Jiang, Z.; Sun, Y.; Zeng, G. Defective C_3N_4 Frameworks Coordinated Diatomic Copper Catalyst: Towards Mild Oxidation of Methane to C1 Oxygenates. *Appl. Catal., B* **2021**, *299*, 120682.
(457) Wang, H.; Xin, W.; Wang, Q.; Zheng, X.; Lu, Z.; Pei, R.; He, P.; Dong, X. Direct Methane Conversion with Oxygen and CO over Hydrophobic dB-ZSM-5 Supported Rh Single-Atom Catalyst. *Catal. Commun.* **2022**, *162*, 106374.
(458) Luo, L.; Fu, L.; Liu, H.; Xu, Y.; Xing, J.; Tang, J. Synergy of Single Atoms Pd and Oxygen Vacancies on In_2O_3 for Highly Selective C_1 Oxygenates Production from Methane under Visible Light. *Research Square Preprint*, September 30, 2021, ver. 1. DOI: 10.21203/rs.3.rs-942037/v1.
(459) Ohyama, J.; Abe, D.; Hirayama, A.; Iwai, H.; Tsuchimura, Y.; Sakamoto, K.; Irikura, M.; Nakamura, Y.; Yoshida, H.; Machida, M.; et al. Selective Oxidation of Methane to Formaldehyde over a Silica-Supported Cobalt Single-Atom Catalyst. *J. Phys. Chem. C* **2022**, *126*, 1785−1792.

https://doi.org/10.1021/acsnano.2c02464
ACS Nano XXXX, XXX, XXX−XXX